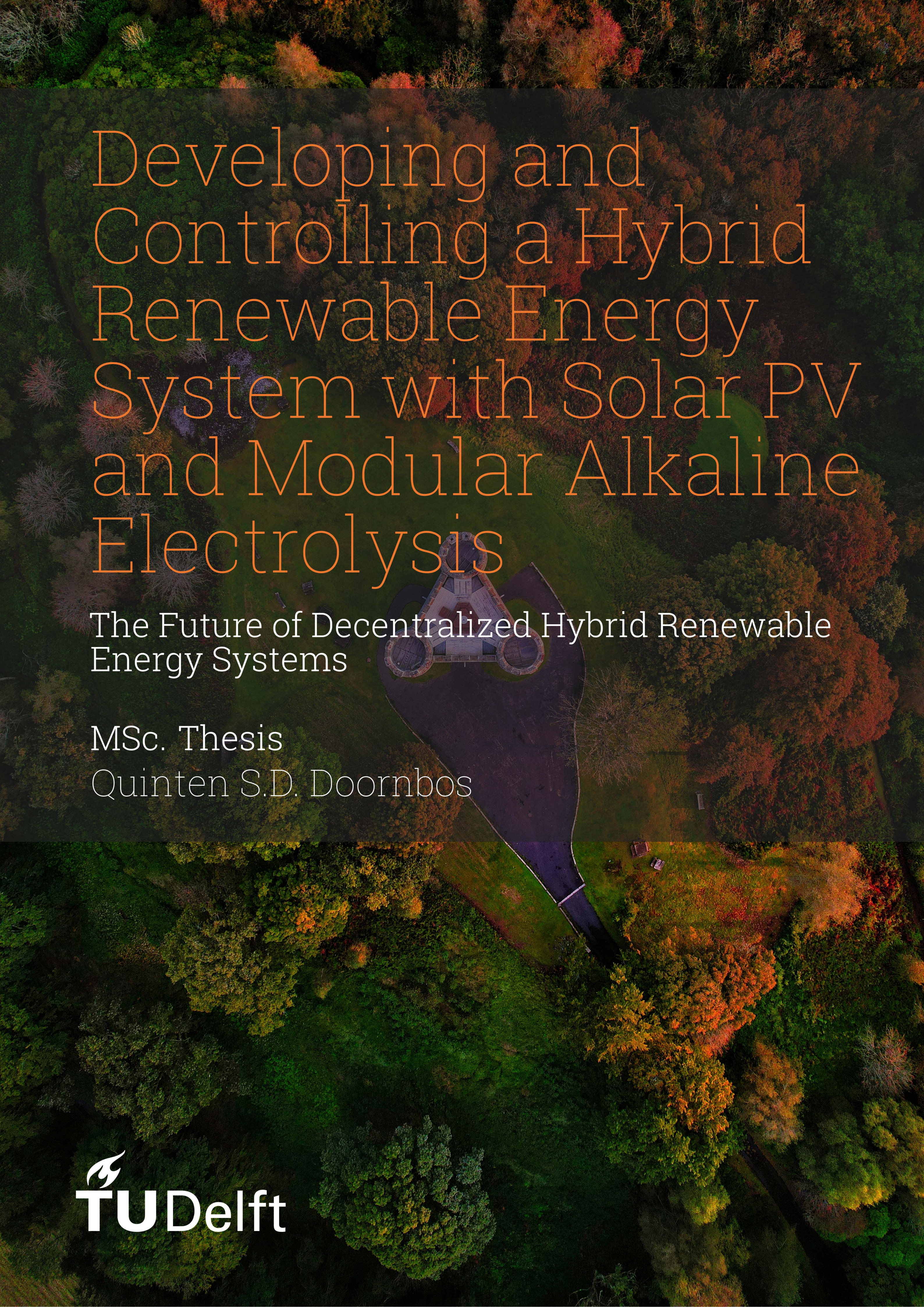

Developing and Controlling a Hybrid Renewable Energy System with Solar PV and Modular Alkaline Electrolysis

The Future of Decentralized Hybrid Renewable Energy Systems

MSc. Thesis

Quinten S.D. Doornbos

Developing and Controlling a Hybrid Renewable Energy System with Solar PV and Modular Alkaline Electrolysis

The Future of Decentralized Hybrid Renewable Energy Systems

by

Quinten S.D. Doornbos

to obtain the degree of Master of Science
at the Delft University of Technology,
to be defended publicly on Monday July 10th, 2023 at 14:00.

Student number:	4647971	
Research duration:	November 21, 2023 – July 10, 2023	
Thesis committee:	Prof. Dr. T. J. H. Vlugt,	TU Delft, chair
	Dr. M. Ramdin,	TU Delft, supervisor
	Prof. Dr. W. de Jong,	TU Delft, member
	Dr. A. Somoza-Tornos,	TU Delft, member
	Dr. A. Rahbari,	XINTC & TU Delft, company supervisor

This thesis is confidential and cannot be made public until July 10, 2025.

TU Delft

Acknowledgements

In the past few months, I have had the pleasure of meeting many new faces. This research project has been unlike any project I have done before. Most notably, learning how to handle absolute responsibility for a project and its outcomes was a valuable learning experience.

First, I would like to thank my daily supervisor, Reza. Without your support, this research would not have developed the way it has. I admire your degree of involvement in all of XINTC's active research projects and I believe that all of those projects benefit from your involvement. Since the start of my thesis, the XINTC R&D office in Delft has grown into one we can all be proud of. I wish you and all of the other colleagues in Delft all the best!

Next, I wanted to show my appreciation for the weekly support from my TU Delft project supervisors, Thijs and Mahinder. From the day I started my research, you have been keen to assist me in developing the project and help me achieve a result to be proud of. I hope you both have enjoyed this new area of research as much as I have!

I would also like to express my gratitude to the XINTC colleagues in Eerbeek. Particularly, the support from Wilko, Albert, Ron, Wesley and Han. You have all played a crucial role in the success of this research paper. There are big things to come for XINTC and I wish all of you the best of luck!

Last but not least, I would like to thank my friends and family. Being able to take a step back from my research and the responsibilities once in a while has really helped me stay motivated throughout these past few months. Everyone needs a support system in order to perform well, and I am super lucky to have so many amazing individuals in mine.

Quinten S.D. Doornbos
Delft, June 2023

Abstract

Renewable energy resources like wind and solar have the potential to revolutionize our energy infrastructure and enable a decarbonized society. The intermittent nature of renewables poses a challenge for ensuring a consistent and reliable electricity supply. Hydrogen technology is emerging as a promising solution for stabilizing renewable energy systems. There is still significant technological development required to cost-effectively integrate hydrogen with renewable energy assets. Conventional PV solar installations require power electronics for their operation, like charge controllers and inverters. Not only are these power electronic components costly and in high demand, but they also degrade faster than PV solar panels. Removing power electronic components could significantly lower the investment costs associated with a PV solar park.

This work focuses on how PV solar panels can be directly coupled to a modular alkaline electrolyzer, without grid-based buffering or the use of an inverter. Literature research revealed that hydrogen technology has seen little exploration in on-grid Hybrid Renewable Energy Systems (HRES) and no exploration in off-grid HRES. To appropriately investigate whether a directly-coupled HRES would be technically feasible, a megawatt-scale system was modelled and simulated. All elements of the HRES were modelled, duly accounting for physical limits and constraints. Components were sized and configured to complement one another, optimizing for maximum hydrogen production. To experimentally verify the validity of the proposed HRES, a 5 kW pilot system was constructed. To control the HRES, a new algorithm was developed using the Incremental Conductance maximum power point tracking algorithm as a basis. Within the new Maximum Hydrogen Production (MHP) algorithm, the step sizing was discretized and a variable step size was implemented which can be applied to any target slope. This allows for the system to target operational points which optimize hydrogen yield instead of electricity yield. Furthermore, the addition of tracking bias helped adjust for the asymmetric nature of the interaction between electrolyzer stacks and the PV solar park.

Simulation results in The Netherlands demonstrated that the feasibility of the HRES is dependent on the configuration of the PV solar park and on the number of electrolyzer stacks in the system. Compared to industrial and research benchmarks, the proposed HRES increased hydrogen production by 14.9% and 4.2%, respectively. Dynamic 'm-tracking' of the MHP algorithm goal increased hydrogen production by 0.8% in months of high irradiance. Months with a lower average irradiance experienced an artefact in the MHP algorithm, resulting in prolonged periods of zero power output. An experimental setup confirmed the simulation results, showing that it is possible to control a system of PV solar panels directly coupled to a modular alkaline electrolyzer. Experimental results revealed the need for moving average filtering to prevent fluctuations due to changing conditions of the electrolyzer and the weather from causing poor algorithm tracking ability. The low performance of the experimental setup can be attributed to a low iteration and measuring frequency, which increase the likelihood of a tracking error due to rapidly changing operating conditions. Economic analysis of the proposed HRES yielded an LCOH of €3.44, 20% and 13% lower than industrial and research benchmarks, respectively. Therefore, an HRES featuring PV solar and modular alkaline electrolysis is technologically and economically viable without the use of charge controllers and inverters.

Contents

List of Figures

List of Tables

Nomenclature

Abbreviations

Abbreviation	Definition
PV	Photovoltaic
GHG	Greenhouse Gas
OEM	Original Equipment Manufacturer
AWE	Alkaline Water Electrolysis
PEM	Polymer Electrolyte Membrane
MPP(T)	Maximum Power Point (Tracker)
PSC	Partial Shading Conditions
INC	Incremental Conductance
P&O	Perturb & Observe
LWE	Liquid Water Electrolysis
AC	Alternating Current
DC	Direct Current
HRES	Hybrid Renewable Energy System
OPEX	Operational Expenses
CAPEX	Capital Expenses
BoP	Balance of Plant
SDM	Single Diode Model
PC	Parasitic Capacitance
LCOH	Levelized Cost of Hydrogen
LCOE	Levelized Cost of Electricity

Symbols

Symbol	Definition	Unit
A	Area	[m^2]
c	Concentration	[wt%]
C_p	Specific Heat Capacity for Constant Pressure	[J kg^{-1} K^{-1}]
E^0	Standard Equilibrium Potential	[V]
F	Faraday Constant	[C mol^{-1}]
G	Gibbs Free Energy	[kJ mol^{-1}]
h, h_{ref}	Height	[m]
H	Enthalpy	[kJ mol^{-1}]
I	Current	[A]
j	Current Density	[A m^{-2}]
k_B	Boltzmann Constant	[J K^{-1}]
K	Constant	[-]
L	Length	[m]
n	Number (Count)	[-]
n_mod, n_I	Ideality Factor	[-]
p	Pressure	[Pa]
P	Power	[W]
q	Charge	[C]
r	Radius	[m]
R	Resistance	[Ω]
$\bar{R}$	Gas Constant	[J K^{-1} mol^{-1}]
Re	Reynolds Number	[-]
S	Entropy	[kJ mol^{-1} K^{-1}]
t	Time	[s]
t_life	Lifetime	[years]
T	Temperature	[K]
V	Voltage	[V]
α	Power Constant / Charge Transfer Coefficient	[-]
γ	Activity Coefficient	[-]
Δ	Difference	[-]
ϵ	Efficiency	[%]
η	Overpotential	[V]
κ	Specific Conductivity	[S m^{-1}]
ρ	Density	[kg m^{-3}]

1

Introduction

After 200,000 years of human civilization on planet Earth, humankind has managed to destroy a significant portion of our environment in merely 160 years (0.000004% of its habitable lifespan) [1]. Almost all of the 8 billion people living on earth are aware of or have experienced the effects of climate change [2]. If not through the plethora of reports, articles, movies, and social media about global warming, then through the direct consequences of climate change itself [3]. The increasing frequency of extreme weather events like droughts, hurricanes, and heatwaves, coupled with the steady rise of average global surface temperature, has resulted in serious consequences in all corners of human civilization [4]. In 1938, British scientist Guy Callendar first linked the warming of land surface to human activity, stating that of the roughly 150 billion tons of CO_2 emissions emitted in the 20th century, approximately three-quarters still remained in the atmosphere [5]. As this theory was proven by other researchers, it was proven without a doubt that human emission of Greenhouse gasses[1] (GHG) is the main cause behind global warming [6]. It took 77 years after its first discovery before the first legally binding international treaty was signed to tackle climate change and limit global warming to 2 °C [7, 8].

The Paris Agreement, signed in 2015, stipulated that all 194 participating countries must change their energy infrastructure. To achieve the demanding targets outlined in the agreement - a minimum 45% reduction in GHG emissions by 2030 and the attainment of 'Net Zero' emissions by 2050 - governments are forced to redesign their energy infrastructure. In 2020, 73.2% of global GHG emissions were a direct result of the energy sector. Of this 73.2%, 24.2% was as a result of industrial applications, 17.5% due to residential applications, and 16.2% for the transport of energy [9]. Countries, industries and consumers need to switch to renewable energy in order to achieve Net Zero GHG emissions by 2050.

1.1. Transitioning Towards a Renewable Energy Grid

Hydroelectric, wind turbine and photovoltaic (PV) solar technologies have emerged as the three best candidates to replace the oil, gas, and coal-based infrastructure [10]. The transition towards a renewable energy grid presents two key problems. Firstly, the wide-scale adoption of renewable technology requires innovation, research and development to drive down product costs. Given the lack of development in renewables in the early 20th century, it is imperative that this backlog is addressed in the coming years.

Secondly, renewable energy sources can be intermittent in terms of power delivery. Hydroelectricity is exempt from intermittency issues as it has been proven to be nearly consistent in time. Wind turbines and PV solar, however, can present as highly irregular sources of electricity, dictated by weather patterns and seasonal influence. Through careful selection of location and positioning, harvesting energy from the wind or incoming solar irradiation can be optimized. However, there will always exist periods without sunlight or wind. From an infrastructure perspective, this requires a large additional investment into grid control and buffering mechanisms, on both hardware and software fronts.

---

[1] Greenhouse gasses are an umbrella term for harmful gasses which cause global warming, including carbon dioxide, methane, nitrogen oxides, halo-carbons, and hydrogen

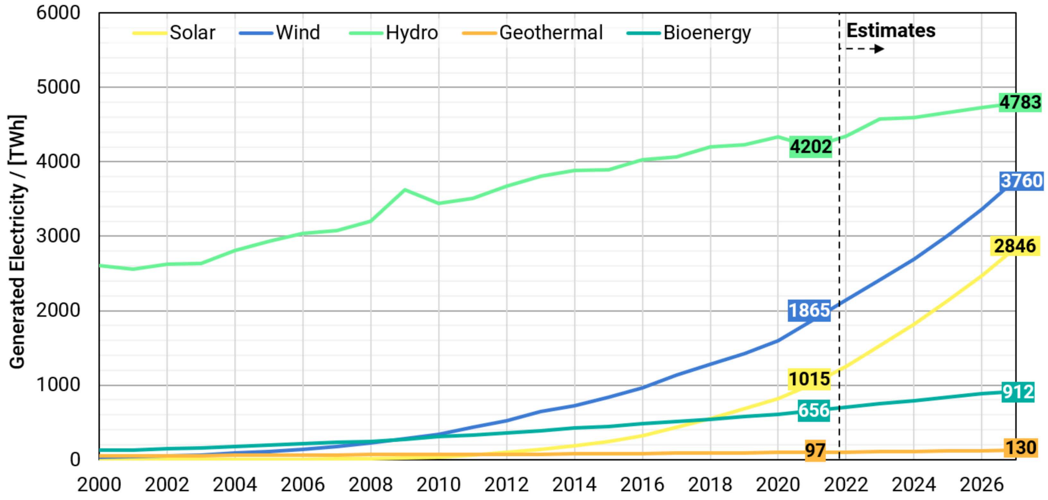

Figure 1.1: Renewable Energy Generation 2000-2027. Despite climate change being a well-understood phenomenon all throughout the 2000s, growth in wind and solar technology only took off after 2015. All figures 2022-2027 and estimates based on public policy and objectives (Data source: IEA [3])

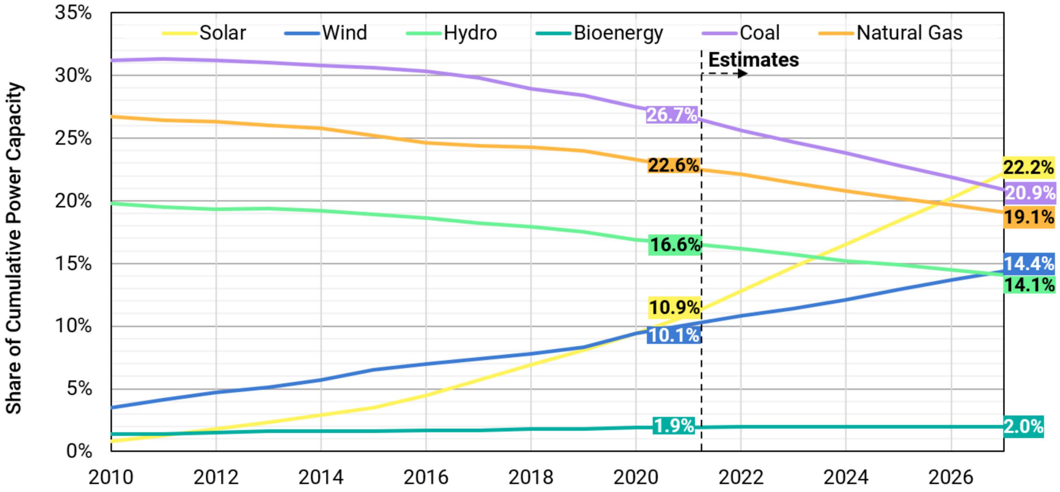

Figure 1.2: Share of cumulative power capacity by technology, 2010-2027. An overview of the most significant sources of energy generation and their relative share in the global cumulative power capacity over the years. PV solar technology has grown considerably, going from the lowest share to potentially the largest share in just 17 years. All figures 2022-2027 and estimates based on public policy and objectives (Data source: IEA [3])

Seven years after the Paris Agreement, a majority of first-world countries have already made steps towards decarbonizing their countries' energy supply. Spearheaded by nations which have abundant natural resources and a strong economy (e.g., Norway, Sweden, and the U.K.), investments in solar parks and wind turbines are increasing. Figure 1.1 illustrates the rise of renewable energy sources in the 21st century. Figure 1.2 depicts the composition of the global power capacity per type of technology, from 2010 to 2027. Both of these figures highlight the rapid growth of renewables, dominated by wind and solar technology. Electricity generated by wind power (both on- and off-shore) amounted to 1870.3 TWh in 2021 (+21% compared to 2020). Electricity generated by solar power amounted to 1002.9 TWh in 2021 (+22% compared to 2020) [3]. However, in order to meet the Net Zero requirements by 2030, generation totals of 7932.5 TWh and 7413.9 TWh will be required for wind and solar, respectively [11]. Wind turbine and solar power generation will need to grow by 17.4% and 24.9% every single year until 2030, respectively. Such high growth rates will require significant governmental aid and technological innovation.

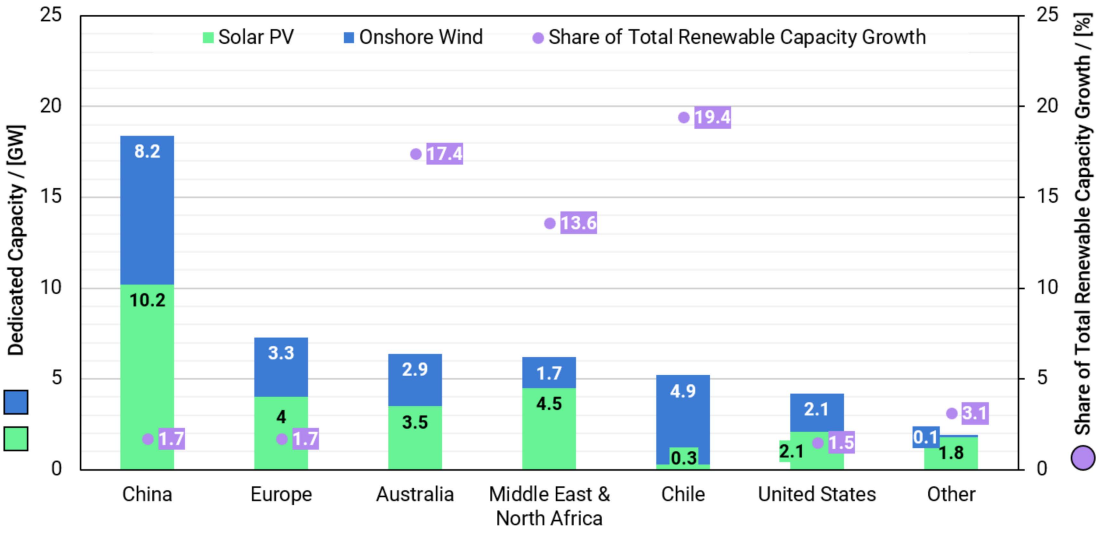

Figure 1.3: Renewable capacity dedicated to green hydrogen production, 2021-2027. China and Europe are leading the charge, whereas regions like Australia, the Middle East, North Africa and Chile are using their renewable energy assets to facilitate the transport and export of their generated energy surplus to external markets (Data source: IEA [3])

1.2. Importance of Hydrogen in the Global Energy Landscape

The transition to renewable energy is not the only change necessary for decarbonization. Large-scale storage facilities will be required to balance the intermittency of renewables. Excess-generated electricity must be stored for use when renewables are unable to fully meet consumer demand. Furthermore, a renewable energy grid will have areas which have a net surplus of generated electricity and areas with a net deficit. Trading and transportation of energy will become crucial in balancing local surpluses and deficits. Finally, industries like maritime, aviation and bulk chemicals are difficult to decarbonize. In such industries, hydrocarbons may remain the only suitable option.

Hydrogen technology can serve as the solution to the aforementioned issues. Hydrogen holds vast potential across various sectors, including industry, transportation, power, and construction. It can be used as feedstock, as a fuel (for transport), and as a storage medium [12]. The European Commission released the European Hydrogen Strategy report in 2020, which detailed the extent to which the EU is incorporating hydrogen technology in their energy infrastructure [12]. The share of hydrogen in the European energy mix is expected to grow from 2% in 2020 to an expected 13-14% by 2050. Furthermore, Europe has emerged as a highly competitive market for clean hydrogen, with cumulative investments in renewable hydrogen potentially accumulating to €180-470 billion by 2050 [10]. According to the European Commission, by 2050, clean hydrogen could meet 24% of the world energy demand, employing 1 million people, and reaching annual sales of €630 billion [13, 14].

In Europe, there is a great opportunity for technological innovation in hydrogen technology and its integration with renewables. This shift towards hydrogen is also observed in other continents. Shown in Figure 1.3 is a summary of all of the renewable energy capacity which is to be built between 2021 and 2027, specifically dedicated towards the production of green hydrogen. China is a notable market on this list, as it uses more energy than both continental Europe and North America [15]. Its fast-paced transition towards renewables is also seen by its leading position in dedicating renewable energy capacity to hydrogen production. Regions with high renewable energy export potential are devoting 13-19% of their capacities towards hydrogen generation to facilitate the transport of their renewable energy to external markets. Examples include Australia, the Middle East & North Africa for the export of solar energy and Chile for wind energy.

1.3. Decentralization of the Energy Grid

When considering PV solar technology, a distinction can be made between different types of installations (see Figure 1.4); residential solar includes solar panels mounted on the roofs of consumer homes, commercial/industrial solar covers solar panels installed for the purpose of providing com-

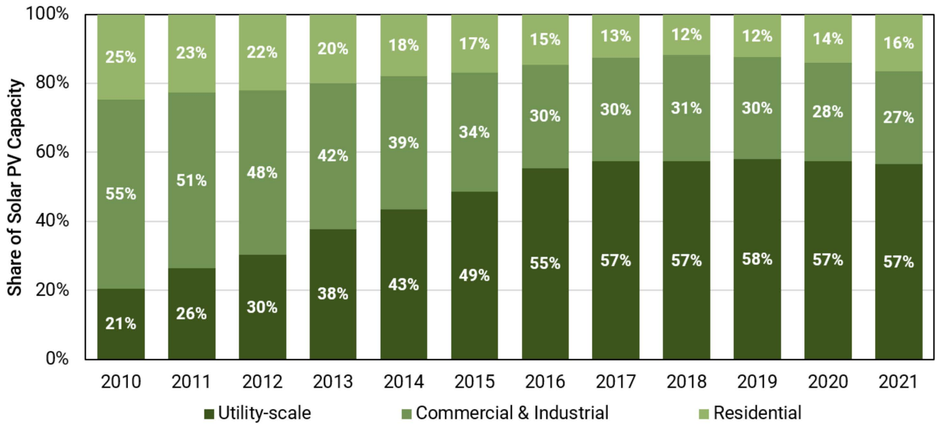

Figure 1.4: Global solar PV capacity per type of installation. Utility-scale solar has grown considerably over the past 10 years, but over 40% of global solar capacity still belongs to commercial/industrial and residential players (Data source: IEA [3])

mercial clients with electricity, and lastly, utility-scale solar covers solar parks installed to supply the general public with electricity. Residential and commercial/industrial scale energy provisions are not comparable in size to conventional hydrocarbon electricity generation plants. Fossil-fuel methods of electricity generation benefit from centralized production due to economies of scale. One example of this can be seen in modern energy generation plants using natural gas. In addition to the electricity generated by the gas turbine, the remaining heat in the cycle is used in additional Rankine steam cycles, for additional electricity generation and local district heating. Renewable energy sources do not reap comparable advantages from a centralized configuration.

The nominal power of modern gas turbines ranges from 100-300 MW, which is significantly larger than the average size of a PV solar panel (approximately 500 W). The panels do not benefit from a larger scale, with the exception of cost savings on power electronics and operation/maintenance. As a result, the increasing presence of residential and commercial/industrial solar installations is enabling the decentralization of the energy grid. Figure 1.4 confirms this trend.

The geographical dispersion of electricity generation capacity highlights the phenomenon of energy grid decentralization. In terms of their efficiency and overall annual production capacity, most renewable energy sources are weather and/or location dependent. Figure 1.5 exhibits a map of all (non-residential) PV solar instalments in The Netherlands. The scattered distribution of instalments as well as the varying size of instalments indicates that the decentralization of the Dutch energy grid is rampant. When compared to the fossil-fuel installations in the Netherlands, there are just 69 facilities producing approximately 20 GW in combined peak power, providing electricity and heat to The Netherlands and its neighbouring countries [16].

The decentralization of electricity production is coupled with rising pressure on energy grid infrastructure. With the accelerated growth of electric vehicles and the electrification of household heating and cooking, existing grid infrastructure is running out of capacity to take on new customers [18, 19, 20, 21]. Temporary suspensions in customer connections by multiple municipalities have left some newly constructed residential properties, businesses, and even vital service centers without access to electricity. To further de-escalate the congestion on national grid infrastructure, netting arrangements (which allow consumers to sell excess solar electricity back to the grid) are ceasing to exist [22].

Therefore, in addition to the decentralization of the energy grid, there is a growing push for the local balancing of renewable energy networks. Without netting arrangements to monetize excess generated electricity, switching to off-grid renewable systems may become a real option for companies with their own renewable energy infrastructure. However, there exists a research gap in solutions for decentralized electricity production, a function which has historically been filled by national energy grid infrastructure.

1.4. Renewable Energy Power Electronics

Almost all renewable energy resources deliver power in the form of electricity. Power electronics for large-scale renewable energy resources are expensive to install and often have a shorter lifetime

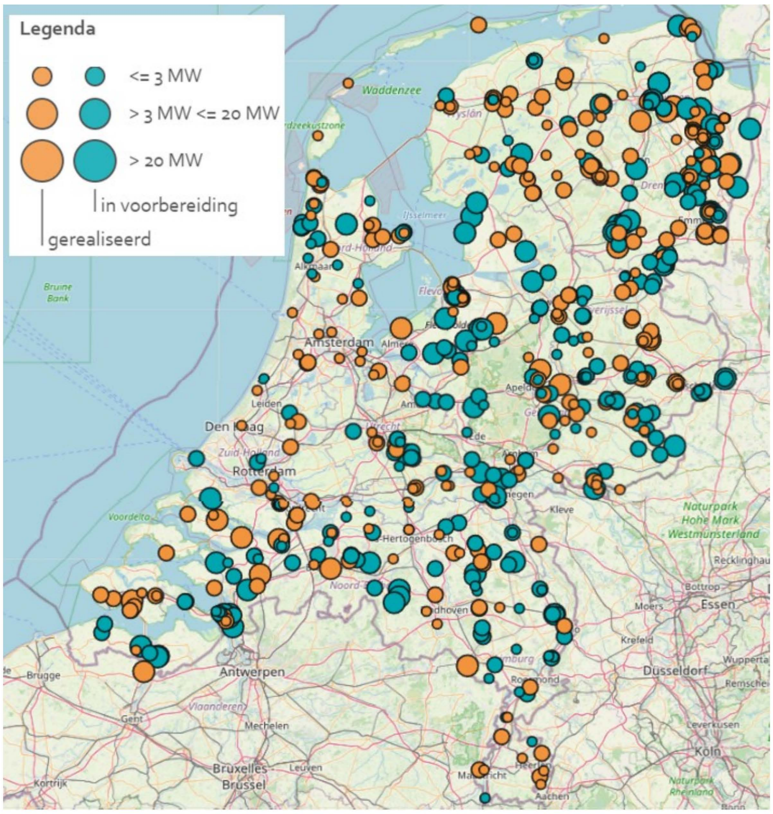

Figure 1.5: Map showing all commercial and utility-scale solar parks in The Netherlands as of 2021. Solar PV is divided into assets located all across the country, as solar irradiation is similar in most areas in the Netherlands. Due to the high population density, finding suitable consumers close by is not a big concern. Permission was granted by ROM3D for use of this image (source: Zon Op Kaart, ROM3D [17])

than the resources these components power. For a utility-scale solar PV park, the IEA estimates that inverters and electrical capital expenditure account for 5% and 12% of the total capital expenditure of the park [3]. Furthermore, inverters have a lifespan of 5-15 years, which is less than the 25-30 year lifespan of PV solar panels. This results in PV solar parks needing to perform frequent maintenance on their power electronics, and replace the inverters entirely within the park lifetime [23]. Lastly, PV solar park operators often under-size the inverter with respect to the nominal maximum power of the PV solar arrays. This increases the profitability of the solar park over time, as inverters tend to perform better near their maximum capacity, and the PV solar park does not reach maximum power frequently during operation. This results in 'clipping losses', which limit the output to the maximum inverter power when the obtainable power of the solar park exceeds the maximum inverter power.

As the energy grid becomes dominated by renewable resources which deliver electricity, there is a drive for technological innovation in the field of renewable power electronics. Overcoming the power losses in system electronics can lead to improved financial outlooks of renewable energy, and consequently, accelerate the transition to a sustainable electricity grid.

1.5. Problem Description

As described in Section 1.1, the growth of renewable energy sources like hydro, wind and solar, coupled with hydrogen, is the future for our energy infrastructure. These technologies play a vital role in the decarbonization of modern society. However, the intermittency of renewables remains a challenge for providing consistent and reliable electricity.

Hydrogen technology, as discussed in Section 1.2, is a versatile energy carrier capable of transport and storage of energy with little-to-no GHG emissions. With significant investments being made into hydrogen infrastructure, hydrogen technologies are becoming a lucrative option for buffering renewable energy systems. That said, there is relatively little research on the integration of hydrogen with

Figure 1.6: XINTC company logo. XINTC was founded in 2012 and currently employs 11 FTE as of 2023 [47]. Permission was obtained by XINTC for the use of this image.

renewable energy assets, when compared to research into conventional energy systems.

As mentioned in Section 1.3, the integration of renewable energy sources has led to the decentralization of electricity production. Wind and solar assets are installed at locations with favourable weather conditions and are no longer centralized in large facilities. Coupled with increased pressure on grid infrastructure, there is more incentive for consumers and industrial players to balance their own renewable energy systems. However, few technologies exist which enable residential and commercial clients to properly decentralize their energy supply.

Lastly, Section 1.4 elucidates that renewable energy resources like PV solar require power electronics in order to operate. In addition to requiring a share of the initial investment costs, power electronics also tend to degrade faster than other components. As a result, reducing the complexity of power electronic systems can lead to increases in overall yield and a reduction in costs over the system lifetime.

1.6. Research Questions

In order to steer the research presented in this report and address the open problems mentioned above, it is necessary to determine a set of questions that need to be answered and discussed. After reading this report the following main research question should be answered:

To what extent can a PV solar park be integrated with a modular alkaline electrolyzer without grid-based buffering and through minimal use of power electronics?

Additionally, secondary research questions pertaining to this research are:

1. How should a directly coupled system of PV solar panels and a modular alkaline electrolyzer be sized with respect to one another to optimize hydrogen production?
2. To what extent is it possible to control a directly-coupled system of PV solar panels and a modular alkaline electrolyzer?
3. How economically-viable is a hybrid renewable energy system consisting of PV solar panels and a modular alkaline electrolyzer?

1.7. Scope

For this report, research is conducted solely on the integration of PV solar technology with modular liquid alkaline water electrolyzers, and the control thereof. Other renewables such as wind [24, 25], hydroelectricity [26, 27, 28], bio-energy [26, 29, 30] and geothermal energy [26, 31, 32] have not been included as these are either highly dependent on natural resource availability or not expected to make up a large portion of the future energy supply. Furthermore, PEM electrolysis has also been excluded from this research. More information on the PEM can be found in [33, 34], with literature concerning large-scale applications to be found in [35, 36, 37, 38]. Lastly, the element of energy storage (in both battery and hydrogen format) has not been included in the research for this report. Although its impact on the consistency of a hybrid renewable energy system can be considerable, it is out of the scope of this research. More information on hydrogen storage can be found in [39, 40, 41], and applications in hybrid renewable energy systems are found at [42, 43, 44, 45, 46].

1.8. Company Introduction (XINTC)

This research was conducted in close collaboration with XINTC, a Dutch Original Equipment Manufacturer (OEM) that designs, produces, assembles and markets smart modular Alkaline Water Electrolyzers (AWEs). With system capacities ranging from 150 kW to 50 MW, XINTC is able to develop

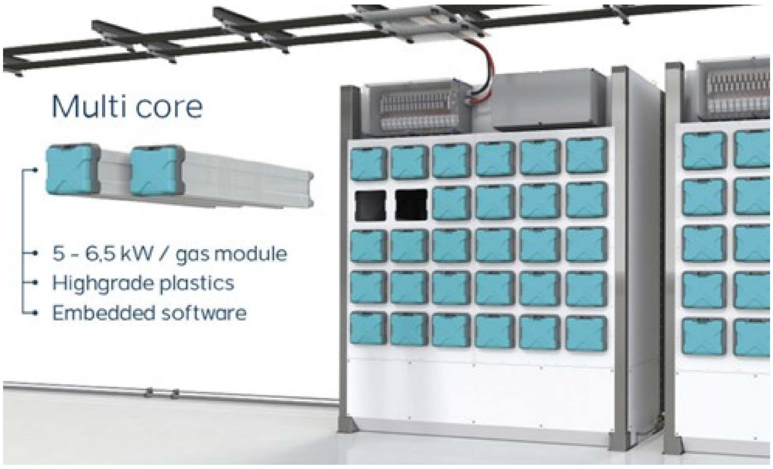

Figure 1.7: XINTC Hydrogen Gas Modules. A single gas module is approximately 25 cm wide and tall, and 60 cm long, with a nominal power of 5-6.5kW. Two modules operate in pairs. Scalable solutions are achieved by adding sections of gas modules together. This modular system design is one of the first of its kind and makes XINTC a pioneer in the mid-market electrolyzer industry [47]. Permission was obtained by XINTC for the use of this image.

Figure 1.8: The XINTC final containerized product. With a final product deliverable in a 40-foot high cube container (12.03 m in length, 2.4 m in width and 2.67 m in height), transportation is cost-effective and globally applicable [47]. Permission was obtained by XINTC for the use of this image.

standardized modular products whilst delivering client-specific solutions. Applications for XINTC electrolyzers include use in manufacturing, bulk chemicals, the built environment and mobility sectors.

XINTC electrolyzers operate at near-atmospheric pressures. After post-processing, final pressures can range from 1-30 bar. The modular electrolyzer units and the associated Balance-of-Plant (BoP) are delivered in a containerized system. As a result, transportation and instalment costs can be kept at a minimum whilst still being able to guarantee structural integrity and build quality.

1.9. Chapter structure

In Chapter 2, the literature related to PV solar and liquid alkaline water electrolysis technology, as well as systems featuring these components, is presented. Next, in Chapter 3, the methodology behind the modelling, design and control of the proposed system is detailed. Subsequently, simulation results are discussed in Chapter 4. Lastly, Chapter 5 provides a conclusion to the research in this paper along with recommendations for future work.

2

Literature Study

This chapter will summarize and discuss the key references and background knowledge pertinent to developing a hybrid renewable energy system for the direct coupling of solar PV to a modular alkaline electrolyzer. Specifically, related works for both the modelling and control of each individual aspect of the proposed system will be discussed, before summarizing the research available on the combination of these aspects.

2.1. Solar Photo-Voltaic Technology

After the inception of solar PV technology in 1883, there was little development in the technology due to its limited economic feasibility and low efficiency (1-2%, compared to 15-20% currently) [48, 49]. The fast-paced development of fossil-fuel electricity generation methods further reduced interest in PV technology. It was not until 1985 that the first power optimization module for solar PV technology was developed [50]. The emergence of information technology sparked interest and research in solar PV modelling, attracting industrial and governmental entities seeking to expand their renewable energy portfolios.

2.1.1. Fundamental Behaviour of a Solar PV Panel

Solar PV systems are made up of individual PV cells, solid-state semiconductor devices converting photons from sunlight directly into electricity. When the semiconductor material absorbs enough photons, electrons are displaced from the semiconductor atoms and are free to move around, generating an electric current [26, 49]. Approximately 95% of all semiconductors used for solar cells are made of silicon [51]. PV solar systems are modular, allowing for multiple panels to be added together in an array to increase the total power output [52].

The generated current of a PV solar cell (I) is dependent on the externally applied voltage (V), the temperature of the cell (T_{cell}), and the irradiation incident on the cell (G). When short-circuited, the current is at a maximum and the voltage taken across the cell is zero. Alternatively, when the PV cell circuit is open, there is no current going through the cell, and the measured voltage is at a maximum. In both edge cases, the generated power is zero [52]. In between the edge cases, a relationship between current and voltage can be drawn, as shown below.

$$I = I_{\text{sc}} \tag{2.1}$$

$$V = V_{\text{oc}} \tag{2.2}$$

If the PV cell is connected to a load resistance (R) the intersection between the I-V curve of the PV cell and the I-V curve of the load resistance becomes the operating point of the system.

$$I = \frac{V}{R} \tag{2.3}$$

As soon as a load is connected to a PV system, the voltage drops below the open-circuit voltage (V_{oc}), and current starts to flow through the cell. The transient state of a PV system sees both the

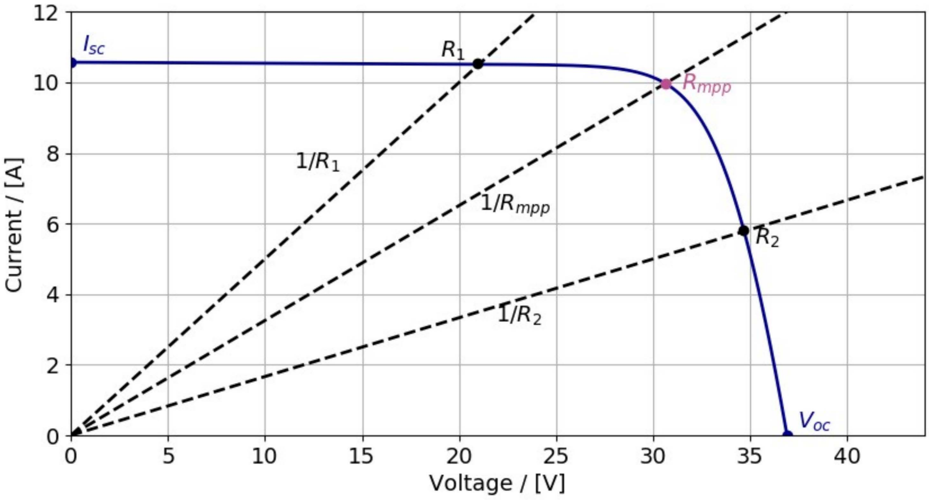

Figure 2.1: Standard I-V curve for a system of PV cells. The intersects between the I-V curve of the solar panel (blue) and the various load resistances (black) mark the operating points of the PV system. At a resistance of $R = R_{\text{mpp}}$, the system delivers the most power operating at the MPP. Curve generated using the Python PVlib library.

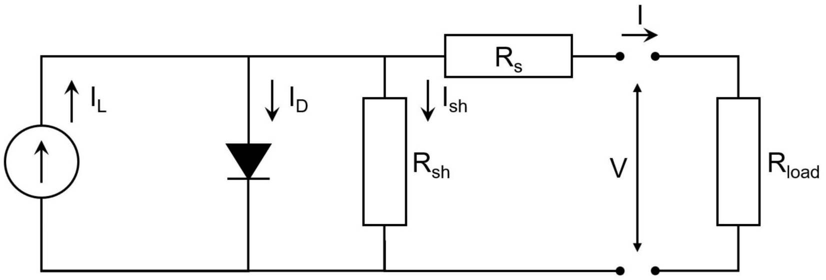

Figure 2.2: The equivalent electrical circuit for a PV solar cell. The Single-Diode Model (SDM) simplifies a PV solar cell to an electrical circuit consisting of a current source (I_L), a diode (with current I_{D}), and a number of resistances which model the shunt (R_{sh}), series (R_{s}), and load resistance (R_{load}) [54].

voltage and current vary around the static I-V curve intersect as mentioned previously. The timescale of these transient effects is in the order of 200-5000 µs, increasing with PV cell degradation [53]. When compared to the relevant time scales for the power delivered by a PV system, the transient effects of a PV system can be considered negligible.

2.1.2. Single-Diode Model

In 2005, W. De Soto et al. devised a solar PV model capable of modelling the I-V curve of any given solar panel based solely on data provided by the manufacturer datasheet [54]. The Single Diode Model (SDM, also known as the Five Parameter model) uses an equivalent circuit for a solar cell. This approach can also be applied to modules consisting of multiple cells and to arrays consisting of multiple modules, under the assumption that every cell behaves identically. The equivalent circuit is shown in Figure 2.2.

The I-V curve of any solar cell based on the SDM is given by the following relationships:

$$I = I_{\text{L}} - I_{\text{D}} \left[\mathrm{e}^{\frac{V + IR_{\text{s}}}{n_{\text{mod}}}} - 1 \right] - \frac{V + IR_{\text{s}}}{R_{\text{sh}}} \tag{2.4}$$

$$n_{\text{mod}} \equiv \frac{N_{\text{s}} n_{\text{I}} k T_{\text{cell}}}{q} \tag{2.5}$$

In the above-mentioned equations, there are five parameters which cannot directly be determined based on manufacturer datasheets: the light current (I_{L}), the diode reverse saturation current (I_{D}), the shunt resistance (R_{sh}), the modified ideality factor (n_{mod}), and the series resistance (R_{s}). The electron

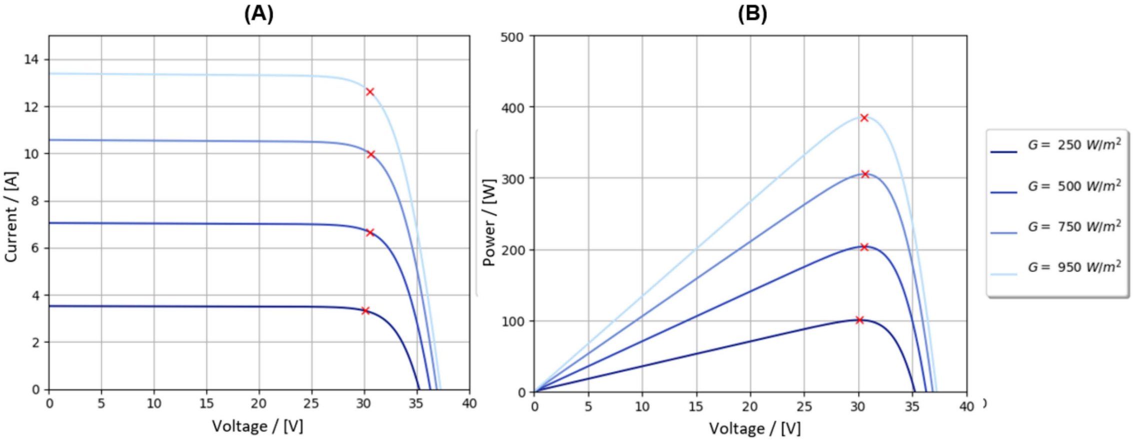

Figure 2.3: I-V (Plot A) and P-V (Plot B) curves for a DMEGC Solar 405W panel operating at a constant temperature of 25 °C, calculated using the Single Diode Model (SDM). Decreasing irradiance causes a lower current response, resulting in a lower power output. Curves are plotted for four different irradiances, ranging from 250-950 $\mathrm{W\,m^{-2}}$. The red crosses denote the Maximum Power Point (MPP). Curve generated using the Python PVlib library.

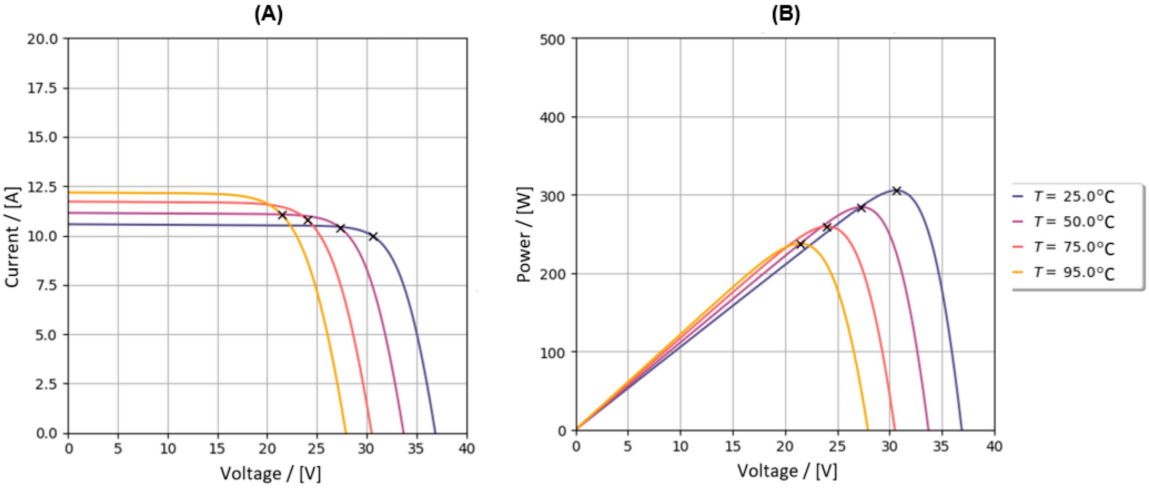

Figure 2.4: I-V (Plot A) and P-V (Plot B) curves for a 405W DMEGC PV Solar panel operating at a constant irradiance of 750 $\mathrm{W\,m^{-2}}$**. Figures were calculated using the Single Diode Model (SDM).** Increasing cell temperature negatively affects PV solar panel behavior. Curves are calculated for varying temperatures, ranging from 25-95 °C. The black crosses denote the Maximum Power Points (MPPs). Curves are generated using the Python PVlib library.

charge (q), Boltzmann constant (k_B), number of cells in series (N_s), and cell temperature (T_cell) are known variables. Lastly, n_I is the usual ideality factor.

Due to the implicit nature of the SDM, an iterative solver is used to compute the I-V curves for a range of irradiances and cell temperatures. With the total solar irradiance incident on the atmosphere equivalent to 1360.8 $\mathrm{W\,m^{-2}}$, the highest solar irradiance incident on the surface of the earth at most latitudes is 1000 $\mathrm{W\,m^{-2}}$ [55]. Shown in Figure 2.3 is the variation in generated current and power for various operating voltages of a PV solar panel. The decrease in incident irradiation shows a proportional decrease in generated current and power. However, the operating voltage ranges of the panel do not change significantly, with only the open-circuit voltage decreasing slightly for lower irradiances.

In addition to changes in irradiance, changes in cell temperature also influence the generated current and power of a PV panel. As shown in Figure 2.4, for constant irradiance, a higher operating temperature increases the panel current but decreases the overall power delivered. This is due to the fact that the decrease in operating voltage exceeds the increase in current, resulting in a net decrease in power.

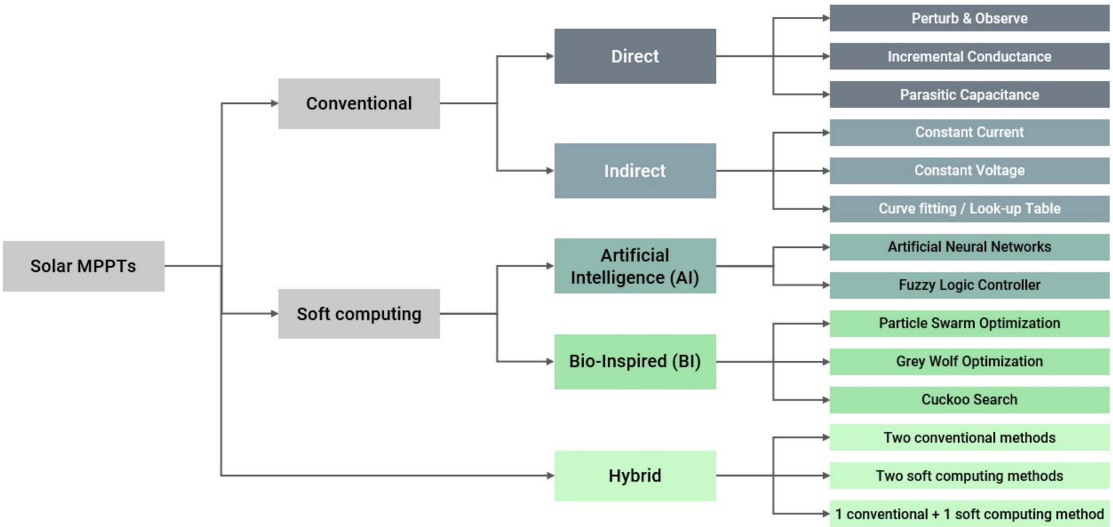

Figure 2.5: General classification of solar MPPTs. Conventional MPPTs use mathematical relations and simple logic to approach the MPPT. Indirect methods use pre-defined mathematical relationships, and direct methods track iteratively based on system variables. Soft computing methods utilize artificial intelligence and have become the industry standard for solar farms. These methods are able to accurately track the global MPPT of large solar parks with minimal power losses, even under PSC. Note: the listed examples per class are non-exhaustive [56]

2.1.3. Maximum Power Point Tracking Methods

Maximum Power Point Trackers (MPPTs) track the maximum power point (MPP) of a PV solar panel given certain operating conditions. The ideal P-V curve of a solar panel (see figures 2.3 and 2.4) has a single maximum, simplifying the identification of the operating point which will yield the highest power delivery. In practice, the P-V curve of the system is not fully known at every time step. Two methods for modelling the PV system are: using SDM to identify the MPP in each time step, or iteratively approaching the MPP by measuring current and voltage. The latter method has become the industry standard for MPP tracking due to its lower computation time and reduced modelling errors.

There are over 50 working MPPT algorithms which have been proven to track the MPP of a given PV solar system [56]. Generally, these algorithms can be split into conventional, soft computing (based on AI or natural selection), and hybrid methods, as shown in Figure 2.5. Conventional methods are renowned for their low cost and ease of implementation, often relying on a few input variables and simple logic. Conventional methods can be further distinguished between direct and indirect methods. Direct methods rely mainly on measurement in order to approach the MPP, whereas indirect methods use fractional calculations of the open-circuit voltage, short-circuit current or a reference dataset. The main drawback of conventional methods, both direct and indirect, are their low performance during periods of fast-changing irradiance and during Partial Shading Conditions[1] (PSC) [56]. Common examples of direct conventional MPPTs are the Perturb and Observe (P&O), Incremental Conductance (INC), and Parasitic Capacitance algorithms [57].

Since the 21st century, the use of soft computing in MPPT technology has proved highly effective. Compared to conventional methods, soft computing MPPTs can minimize MPP oscillations, increase tracking speed and identify the global MPP, even under PSC.

Regardless of the type of MPPT, the efficiency of the algorithm (ϵ_{MPPT}) can be defined as the ratio of the actual power delivered by the solar PV system to the power achieved if the maximum power point was always tracked.

$$\epsilon_{\text{MPPT}} = \frac{\int_0^t P_{\text{actual}}(t)\,\mathrm{d}t}{\int_0^t P_{\text{MPPT}}(t)\,\mathrm{d}t} \tag{2.6}$$

---

[1] Partial shading conditions refer to situations where only a portion of a PV module or array is shaded, leading to variations in the amount of sunlight received by different sections. This shading can occur due to obstructions such as trees, nearby buildings, or equipment, and it can adversely impact the performance and efficiency of the PV system by reducing the overall power output. For this research, it is considered outside of the scope.

2.1.4. Perturb and Observe MPPTs

The Perturb and Observe (P&O) MPPT makes use of the fact that the P-V curve of a PV solar panel has a single maximum. This means that the MPP of a solar panel for given irradiance and cell temperature is given by:

$$\frac{\mathrm{d}P}{\mathrm{d}V} = 0 \text{ at the MPP} \tag{2.7}$$

Using this relationship, if this differential is greater than zero, indicating a rising slope, it can be concluded that the MPP lies to the right of the current point. Similarly, if the differential is less than zero (i.e., a decreasing slope) the MPP lies to the left of the current point. With this differential, which is discretely measurable, a simple algorithm can be made to approach the MPP iteratively through constant measurement of system voltage and current.

Sera et al. showed that the Incremental Conductance (INC) algorithm is a sub-set of the P&O algorithm, as opposed to its own type [57]. INC makes use of simple relationships and the chain rule to express the same hill-climbing algorithm in current and voltage measurements instead of power and voltage. The derivation of the INC method is given below:

$$\begin{aligned}
\frac{\mathrm{d}P}{\mathrm{d}V} &= \frac{\mathrm{d}(VI)}{\mathrm{d}V} && \text{(2.8a)}\\
&= I_{\text{MPP}} + V_{\text{MPP}} \cdot \frac{\mathrm{d}I}{\mathrm{d}V} && \text{(2.8b)}\\
&= 0 \text{ @ the MPP} && \text{(2.8c)}
\end{aligned}$$

Discretizing the relationship and rearranging:

$$\begin{aligned}
\frac{\Delta I}{\Delta V} &= -\frac{I}{V} \text{ at the MPP} && \text{(2.9a)}\\
\frac{\Delta I}{\Delta V} &> -\frac{I}{V} \text{ left of the MPP} && \text{(2.9b)}\\
\frac{\Delta I}{\Delta V} &< -\frac{I}{V} \text{ right of the MPP} && \text{(2.9c)}
\end{aligned}$$

Using these three relationships, it is possible to determine the direction in which the incremental step in voltage must be taken. In a practical system, the direction and size of the voltage step to be taken are translated into a duty cycle for a DC-DC converter. The DC-DC converter (known in the industry as a charge controller) receives the duty cycle and adjusts its supply voltage to the PV solar panels accordingly. In response (on a microsecond timescale), the PV panel array responds with a current corresponding to the applied voltage. This current, coupled with the new input voltage to the PV array, constitute the next initial values of the control loop.

The advantage of P&O algorithms is their inherent simplicity, voiding the need for expensive computational power or additional sensors. One of the disadvantages of P&O algorithms, however, is their relatively low response time compared to other conventional methods. The algorithm incrementally approaches the MPPT in every instance. For a constant step size, the time taken to reach the MPPT can be considerable when the change in irradiance is significant [57]. One way to solve this is by varying the step size taken. A paper by Loukriz et al. provides an in-depth review of the common variable step sizes taken by various papers in literature [58]. Shown in Figure 2.6 is a graph showing three of these possible variable step sizes. Selecting a suitable function for the variable step size can depend on the desired configuration of the solar panel.

During experimental testing, Sera et al. showed that the MPPT efficiency of P&O algorithms is consistently greater than 95% for trapezoidal irradiance profiles (switching frequencies of 5-10 Hz) [57]. Variable step sizes increase the MPPT efficiency of a conventional P&O algorithm [58].

However, one critical drawback of P&O algorithms is their inability to handle partial shading conditions (PSC). In the presence of PSC, PV solar panels within the same array exhibit variations in their I-V and P-V curves. This disparity arises from the differing incident irradiation levels on each section of panels within the array. As a result, the combined P-V curve describing the array will have multiple local maxima. Conventional MPPT methods are unable to differentiate between a local and a global

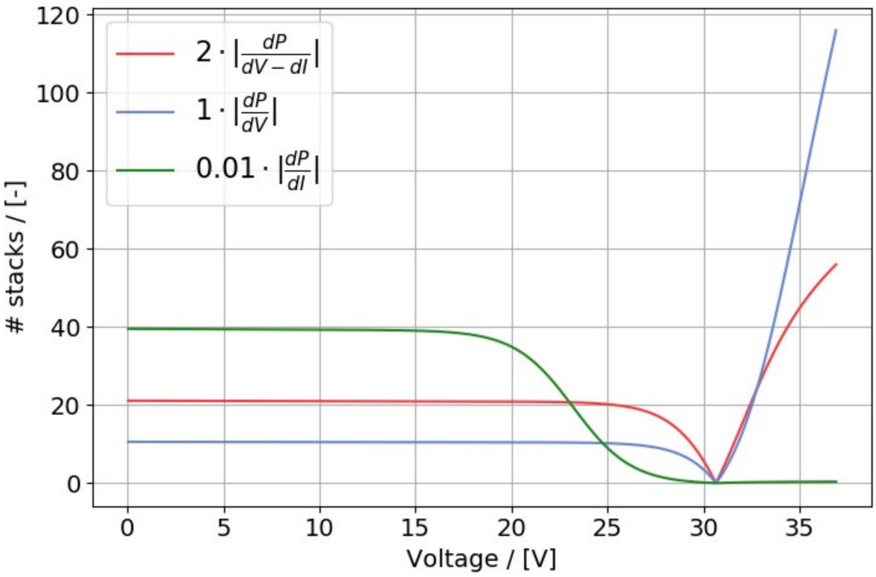

Figure 2.6: Variable step size functions for P&O MPPT algorithms. The point where all curves cross the voltage axis coincides with the voltage of the MPP. In order to ensure the step size always decreases closer to the MPP, the functions must be dependent on the measured voltage, current or power [58]. P-V curve generated using the Python PVlib library.

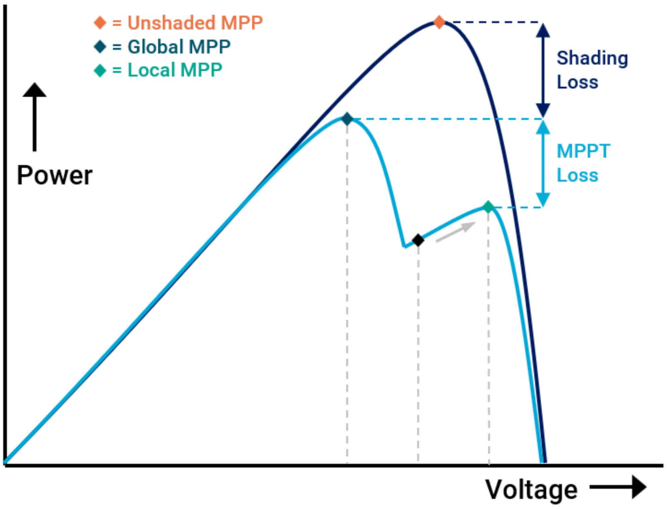

Figure 2.7: P-V curve of a solar PV array in normal conditions (dark blue) and partial shading conditions (light blue). Using a conventional (i.e., P&O) algorithm, the MPP that would be found under PSC would not be the global MPP. The difference in power between the locally found MPP and global MPP is considered the MPPT PSC loss [59].

maximum, resulting in efficiency losses if a local maximum is found by the algorithm under PSC. This is visualized in Figure 2.7.

Table 2.1: Comparison of Alkaline Water Electrolysis (AWE) and Polymer Electrolyte Membrane (PEM) electrolysis using a range of relevant parameters. While PEM electrolyzers exhibit higher current and volumetric densities, AWE electrolyzers are more durable and cheaper due to the lack of rare earth metals required [34].

Metric	Unit	AWE	PEM
Current Density	$\mathrm{A\,cm^{-2}}$	0.2-0.4	1-2
Max. Pressure	bar	32	50
Operating Temperatures	°C	30-80	20-80
Operating Characteristics	-	Isobaric	Pressure driven
Industrial Efficiencies	%	62-82	50-85
Relative size	-	Large	Small
Corrosion	-	Yes, Alkaline	No
Hydrogen Purity	%	>99.8	>99.99
Required Materials	-	Fe, Ni	Pt, Pd, Ir
Electrolyte	-	KOH or NaOH	Solid plastic polymers
Lifetime	years	10	3-4

2.2. Liquid Water Electrolysis Technology

The act of splitting water (H_2O) into its constituents, hydrogen (H_2) and oxygen (O_2), was first discovered in Amsterdam in 1789, by Dutch merchant and businessman Adriaan P. van Troostwijk and medical doctor Johan R. Deiman. Through the use of gold wire as an electrode, connected to a powerful electrostatic generator, the electric discharge was enough to split the water molecules into their gas constituents [60]. It was not until 1900 that the first industrial electrolyzer was commissioned by O. Schmidt, and in the 1920s electrolyzer demand soared due to the increased demand for ammonia production for use of fertilizer for global food security [61]. The manufacturing of synthetic ammonia (NH_3) using the Haber-Bosch process was of great importance to countries with abundant hydroelectric power and little access to fossil fuels [62].

As the industrial revolution pursued, the widespread availability and adoption of fossil fuels drove down research and development into hydrogen technology. Throughout the 20th century, Norway, a country with an abundance of hydroelectric power, lead the way in total installed electrolyzer capacity. However, the largest electrolyzer project of the 20th century was realized in Egypt in 1960, with a capacity of 200 MW [63]. As of 2023, Shell is constructing the biggest green hydrogen plant in Rotterdam (The Netherlands), with a capacity of 200 MW, operational in 2025 [64]. The largest green hydrogen project announced to date is that of Sinopec, located in Xinjiang (China), with a maximum power of 300 MW [65]. It should be noted that hydrogen technology has become significantly more efficient since the 1960s, and actual production volumes and efficiencies of modern plants have improved.

Commercially, there exist two leading forms of liquid water electrolysis, Alkaline Water Electrolysis (AWE) and Polymer Electrolyte Membrane Electrolysis (PEM). Other forms of liquid water electrolysis like solid oxide electrolysis and microbial electrolysis are still in the research and development phases and are not expected to become industrially competitive in the next decades [34]. Both AWE and PEM electrolysis split water into hydrogen and oxygen by applying a potential difference across two electrodes (a negatively charged cathode and a positively charged anode) which are connected via an ionically conductive medium. For AWE, the electrolyte medium is liquid in the form of water with KOH or NaOH, whereas PEM electrolysis uses a solid electrolyte made up of plastic polymers. Shown in table 2.1 is a comparison of both of these methods for electrolysis.

Large-scale PEM electrolysis has not matured the same as AWE, given the fact that most electrolyzers in the 20th century were manufactured using AWE technology. Low production and materials costs make AWE a suitable option for large-scale green hydrogen plants. However, PEM electrolyzers have several advantages over AWE electrolyzers. Firstly, both the current density and overall efficiency of the PEM electrolyzer systems are higher, making PEM electrolysis the intuitive first choice in high-performance applications albeit at a higher capital expenditure. Furthermore, the small physical footprint of PEM electrolyzers extends its possible applications to industries where low volumetric density is of great value (e.g., mobility, aerospace). Lastly, PEM electrolyzers tend to respond better to varying input powers, often a result of intermittent electricity generation sources like wind and solar.

For alkaline electrolysis, hydroxide ions (OH^-) are used to transport charge between the electrodes.

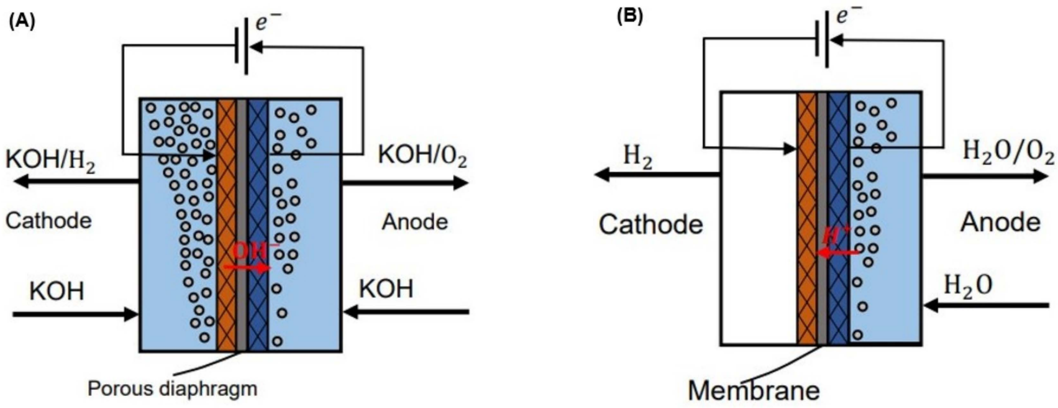

Figure 2.8: Schematic diagrams of an AWE electrolyzer (Diagram A) and a PEM electrolyzer (Diagram B). AWE electrolyzers use KOH or NaOH as the electrolyte to conduct the ions, whereas PEM electrolyzers use a solid polymer membrane [66].

In practice, potassium hydroxide (KOH) is used as an electrolyte to increase the ionic conductivity of the electrolyzer. A schematic overview of both AWE and PEM electrolysis is shown in Figure 2.8. For PEM electrolysis, a solid polymer acts as the electrolyte, integrated with the catalyst together inside the membrane of the PEM electrolysis cell.

2.2.1. Alkaline Water Electrolysis Fundamentals

For alkaline electrolysis, the reactions are as follows:

$$\text{Anode: } 4\,\mathrm{OH^-} \longrightarrow \mathrm{O_2} + 2\,\mathrm{H_2O} + 4\,\mathrm{e^-} \tag{2.10a}$$

$$\text{Cathode: } 2\,\mathrm{H_2O} + 2\,\mathrm{e^-} \longrightarrow \mathrm{H_2} + 2\,\mathrm{OH^-} \tag{2.10b}$$

$$\text{Overall: } 2\,\mathrm{H_2O} \longrightarrow \mathrm{O_2} + 2\,\mathrm{H_2} \tag{2.10c}$$

Thermodynamics

For every chemical reaction, the change in Gibbs free energy (ΔG^0) can be calculated to obtain an insight into the thermodynamics of the reaction. The standard equilibrium potential of the overall reaction is $E^0 = -1.23$ V (at atmospheric pressure and a temperature of $T = 298.15$ K). From this value, the standard Gibbs free energy, and the subsequent standard enthalpy of the reaction can be calculated:

$$\Delta G^0 = -nFE^0 \tag{2.11a}$$

$$= -2 \cdot 96485.3 \cdot (-1.23)\ \mathrm{kJ\,mol^{-1}} \tag{2.11b}$$

$$= +237.35\ \mathrm{kJ\,mol^{-1}} \tag{2.11c}$$

The standard equilibrium potential is the theoretical minimum voltage required to start the reaction. From this, the Gibbs free energy required to start the reaction can be calculated, using the number of electrons transferred in the reaction ($n = 2$, as per the cathode half-reaction), and the Faraday constant ($F = 96485.3$ $\mathrm{s\,A\,mol^{-1}}$). Note that the resulting change in Gibbs free energy is positive, indicating that the reaction is endergonic and non-spontaneous. This means that the reaction will not take place unless driven by an external source (i.e., an applied potential over the electrolyzer electrodes).

From the Gibbs free energy, using tabulated values for the standard entropy of hydrogen, oxygen and water, as well as the assumed standard temperature of $T = 298.15$ K, the standard enthalpy of formation can be calculated:

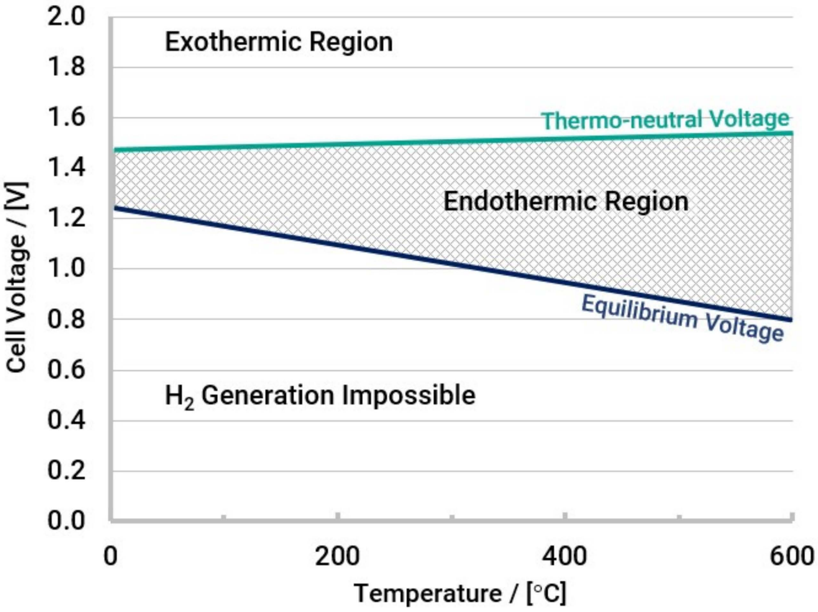

Figure 2.9: Single-cell relationship between cell voltage and temperature. For increasing temperature, the Nernst equation shows that the standard reduction potential decreases with temperature. The enthalpy of formation increases with temperature and as a result, the endothermic region separating the equilibrium and thermoneutral voltages of a single-cell increases with temperature.

$$\begin{aligned}\Delta H^0 &= \Delta G^0 + T\Delta S^0 && (2.12a)\\ &= 237.35 + 298.15 \cdot \left(130.7 + \frac{1}{2} \cdot 205.1 - 69.9\right) \cdot 10^{-3}\ \text{kJ mol}^{-1} && (2.12b)\\ &= +285.8\ \text{kJ mol}^{-1} && (2.12c)\end{aligned}$$

The enthalpy of formation is larger than the Gibbs free energy. This occurs due to the positive molar entropy of the reaction, which can be attributed to the fact that for every liquid water molecule, the reaction produces 1.5 molecules of gas. If only ΔG^0 was applied to the electrolysis reaction, heat would be extracted from the environment. In order to operate an electrolysis cell at such potentials, an external heat source would be required to provide the additional heat. Instead, in order to overcome this endothermic reaction, sufficient potential needs to be applied to reach a 'thermo-neutral state'.

$$E^0_{\text{thermo-neutral}} = -\frac{\Delta H^0}{nF} = -1.48\ \text{V} \tag{2.13}$$

It should be noted that the above-mentioned thermo-neutral cell potential includes the enthalpy of vaporization of water [67]. The temperature dependence of the equilibrium voltage and thermoneutral voltage can be seen in Figure 2.9. It is evident that the equilibrium voltage decreases linearly for larger temperatures. This can be explained by evaluating the Nernst equation:

$$E^0_{\text{eq}} = E^0 - \frac{\bar{R}T}{nF} \ln\left(\frac{[\gamma_{\text{ox}}]}{[\gamma_{\text{red}}]}\right) \tag{2.14}$$

Here, E^0 is the equilibrium potential under standard conditions, and E^0_{eq} is the same potential under non-standard conditions. F is the Faraday constant, $\gamma_{\text{ox/red}}$ is the activity coefficient of the oxidation/reduction reaction, T is the temperature (in Kelvin), $\bar{R}$ is the gas constant, and n is the number of electrons transferred in the reaction.

Overpotential & Current Density

In practice, the applied potential across the cell electrodes exceeds the thermo-neutral voltage. The sum of the extra potential applied to the electrodes is called the overpotential (η) and is commonly made up of three elements. The Ohmic overpotential (η_{ohm}) is applied to overcome the electrical resistance of the electrodes and electrolyte (among other components). The transport resistance faced by the electrons due to gas bubbles, ionic transfer and membrane resistivity is also included in this overpotential. The activation overpotential (η_{act}) is the overpotential pertaining to the activation energies of hydrogen and oxygen formation reactions on the electrode surface. Lastly, the concentration overpotential (η_{con}) is the overpotential due to mass transport limitations on the electrode surface at high currents [68]. During high currents, the rapid build-up of bubbles and the resultant flow field can drastically increase the overpotential required at these currents. As a result, the final cell voltage is given by the following relation:

$$E_{\text{cell}} = E^0_{\text{reversible}} + \eta_{\text{ohm}} + \eta_{\text{act}} + \eta_{\text{con}} \tag{2.15}$$

In order to plot the electrolyzer response to a given applied potential E_{cell}, the Butler-Volmer equation is used. This equation relates the current density (j), which is the current flowing through the electrolysis cell divided by the cell area (values are usually presented in mA cm^{-2} $= 10$ A m^{-2}), to the applied overpotential:

$$j = j_{\text{anodic}} + j_{\text{cathodic}} \tag{2.16a}$$

$$j = j_0 \cdot \text{exp}\left(\frac{\alpha F \eta}{\bar{R}T}\right) - j_0 \cdot \text{exp}\left(\frac{-(1-\alpha)F\eta}{\bar{R}T}\right) \tag{2.16b}$$

Here, j_0 is the current exchange density, α is the dimensionless charge transfer coefficient, F is the Faraday constant, and $\bar{R}$ is the gas constant. This equation can be difficult to model due to its complexity, so for sufficiently large overpotentials ($\eta \geq 0.12$ V), the Butler-Volmer equation simplifies to the Tafel equation:

$$j = j_0 \cdot \text{exp}\left(\frac{\alpha F \eta}{RT}\right) \tag{2.17a}$$

$$\text{log}_{10}(j) = \text{log}_{10}(j_0) + \frac{\alpha F}{2.3\bar{R}T} \cdot \eta \tag{2.17b}$$

From this result, the voltage can be plotted over varying current densities, as is shown in figures 2.10 and 2.11. When the electrolysis cell is operated at increasing temperatures, less overpotential is required to achieve the same current density.

The upper limit of cell operating temperature is determined by the vapour pressure curve of the electrolyte, which in most cases is demineralised water with 20-40 wt% KOH or NaOH. As shown in Figure 2.12, the addition of KOH to pure water lowers the vapour pressure curve. A decrease in the vapour pressure curve means that a higher temperature is required for evaporation at the same pressure. From the figure, at atmospheric pressures, the boiling point moves to approximately 130 °C at a weight percentage of 45 wt%. However, given that evaporation commences well before the boiling point is reached, cell operating temperatures are rarely seen above 100 °C, with most alkaline electrolyzers operating at 60-80 °C.

Stack Configuration

Given that the maximum potential which can be applied to a single electrolyzer cell is between 2-3 V, multiple cells can be arranged in different configurations in order to increase voltage and/or current. Within an electrolyzer 'stack', there are monopolar and bipolar configurations. As shown in Figure 2.13, monopolar stack configurations see each electrode have a single polarity (positive or negative). An ionically conductive membrane is used in between each electrode to minimize gas crossover. Within monopolar configurations, there is still the possibility of wiring the cells in series or parallel. In series, the voltage of the stack is the single-cell voltage (V_{cell}) multiplied by the number of cells (n_{cells}). The current for a series monopolar configuration is the same as the current for a single cell (I_{cell}). For a parallel monopolar configuration, the stack voltage is equivalent to the single-cell voltage, and instead, the current of the stack is the multiple of the single-cell current multiplied by the number of cells. In both cases, for the same number of cells per stack, the total delivered theoretical power is equivalent to:

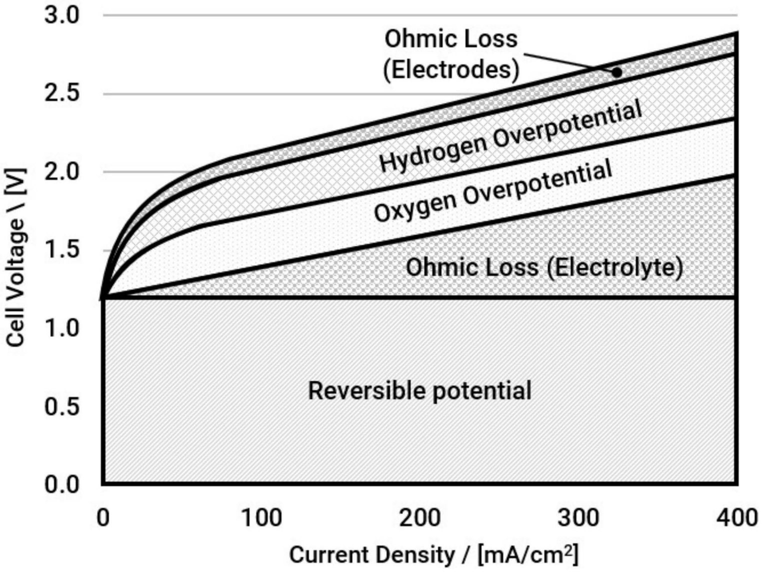

Figure 2.10: Single-cell relationship between cell voltage and current density. Above the reversible potential, the ohmic loss through the electrolyte is linearly proportional to the applied current density. A higher cell potential and driving force result in more gas bubbles, increasing the ohmic resistance of the electrolyte. The overpotentials on the hydrogen and oxygen side are governed by the Butler-Volmer equation, and approximate linear relationships for higher activation overpotentials [69].

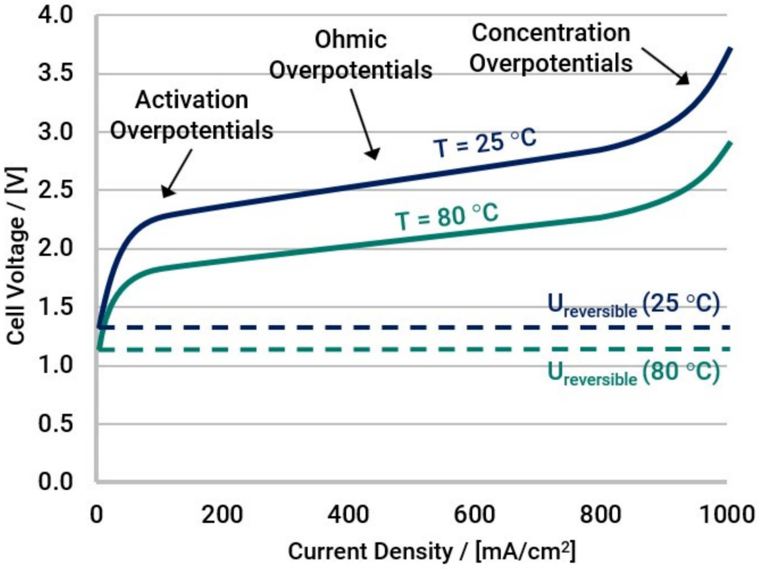

Figure 2.11: Complete cell voltage vs. current density curve for a single cell electrolyzer operating at two different temperatures. For large current densities ($j >$800 mA cm^{-2}), mass transport limitations cause an exponential increase in required overpotential. For higher temperatures, a lower overpotential is required for the same current density [68]

$$P_{\text{stack}} = n_{\text{cells}} \cdot V_{\text{cell}} \cdot I_{\text{cell}} \tag{2.18}$$

The bipolar configuration of an electrolyzer stack uses bipolar plates instead of regular electrodes in the middle of the stack (both end plates are regular electrodes with a single polarity). The bipolar plate has a negative polarity on one side, and a positive polarity on the other. It electrically conducts the applied potential, removing the need for a separate electrical connection between plates. Due to this property, a bipolar configuration is only possible in series and has the same voltage and current properties as the monopolar configuration in series.

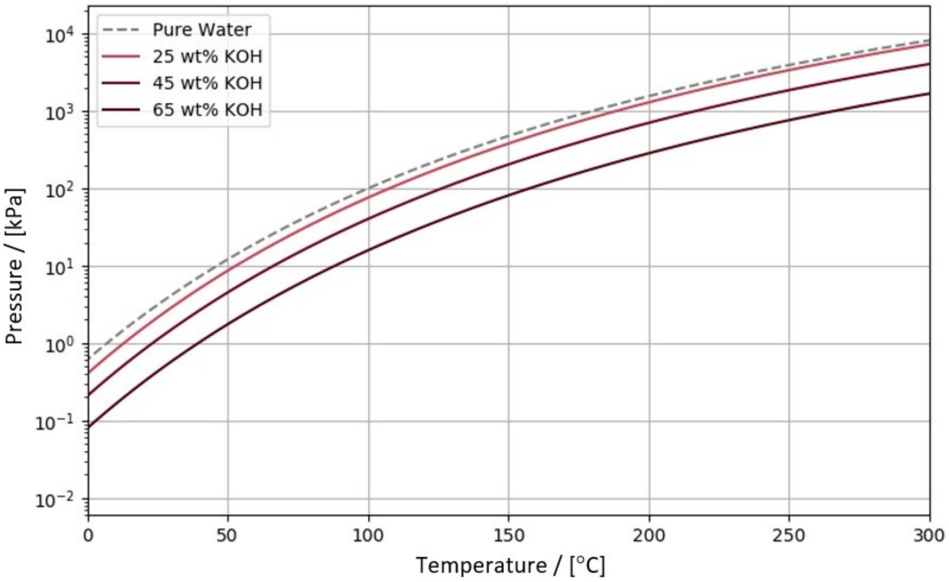

Figure 2.12: Vapour pressure curve of water for varying concentrations of added KOH. For increasing concentrations of KOH, the vapour pressure curve shifts downwards. For the same pressure, a higher temperature is required to reach the vapour phase of the mixture [70].

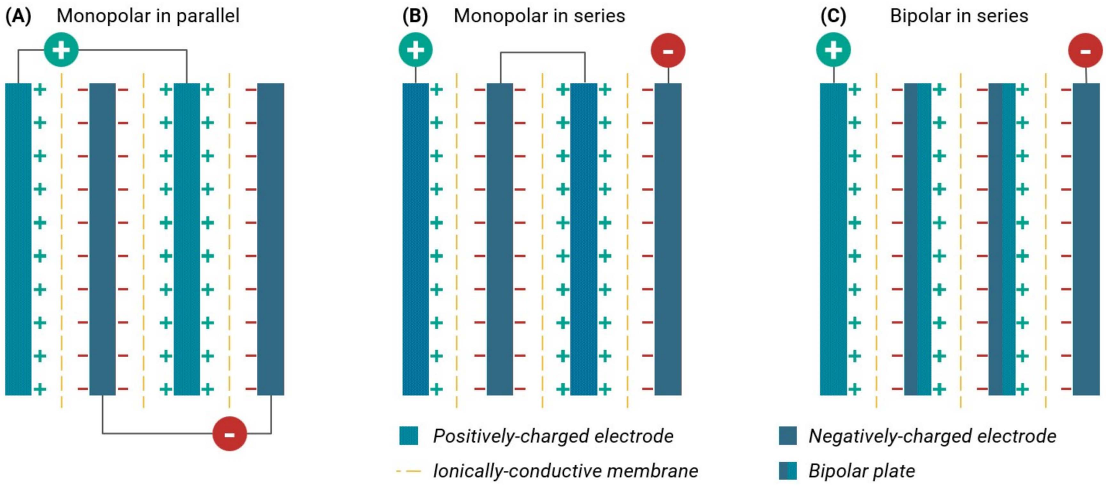

Figure 2.13: Possible cell configurations for an alkaline electrolyzer stack. Configurations (A) and (B) are both monopolar, as every electrode has a single charge. Configuration (C) is bipolar, as the electrodes in the middle of the stack are bipolar. Bipolar stacks can only be configured in series.

2.2.2. AWE Modelling

Models which accurately model the various non-linear relationships exhibited by an alkaline electrolyzer can become extremely complex. However, the modelling of an electrolyzer stack can be of great importance in optimizing stack design and improving system performance.

The modelling of an AWE electrolyzer can be split up into three elements: material property relations, cell potential relations, and efficiency relations. Firstly, there are the relationships which describe the temperature dependence of the material properties. These properties include the KOH concentration in the solution (c_{KOH}), specific conductivity (κ), specific heat capacity for constant pressure (C_p), density (ρ) and viscosity (μ) [71, 72, 73]. All of the aforementioned properties depend on temperature and the weight percentage of KOH added to the solution.

Cell potential relations can vary greatly depending on the type and production scale of the electrolyzer. Due to the high variability in cell potential, relationships are defined empirically. The final relationship for the cell potential (U_{cell}) is given in the form:

$$U_{\text{cell}} = U_{\text{rev}}(T,p) + (\eta_{\text{act}}^{\text{anode}} + \eta_{\text{act}}^{\text{cathode}}) + (\eta_{\text{act,bubble}}^{\text{anode}} + \eta_{\text{act,bubble}}^{\text{cathode}}) + I_{\text{cell}} \cdot (R_{\text{mem}} + R_{\text{electrode}} + R_{\text{KOH}}) \quad (2.19)$$

In the above equation, $U_{\text{rev}}(T,p)$ is the reversible cell potential. Concerning the overpotentials, η_{act} is the activation overpotential and $\eta_{\text{act,bubble}}$ is the activation potential due to bubble formation. Lastly, R_{mem}, $R_{\text{electrode}}$, and R_{KOH} are the ohmic resistances of the membrane, electrode, and electrolyte, respectively. Each term can be expanded and defined empirically on its own. Analogous to the cell potential, the thermo-neutral voltage of the cell can be expressed as [74]:

$$U_{\text{thermoneutral}}(T,p) = K_1 + K_2 \cdot T + K_3 \cdot T^2 + \frac{1.5 \cdot P_{\text{w}}}{nF\,(P - P_{\text{w}})} \cdot \left(K_4 + K_5 \cdot T + K_6 \cdot T^2\right) + f(T,P) \quad (2.20)$$

Here, temperature (T) is in °C, and $f(T,P)$ is a function that corrects for the difference between an ideal gas and a real gas. Constants K_1 through K_6 are defined using empirical data. The last set of modelling relationships focuses on the efficiency (ϵ) of the electrolyzer. The total efficiency of an electrolyzer is a product of the voltaic and Faradaic efficiencies:

$$\epsilon_{\text{cell}} = \epsilon_{\text{voltaic}} \cdot \epsilon_{\text{Faradaic}} \quad (2.21)$$

$$\epsilon_{\text{voltaic}} = \frac{U_{\text{thermoneutral}}}{U_{\text{cell}}} \quad (2.22)$$

$$\epsilon_{\text{Faradaic}} = 1 - \frac{I_{\text{loss}}}{I_{\text{cell}}} \quad (2.23)$$

Literature suggests that the Faradaic efficiency can also be expressed as an empirical relationship which is a function of temperature (T, in °C) and current density (j, in $\text{mA}\,\text{cm}^{-2}$) [75]:

$$\epsilon_{\text{Faradaic}} = \frac{j^2(1 - 2.5 \cdot 10^{-4}T)}{50 + 2.5T + j^2} \quad (2.24)$$

2.2.3. AWE System

In addition to a stack of alkaline electrolyzer cells, there are several other components required to produce an operation AWE system. Two pumps are responsible for providing electrolyte flow. The forced flow regime helps reduce the residence time of bubbles which form on the electrode surfaces. This can reduce the electrolyte resistance and activation potential due to bubble formation. After passing by the electrodes, the two-phase mixture of H_2/O_2 bubbles and water is fed into two flash tank phase separators. With gravity as the driving force, the gasses rise to the top of the tank whilst the electrolyte exits through the bottom. After the electrolyte and gasses have been separated, the electrolyte can take two routes back to the electrolyzer. There is a direct valve connecting the flash tank separator and the pump inlet. This keeps the anodic and cathodic sides of the electrolyzer (and the corresponding volumes of electrolyte on either side) separate. However, some configurations prefer that the electrolyte is collected in a tank and mixed into a homogeneous mixture prior to being re-fed into the electrolyzer. Figure 2.14 shows a simplified process flow diagram of an alkaline water electrolyzer.

2.3. Hybrid Renewable Energy Systems

This section will discuss the Hybrid Renewable Energy Systems (HRES) which are relevant to this research. First, an analysis is made for several on-grid HRES, which have seen more investment and technological development than their off-grid counterparts. Secondly, off-grid HRES are considered. These systems are more prevalent in developing economies and often feature simpler technology or are of smaller scale. Lastly, the economic considerations relevant to the development of HRES are discussed.

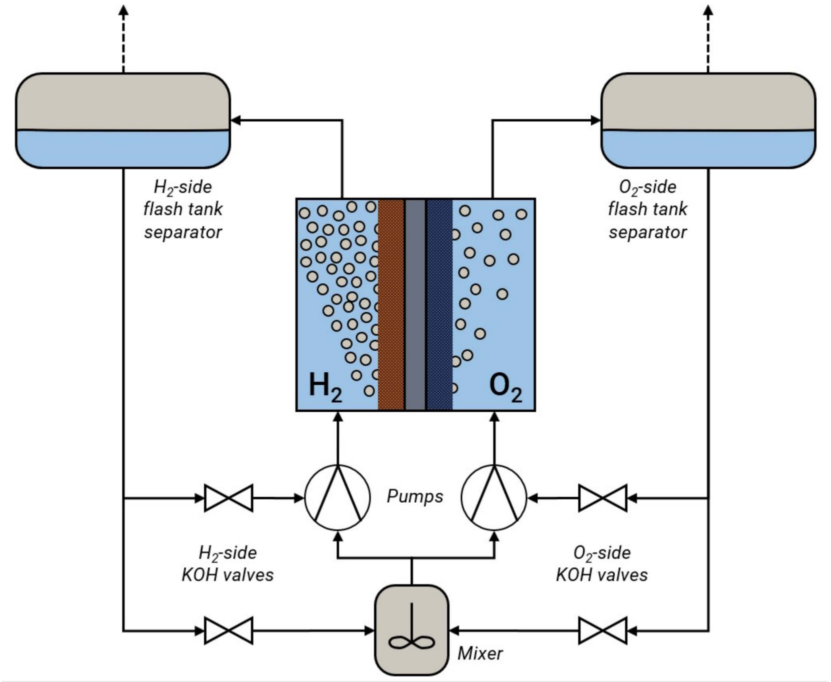

Figure 2.14: Simplified process flow diagram of a conventional alkaline water electrolysis system. Two individual pumps create a pressure-driven flow through both sides of the electrolyzer to minimize gas crossover and bubble residence time. The two-phase mixture of electrolyte and gas bubbles is pumped into two flash tanks. These tanks serve to separate the gaseous O_2 and H_2 from the electrolyte using relative differences in density. A mixer ensures a homogeneous mixture before the electrolyte is recycled and fed into the pumps. The operation can be chosen such that the electrolyte is not mixed, keeping the flow separated for each side of the electrolyzer.

2.3.1. On-Grid HRES

HRES connected to the grid are often of utility-scale size. The importance of energy security has resulted in many developing nations maintaining control over their own energy supply. The integration of multiple renewable energy sources is an active topic of research [76]. C. Hoicka and I. Rowlands investigated the complementarity of wind and PV solar resources in Ontario, Canada [77]. The aim of the study was to investigate the combination of wind and solar resources as a means of reducing the variability in power production compared to the production of electricity from each source on its own. Results showed that, for two or more locations, the variability (i.e., the peak net load) is indeed lower. The variability further increased for an increasing number of connected locations.

One proposed solution to reducing the net peak load of HRES is the implementation of batteries for 'peak shaving'. This solution sees large-scale batteries being used to off-load peak surplus' and deficits in the grid [78]. Although proven effective at smaller scales, the technology of large-scale battery systems and the required operating systems are not yet feasible [79, 78]. Furthermore, the largest battery projects have capacities of 100-400 MW. When compared to the electricity generation capacity of larger economies like the US (1.2 TW in 2022), the number of required batteries and the corresponding costs of these installations are astronomical [80].

Grid-connected HRES using hydrogen have not been researched extensively, and when researched, have only been at a small scale. Das et al. investigated the effectiveness of an HRES composed of a wind turbine, PV solar array and hydrogen fuel cell, with capacities of 20 kW, 15 kW, and 10 kW, respectively [81]. Each of the three energy sources had its own DC-DC converter to control power output and was subsequently connected to a single inverter for connection to the grid. The control of the system was aimed at optimizing the power delivered by both wind and solar, using their respective MPPTs. Additionally, the fuel cell control was set to deliver the remaining total required for a 10 kW supply of electric power to the grid. The system proved effective, generating up to 35 kW in wind/solar power at its peak, and consistently delivering a 10 kW minimum, even in worsening climate conditions [81].

2.3.2. Off-Grid HRES

Off-Grid capacity amounted to 11.2 GW in 2021 (excluding Eurasia, Europe, and North America, which are known for having excellent on-grid infrastructure). This is only 0.37% of global renewable generation capacity (0.61% when excluding Eurasia, Europe, and North America) [82]. Most off-grid systems are found in areas where there is insufficient infrastructure to realize a reliable electricity grid. As a result, most research into off-grid HRES concentrates on feasibility studies for remote locations like rural India [83], Ethiopia [84] or Saudi Arabia [85]. Literature sources which modelled and tested off-grid HRES configurations conclude that off-grid systems are less cost-effective than on-grid systems. Furthermore, almost all off-grid HRES cannot function without a battery and/or a continuous source of energy (often chosen to be biomass, as it is abundant in remote and rural areas) [86, 87, 88, 89]. Research into off-grid HRES located in urban/developed areas is scarce, as the need for decentralization of the electricity grid is only of recent importance.

2.3.3. Direct Coupling of Renewables and Electrolyzers

The integration of technologies often leads to increased system complexity. To address this complexity, synergies can be achieved through component integration. For HRES, this pertains to the system electronics in particular. General Electric designed technology which enabled solar panels to be directly integrated into the DC-circuitry of wind turbines. This reduced required power electronics equipment and eliminated the need for an extra DC-AC inverter [90].

Wind technology and the integration with electrolyzers for the production of green hydrogen is a field of research which is extensively covered, both in literature and in industry. In 2006, L. Gandia et al. demonstrated that an Alkaline Water Electrolyzer is able to closely match the current-time profile of a wind turbine [91]. Despite unstable stack temperatures, efficiency remained between 74-85% based on stack voltage, with the inefficiencies stemming from the transient regimes of operation [91]. In a more recent paper, Firtina-Ertis et al. investigated the sizing of an off-grid HRES consisting of a wind turbine, electrolyzer, fuel cell, and hydrogen storage facility [92]. Results showed that the system needed a rated power equivalent to 10x the average consumption of the load, whereas a conventional off-grid system only required a turbine with a power of 3x the average consumption. The sizing of the hydrogen storage tank and fuel cell proved difficult. Due to the fact that the final mode of energy consumption was electricity (and not hydrogen), it was concluded that such an HRES is not suitable for small-scale electricity applications [92].

The integration between PV solar technology and electrolyzers has also been explored in literature. Similar to the HRES presented by Firtina Ertis et al., Ganguly et al. modelled and analyzed a small-scale system combining solar, electrolysis and fuel cell technology, for integration in a greenhouse [93]. Results showed such a system could be viable for the given scale (3.3 kW in electrolysis capacity, 0.96 kW in fuel cell capacity). In a 2022 paper, Ibáñez-Rioja et al. simulated an off-grid system for generating green hydrogen, made up of a PV solar array, a battery and a PEM electrolyzer [94]. The proposed system used a battery to supplement the electricity demand of the PEM electrolyzer in times of low solar irradiance. This prevents monetary penalties resulting from the shutdown of the PEM electrolyzer due to insufficient power input. However, the high relative cost of the battery system resulted in the conclusion that it was not an effective method of guaranteeing green hydrogen production during periods of limited solar irradiance. The price of the PEM electrolyzer also proved of a similar impact on the final price of produced green hydrogen [94].

In order to improve the efficiency of electrolyzers connected to intermittent renewables, a HRES made up of multiple, smaller electrolyzers could serve as a better alternative. S. Muyeen et al. tested such a system, combining a variable-speed wind turbine and 10 individually controllable electrolyzers [95]. Through the use of a First-In-First-Out switching algorithm to select which of the 10 electrolyzers is active at any given time, the paper was able to prove improved single electrolyzer performance and reduce overall system degradation. Furthermore, it was suggested that performance could improve further if the DC bus of the electrolyzers was integrated directly into that of the wind turbine, similar to the efforts of General Electric mentioned earlier [90, 95]. Another paper, written by Yamashite at al., demonstrated an increase in the overall system efficiency of a solar-to-hydrogen system when using multiple electrolyzers [96]. The system discussed in the paper used four individual DC-DC converters, each connected to a separate electrolyzer. In this configuration, an 8.5%-point increase was observed compared to a system with a single converter-electrolyzer system of the same total capacity [96].

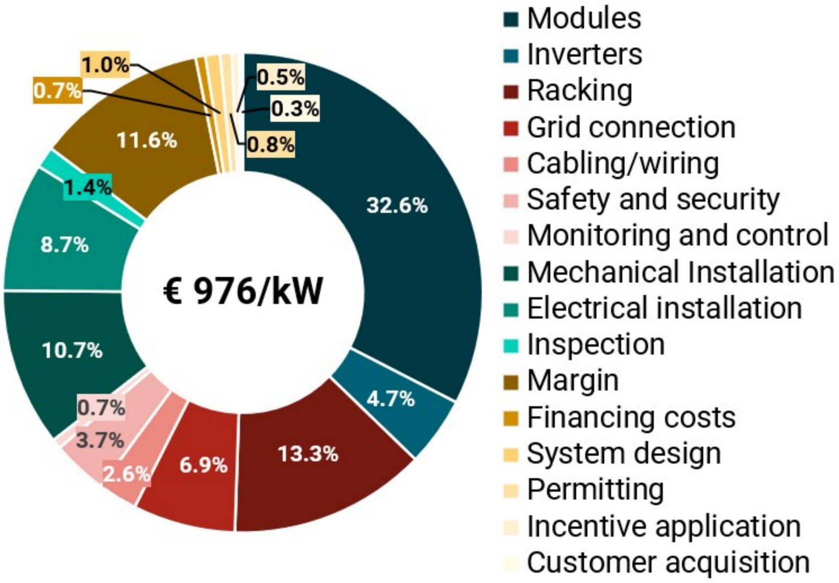

Figure 2.15: Capital expenditure breakdown of a PV solar park. Shown expenditure covers all of the capital expenditure needed to build and install a utility-scale PV solar park. Currency values exchanged to be expressed in 2022 Euro. Data source: Fraunhofer Institute for Solar Energy Systems [97]

2.3.4. Economical Considerations

The integration of new, state-of-the-art HRES is dependent on both the technological and economic feasibility of the innovations. Money remains the main driver in the adoption of new technologies in the industry.

In order to develop a better understanding of the economic considerations for HRES, a closer look can be taken at the costs which make up the constituent components of an HRES. Shown in Figure 2.15 is a breakdown of the capital expenditure (CAPEX) for a utility-scale solar PV park. It can be seen that the PV panels themselves only make up 33% of the total costs. Together, the installation, electrical and racking (mounting) costs cost more than the PV panels. From a development perspective, it is therefore of value to explore innovative ways of decreasing costs for other subsystems for solar parks.

For hydrogen technology, there is a profound difference in costs when comparing alkaline electrolyzers and PEM electrolyzers. Whilst PEM electrolysis requires rare-earth metals for its electrodes, AWE electrolyzer CAPEX mainly consists of manufacturing costs. Given that the electrodes are often made of common metals like iron and nickel, overall costs are significantly lower than that of PEM electrolyzers. An overview of the CAPEX breakdown of an AWE electrolyzer is given in Figure 2.16.

As mentioned in earlier chapters, sources of renewable energy are heavily dependent on location, and lifetime performance is strongly correlated with the local weather. Therefore, the design of an HRES should take into account the target area of operation of the system. The method used for taking location into account makes use of the Levelized Cost of Energy (LCOE), or in the hydrogen markets, the Levelized Cost of Hydrogen (LCOH).

Expenses (CAPEX, OPEX) can vary depending on geography, with labour costs being subject to local regulations and materials having varying tariffs depending on trade deals and supply chain logistics. The amount of electricity/hydrogen produced over the HRES lifetime is a function of the capacity factors of renewable energy sources used in the system. Countries close to the arctic circle see significantly fewer sun hours compared to countries closer to the equator. Alternatively, coastal regions have higher average wind speeds than inland regions. All of these factors influence the total production of electricity or hydrogen. Figure 2.17 shows the Levelized Cost of Hydrogen (LCOH) when coming directly from solar [98].

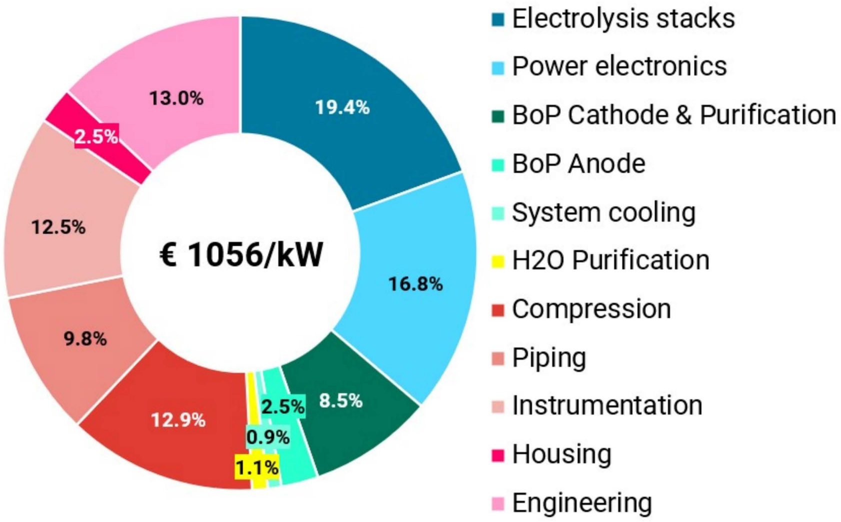

Figure 2.16: Capital expenditure breakdown of an alkaline electrolyzer. Shown expenditure covers all of the capital expenditure needed to build and install a utility-scale liquid alkaline electrolyzer. Currency values exchanged to be expressed in 2022 Euro. Data source: International Renewable Energy Agency [10]

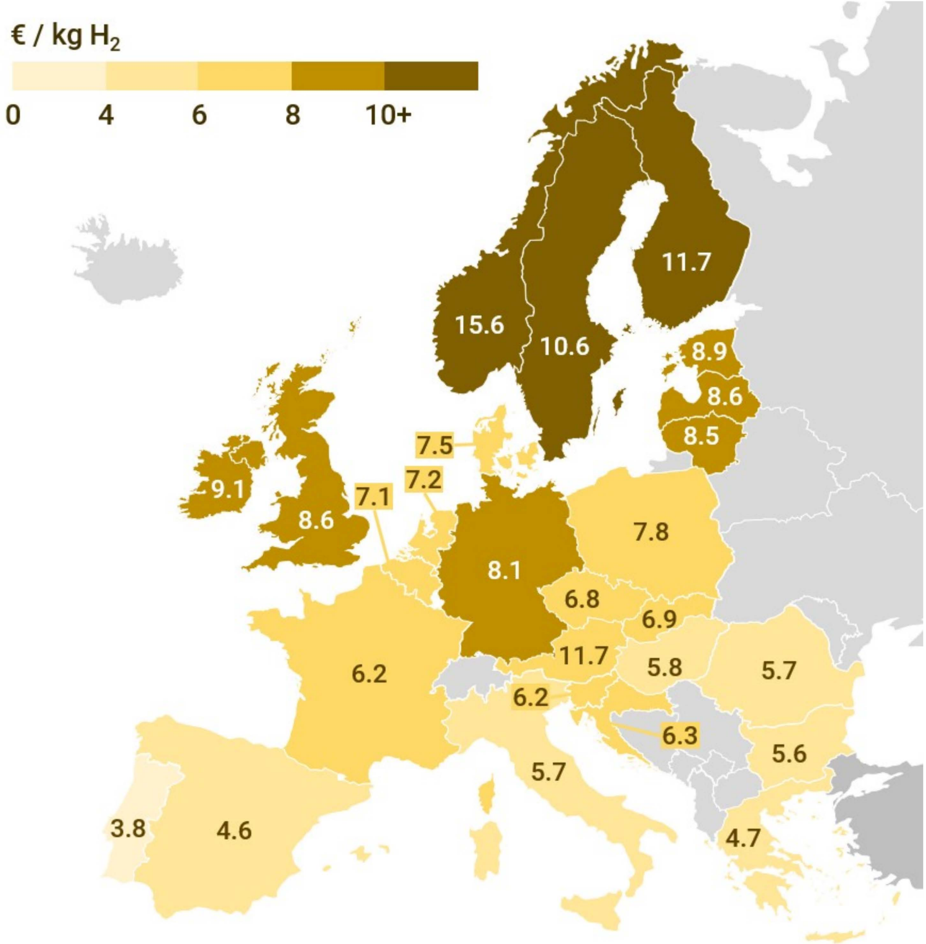

Figure 2.17: Map of Levelized Cost of Hydrogen when directly connected to PV solar energy for the EU, Norway and the U.K. Scandinavia sees a disproportionately high LCOH for PV solar due to the limited sun hours in winter times. Southern Europe and the Mediterranean benefit from more sun exposure and less cloudy weather (Data source: FCHO [98])

3

Methodology

This chapter presents the methodology employed to address the research objectives outlined in Chapter 1. The Methodology chapter is structured into three main sections: System Modelling, System Design, and System Control. Section 3.1 focuses on system modelling, which involves developing models for the two main components of the HRES: the PV solar park and the modular alkaline electrolyzer. In Section 3.2, system design is discussed, encompassing the sizing of system components relative to each other and optimizing operating points to maximize hydrogen production. Lastly, Section 3.3 delves into system control, elucidating the control algorithm that facilitates direct coupling of the system. This chapter provides a comprehensive account of the methodology employed to achieve the research objectives.

3.1. System Modelling

This section will cover the modelling of each element of the HRES covered in this research. Starting with the modular alkaline electrolyzer and subsequently covering the modelling of the PV solar array.

3.1.1. XINTC Modular Alkaline Electrolyzer

In the following subsection, the modelling of the modular alkaline electrolyzer system is discussed. This starts with the various assumptions and constraints that are made to ensure the validity of the model. Next, the voltage-current relationship for a single stack is discussed, together with the system composition of the electrolyzer in terms of voltage and current. Consequently, the modelling of system power is explained. Lastly, the hydrogen production and specific cost of hydrogen production are derived.

Constraints & Assumptions

In this work, the collaboration with alkaline electrolyzer OEM XINTC has provided the initial constraints for the electrolyzer. The XINTC containerized modular alkaline electrolyzer is made up of 120 stacks, which can be independently turned on and off. Each stack is made up of two gas modules and has a nominal power 10-13 kW, depending on the operating conditions. The full system has a nominal power of 1.2 MW and a peak power of 1.56 MW. The full system of stacks is subdivided into 8 sections, with each section having its own flash tanks and electrolyte pump. In addition to the number of stacks, the physical stack dimensions, the degradation rate and the operating pressure/temperature of the stacks are all constrained and assumed as constant.

The voltage is constrained on the lower end by the laws of thermodynamics. As mentioned in Chapter 2 (Section 2.2.1, Figure 2.9), the lower limit of voltage can be taken as a figure close to the thermoneutral voltage, depending on the operating temperature of the electrolyte (which is between 30-50 °C for the electrolyzers discussed in this work). The upper voltage limit for each stack is set to 572 V, as an absolute boundary to prevent cell damage in the long run (i.e., corrosion and electrolyte degradation).

For the stack current, there is no lower limit as an idle stack will have a current of zero. The upper limit is defined by the rate of bubble formation on the electrode surface and mass diffusion limitations.

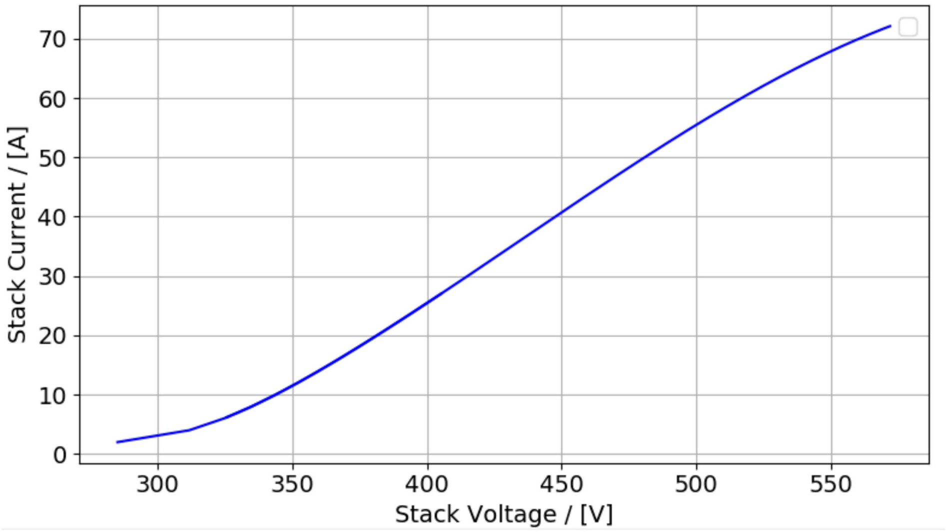

Figure 3.1: Voltage-current graph for a single alkaline electrolyzer stack. The voltage-current characteristics used for modelling and simulations in this work are the result of a model developed by XINTC. All data >405 V are estimates based on model data [99].

In this work, the soft limit for current is set to 27 A. with 'soft' indicating that the limit can be exceeded, but this goes at the expense of reduced system efficiency.

One critical assumption about the electrolyzer in this work is that there is zero bypass current. Bypass current is a current leak, which can take place at both system- and stack-level. At both levels, current can be conducted through the electrolyte or the frame from one pole to another. In a single stack, bypass current can result in less current passing through the electrodes, leading to a lower hydrogen production rate for the same power input. Due to a lack of empirically-defined loss parameters, losses due to bypass currents are not taken into account.

Another limitation to the modelling of the electrolyzer is that the modelled characteristics are not temperature-dependent. The temperature of the electrolyte is assumed to be constant during both start-up and regular operation. In practice, electrolyte temperature will vary between the ambient temperature and the operational temperature of the electrolyzer. However, the XINTC electrolyzer operates at relatively low temperatures meaning that errors as a result of assuming a constant temperature are negligible on a large timescale.

Voltage and Current

In accordance with the above-mentioned constraints and assumptions, it is possible to define the characteristic curves for the voltage and current behaviour of the system. As a starting point, experimental data from K. Mera can be used [99]. This dataset describes the voltage-current relationship of a single electrolyzer stack, as shown in Figure 3.1 below:

The 572 V upper voltage limit is not the limiting factor for high voltage/current performance. The 27 A soft limit on the current limits the experimental dataset from reaching higher stack voltages. In order to accurately model the full range of voltages for the full electrolyzer system, a cubic spline was made through the experimental dataset. With this cubic spline, a voltage and current model can be constructed which describes the behaviour of a modular system of alkaline electrolyzers. An overview of the system is shown in Figure 3.2.

Each stack in the system is connected in parallel. As a result, the system voltage is equivalent to the single-stack voltage.

$$V_{\text{EL, model}} = V_{\text{section}} = V_{\text{stack}} \tag{3.1}$$

In a real system, the voltage per stack will not be equal due to noise and varying cable resistances. Therefore, a different approach must be taken to calculate the system voltage. The real electrolyzer voltage is given as the average voltage over all active stacks:

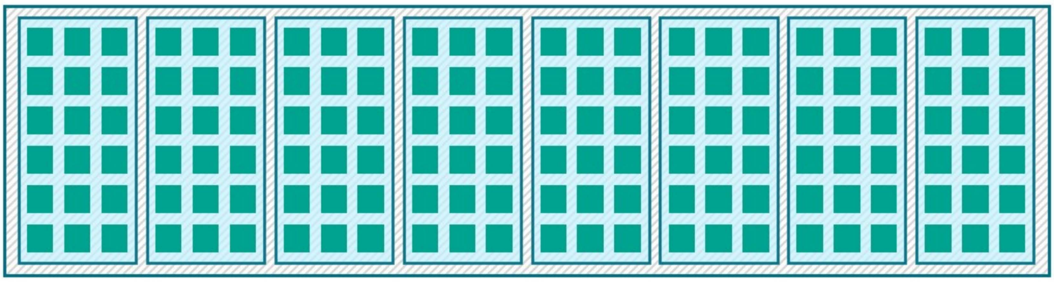

Figure 3.2: Diagram of the full modular alkaline electrolysis system. The full system consists of 120 stacks divided over 8 sections. Each section contains 15 stacks and its own pump and gas separator system.

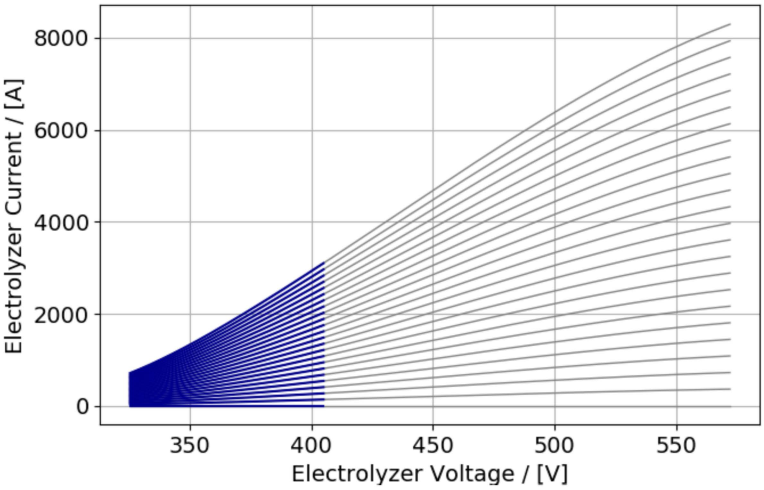

Figure 3.3: Voltage-current curves for a modular alkaline electrolyzer system of 120 stacks. Each line represents an increment of 5 stacks, going from 0 to 120 stacks. The line parallel to the voltage axis denotes 0 active stacks, and the line furthest away from the voltage axis denotes 120 active stacks. The grey area of the line indicates the part of the curve which exceeds the soft current limit imposed in this work.

$$V_{\text{EL, real}} = \frac{1}{n_{\text{active stacks}}} \cdot \sum_{n=1}^{120} V_{\text{active stack, i}} \tag{3.2}$$

The current flowing through the system does not stay constant with the number of stacks. Due to the series configuration of the cells in the stack, the single-cell current is equivalent to the stack current. However, the parallel configuration of stacks in the system sees the total electrolyzer current as a product of the number of active stacks in the system and the single-stack current.

$$I_{\text{EL, model}} = I_{\text{stack}} \cdot n_{\text{stacks, active}} = I_{\text{cell}} \cdot n_{\text{stacks, active}} \tag{3.3}$$

In the real system, the current delivered to each stack can vary. The temperature of the electrolyte, the degradation of the stack and sensor noise all cause differences in current between two otherwise identical stacks. As such, the total current delivered by the PV solar arrays is equally divided over all of the stacks (connected in parallel). It is important to note that inactive stacks experience no current flow, and are therefore assumed to have zero current.

$$I_{\text{active stack, i}} = \frac{I_{\text{EL, real}}}{n_{\text{stacks, active}}} \tag{3.4}$$

Combining the voltage-current relationship expressed in Figure 3.1 and the relationships for voltage and current at the full electrolyzer sub-system level, an overview can be made regarding the full system electrolyzer current for a given voltage. This is shown in Figure 3.3.

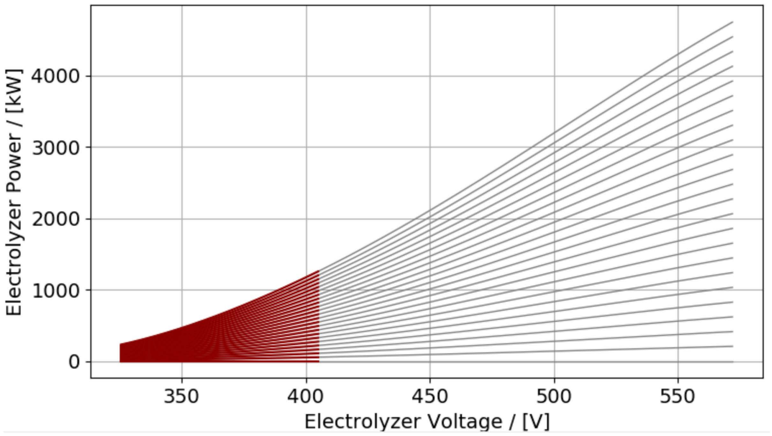

Figure 3.4: Voltage-power curves for a modular alkaline electrolyzer system of 120 stacks. Each line represents an increment of 5 stacks, going from 0 to 120 stacks. The line parallel to the voltage axis denotes 0 active stacks, and the line furthest away from the voltage axis denotes 120 active stacks. The grey area of the line indicates the part of the curve which exceeds the soft current limit imposed in this work.

Power

With existing relationships for current and voltage, the power consumed by the electrolyzer at any moment can be expressed as the product of the voltage and current experienced by the electrolyzer:

$$P_{\text{EL}} = V_{\text{EL}} \cdot I_{\text{EL}} \tag{3.5}$$

The values used for the voltage and current of the system are chosen according to the situation. For modelling work, the model voltage and current are taken, whereas the real power is calculated according to the real voltage and current relationships. Shown in Figure 3.4 is the power curve for a full electrolyzer.

Hydrogen Mass Flow Rate

The rate of production of hydrogen ($\dot{n}_{\text{H2, molar}}$) can be expressed as a function of the number of active stacks ($n_{\text{active stacks}}$), the Faradaic efficiency (ϵ_{F}), the single-stack current (I_{stack}), the number of cells per stack (n_{cells}), and the Faraday constant. The molar production rate of hydrogen is directly proportional to the current flowing through any given cell through the following relationship:

$$\dot{n}_{\text{H2, molar}} = n_{\text{active stacks}} \cdot n_{\text{cells}} \cdot \epsilon_{\text{F}} \cdot \frac{I_{\text{stack}}}{2F} \tag{3.6}$$

The Faradaic efficiency is a function of the current flowing through the cell. A model for the Faradaic efficiency was developed by A. Rahbari at XINTC based on various sources from literature [47, 99, 100, 101]. Figure 3.5 shows the relationship of the Faradaic efficiency for varying currents.

The mass flow rate of hydrogen is expressed in $\text{kg}\,\text{h}^{-1}$. For this conversion, the molar mass of hydrogen is required. It is assumed that the purity of hydrogen is sufficiently high that the molar mass of other byproducts is negligible.

$$\dot{m}_{\text{H2}} = \dot{n}_{\text{H2, molar}} \cdot M_{\text{H2}} \tag{3.7}$$

The mass flow rate for varying numbers of active stacks is shown in Figure 3.6.

Specific Production Cost of Hydrogen

The specific production cost of hydrogen (ψ_{H2}) is defined as the electrical power required per kilogram of produced hydrogen (units $\text{kW}\,\text{h}\,\text{kg}^{-1}$). This is expressed as the ratio of the electrolyzer power to the mass flow rate of hydrogen as a result of that same electrolyzer power.

$$\psi_{\text{H2}} = \frac{P_{\text{EL}}}{\dot{m}_{\text{H2}}} \tag{3.8}$$

This is displayed graphically in Figure 3.7.

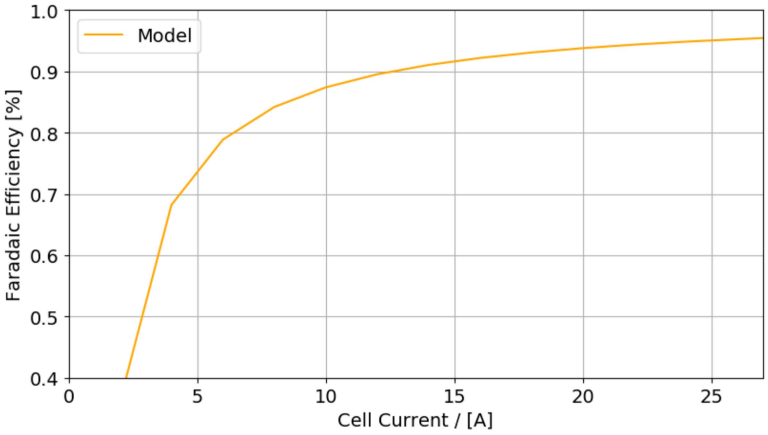

Figure 3.5: Faradaic efficiency curve for an alkaline water electrolyzer. This curve was generated from a model developed by XINTC based on multiple sources from literature [99, 100, 101].

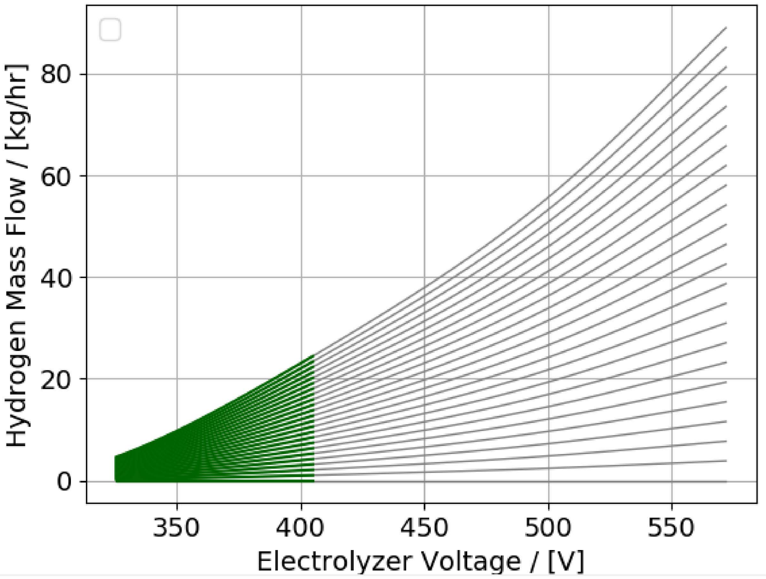

Figure 3.6: Voltage-Hydrogen mass flow curves for a modular alkaline electrolyzer with 120 stacks. Each line represents an increment of 5 stacks, going from 0 to 120 stacks. The line parallel to the voltage axis denotes 0 active stacks, and the line furthest away from the voltage axis denotes 120 active stacks. The grey area of the line indicates the part of the curve which exceeds the soft current limit imposed in this work.

As can be interpreted from Figure 3.7, there is a single optimal point of hydrogen generation regardless of the number of active stacks. At a voltage of 348.5 V, there is a minimum specific cost of hydrogen production of 47.5 $\mathrm{kW\,h\,kg^{-1}}$. Whilst the hydrogen production at this voltage may not be maximum, it will lead to the lowest average cost. Alternatively, for higher electrolyzer voltages, the increasing resistances in the electrodes and the electrolyte will result in higher specific costs of production.

3.1.2. PV Solar Array

This subsection aims to explain how the PV solar array for this research was modelled. After detailing the relevant constraints and assumptions for modelling, the model behind the PV solar panel cell temperature is explained. Next, the model for a PV solar panel is discussed and the model is tested against a benchmark data set of incident irradiance and ambient temperature data.

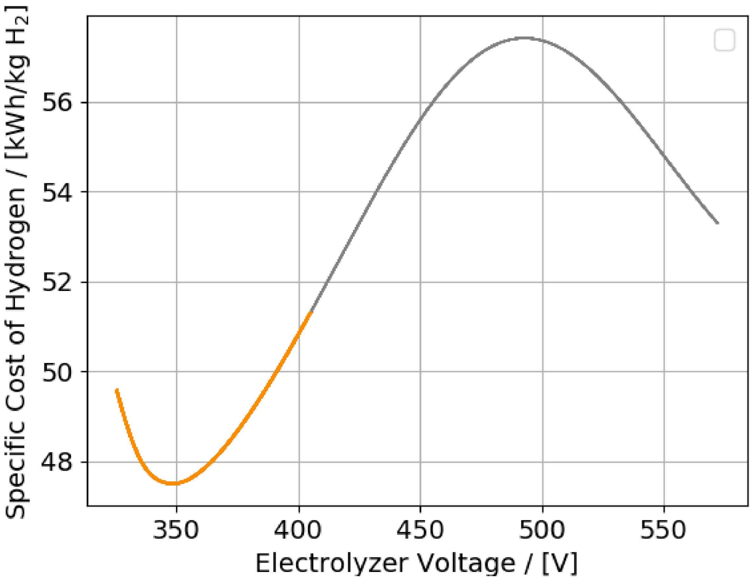

Figure 3.7: Specific cost of hydrogen production expressed in terms of voltage for a modular alkaline electrolyzer with 120 stacks. The curve is independent of the number of stacks since these stacks are in parallel with one another. The grey area of the line indicates the part of the curve which exceeds the soft current limit imposed in this work.

Constraints & Assumptions

For the modelling of an array of PV solar panels, several assumptions are made to construct an efficient yet accurate model. Firstly, concerning the modelling of the cell temperature, solar panel heat loss through forced convection as a result of wind is not included. This is due to a lack of wind speed data that matches the measurements for incident irradiance and ambient cell temperature. Solar parks are often located in areas with high solar exposure, which is often negatively correlated with average wind speed (expressed geographically in Figure 2.17).

Another assumption essential to the modelling of the PV solar array is that there is no partial shading. The P-V curve for a PV system under partial shading conditions varies significantly from that same system under non-partial shading conditions. Given that partial shading only occurs when two different areas of the same solar array experience different incident irradiances, the total time in which partial shading is applicable is assumed as negligible.

Concerning the PV solar panel itself, each panel is assumed equal in rated performance, internal circuitry and in orientation. In an array, the panels are mounted next to each other, horizontally on the ground and oriented facing True North. Furthermore, for an array of panels connected in series, the voltage is equal to the single panel voltage multiplied by the number of panels in series and the current is the same through each panel. Consequently, for an array of panels connected in parallel, the voltage is the same and equal across each panel and the current is equal to the current of a single panel multiplied by the number of panels placed in parallel.

The irradiance data used for the modelling is assumed to be the sum of the direct and diffuse radiation. Direct irradiation refers to the unobstructed solar radiation that reaches the surface of the Earth, while diffuse irradiation represents the scattered sunlight that is deflected by the atmosphere, clouds, or surrounding objects. These metrics serve as suitable indicators for modelling PV solar panel performance. Direct irradiation directly impacts the electricity generation of PV panels, representing the unimpeded solar radiation incident on the panels. Conversely, diffuse irradiation contributes to the overall energy received by the panels, accounting for scattered sunlight from various angles, compensating for instances when direct sunlight is obstructed by factors such as clouds, haze, or shading. By incorporating both direct and diffuse irradiation, the model can accurately assess the energy generation potential of PV solar panels under diverse environmental conditions.

Cell Temperature

PV Solar panels are solid-state semiconductor machines. As such, the performance of the cells that constitute a panel is dependent on its surroundings. Semiconducting materials like silicon have

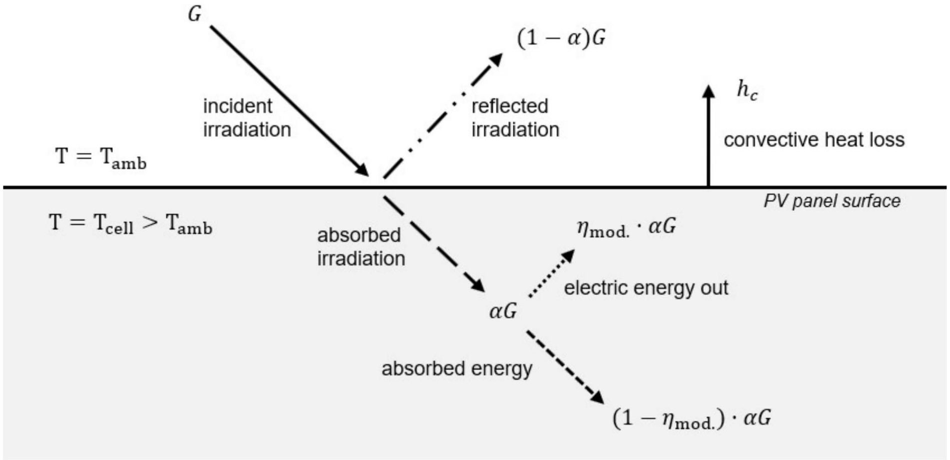

Figure 3.8: Energy balance diagram of a PV solar panel. The cell temperature is defined as the ambient temperature plus the ratio of the absorbed radiation to the heat loss transfer coefficient. Shown variables are incident irradiation (G), solar radiation absorption coefficient (α), PV module efficiency (η_{mod}), cell temperature (T_{cell}), ambient temperature (T_{amb}), and heat transfer coefficient (h_c). Radiative and conductive heat losses are assumed to be negligible. Forced convective heat losses due to wind are ignored due to a lack of data.

temperature-dependent properties, requiring an accurate model of cell temperature for useful simulations.

Shown in Figure 3.8 is a diagram of the heat balance which can be made over the surface of a PV panel. Incident irradiation (G) hits the panel surface (A_{s}) and is both reflected and absorbed. The absorbed fraction of the irradiation is calculated using the solar radiation absorption coefficient (α). The absorbed irradiance is further split up into radiation which can be usefully transferred to electrical energy and the remaining energy which must be dissipated as heat. The useful electrical energy is obtained through the PV module efficiency (η_{mod}), which is provided by the PV panel manufacturer and ranges between 15-25% [102]. This absorbed energy results in the gradual heating of the PV panel, raising its temperature (T_{cell}) above that of the environment (T_{amb}). As a result of this temperature difference, heat is lost to the environment through convection (with heat transfer coefficient h_c)
The true thermal energy that is absorbed can be written as:

$$\dot{Q}_{\text{absorbed}} = \alpha(1-\eta_{\text{mod}}) \cdot G \cdot A_{\text{s}} \tag{3.9}$$

When divided by the panel surface area to express the thermal energy per unit area, this can be set equivalent to the heat lost to the environment. The heat loss can be written as:

$$\dot{q}_{\text{absorbed}} = h_c(T_{\text{cell}} - T_{\text{amb}}) \tag{3.10}$$

Setting both equations equivalent to one another, and solving for the cell temperature, the following result is obtained:

$$T_{\text{cell}} = T_{\text{amb}} + \frac{\alpha(1-\eta_{\text{mod}}) \cdot G}{h_c} \tag{3.11}$$

Radiation heat losses are negligible due to the low emissive properties of PV solar panel materials. This relationship was experimentally proved to be accurate to ± 2 °C by D. Faiman in 2008 [103]. The Python PVlib library has incorporated this model into one of its functions, allowing for an accurate and computationally efficient method of modelling the cell temperature for a PV solar cell.

Irradiance

The irradiance incident on PV solar panels is highly dependent on the location of the panel, as well as its mounting angle and orientation. Modelling the characteristic curve of a PV cell from its irradiance is achieved through the use of the Single-Diode Model (SDM). The Single Diode model aims to solve the following equation:

Table 3.1: Datasheet parameters of the DMEG DM405 Solar panel. This PV panel is used as the basis for all PV modelling and simulation in this research.

Variable	Value	Units	Description
Company	DMEGC Solar	-	Company name
Version	DM405	-	Product version
Technology	Mono-c-Si	-	Semiconductor used in the PV panel
Date	04/10/2021	-	Date of first production
P_{max}	405	W	Maximum power
$V_{\text{OC,ref}}$	37.33	V	Open-circuit voltage at reference conditions
$I_{\text{SC,ref}}$	13.68	A	Short-circuit current at reference conditions
$V_{\text{MP,ref}}$	30.52	V	Voltage at maximum power point at ref. conditions
$I_{\text{MP,ref}}$	13.28	A	Current at maximum power point at ref. conditions
α	0.0306432	$\text{A}\,\text{C}^{-1}$	Current temperature coefficient
β	-0.0918318	$\text{V}\,\text{C}^{-1}$	Voltage temperature coefficient
γ	-133.65	$\text{W}\,\text{C}^{-1}$	Power temperature coefficient
N_{cells}	108	-	Number of cells in series on the PV panel
EgRef	1.121	eV	Energy bandgap at reference temperature
dEgdT	-0.0002677	K^{-1}	Temperature dependence of the energy bandgap
G_{ref}	1000	$\text{W}\,\text{m}^{-2}$	Reference irradiance
T_{ref}	25	°C	Reference temperature

$$I = I_L - I_0 \left(\exp \frac{V + IR_s}{n \cdot N_{\text{series}} \cdot V_{\text{thermal}}} - 1 \right) - \frac{V + IR_s}{R_{\text{shunt}}} \tag{3.12}$$

$$V_{\text{thermal}} = \frac{k \cdot T_{\text{cell}}}{q} \tag{3.13}$$

Here, I_L and I_0 are the light-generated current and the diode reverse saturation current, respectively. R_s and R_{shunt} are the series resistance and shunt resistance, respectively. The usual diode ideal factor (n), the number of cells in series (N_{series}), and the cell thermal voltage (V_{thermal}) under the desired I-V curve conditions make up the remaining variables. The thermal voltage can be further expressed in terms of the Boltzmann constant (k), cell temperature (T_{cell}) and elementary charge of an electron (q).

Due to the presence of I on both sides of the equation, the equation must be solved iteratively. In 2004, A. Jain et al. proved that it was possible to solve for an exact closed-form solution of the SDM equation using the Lambert W-function [104]. Other methods of iterative solving like the Newton-Raphson root-finding method or the Brent bisection search method can also be used to solve the SDM equation, albeit not as an exact solution.

The above-mentioned variables that are required for the SDM cannot be found in the datasheet of a PV panel. Manufacturer datasheets only contain information about the performance at the MPP. For the SDM equation, more information is required to calculate the input parameters. As a result, W. De Soto et al. created the Five Parameter model in 2006. This model estimates the required variables for the SDM using datasheet-provided parameters and semi-empirical equations [54]. For this paper, the PV panel used for modelling and simulation is detailed in table 3.1.

This data can be combined with a dataset containing the incident irradiance and corresponding cell temperature to generate the I-V curve of the PV panel at every time step. As a baseline, the cell temperature is kept constant at 25 °C and the irradiance is varied linearly between 0-900 $\text{W}\,\text{m}^{-2}$, in steps of 100 $\text{W}\,\text{m}^{-2}$. Using the Python PVlib library, figures 3.10 and 3.9 show the I-V and P-V curves for the above-mentioned constant step scenario, respectively. The Python PVlib library utilizes the Single-Diode Model by W. De Soto et al. to iteratively compute the I-V curves [54]. This is the same method discussed earlier in this paper, in Section 2.1.2.

The result above show a range in power delivered, varying proportionally with the imposed irradiance. Both the short-circuit current and open-circuit voltage vary with irradiance. However, for irradiances greater than 300 $\text{W}\,\text{m}^{-2}$, the voltage at which maximum power is reached does not vary significantly. This changes once the cell temperature is no longer maintained constant.

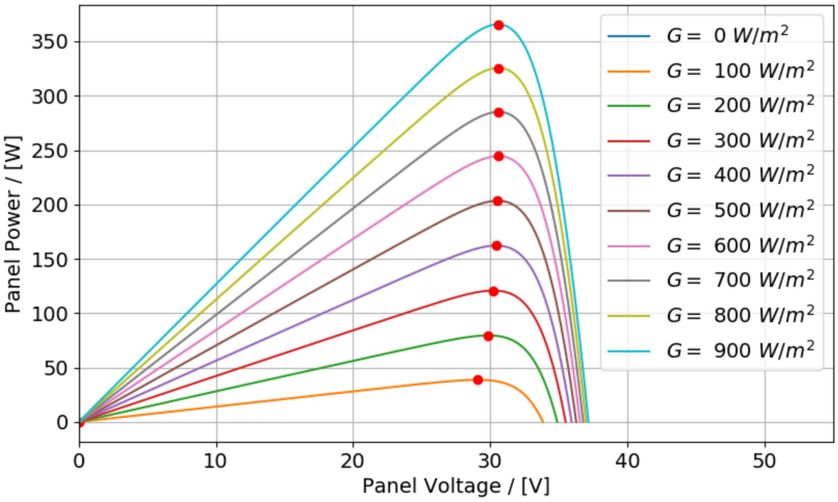

Figure 3.9: P-V curve of a PV solar panel exposed to various irradiances at a constant cell temperature of 25 °C. The red dot denotes the maximum power point (MPP) of each curve. If the cell temperature is kept constant, there is little variation in the voltage at which the MPP is achieved. Results were generated using the Python PVlib library.

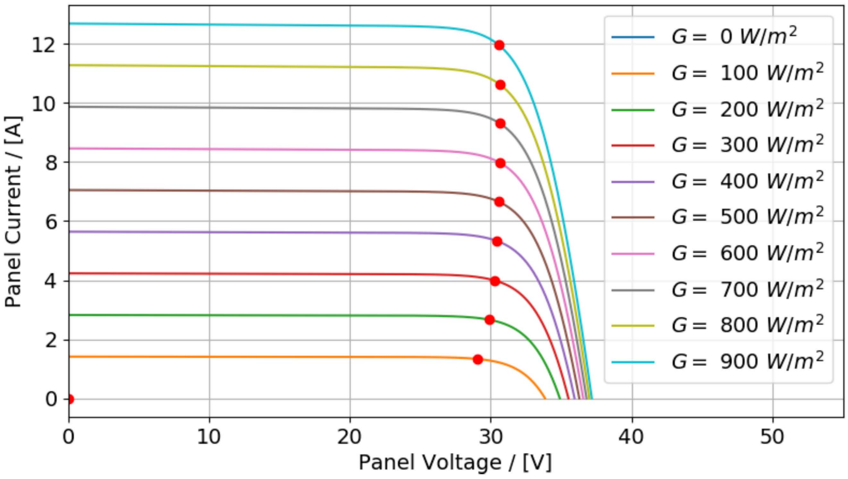

Figure 3.10: I-V curve of a PV panel exposed to various irradiances at a constant cell temperature of 25 °C. The maximum power point (MPP) of each curve is denoted by the red dot. Results were generated using the Python PVlib library.

In order to evaluate the performance of the PV panel model, real weather data is used. Shown in Figure 3.11 is the hourly irradiance and ambient air temperature data for the Cabauw weather station in The Netherlands on the 1st of October, 2022. Provided by the Royal Netherlands Meteorological Institute (KNMI), this data can be used to calculate the cell temperature data using the method described in 3.1.2. The resulting cell temperature has also been shown in figure 3.11.

From the figure shown above, it can be seen that the cell temperature varies compared to the ambient air temperature. With these datasets for irradiance and cell temperature, the P-V curves for a single PV panel which is exposed to these conditions can be calculated. Shown in Figure 3.12 are 24 P-V curves, a result of the 1-hour sampling rate of the irradiance and ambient air temperature data. Red dots and lines in the figure denote the maximum power point and the movement thereof. It can be noted that the variation in MPP is greater than originally displayed in Figure 3.9. This is due to the cell temperature no longer being assumed constant throughout the day, and due to the volatility of irradiance incident on the panel. Cloud coverage and other rapidly changing weather conditions heavily influence the performance of the PV panel, causing changes in P-V curve values and corresponding MPP.

Variation in MPP further increases with a higher sampling rate. A sampling rate of 5 minutes provides 288 data points. This level of irradiance sampling allows for short-term variations in irradiance

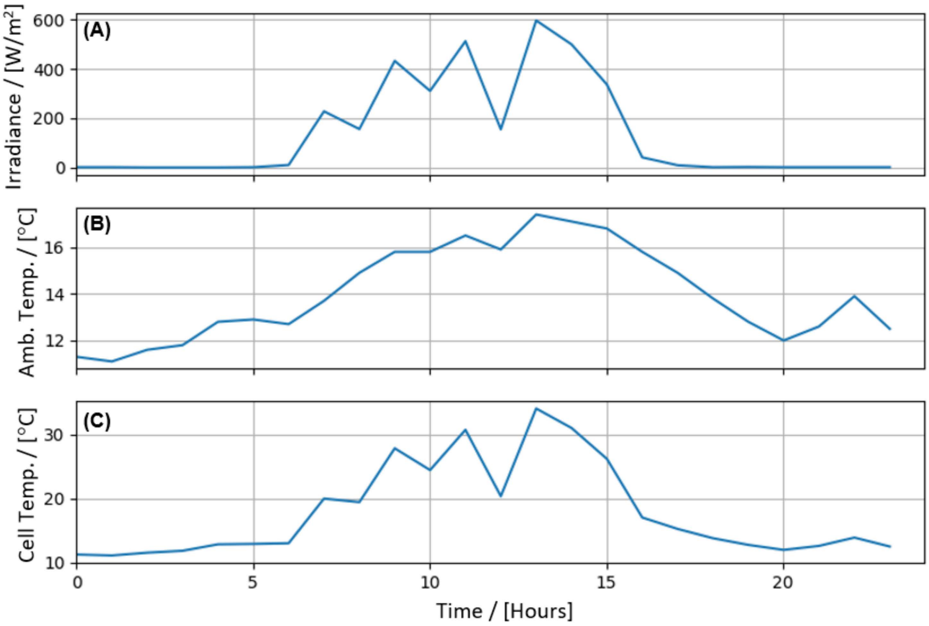

Figure 3.11: Irradiance (Plot A), ambient air temperature (Plot B) and PV panel cell temperature (Plot C) at the Cabauw weather station in The Netherlands on 01-10-2022 at a sampling interval of 5 minutes. Data was obtained from the Royal Netherlands Meteorological Institute (KNMI). Results were generated using the Python PVlib library. Data source: KNMI, in collaboration with the BSRN [105, 106]

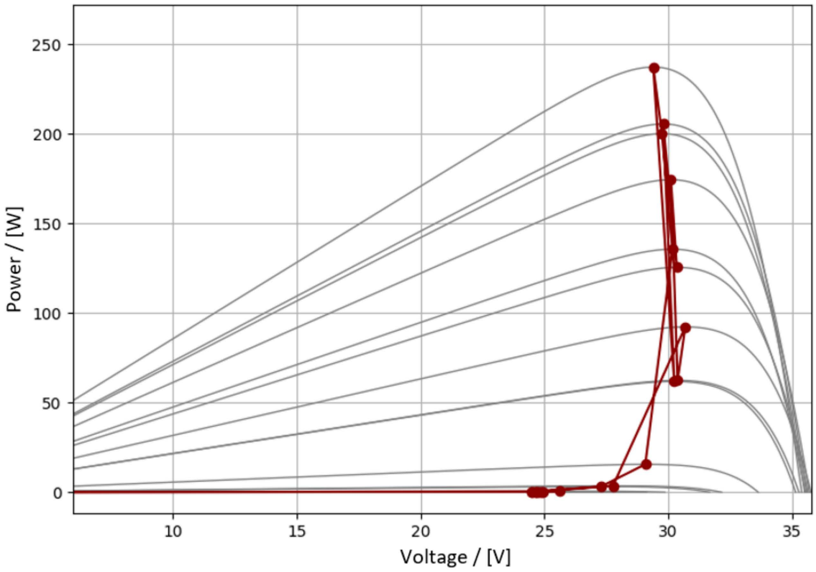

Figure 3.12: P-V curves of KNMI Cabauw weather station data on 01-10-2022. Sampling time of 60 minutes provided 24 data points and curves. Results were generated using the Python PVlib library. Data source: KNMI, in collaboration with the BSRN [105, 106]

(i.e., temporary cloud coverage) to be recorded. Shown in figures 3.13 and 3.14 are the resulting datasets and P-V curves of the same Cabauw weather station, but now at a sampling rate of 5 minutes.

The incident irradiance is more volatile, and the P-V curves denote an MPP range between 24-31 V. The KNMI dataset (provided through the Baseline Surface Radiation Network) has a maximum resolution of 1 minute, which further increases observed signal volatility [105, 106]. For simulation purposes, a 1-minute interval is chosen.

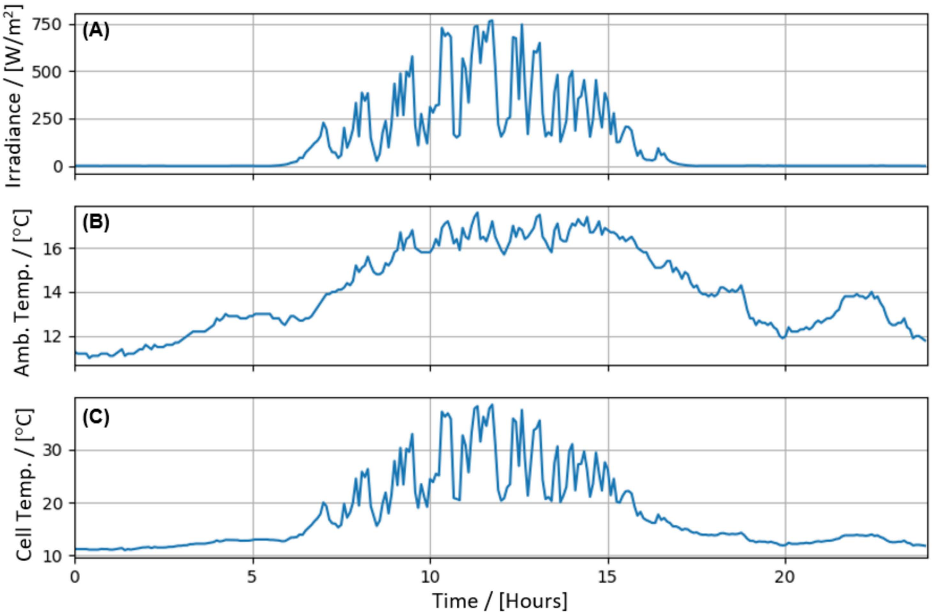

Figure 3.13: Irradiance (Plot A), ambient air temperature (Plot B) and PV panel cell temperature (Plot C) at the Cabauw weather station in The Netherlands on 01-10-2022 at a sampling interval of 5 minutes. Compared to the 60-minute interval data, there is more variation, resulting in increased control difficulty. Data was obtained from the Royal Netherlands Meteorological Institute (KNMI). Results were generated using the Python PVlib library. Data source: KNMI, in collaboration with the BSRN [105, 106]

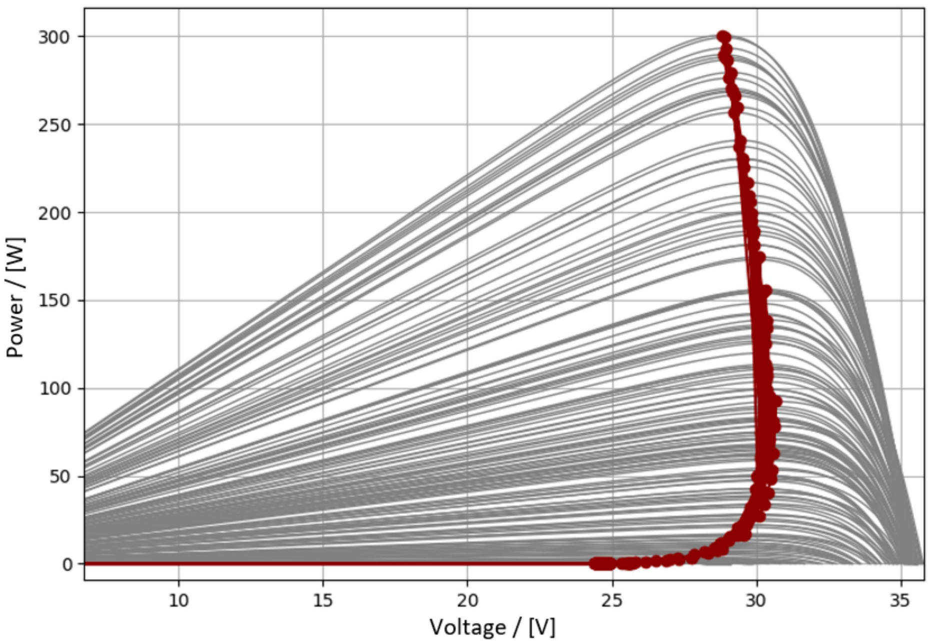

Figure 3.14: P-V curves of KNMI Cabauw weather station data on 01-10-2022. Sampling time of 5 minutes provided 288 data points and curves. Whilst the red MPP tracker reveals a relatively narrow range of results, the repeated variation between low and high irradiance still causes difficulty during control. Results were generated using the Python PVlib library. Data source: KNMI, in collaboration with the BSRN [105, 106]

3.2. System Design

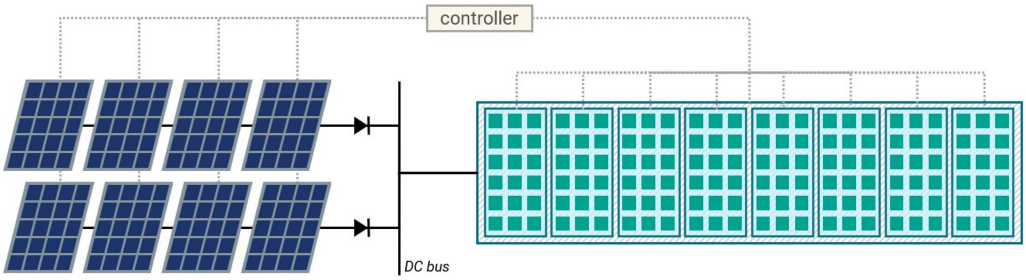

Figure 3.15: Schematic diagram of an HRES consisting of a PV solar array and a modular alkaline electrolyzer. The PV solar array is directly coupled to the electrolyzer, separated only by a selection of diodes to prevent a backward flow of current. A controller is implemented to gauge the ideal voltage for the PV panels and subsequently turns on/off enough stacks to generate a resistance which results in the desired bus bar voltage.

Contrary to HRES found in literature, which featured a DC-DC converter between the PV array and the load resistance, a directly coupled system requires more design considerations to ensure proper working. Shown in Figure 3.15 is a diagram of the proposed HRES, featuring a direct coupling between the PV array and the modular alkaline electrolyzer. Diodes are required in between to ensure there is no backward flow of current and to ensure current does not flow from one series PV array to another.

The DC-bus bar marks the center of the HRES, and the metal bar can only have one potential across its volume. Therefore, the proposed HRES will seek to have every element draw or supply the same potential. Compared to existing HRES, this would not be the case as the PV array would be able to assume any potential that the DC-DC converter was capable of converting.

As discussed in Chapter 2, the timescale of the transient interaction between a PV panel and an electrolyzer is on the order of microseconds. The system is expected to reach a steady state within seconds after establishing an electrical connection. The point of operation reached in a steady state can be defined as any of the finite points of operation between the PV array and the electrolyzer. For any number of stacks ranging from 1 to the maximum number of stacks in the system (120 for this application), there will be an equivalent load resistance which is experienced by the PV array. In practice, as the electrochemical reaction within the electrolyzer matures, the true electrical resistance may vary depending on gas bubble formation on the electrodes and the changing temperature of the electrolyte.

It can be stated that there is a single point of operation for a given PV array and number of active stacks in the system, for a given irradiance and ambient air temperature. If this point of operation is found for every possible irradiance curve and cross-referenced with every single configuration of active stacks, a graph can be made which displays all of the possible points of operation in the HRES. Figure 3.16 shows the P-V curve of an HRES consisting of a PV array and a modular alkaline electrolyzer.

From the figure, the intersects between the irradiance curves and the electrolyzer curves are denoted by crosses. On the lower side of the voltage range, the stacks in the electrolyzer are voltage limited. Similarly, operating points at higher voltages than 405 V are also not preferred as these would lead to exceeding the 27 A soft limit for current imposed in this work. Theoretically, there are 120 unique operating points for a given irradiance. However, due to voltage and current limitations, the true number of operating points is lower, decreasing with increasing irradiance.

The unique shape of the electrolyzer curves also provides a varying spacing between any two operating points. For lower irradiances, spacing between operating points (especially for a low number of active stacks) is larger than at higher irradiances or for a larger number of stacks. When evaluating the MPP of the system for a given irradiance, the nearest operating point to the true MPP serves as the operational point of maximum power delivery. It can be seen in the figure (see the red dot for the 700 and 800 $\mathrm{W\,m^{-2}}$ irradiance curves) that the true MPP may not always lie within the operating range of the HRES. In such a scenario, the operating point closest to the MPP can be chosen, although this may vary.

Whilst the MPP is the main control objective for ordinary PV solar parks, HRES with electrolyzers aim to maximize hydrogen production, not electrical power. This distinct difference with respect to

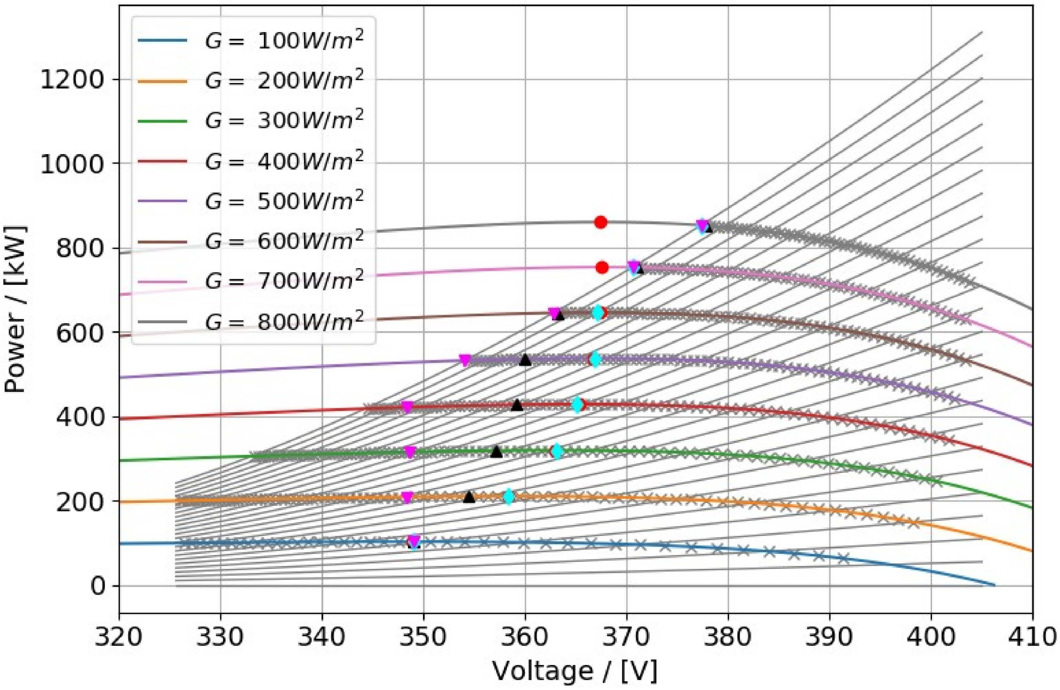

Figure 3.16: P-V curve of an HRES consisting of a 1.07 MW **PV solar array and a 1.25** MW **modular alkaline electrolyzer.** PV array configuration is 12 panels in series and 220 panels in parallel. The electrolyzer curves are only shown for every 5 stacks, with the grey curve at the top of the figure indicating 120 stacks. Grey crosses mark the operating points of the system. Red dots indicate PV array MPPs, cyan diamonds indicate the MPP operating points of the HRES, and magenta triangles indicate the operating points which have the lower specific cost of hydrogen production. The magenta dotted line indicated the voltage at which the lower specific cost of hydrogen production is achieved ($\psi_{\text{min}} = 47.5$ kW h kg^{-1}). The black triangles denote the operation points which produce the highest hydrogen mass flow rate. Curves were created using the Python PVlib library.

previous work requires a new design methodology. Indicated by the cyan line, the point of lowest specific cost of operation is independent of the irradiance and, for this system, provides hydrogen at a cost of 47.5 kW h kg^{-1}, as is confirmed by earlier Figure 3.7. Combining the specific cost of hydrogen production and the power delivered by the PV array, Figure 3.17 shows the points of operation with respect to power. It can be seen that the mass flow rate of hydrogen is positively correlated with the power delivered to the electrolyzer, but the desired point of operation does deviate with respect to the MPP.

The difference between solar park configurations can also be seen when evaluating the current and hydrogen production rate relationships with respect to voltage. Shown in Figure 3.18 is the hydrogen production rate for varying voltages, for a configuration of 13 panels in series and 220 in parallel. Additional figures illustrating these differences are provided in Appendix B (Figures B.5, B.4, B.6, B.7, B.8, and B.7).

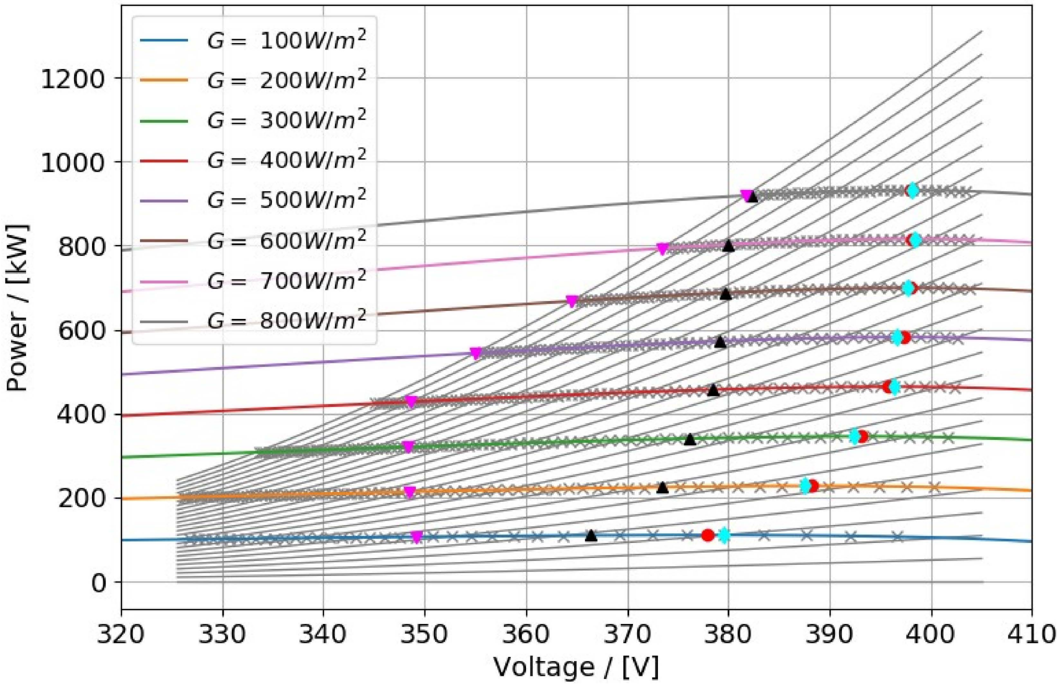

Figure 3.17: P-V curve of an HRES consisting of a 1.16 MW PV solar array and a 1.25 MW modular alkaline electrolyzer. PV array configuration is 13 panels in series and 220 panels in parallel. The electrolyzer curves are only shown for every 5 stacks, with the grey curve at the top of the figure indicating 120 stacks. Grey crosses mark the operating points of the system. Red dots indicate PV array MPPs, cyan diamonds indicate the MPP operating points of the HRES, and magenta triangles indicate the operating points which have the lower specific cost of hydrogen production. The magenta dotted line indicated the voltage at which the lower specific cost of hydrogen production is achieved (ψ_{min} =47.5 kW h kg^{-1}). The black triangles denote the operation points which produce the highest hydrogen mass flow rate. Curves were created using the Python PVlib library.

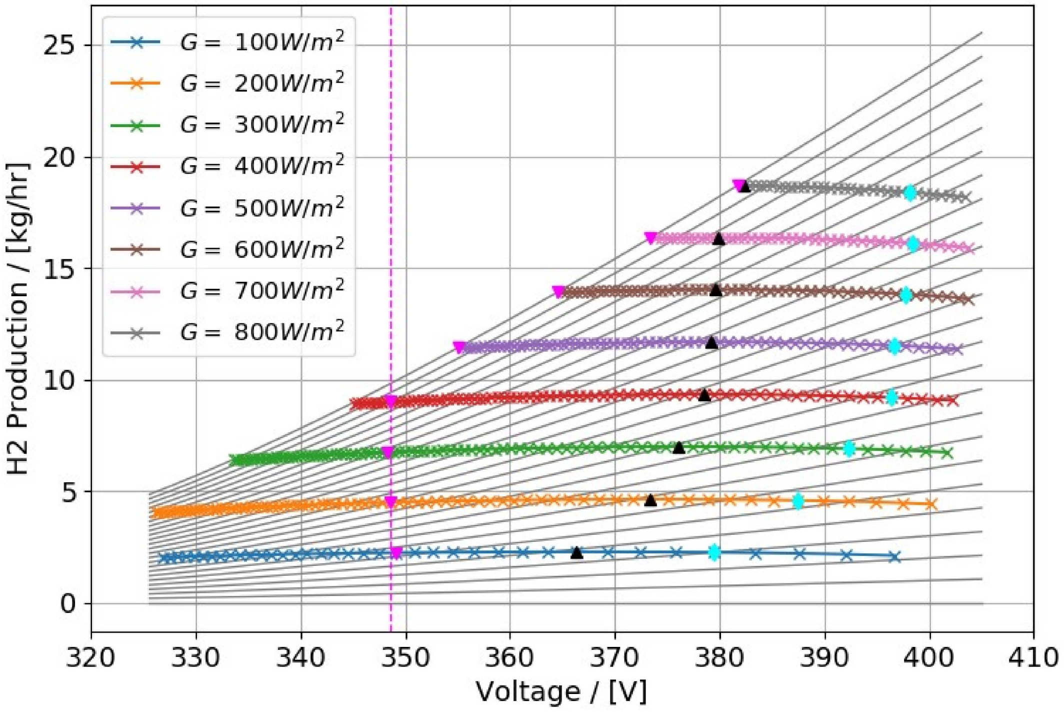

Figure 3.18: Hydrogen production rate vs. voltage curve of an HRES consisting of a 1.16 MW PV solar array and a 1.25 MW modular alkaline electrolyzer. PV array configuration is 13 panels in series and 220 panels in parallel. The electrolyzer curves are only shown for every 5 stacks, with the grey curve at the top of the figure indicating 120 stacks. Colored crosses mark the operating points of the system. The cyan diamonds indicate the MPP operating points of the HRES, and magenta triangles indicate the operating points which have the lower specific cost of hydrogen production. The magenta dotted line indicates the voltage at which the lower specific cost of hydrogen production is achieved (ψ_{min} =47.5 kW h kg^{-1}). The black triangles denote the operation points which produce the highest hydrogen mass flow rate. Curves were created using the Python PVlib library.

3.3. System Control

This section presents the control algorithm used to connect a PV solar array to a modular alkaline electrolyzer. The primary objective of this control algorithm is to maximize the hydrogen produced for the given weather conditions. This differs from the MPP, as the operating point where maximum power is achieved does not coincide with the overpotential and current density suitable for maximum hydrogen production. The control algorithm must also ensure that renewable energy resources are efficiently utilized to generate hydrogen at both extremely high production values and extremely low production values. The design and implementation of the control algorithm are discussed in detail in this chapter. The performance of the control algorithm is evaluated by conducting simulations under different operating conditions to validate its effectiveness in ensuring the stable operation of the system.

3.3.1. Calibration Data

Calibration data is critical for testing the validity of a control algorithm. It provides an opportunity to back-test the performance of the algorithm in various operating conditions and identify areas of improvement. A data set of irradiance data is constructed to test the algorithms' tracking capabilities. Shown in Figure 3.19 is an overview of the irradiance and cell temperature dataset used to evaluate the control algorithm for a system of a PV solar array and an alkaline water electrolyzer.

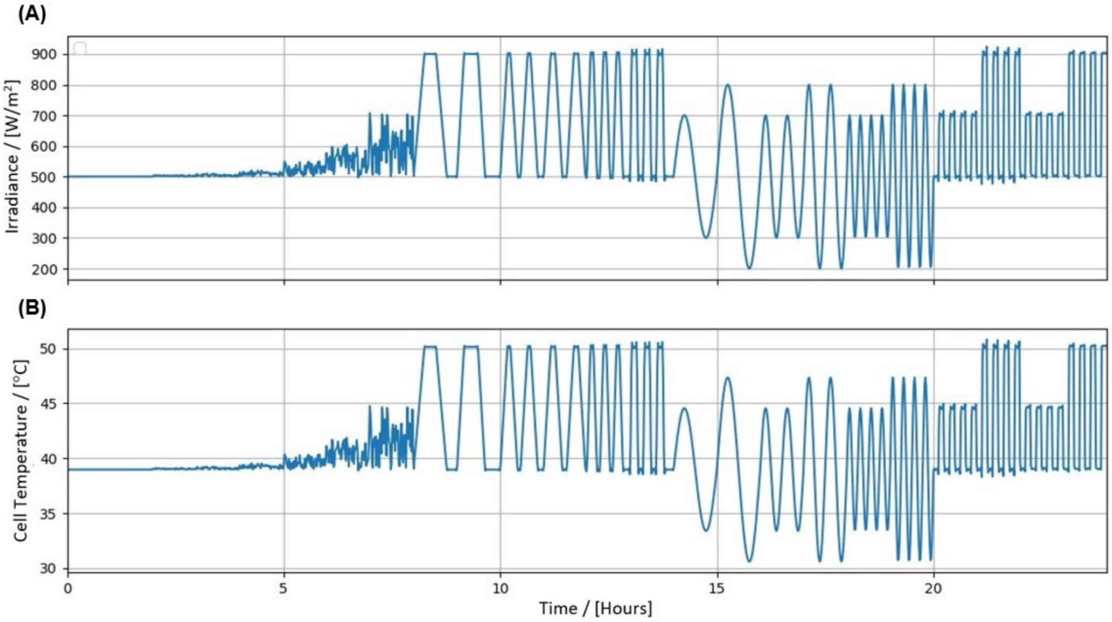

Figure 3.19: Calibration dataset of irradiance (Plot A) and cell temperature (Plot B) for the PV Solar & Alkaline Water Electrolyzer system. Dataset tests the ability of the algorithm to handle random noise of increasing amplitude, as well as periodic signals of trapezoidal, sinusoidal, and block format. Random noise is added to several of the dataset curves to model random error and noise on the sensors. Cell temperature result is proportional to the irradiance plot as the ambient temperature is maintained constant at 25 °C. Therefore, the only factor changing the cell temperature is the incident irradiance.

Cell temperature has the same shape as the irradiance curve because the ambient air temperature is kept constant at 25 °C for the entire dataset. As per the energy balance over the PV panel exhibited earlier in this paper, this results in a direct correlation between incident irradiance and cell temperature.

The simulation of random noise is essential in tuning the control algorithm to handle minute variations in operating conditions. The solid-state semiconductor nature of a PV solar panel means that any small change in irradiance is guaranteed to lead to a change in operating conditions, regardless of how small the change is. Furthermore, the large size of the PV solar park increases the likelihood of random noise due to cabling or other small disturbances to the system. Therefore, random noise of increasing amplitude is modelled to test the ability of the algorithm to track a random signal.

The irradiance signal is further divided into periodic signals which aim to test the response to

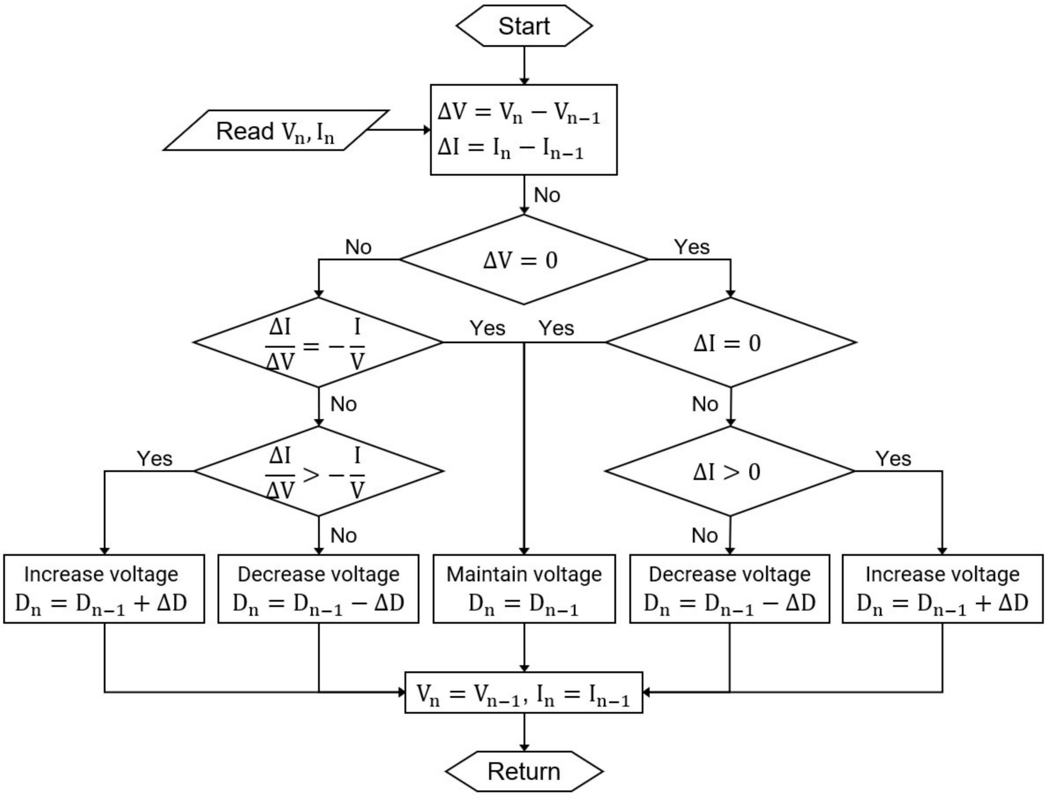

Figure 3.20: Standard Incremental Conductance MPPT Flowchart. This algorithm uses the voltage and current of the system as inputs, and the duty cycle ($0 < D \leq 100\%$) of the DC-DC converter as an output. Increasing the duty cycle results in a proportional increase in operating voltage, and vice versa. If the differences in voltage and current are sufficiently small, the algorithm decides not to make any choice, as the current operating point is sufficient [57].

rapidly increasing/decreasing irradiance. The slope by which the irradiance changes is varied, going from sinusoidal to linear (trapezoidal) to instantaneous (block). The signals are modified in period and amplitude to increase the variability of the signal and rigorously test the algorithm.

3.3.2. The Incremental Conductance Algorithm

The control algorithm for a system of PV solar panels and a modular alkaline electrolyzer starts from an existing control algorithm for PV solar panel maximum power point tracking [57]. As mentioned in Section 2.1.4, conventional solar parks vary the duty cycle of DC-DC converters to change the voltage of the PV solar system and stay at the maximum power point. Perturb & Observe MPPTs are a subset of algorithms which are widely researched, low in mathematical complexity and widely used in PV solar tracking (see Section 2.1.4). Shown in Figure 3.20 is the algorithm flowchart for a standard Incremental Conductance MPPT.

In order for the above-mentioned algorithm to work for a renewable energy system featuring a modular alkaline electrolyzer, several changes need to be made. First, the duty cycle must be replaced by the number of active stacks in the electrolyzer. This mandates a change from a continuous output signal (i.e., the duty cycle of a DC-DC converter) to a discrete output signal (i.e., an integer number of electrolyzer stacks). Following that is the modification of the INC algorithm method to allow the algorithm to approach other points aside from the MPP. Next, variable step sizing is introduced. Lastly, a dynamically programmable tracking bias is introduced in addition to a method of optimizing stack selection to minimize long-term degradation.

3.3.3. Changing Duty Cycle for Stack Number

The duty cycle in a DC-DC converter results in a Pulse-Width Modulation (PWM) signal, where the key parameter (D) indicates the percentage of time that the signal is in the ”on” state. Depending on whether the DC-DC converter aims to step up or step down the voltage, increasing the duty cycle can increase or decrease the voltage, respectively. As per Figure 3.20, it is indicated that increasing the duty cycle by ΔD will lead to an increase in voltage, and vice versa.

For the HRES discussed in this research, there is no duty cycle or PWM signal that can be altered between 0-100%. Instead, the number of stacks connected to the PV solar park (S) can be changed between 1 stack and the maximum stack number (assumed to be 120). In order to translate the duty cycle changes (ΔD) into changes in the number of stacks (ΔS), the behaviour of a system of electrolyzer stacks must be considered. Under the same load, an increase in the number of stacks connected to the system (in parallel) will lead to a decrease in the voltage per stack. This is directly opposite to the aforementioned behaviour of voltage for a change in the duty cycle. As a result, to increase the operating voltage of the PV solar array, the number of stacks should be decreased to $S_n = S_{n-1} - \Delta S$. Similarly, a desired decrease in PV solar array operating voltage can be achieved by increasing the number of stacks to $S_n = S_{n-1} + \Delta S$.

3.3.4. Adding Variable Tracking Point

See the original derivation of the INC method in 2.1.4. Instead of setting the gradient of power with respect to voltage to zero, it is set equivalent to a constant m.

$$\frac{\mathrm{d}P}{\mathrm{d}V} = m \tag{3.14}$$

Substituting power with the product of current and voltage, and using the chain rule:

$$\begin{aligned}
\frac{\mathrm{d}P}{\mathrm{d}V} &= \frac{\mathrm{d}(V \cdot I)}{\mathrm{d}V} && \text{(3.15a)}\\
&= I \cdot \frac{\mathrm{d}V}{\mathrm{d}V} + V \cdot \frac{\mathrm{d}I}{\mathrm{d}V} && \text{(3.15b)}\\
&= I + V \cdot \frac{\mathrm{d}I}{\mathrm{d}V} && \text{(3.15c)}\\
&= m && \text{(3.15d)}
\end{aligned}$$

For the INC method (and any variations thereof) to be applicable in a real-life setting, it must be discretised. This is done using n as the current time step and $n-1$ as the previous time step:

$$\begin{aligned}
\Delta I &= I_n - I_{n-1} && \text{(3.16a)}\\
\Delta V &= V_n - V_{n-1} && \text{(3.16b)}
\end{aligned}$$

Substituting the discretizations into Equation 3.15:

$$\begin{aligned}
I + V \cdot \frac{\Delta I}{\Delta V} &= m && \text{(3.17a)}\\
\frac{\Delta I}{\Delta V} &= \frac{m - I}{V} && \text{(3.17b)}
\end{aligned}$$

If $m = 0$, the algorithm defaults back to the original version of the Incremental Conductance algorithm, as it aims to find the point where the slope is zero (i.e., the MPP). However, if $m > 0$, then the algorithm attempts to find a slope greater than zero. Assuming no partial shading conditions, the P-V curve of the PV array only has a positive slope to the left of the MPP. Similarly, when $m < 0$, the algorithm goal is to find a slope less than zero, occurring only to the right of the MPP.

3.3.5. Variable Step Sizing

As mentioned in Section 2.1.4 (see Figure 2.6), varying the step size depending on the deviation from the MPP results in a superior tracking ability, especially for rapidly changing irradiance [58]. Shown below are two variable step size relationships which have been proven effective in conventional solar MPPTs:

$$\text{step}_1 = \left|\frac{\mathrm{d}P}{\mathrm{d}V}\right| \tag{3.18}$$

$$\text{step}_2 = \left|\frac{\mathrm{d}P}{\mathrm{d}V - \mathrm{d}I}\right| \tag{3.19}$$

In order to apply these variable step size relationships, a non-dimensionalization process must be performed first. In order to do so, a reference state (V_{ref}, I_{ref}) is defined which is applicable for all of the PV solar array operating conditions. To ensure that the reference state is known for all PV solar panels and all HRES configurations, the reference state was chosen to be the MPP as defined on the PV panel datasheet. This MPP is established under standard testing conditions (1000 $\mathrm{W\,m^{-2}}$ and 25 °C), and operational MPPs will be of the same order of magnitude. Non-dimensionalizing the variable step-size relationships using the reference state:

$$P_{\text{ref}} = V_{\text{ref}} \cdot I_{\text{ref}} \tag{3.20}$$

$$\text{step}_1 = \left|\frac{\mathrm{d}P/P_{\text{ref}}}{\mathrm{d}V/V_{\text{ref}}}\right| \tag{3.21}$$

$$\text{step}_2 = \left|\frac{\mathrm{d}P/P_{\text{ref}}}{\mathrm{d}V/V_{\text{ref}} - \mathrm{d}I/I_{\text{ref}}}\right| \tag{3.22}$$

The point of maximum hydrogen production does not coincide with the point of maximum power. Similarly, the point where the production of hydrogen costs the least amount of energy also does not coincide with the MPP. Therefore, as derived in the previous section, it may be advantageous to vary the target slope of the P-V curve for the HRES. In order to do so, the variable step size needs to be adjusted to include a varying value of the target slope (m). Intuitively, the new variable step size relationship must be such that at a value of $m = 0$, the step size reverts back to equations 3.21 and 3.22. To realize this, the variable step size can be amended with an extra term which would be equal to zero at $m = 0$. Let $\text{step}_{\text{1,m}}$ and $\text{step}_{\text{2,m}}$ be the additional terms which are added to the existing non-dimensional variable step size relationships such that:

$$\text{step}_1' = \text{step}_1 + \text{step}_{\text{1,m}} \tag{3.23}$$

$$\text{step}_2' = \text{step}_2 + \text{step}_{\text{2,m}} \tag{3.24}$$

Starting with method 1, let the additional term be defined as:

$$\text{step}_{\text{1,m}} = -\frac{m}{I_{\text{ref}}} \tag{3.25}$$

$$\text{step}_1' = \left|\frac{\mathrm{d}P/P_{\text{ref}}}{\mathrm{d}V/V_{\text{ref}}}\right| - \frac{m}{I_{\text{ref}}} \tag{3.26}$$

Here, m is non-dimensionalized using the reference current, I_{ref}. The unit of m is ampere, as it is the slope of a power-voltage curve:

$$m = \frac{\mathrm{d}P}{\mathrm{d}V} \tag{3.27}$$

Adding a variable correction factor (F_1) to proportionally scale the step size gives the final form of the adjusted step size using method 1:

$$\text{step}_1' = F_1 \cdot \left(\left|\frac{\mathrm{d}P/P_{\text{ref}}}{\mathrm{d}V/V_{\text{ref}}}\right| - \frac{m}{I_{\text{ref}}}\right) \tag{3.28}$$

To plot the above-derived variable step size, it is helpful first to consider the different values that m can realistically assume. Shown in Figure 3.21 is the P-V curve for a single PV solar panel for an irradiance of 750 $\mathrm{W\,m^{-2}}$ and a cell temperature of 25 °C:

Due to the asymmetrical shape of the P-V curve and through calibration, the correction factors were not kept constant for all values of m:

$$F_1 = \begin{cases} 25 & \forall\, m \geq 0 \\ 5 & \forall\, m < 0 \end{cases} \tag{3.29}$$

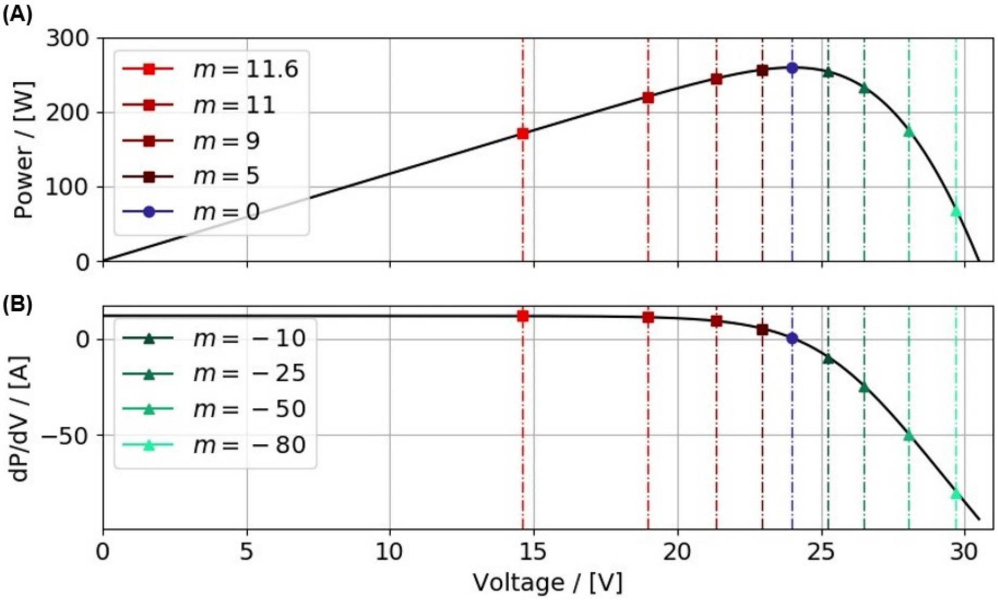

Figure 3.21: Various values of the slope (m) for a P-V curve of a single PV solar panel at an irradiance of 750 $\mathrm{W\,m^{-2}}$ **and a cell temperature of 25** $^{\circ}$**C.** Plot A shows a P-V curve and Plot B shows the derivative of that same P-V curve. Positive values of m only reach until $m \approx 11.72$, whereas negative values of m reach as far as $m \approx -93.40$. Curve generated using the Python PVlib library.

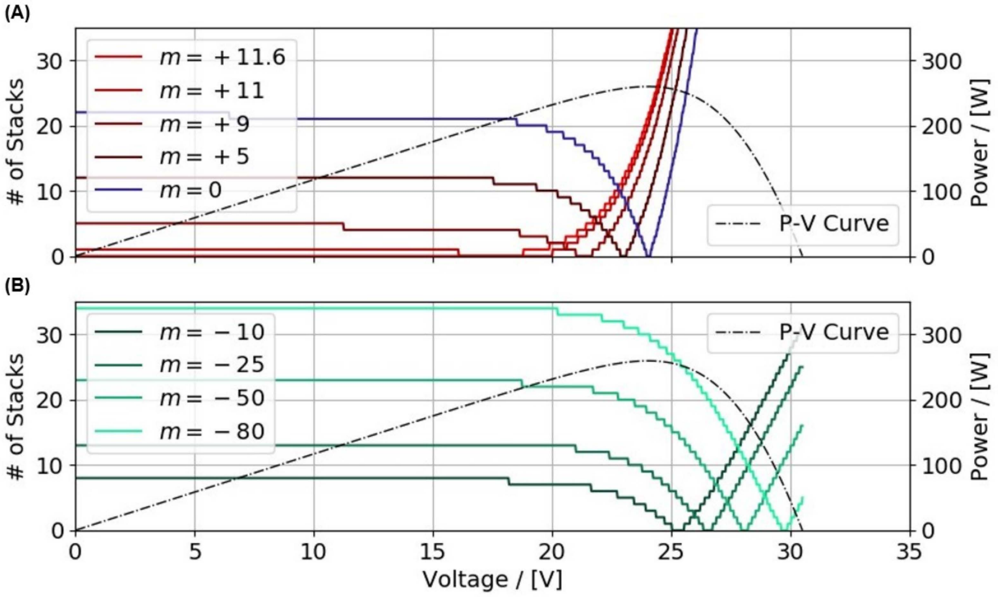

Figure 3.22: Variable step size for varying values of m, using the adjusted step size method 1. Plot A shows results for values of $m \geq 0$, and Plot B shows results for values of $m < 0$. Variable step size curves discretized to signify individual stacks based on a maximum stack number of 120. The variable step size curve for varying values of m intersects the voltage axis precisely at the voltage at which the slope of the P-V curve is equal to m. P-V curve is illustrative and generated using the Python PVlib library.

Using these correction factors, shown in Figure 3.22 is the result of the variable step size for varying values of m, using the relationship defined in Equation 3.28.

The step size function performs well for values of $m < 0$, as there is a large step far away from the target point which decreases exponentially as the target draws closer. For $m \geq 0$, however, there is little increase in step size for deviations to the left of the target point.

For method 2, the derivation starts with the less strict (non-absolute) dimensional form of the conventional step size, as per Equation 3.19:

$$\text{step}_{2,\text{m}} = \frac{\mathrm{d}P}{\mathrm{d}V - \mathrm{d}I} \tag{3.30a}$$

$$\text{step}_{2,\text{m}} \cdot (\mathrm{d}V - \mathrm{d}I) = \mathrm{d}P \tag{3.30b}$$

$$\text{step}_{2,\text{m}} \cdot \left(1 - \frac{\mathrm{d}I}{\mathrm{d}V}\right) = \frac{\mathrm{d}P}{\mathrm{d}V} \tag{3.30c}$$

$$\text{step}_{2,\text{m}} \cdot \left(1 - \frac{\mathrm{d}I}{\mathrm{d}V}\right) = m \tag{3.30d}$$

Defining a relation for $\frac{\mathrm{d}I}{\mathrm{d}V}$:

$$\frac{\mathrm{d}I}{\mathrm{d}V} = \frac{\mathrm{d}\,(P/V)}{\mathrm{d}V} \tag{3.31a}$$

$$= \frac{\mathrm{d}P}{\mathrm{d}V} \cdot \frac{1}{V} + P \cdot \frac{\mathrm{d}}{\mathrm{d}V}\left(\frac{1}{V}\right) \tag{3.31b}$$

$$= \frac{\mathrm{d}P}{\mathrm{d}V} \cdot \frac{1}{V} - \frac{P}{V^2} \tag{3.31c}$$

$$\therefore \frac{\mathrm{d}I}{\mathrm{d}V} = \frac{\mathrm{d}P}{\mathrm{d}V} \cdot \frac{1}{V} - \frac{1}{V} \tag{3.31d}$$

Rearranging and substituting into Equation 3.30:

$$\text{step}_{2,\text{m}} = \frac{m}{1 + \dfrac{(I - m)}{V}} \tag{3.32}$$

Here, V and I are the instantaneously measured voltage and current for each algorithm iteration. Inserting this result into the new variable step size and non-dimensionalizing each term gives:

$$\text{step}'_2 = \text{step}_2 + \text{step}_{2,\text{m}} \tag{3.33a}$$

$$= \left|\frac{\mathrm{d}P}{\mathrm{d}V - \mathrm{d}I}\right| + \frac{m}{1 + \dfrac{(I - m)}{V}} \tag{3.33b}$$

$$= \left|\frac{\mathrm{d}P/P_{\text{ref}}}{\mathrm{d}V/V_{\text{ref}} - \mathrm{d}I/I_{\text{ref}}}\right| + \frac{m/I_{\text{ref}}}{1 + \dfrac{(I - m)/I_{\text{ref}}}{V/V_{\text{ref}}}} \tag{3.33c}$$

$$= \left|\frac{\mathrm{d}P/P_{\text{ref}}}{\mathrm{d}V/V_{\text{ref}} - \mathrm{d}I/I_{\text{ref}}}\right| + \frac{m}{I_{\text{ref}} + V_{\text{ref}} \cdot \left(\dfrac{I - m}{V}\right)} \tag{3.33d}$$

Analogous to method 1, a correction factor (F_2) is introduced to proportionally scale the variable step size:

$$\text{step}'_2 = F_2 \cdot \left(\left|\frac{\mathrm{d}P/P_{\text{ref}}}{\mathrm{d}V/V_{\text{ref}} - \mathrm{d}I/I_{\text{ref}}}\right| + \frac{m}{I_{\text{ref}} + V_{\text{ref}} \cdot \left(\dfrac{I - m}{V}\right)}\right) \tag{3.34}$$

$$F_2 = \begin{cases} 35 & \forall\, m \geq 0 \\ 25 & \forall\, m < 0 \end{cases} \tag{3.35}$$

The resulting graph of step sizes for varying values of m is shown in Figure 3.23.

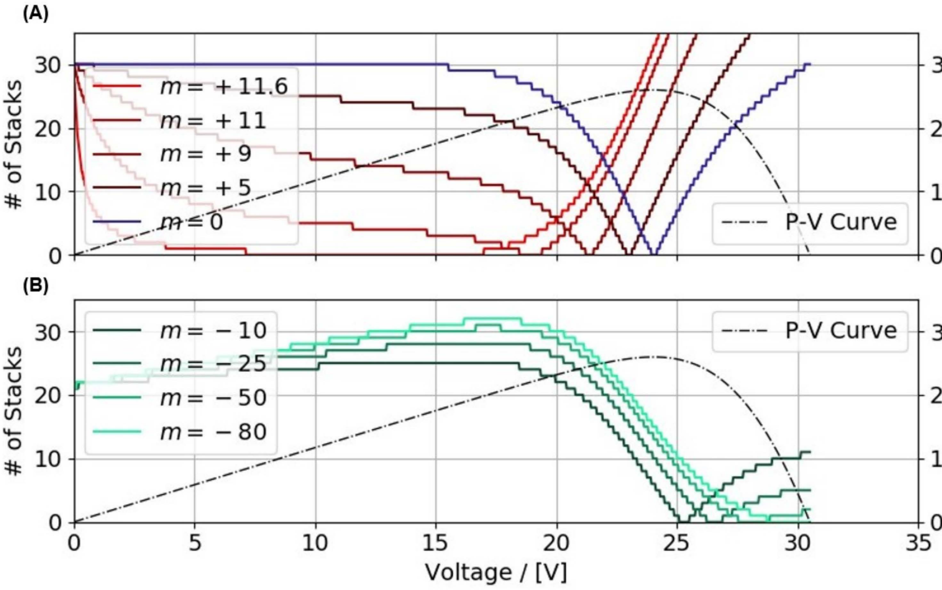

Figure 3.23: Variable step size for varying values of m, using the adjusted step size method 2. Plot A shows results for values of $m \geq 0$, and Plot B shows results for values of $m < 0$. Variable step size curves are discretized to signify individual stacks based on a maximum stack number of 120. The variable step size curve for varying values of m intersects the voltage axis precisely at the voltage at which the slope of the P-V curve is equal to m. P-V curve is illustrative and generated using the Python PVlib library.

In contrast to method 1, the step sizes for method 2 are worse in shape and performance for $m < 0$, and better for $m \geq 0$. For values of $m > 11$, the relative change in slope is too minute to produce any variable step size relationship which can evenly ramp up the step size on both sides of the target point. However, in practice, it is not expected that the target point will be set so far away from the MPP. The design of the HRES can be made such that optimal operation is far away from values of $m > 10$.

Given the two methods of variable step sizing, a final adjusted step size relationship can be made by combining the two methods. Method 1 can be used for values of $m < 0$ and method 2 for values of $m \geq 0$. This gives the following final equation:

$$\text{step}' = \begin{cases} 35 \cdot \left(\left| \dfrac{\mathrm{d}P/P_{\text{ref}}}{\mathrm{d}V/V_{\text{ref}} - \mathrm{d}I/I_{\text{ref}}} \right| + \dfrac{m}{I_{\text{ref}} + V_{\text{ref}} \cdot \left(\dfrac{I - m}{V} \right)} \right) & \forall\, m \geq 0 \\ 5 \cdot \left(\left| \dfrac{\mathrm{d}P/P_{\text{ref}}}{\mathrm{d}V/V_{\text{ref}}} \right| - \dfrac{m}{I_{\text{ref}}} \right) & \forall\, m < 0 \end{cases} \tag{3.36}$$

3.3.6. Adding Variable Tracking Bias

Each element of the HRES has its own characteristic curve. The operating points of the system are defined as the intersects between these curves. However, the nature of their interaction can cause asymmetrical behavior if the characteristic curves themselves are not symmetrical. In such events, adding a bias may improve the ability to track the target point.

To provide a better understanding, figures 3.24 and 3.25 display two control scenarios.

In the first scenario, the operating point is to the left of the MPP, and the algorithm should decide that, in order to close the distance to the MPP, stacks should be reduced. However, in the next iteration, the irradiance has doubled to 800 W m^{-2}. Such an event could occur as a result of intermittent cloud coverage. Due to the large change in irradiance, the new P-V curve is not located close to the old curve. As a result, the newly selected lower stack number is now far to the right of MPP. This overshoot error is a consequence of how the curves interact with one another.

In the event of increasing irradiance and an operating point to the right of the MPP, it is more

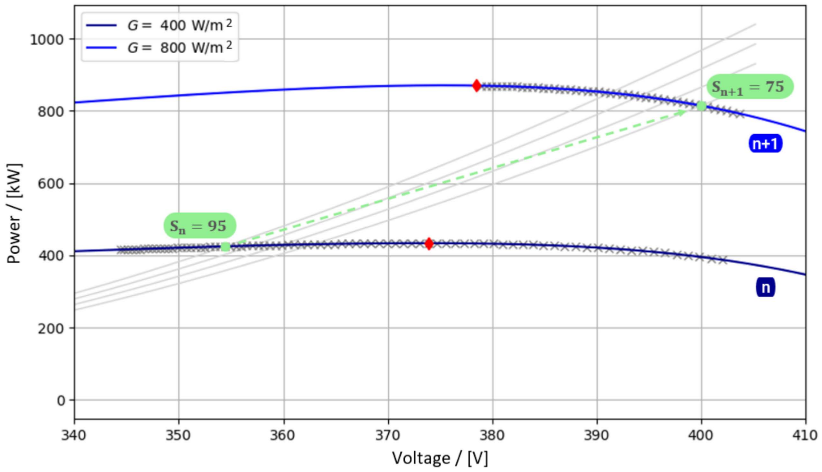

Figure 3.24: MPP tracking overshoot error when prompting a decrease in stacks. The required decrease in stacks, coupled with a rapidly increasing irradiance, cause a large overshoot in the next iteration. P-V curves were generated using the Python PVlib library.

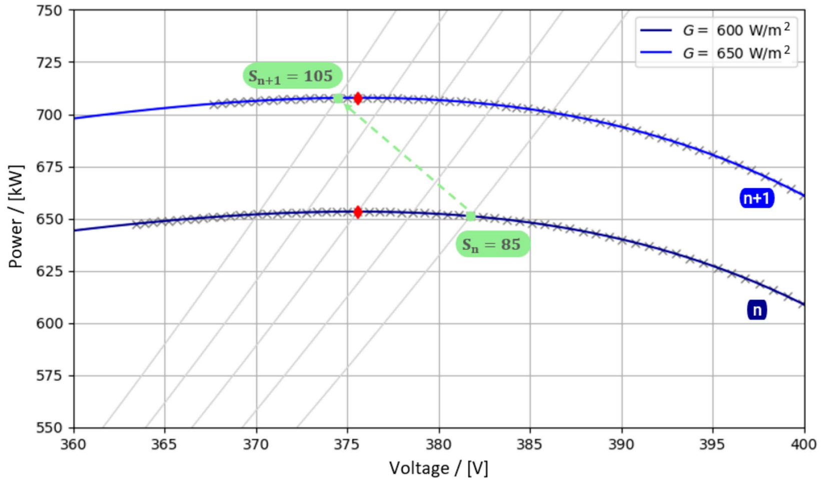

Figure 3.25: MPP tracking overshoot error when prompting an increase in stacks The prompted decrease in stacks needs to be significantly greater than necessary in order to lead to overshoot. P-V curves were generated using the Python PVlib library.

difficult to overshoot. As shown in Figure 3.25, only a ten-stack increase is required to approach the MPP. However, it would take 20 stacks of increase to lead to the same overshoot as in Figure 3.24. It should be noted that the irradiance increase here is only 50 $\mathrm{W\,m^{-2}}$, compared to the 400 $\mathrm{W\,m^{-2}}$ in the first example.

The same concept holds for decreases in irradiance. Overshoot is much larger for decreases in irradiance when the operating point is to the right of the MPP (see Figure 3.24 with n and $n+1$ swapped). Similarly, overshoot is difficult to achieve for decreasing irradiances when the operating point is to the left of the MPP.

Therefore, adding a bias (to amplify or dampen) the outputs can be beneficial to the reduction of overshoot and should lead to the improved ability to control such an HRES.

3.3.7. Stack Selection Algorithm

Besides determining the required number of active stacks in each iteration for the PV solar array, the specific selection of stacks to turn on/off holds significant importance. Thoughtful stack selection can lead to reduced maintenance costs, enhanced system responsiveness to power input fluctuations, and improve overall energy efficiency.

As defined earlier, the S^n is defined as the number of stacks turned on in each iteration. For each stack, let s^n_i be the status of stack i. When the stack is turned on, the status registers $s^n_\text{i} = 1$. If turned off, the stack status registers a zero.

$$s^n_\text{i} = \begin{cases} 1 & \text{if stack } i \text{ is turned on} \\ 0 & \text{if stack } i \text{ is turned off} \end{cases} \tag{3.37}$$

Relating the individual stack status to the total number of active stacks:

$$S^n = \sum_{i=1}^{n_\text{active stacks}} s^n_\text{i} \tag{3.38}$$

In order to keep track of electrolyzer stack lifetime and degradation, another parameter is necessary to track single stack lifetime ($t^n_{\text{life},i}$). This can be defined as the single stack lifetime in the previous iteration plus the stack status in the current iteration:

$$t^n_{\text{life},i} = t^{n-1}_{\text{life},i} + s^{n-1}_i \tag{3.39}$$

This reduces the computational intensity, as there is no need to log individual stack status for every iteration since the start of the operation. Furthermore, the single-stack lifetime can be recorded at the end of every day to track long-term degradation. Using these definitions for stack status and lifetime, relationships for combining the single-stack voltages and currents are detailed below:

$$V^n_\text{sys} = \frac{1}{S^n} \sum_{i=1}^{n_\text{active stacks}} V^n_\text{i} \tag{3.40}$$

$$I^n_\text{sys} = \sum_{i=1}^{n_\text{stacks}} I^n_\text{i} \tag{3.41}$$

Due to the parallel configuration of stacks in the system, the voltage is equal across each stack, varying only slightly due to noise and varying cable resistance. Therefore, the system voltage is taken as the average voltage measured across all active stacks. For the current, the parallel configuration means that the system currently is the sum of all single-stack currents, including both active and inactive stacks.

In order to select an S^n number of stacks to turn on/off in each iteration, a criteria-based ranking system can be constructed. Each stack is evaluated based on a predefined list of criteria. The S^n stacks with the highest rank are chosen to be turned on/off in each iteration. While other methods, like a pseudo-random or a sequential selection method, may be easier to implement and computationally faster, these methods lack the ability to calibrate the system based on sensor data. Criteria-based stack selection allows for voltage, current, and temperature data to be used as key inputs to the selection of active stacks in the next iteration.

Each criteria relationship is non-dimensional (obtaining a value between 0 and 1), allowing for accurate weighting of criteria and an easier calibration process applicable for all ranges of system operation. The higher the value of a criterion, the more preferable that stack is for an active role in the next iteration. The first criterion non-dimensionalizes stack lifetime. Resetting to zero at the start of every day or operational run, the single-stack lifetime is divided by the largest stack lifetime of the stacks.

$$\text{criteria}^n_{1,i} = 1 - \frac{t^n_{\text{life},i}}{\max\left(t^n_\text{life}\right)} \tag{3.42}$$

The longer the stack lifetime, the closer the criteria will be to zero. Similarly, a stack that has never been turned on will have a value of one.

The second criterion used for stack selection focuses on whether the stack was turned on in the previous iteration. This criterion is mathematically simple, in that a stack whose status is 'on' will have an assigned value of one and one that is 'off' will have a value of zero. This aligns with the underlying principle that a lower criteria score corresponds to a decreased preference for stack selection. Thus, stacks with an 'off' status exhibit a diminished likelihood of being selected, given their lower criteria value.

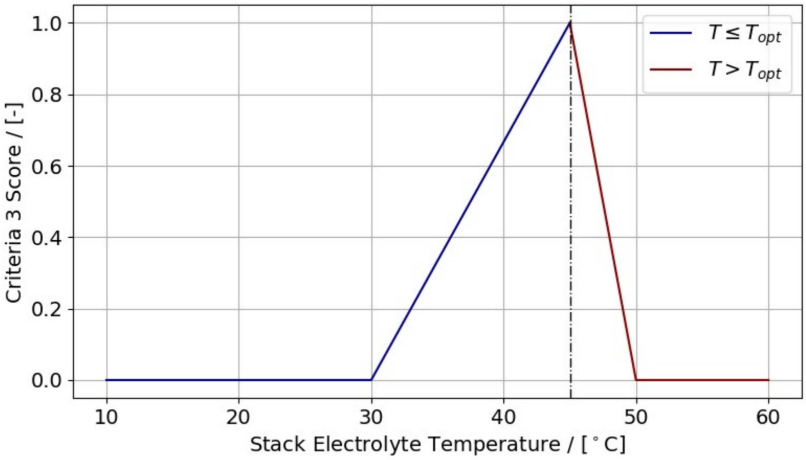

Figure 3.26: Criteria 3 score for varying stack electrolyte temperatures. The closer the stack temperature is to the optimum stack electrolyte temperature ($T_{\text{opt}} = 45$ °C), the higher the criteria score. A different function defines the relationship on either side of the optimum temperature. Temperatures higher than the optimum value are evaluated more stringent than temperatures lower than the optimum. This is done to prevent operation at higher (inefficient) temperatures and prevent degradation of the plastic electrolyzer housing.

$$\text{criteria}_{2,i}^{n} = s_i^n \tag{3.43}$$

The third criterion for stack evaluation focuses on stack temperature. It is worth noting that the temperature of a stack is influenced by its location within the system. Specifically, the gas separator tanks and electrolyte pump cover all stacks within a given section. With a configuration consisting of 8 sections and 15 stacks per section, significant temperature variations can arise between the 15th stack in a fully activated section and the 1st stack in a completely deactivated section. The operational temperature range for the stacks is set between 30-50 °C. Consequently, a notable disparity in electrolyte temperature can exist between the ambient environment and the operating conditions. Thus, stacks that have already experienced elevated electrolyte temperature, resulting from the exothermic reactions occurring in other stacks within the same section, should be prioritized over stacks at ambient temperature.

Moreover, it is crucial to consider the upper limit of operating temperature, as exceeding this threshold could lead to the failure of the plastic polymer compounds that constitute the casing and structural framework of the electrolyzers. To mitigate this risk, any deviation from the optimal temperature (approximately 45 °C, denoted as T_{opt}) should be penalized. Accordingly, a criterion function can be defined as the maximum value between zero and the proportionate difference between the operating temperature and the optimal temperature. This approach ensures that deviations from the desired temperature range are duly accounted for in the evaluation process.

$$\text{criteria}_{3,i}^{n} = \begin{cases} \max\left(0, 2\left(\frac{T_i^n - (T_{\text{opt}} - 15)}{T_{\text{opt}} - 15}\right)\right) & \forall\, T \leq T_{\text{opt}} \\ \max\left(0, 5 - 5\left(\frac{T_i^n - (T_{\text{opt}} - 20)}{T_{\text{opt}} - 20}\right)\right) & \forall\, T > T_{\text{opt}} \end{cases} \tag{3.44}$$

These three criteria have a range between zero and one and can be combined using a weighting array that evaluates the relative importance of the criteria to one another. The sum of these weights should always be equal to one.

$$\sum_{i=1}^{3} \alpha_i = \alpha_1 + \alpha_2 + \alpha_3 \tag{3.45a}$$

$$= 1 \tag{3.45b}$$

The final score per stack is calculated as the product of each criterion result and its corresponding criteria weight. A high criteria score corresponds to a higher preference for activation in the next

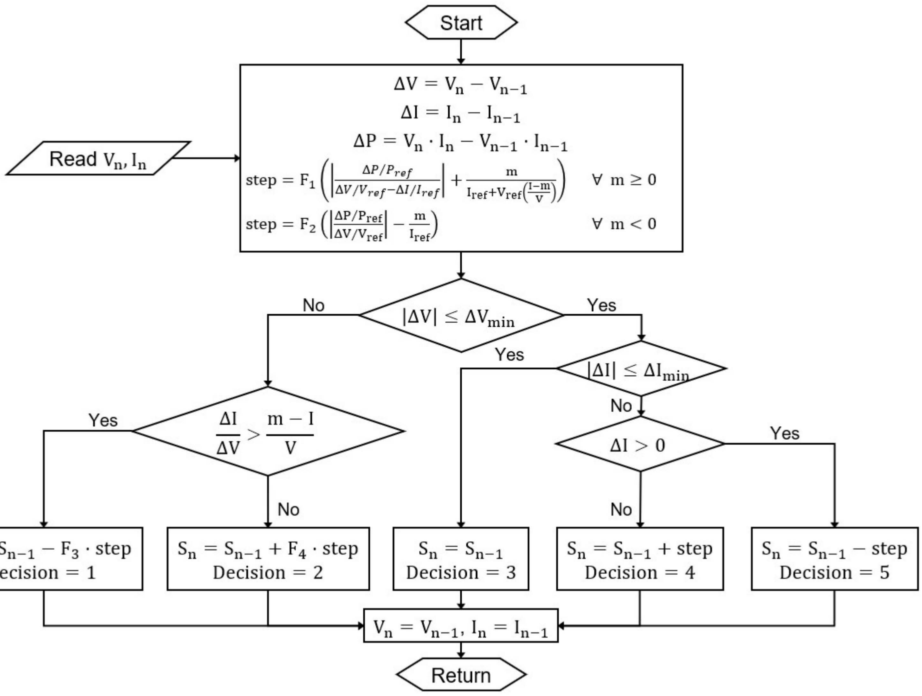

Figure 3.27: Final MHP Algorithm Flowchart. This algorithm uses the voltage, current, and power of the system as inputs. The step size of the algorithm is not constant. The output of the algorithm is the number of electrolyzer stacks which need to be turned on ($0 < S \leq n_{\text{stacks}}$). Variables F_1, F_2, F_3, and F_4 are constants and may be calibrated unique to each system. Each outcome is labelled with a different decision number as this assists in validating the algorithm is working correctly.

iteration. Therefore, the higher the final combined score, the more suitable that stack is for selection in the next iteration.

$$\text{score}_i^n = \alpha_1 \cdot \text{criteria}_{1,i}^n + \alpha_2 \cdot \text{criteria}_{2,i}^n + \alpha_3 \cdot \text{criteria}_{3,i}^n \tag{3.46}$$

3.3.8. Final Modified INC Algorithm

Incorporating all of the aforementioned modifications to the INC algorithm, a new flowchart can be made to represent the newly generated Maximum Hydrogen Production (MHP) algorithm. Shown in Figure 3.27 is a flowchart representing the MHP algorithm.

There are several key differences with respect to the original INC algorithm. Firstly, the acceptable values for ΔV and ΔI have been set to ranges ΔV_{min} and ΔI_{min}, respectively. Due to the high standard of computational resolution achieved by control electronics, there exists a near-zero change of the changes in voltage or current ever being exactly zero. Such events are only seen in simulations, which are void of static noise and current leaks.

The second main difference is the addition of the variable m, the slope of the P-V curve. This variable represents the target slope that the algorithm uses as its goal. If set to zero, the algorithm (and corresponding step sizes) revert back to the original INC algorithm goal.

The next modification covers the removal of the equality:

$$\frac{\Delta I}{\Delta V} = \frac{m - I}{V} \tag{3.47}$$

To practically implement such a logic rule, a range of acceptable values is required. However, it is not possible to define a range of values for a relationship that compares the fraction of two differences with a fraction of absolute variables. The above-stated equation only has an effect when it is exactly equal, which is not practically feasible. As a result, it was removed from the algorithm, and replaced by more lenient definitions of ΔV_{min} and ΔI_{min} to ensure that the algorithm does not change its operating point when sufficiently close to its goal.

The last two additions to the algorithm were the modification of step sizes and the addition of bias through multiplication with constants. Both of these additions require the introduction of four new constants: F_1, F_2, F_3, and F_4. All in all, these modifications aid in designing an algorithm which maximizes the hydrogen production of a given HRES.

4

Results

In this Chapter, the dataset used for the simulations and the economic analysis is introduced in Section 4.1. The simulation results, covering three different analyses, are presented and discussed in Section 4.2. The first simulation explores the impact of the number of stacks available in the HRES, the second simulation focuses on evaluating various configurations of the PV solar park, and the third simulation examines the effectiveness of m-tracking. Section 4.3 shifts the focus to the experimental results, which aim to validate the proposed HRES and identify any disparities between the simulated system and the pilot system. Finally, in Section 4.4, the economic results are discussed, comparing the proposed HRES to existing research and industrial benchmarks. The LCOH is calculated for each benchmark to facilitate a comprehensive comparison with the proposed system.

4.1. Dataset

The evaluation of the MHP algorithm performance utilizes a dataset obtained from the Baseline Surface Radiation Network (BSRN) [105]. This network acquires radiation data from various stations worldwide through the World Radiation Monitoring Center (WRMC). The data collection frequency of the BSRN is set at 1-minute intervals, rendering it suitable for testing the MHP algorithm. Within the WRMC, The Netherlands has a weather station in Cabauw, operated by the KNMI. To determine the appropriate date selection of the dataset for evaluation, the Typical Meteorological Year (TMY) methodology is employed. A TMY dataset consists of meteorological data values throughout the years, specifically tailored to a specific geographical location. Data from 2005 to 2023 was used in the selection of the TMY. From this data, for each month of the year, data was chosen that accurately represents the meteorological conditions of that particular time of year. Shown in table 4.1 are the twelve months which make up the TMY, along with characteristic data for each month.

4.2. Simulation Results

This section discusses the results pertaining to three simulations. First, a simulation is carried out to investigate the effect of increasing the tracking resolution. This is achieved by increasing the number of stacks in the system. Next, a simulation investigates the effect of PV solar park configuration on the performance and yield of the system. Lastly, a full-year TMY simulation investigates the difference between an algorithm which has a static goal ($m = 0$), and one that has a dynamically varying goal dependent on the estimated irradiance.

4.2.1. Increasing Tracking Resolution

In the first simulation, the objective was to augment the number of points that the MHP algorithm could use in approaching its target. This involved varying the number of stacks, ranging from 60 to 1920, resulting in a total of six configurations wherein the number of stacks was doubled each time. To maintain a consistent total power output, the current delivered per cell was proportionally reduced by the same factor employed to multiply the number of stacks. The entire month of June 2009 (from the TMY dataset) was used as a basis for the simulation. Table 4.2 presents a summary of the simulation

Table 4.1: Monthly statistics for all of the months which make up the Typical Mean Year (TMY) used for simulations. The chosen location is Cabauw, The Netherlands. Active sun hours are defined as the moment from which the incident solar irradiation is > 5 W m^{-2}, which can occur before sunrise or after sunset.

	TMY Year	Active Sun Hours (> 5 W m^{-2}) -	Average Irradiance W m^{-2}	Median Irradiance W m^{-2}	Average Temperature (when sunny) °C	Median Temperature (when sunny) °C
January	2019	249.1	163.5	65.0	4.0	4.9
February	2018	274.4	439.4	401.0	2.1	2.6
March	2015	358.7	339.5	209.0	7.4	7.2
April	2015	411.1	496.8	451.0	10.6	10.6
May	2009	497.7	185.4	159.6	15.1	15.3
June	2009	486.8	462.1	374.0	16.8	16.5
July	2017	482.1	419.5	341.0	19.3	19.1
August	2013	428.4	455.9	382.0	20.2	19.8
September	2011	366.5	374.5	275.0	17.6	17.1
October	2019	320.8	240.2	139.0	12.8	13.1
November	2007	249.5	178.9	75.0	8.0	7.5
December	2015	230.4	175.9	79.0	9.2	9.3

Table 4.2: Simulation results of increasing the stack number. For every increase in stacks, there is a proportional decrease in the current delivered by a single stack. MPPT efficiency is the true power delivered divided by the maximum power attainable for the given irradiance and cell temperature, as per Equation 2.6. This ensures the total power delivered remains equivalent. (Data source: BSRN [105])

# of Stacks #	Total Power Delivered *MWh*	Total Hydrogen Produced *kg*	Average Cost of Production *kWh/kg*	Overall MPPT Efficiency *%*	Switches per stack per hour *#/hr*
60	12.4	262.4	47.3	91.3%	2.23
120	12.4	251.8	49.2	92.9%	1.68
240	12.4	233.4	52.9	96.9%	1.01
480	12.4	201.0	61.5	98.7%	0.51
960	12.3	130.7	94.3	98.4%	0.25
1920	12.3	101.5	121.2	98.8%	0.14

outcomes for each of the six configurations.

Results indicate that increasing the number of stacks has a positive impact on the overall MPPT efficiency of the algorithm. Comparing the results to the benchmark range of 94% to 98% efficiency for conventional MPPT tracking algorithms, the enhanced resolution brings the discrete tracking resolution closer to the continuous tracking resolution achieved with a duty cycle on a DC-DC converter. However, the decrease in current per cell has adverse consequences on total hydrogen production, leading to an increase in the average production cost of hydrogen. This can be attributed to insufficient current per cell to overcome the resistances encountered, such as electrode, electrolyte, and membrane resistances. Additionally, the decreasing number of switches per hour can be attributed to the algorithm step size scaling, which remains unchanged despite varying stack resolutions. As a result, increasing the number of stacks leads to smaller steps in the algorithm.

4.2.2. Altering Solar Park Configuration

The next simulation in this study aimed to examine how the configuration of the PV solar park impacts the overall yield of the system. To achieve this, data from the 1$^{\text{st}}$ day of the TMY months of March, June, September, and December was utilized. This selection aimed to represent system performance on one day during each season throughout the year. The number of panels in series was varied within the range of 11 to 14, with increments of 1 panel. In order to maintain an approximate equivalence in the total power delivered by the PV solar field, the number of panels in parallel was adjusted ac-

Table 4.3: Results of changing the configuration of the PV solar panels whilst keeping the total panel count constant. Increasing the number of panels in series raises both the average voltage and current, as the operational range of the PV arrays sees more overlap with that of the electrolyzer. Configurations A, B, C, and D correspond to the PV solar park including 11, 12, 13 and 14 panels in series, respectively. Configuration C results in a high hydrogen yield whilst not exceeding the soft current limit frequently. (Data source: BSRN [105])

Variable	Unit	Config. A	Config. B	Config C.	Config D.
Panels in series	-	11	12	13	14
Panels in parallel	-	260	238	220	204
Total # of panels	-	2860	2856	2860	2856
Average stack voltage	*V*	321.0	341.2	363.1	377.5
Average stack current	*A*	11.0	14.9	20.2	24.8
Total power delivered	*MWh*	4.5	5.7	6.4	6.6
Tot. hydrogen produced	*kg*	94.0	117.8	129.5	130.1
Average cost of hydrogen	*kWh/kg*	48.2	49.1	50.1	51.3
Overall MPPT efficiency	*%*	94.1%	93.8%	92.3%	92.1%
% Soft current limit exceeded	*%*	0.0%	3.1%	19.6%	35.3%
% Voltage limit exceeded	*%*	90.3%	22.3%	3.2%	0.6%

cordingly, striving to keep the total panel count as consistent as possible across configurations. Data was collected and averaged for all four days in each configuration. The results of this analysis are presented in Table 4.3.

A consistent increase in both stack voltage and current is observed as the number of panels in series increases. There is a corresponding increase in the number of instances where the soft current limit is exceeded, while the minimum voltage limit is exceeded less frequently. Furthermore, the total power delivered by the system shows progressive growth with an increasing number of panels in series, albeit the increase becomes marginal beyond 13 panels. This trend is also observed in the total mass of hydrogen produced.

However, the average cost of hydrogen production is optimal for the smallest number of series panels. This observation aligns with Figure 3.7, which confirms that the average cost of hydrogen production increases from 47.5 $\mathrm{kW\,h\,kg^{-1}}$ at 348.5 V to over 50 $\mathrm{kW\,h\,kg^{-1}}$ beyond 400 V. Thus, an increase in the average voltage leads to higher costs of hydrogen production.

Upon examining the sizing figures for 12 and 13 panels (see Figures 3.16 and 3.17), the number of series panels increases, causing a rightward shift of the P-V curves. This shift can result in sub-optimal system operation, irrespective of the number of stacks employed.

Configuration C emerges as the most favourable configuration, as it achieves optimal power delivery and hydrogen production without exceeding voltage and current limitations excessively.

4.2.3. Implementing Dynamic Goal Seeking

This simulation aimed to investigate the effect on electricity and hydrogen yields if the algorithm can dynamically adapt its objective based on input conditions. To enable this dynamic adjustment of the algorithm goal, a function can be established to determine the optimal value of m ($m_{\text{max H2}}$) that maximizes hydrogen production. This function is derived from Figure 4.1, which represents the relationship between hydrogen production, voltage, and a range of irradiances. By identifying the operating point that corresponds to the maximum hydrogen production on this plot, the same operating point can be projected onto a P-V curve. The slope of this operating point, associated with the highest hydrogen production ($m_{\text{max H2, true}}$), can then be documented and fitted using a linear relationship.

In the absence of a sensor for the true irradiance incident on the PV solar arrays, an irradiance estimator function can be made based on empirical measurements. There exists a high correlation between the output power of the PV solar park and the irradiance. Utilizing this correlation, the power of the PV solar park can be divided by the reference power (i.e., the maximum power point under standard test conditions). Subsequently, a linear function can be fit to provide an estimator function for the irradiance.

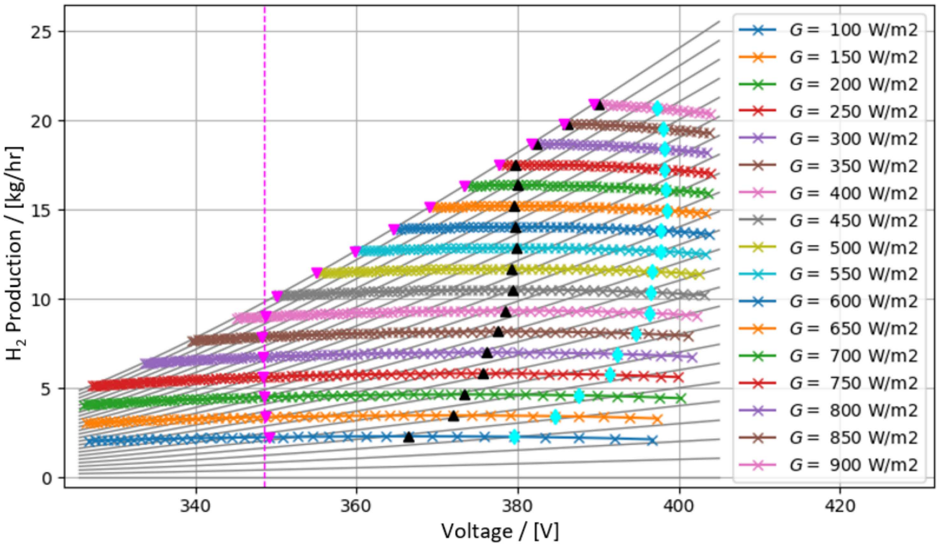

Figure 4.1: Hydrogen production - Voltage graph of a directly coupled HRES containing a PV solar park and an alkaline electrolyzer. The grey lines indicate electrolyzer power curves, increasing in steps of 5 stacks (up to 120). Cyan points indicate MPPs, and magenta points indicate the points of lowest cost of hydrogen production. Black points indicate the points of highest hydrogen production. (Data source: BSRN [105])

$$G_{\text{est.}} = 10.586 + 0.368 \cdot \frac{n_{\text{panels}} \cdot P}{P_{\text{ref}}} \tag{4.1}$$

Back-testing the estimator function against real irradiance data reveals a median absolute error of 5.3%, which was within the acceptable range for use in the simulation. The irradiance is used to calculate the target for the algorithm. However, the rapidly changing irradiance conditions bar the need for highly accurate estimates of the irradiance. This is further confirmed when evaluating the simulation results between the algorithm using the irradiance estimator and the algorithm using the true irradiance.

$$m_{\text{max H2, calc.}} = 0.0019 \cdot G_{\text{est.}} - 0.0177 \tag{4.2}$$

The data which served as the basis for the above-mentioned relationships can be found in appendix B (table B.1).

These functions, referred to as ’m-tracking,’ empower the algorithm to dynamically select the target slope, m. The simulation conducted in this section modelled the entire dataset, representing a complete TMY. Two distinct cases were compared: the first case involved the algorithm consistently tracking the point where $m = 0$. The second case employed m-tracking, allowing the algorithm to dynamically target a different point that maximizes hydrogen production.

In order to validate the accuracy of the irradiance estimator function, a third case was executed where the true irradiance served as input for the m-tracking function. Results indicated that the discrepancy between the estimated irradiance (G) and the true value of G was minimal, confirming the accuracy of the estimator function. A summary of the simulation results for the aforementioned cases is presented in Table 4.4. Further results can be seen in Appendix B, Table B.2.

The analysis of the full-year simulation results reveals that the m-tracking function implemented in the algorithm yields lower power and a reduced hydrogen output. Moreover, the m-tracking functions exhibit a 52% increase in the number of switches per stack per hour, which can impact the lifespan of the electrolyzer stacks.

Comparing the performance of the m-tracking function using the irradiance estimator function to that using the true irradiance, no significant difference is observed, except for the number of instances where voltage and current limits were exceeded. Without m-tracking, an average of 6.8% of iterations exceeded the minimum voltage threshold, and 23.0% exceeded the soft current threshold throughout the year. In contrast, when employing m-tracking, these thresholds were surpassed on 18.3% and 7.1% of the iterations, respectively.

Table 4.4: Summarized results from a simulation investigating the difference between m-tracking and conventional MPPT algorithm goals. M-tracking performance was modelled using both an estimator function for the irradiance and using the true value for the irradiance itself. Temperature effects were not taken into account in the irradiance estimator. (Data source: BSRN [105])

m-tracking	**Total Power Delivered** MW h	**Total Hydrogen Produced** *tons*	**Overall MPPT Efficiency** %	**Switches per Stack per Hour** *#/hr*	**% of Times Soft Current Limit Exceeded** %	**% of Times Voltage Limit Exceeded** %
no	1580.7	31.6	94.5%	15.6	23.0%	6.8%
yes ($G_{\text{est.}}$)	1564.5	31.4	92.3%	23.8	7.1%	18.3%
yes (G_{true})	1564.7	31.5	92.3%	23.8	7.3%	20.4%

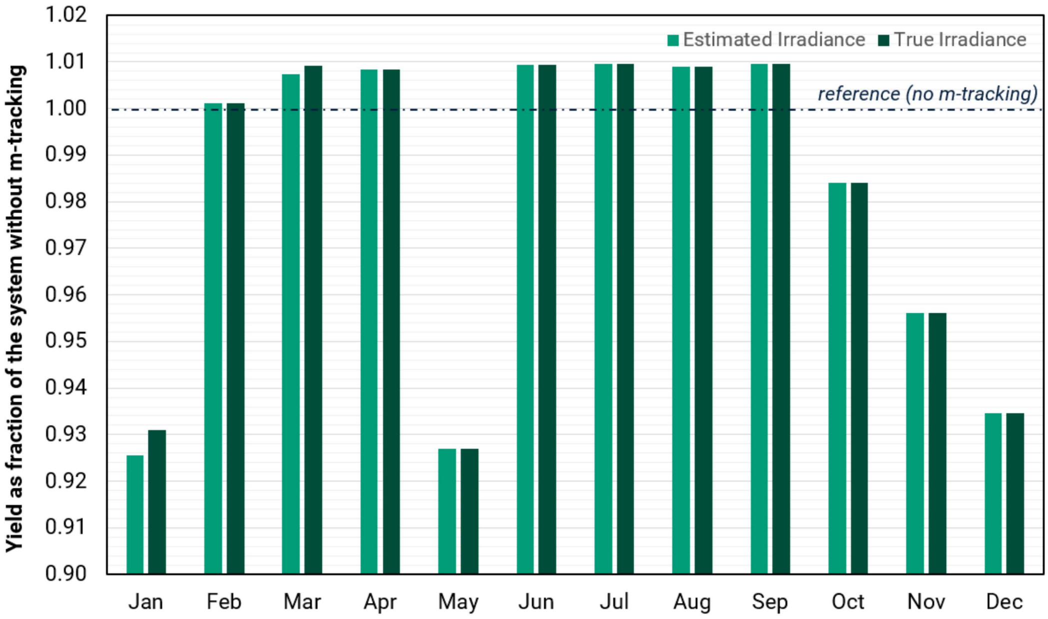

Figure 4.2: Hydrogen yield with m-tracking as a fraction of the yield without m-tracking. Weather data and resulting hydrogen yield for the month of May indicate an outlier resulting in low average irradiance. Yield in the months with low average irradiance is low due to an artefact in the algorithm resulting in repeated zero hydrogen production if close to zero power output. The derivation of the m-tracking algorithm can be found in Section 3.3.5 (Data source: BSRN [105]).

To determine whether the m-tracking functions universally result in lower yields compared to the scenario without any m-tracking, a closer investigation of the monthly yields is warranted. This is depicted as a fraction of the yield without m-tracking in Figure 4.2.

When looking at the monthly yields, the months of January, May, October, November, and December exhibit lower yields compared to the simulation without m-tracking. In these specific months, the average irradiance amounts to 188 $\mathrm{W\,m^{-2}}$.

To provide a comprehensive overview of the simulation results, Table 4.5 presents the outcomes for all months, excluding the aforementioned months characterized by their low average irradiance. This table offers a more representative evaluation of the performance of the m-tracking function in months when solar power is more abundant.

In the months characterized by a higher average irradiance, the total power delivered by the system with m-tracking functions is comparable to that of the scenario without m-tracking. However, there is an increase in hydrogen yield, which is 0.81% higher than the case without m-tracking. Additionally, the percentage of instances where the soft current limit is exceeded exhibits a decrease.

Similar to the findings for the entire TMY, the switching frequency per stack per hour remains significantly higher when employing the m-tracking functions compared to the scenario without m-tracking.

Table 4.5: Summarized results from a simulation investigating the difference between m-tracking and conventional MPPT algorithm goals, excluding the months of January, May, October, November and December. M-tracking performance was modelled using both an estimator function for the irradiance and using the true value for the irradiance itself. Temperature effects were not taken into account in the irradiance estimator. Five months are excluded as their average irradiance is below 250 W m^{-2}, which hinders the ability of the m-tracking function to work properly. (Data source: BSRN [105])

m-tracking	**Total Power Delivered** MW h	**Total Hydrogen Produced** *tons*	**Overall MPPT Efficiency** *%*	**Switches per stack per hour** *#/hr*	**% of Times Soft Current Limit Exceeded** *%*	**% of Times Voltage Limit Exceeded** *%*
no	1262.3	25.3	95.0%	20.0	20.7%	5.1%
yes ($G_{\text{est.}}$)	1263.7	25.5	95.0%	32.7	7.7%	13.9%
yes (G_{true})	1263.7	25.5	95.0%	32.7	5.5%	9.3%

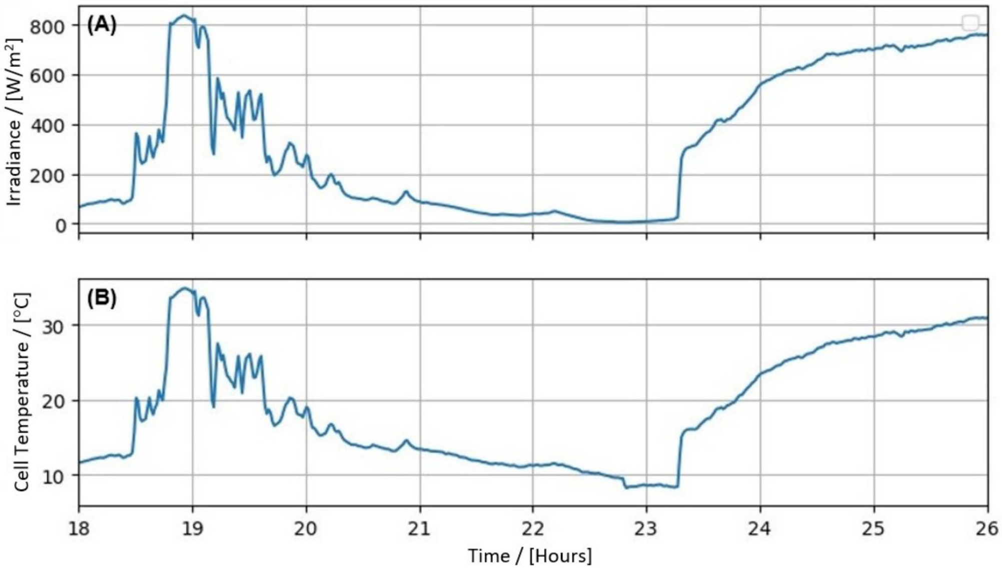

Figure 4.3: Irradiance and cell temperature for a simulation of weather data from December 2015 in Cabauw, The Netherlands. Plot (A) shows the irradiance data (diffuse + direct) at the Cabauw weather station. Plot (B) shows the calculated cell temperature, a function of the incident irradiance and the ambient temperature at the Cabauw weather station.

The m-tracking function exhibits interesting behaviour when confronted with low irradiances. Shown in figures 4.3, 4.4, and 4.5 are the simulation results for the TMY month of December 2015.

Between 21 and 23 hours, the incident irradiance is <100 W m^{-2}. As seen from the figures, the voltage and current suddenly jump to zero. In the following iterations, the algorithm gets stuck at zero power, as the differentials used to change the stack numbers are exactly equal to zero. This does not prompt a change in the number of stacks as the algorithm is convinced it is exactly where it needs to be. It is only once the irradiance increases again, after hour 23, that the algorithm is pulled out of the cycle and continues normal operation.

This algorithm artefact only occurs during periods of extremely low irradiance, and there is no physically correct explanation for the initial jump to zero voltage/current. In a practical system, whilst there are still periods of extremely low irradiance, sensor noise and varying resistances will always result in minute changes in voltage and/or current. As a result, it is not expected that such an error occurs in a practical setting. Even if it were to occur, it would be of shorter duration as minor changes in voltage and current can prompt the algorithm to change its number of active stacks and pull itself out of the loop.

More simulation results can be found in Appendix B. In particular, two more simulation excerpts are detailed, covering the system response to both sunny and cloudy weather conditions.

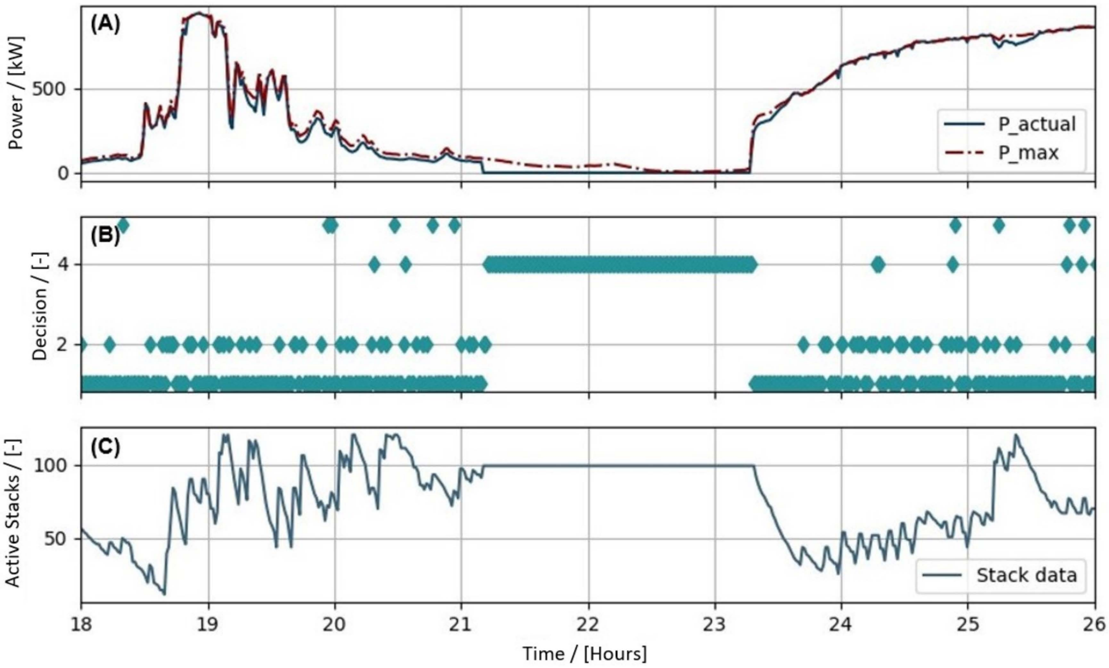

Figure 4.4: System power, decision log, and active stack log for a simulation of weather data from December 2015 in Cabauw, The Netherlands. Plot (A) shows the power delivered to the modular alkaline electrolyzer as well as the reference maximum possible power if the system operated at the MPP in every iteration. Plot (B) shows the decision made in each iteration. Decision choices 1 and 6 indicate a decrease in stacks, choices 2 and 5 indicate an increase in stacks, and choices 3 and 4 indicate the stack number stays the same. Plot (C) shows the number of stacks active in each iteration.

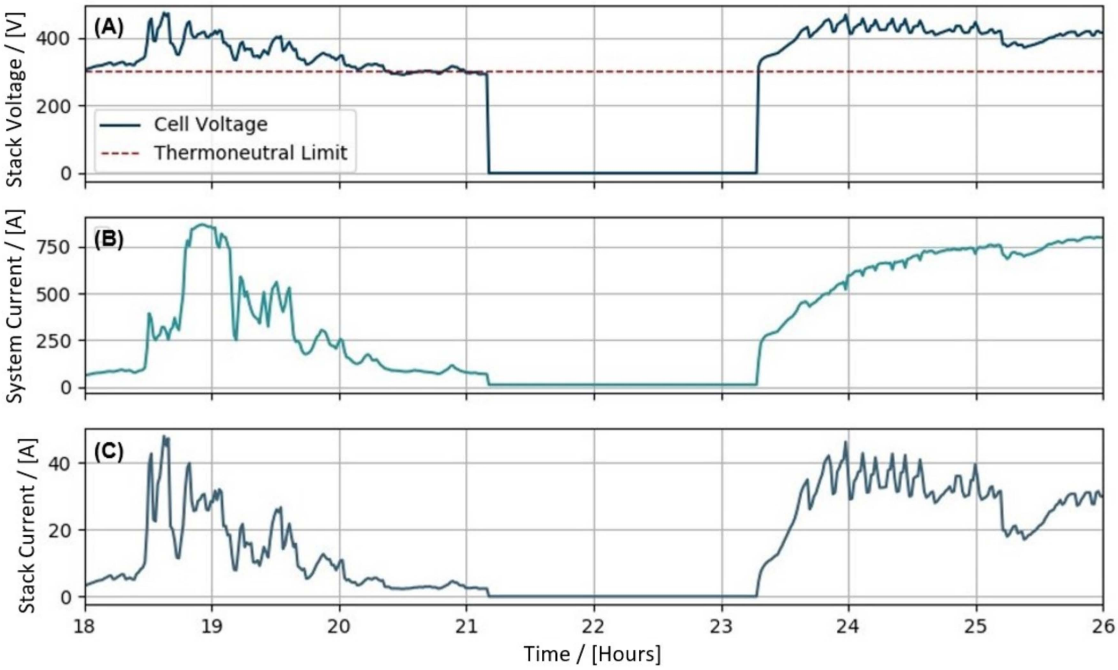

Figure 4.5: Stack voltage, system current and stack current for a simulation of weather data from December 2015 in Cabauw, The Netherlands. Plot (A) shows the stack voltage, including the thermo-neutral voltage limit. Plot (B) shows the system current, which is the sum of all current flowing through each of the stacks. Plot (C) shows the current divided by the number of active stacks, representing the stack current.

4.3. Experimental Results

This section discusses the experimental setup used to demonstrate the proof-of-concept for directly coupled HRES containing a PV solar array and a modular alkaline electrolyzer. First, the experimental setup is explained. Second, several preliminary observations are shared pertaining to the performance of the system. Next, an overview is given of the three experiments which were conducted on the setup. Last, the results of these experiments are discussed.

4.3.1. Experimental Setup

The experimental setup consists of two sub-systems, the PV solar panel array and the modular alkaline electrolyzer. The PV solar panel array is composed of 12 panels connected in parallel. Shown in Figure 4.6, the panels are oriented at a slight angle. Six panels are East-facing, and six panels are West-facing. Contrary to the PV solar panels used for the simulations, the panels in the experimental setup are made of gallium-doped wafers. Each PV solar panel has a nominal maximum power of 370 W and an open-circuit voltage of 40.9 V, both under standard test conditions[1]. The full PV solar panel array has a maximum nominal power of 4.44 kW, although the actual power output will be slightly lower due to higher cell temperature decreasing the performance. In order to ensure the safe operation of the PV solar array, bypass diodes are installed on each PV solar panel. During the partial shading of one of the panels in the array, the bypass diodes will prevent the flow of current from the unshaded panels to the shaded panel. In addition, blocking diodes are installed in between the PV solar array and the electrolyzer stacks. These diodes prevent the discharging of current in electrolyzers to the PV solar panels and are implemented as a safety measure.

The modular alkaline electrolyzer consists of 12 individual stacks[2]. The entire electrolyzer sub-system uses a single electrolyte pump and two separator tanks for the separation of hydrogen and oxygen gas. The produced gasses are vented to the atmosphere through tubing leading to the roof. An overview of the electrolyzer stacks and associated control electronics is shown in Figure 4.7.

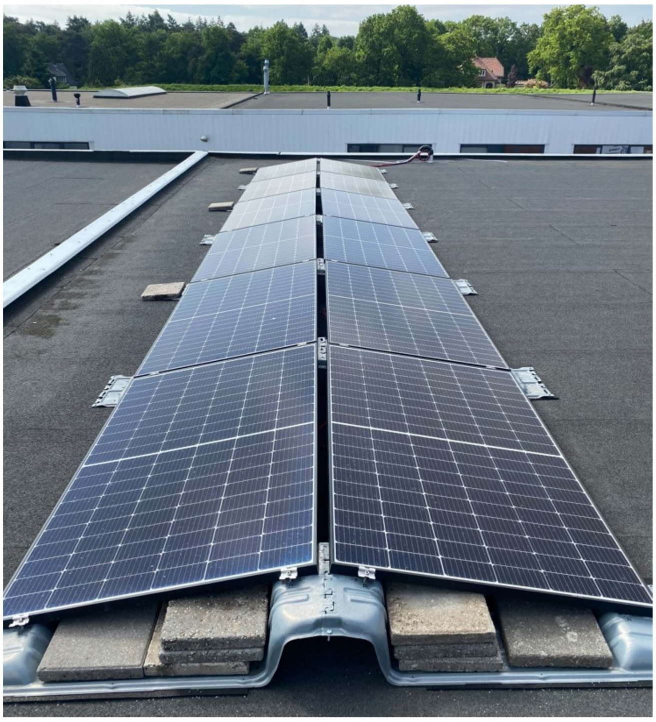

Figure 4.6: PV solar panels used for the experimental setup. The setup features 12 PV solar panels, connected in parallel. The panels are divided into two 6-panel groups. One group is East-facing and one group is West-facing.

---

[1] Standard Test Conditions (STC) refer to a laboratory-environment where the panels are exposed to an irradiance of 1000 $\mathrm{W\,m^{-2}}$ at a temperature of 25 °C.

[2] The stacks that make up the alkaline electrolyzer were made exclusively for this experimental setup. Therefore, these stacks and any performance results thereof do not in any way reflect the performance and development of commercial XINTC electrolyzer systems.

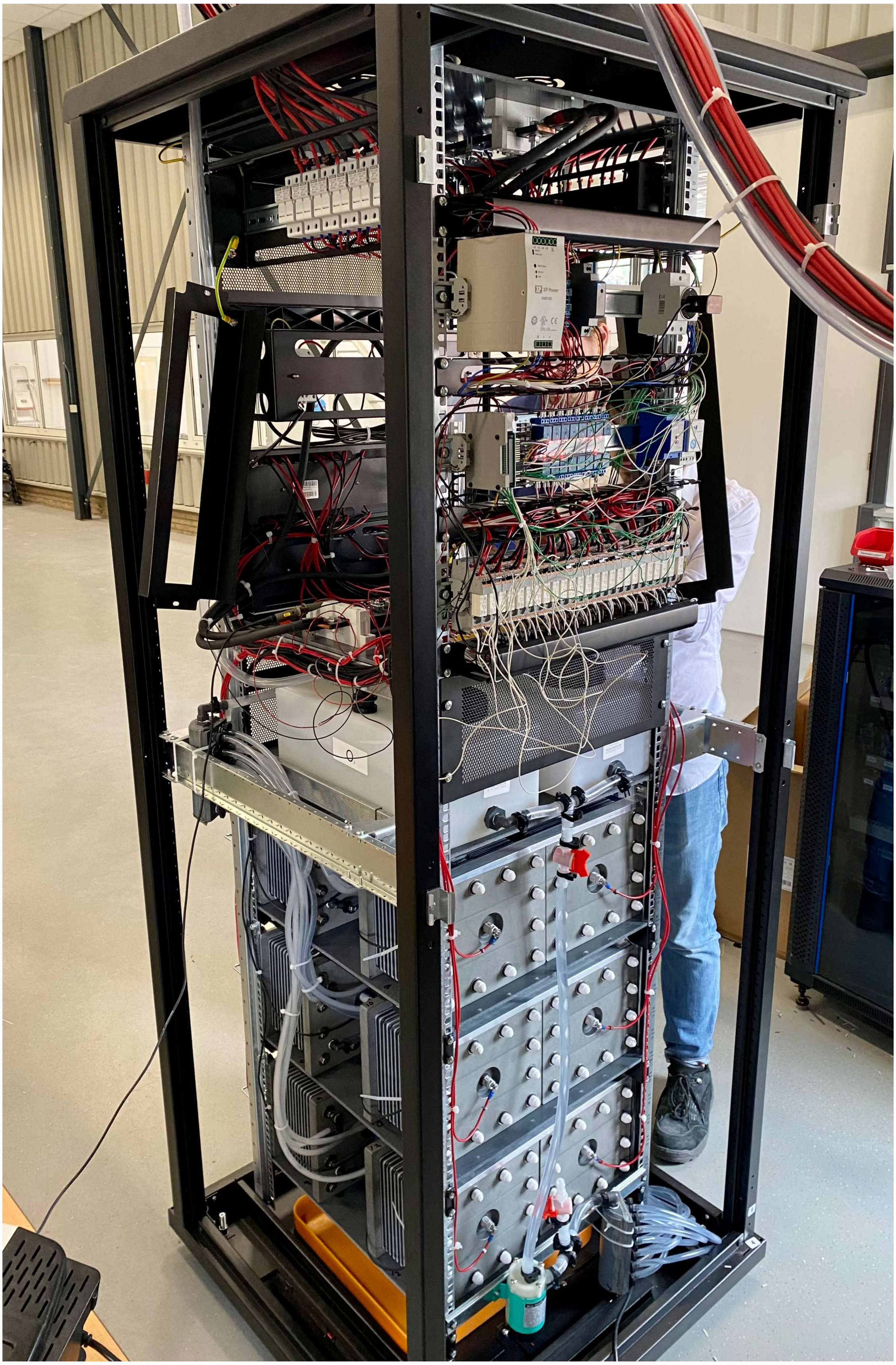

Figure 4.7: Control electronics and electrolyzer stacks for the experimental setup. There are 12 stacks. The pilot system was specifically constructed for this research. The stacks are configured in parallel and are all fed by one pump.

The current flowing through each stack is measured by measuring the voltage drop over a large resistor placed in series with each stack. Given that both the PV panels and the electrolyzer stacks are placed in parallel, the voltage through each panel and the electrolyzer stacks can be assumed equal to the voltage on the DC bus bar. Although true voltages may vary slightly, these variations are not expected to be significant.

4.3.2. Preliminary Observations

Before running official experiments, the system was tested to ensure correct operation. During this testing, several preliminary observations could be made.

The first difference between the simulations and the physical system was observed to be the erratic behaviour of the stack currents and the bus bar voltage. Upon visual investigation of the electrolyte flow exiting the various electrolyzer stacks, the flow was noticeably unsteady despite constant irradiance conditions and no change in the number of active stacks. The hypothesis is that there are periodic build-ups of gasses inside the stacks. The increase in electrical resistance is due to the decrease in effective area of the electrode where reactions can take place, due to the formation of bubbles on the electrode surface. The produced 'bubble-curtain' also results in pressure fluctuations which affect the electrolyte flow of the system. With the electrical resistance of each stack independently varying with time, the combined total current of 12 stacks can vary significantly despite otherwise steady conditions. The same effect was noticed for the bus bar voltage of the system, although the resulting variations were proportionally less than seen for the current. To remedy these fluctuations and increase the likelihood that the algorithm uses the correct differences in voltage and current measurements to decide how many stacks to activate, a moving average filter was added. With a measuring frequency of every 5 seconds and a decision frequency of every 15 seconds, a 7-value moving average filter was added to smoothen the data used to decide the number of active stacks in the next iteration.

The second observation that was made regarded the polarization curve of the electrolyzer stacks. The simulations used a polarization curve which was measured and modelled based on an electrolyzer stack with more cells than used in the stacks for this system. The data points were also collected under laboratory conditions with a constant electrolyte temperature. The experimental setup featured a lower number of cells in the stack, changing the magnitudes of the losses (i.e., bypass current losses or gas leakages through the rubber gaskets). Furthermore, the exothermic nature of the electrolyzer stacks, coupled with insufficient cooling, resulted in large fluctuations in the electrolyte temperature. This has a great effect on the polarization curve of the stacks and resulted in differences between the modelled ideal sizing of the electrolyzer stacks and the true performance of the stacks in the experimental setup. Under constant sunny conditions with a measured irradiance of 950 $\mathrm{W\,m^{-2}}$, the maximum power delivered to the electrolyzer stacks was in the order of magnitude of 3.300 kW. While the cell temperature was estimated to be double that under standard test conditions at 50 °C, the maximum power is far below the nominal maximum power of the solar field at 4.44 kW. This can be explained when considering that the electrolyzer stacks perform worse than the modelled polarization curves, shifting the electrolyzer curves to the right with respect to the P-V curves of the solar field (see Figures 3.16 and 3.17). Shown in Figure 4.8 is the polarization data for the electrolyzer stacks in the experimental setup, together with an estimated curve-fit function for an alkaline electrolyzer.

4.3.3. Experimental Overview

Three experiments were carried out on the experimental setup. The aim of the experiments was two-fold. The first goal was to provide a proof-of-concept for the HRES and the ability of a directly-coupled modular alkaline electrolyzer to regulate the power coming from a PV solar array. The second goal was to test the effectiveness of the MHP algorithm defined in Section 3.3 and identify any phenomena which were not accounted for during the simulations.

The first experiment (Experiment 1) was a benchmark. For 30 minutes, the entire system would operate with all twelve stacks active. The absence of control would provide a set of reference results to compare the results for the other experiments. The second experiment (Experiment 2) was a test of the MHP algorithm as defined in Figure 3.27. Due to the small number of stacks in the system, the step size was assumed constant at one stack. The MHP algorithm also used the moving average filtered voltage and current as input data to make decisions, as this was more likely to lead to the correct control decision. The last experiment (Experiment 3) was identical to Experiment 2, with the exception of Decisions 4 and 5 in the MHP algorithm. This experiment saw the signs for these decisions flipped

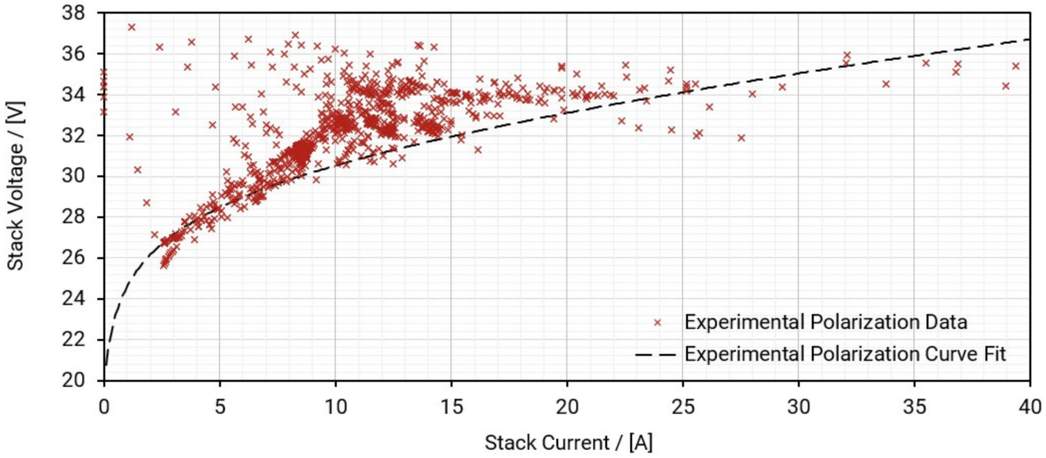

Figure 4.8: Polarization data for the electrolyzer stacks in the experimental setup. Curve-fit function is an estimate which aims to show the modelled behaviour for an alkaline electrolyzer stack. The plotted polarization data is for varying electrolyte temperatures and for a system with 12 electrolyzer stacks. The stacks used in this experimental setup were constructed solely for research purposes and their geometry and performance do not carry over to commercial XINTC systems.

(see Figure 3.27), so the number of stacks would increase if $\Delta I > 0$ (Decision 5) and decrease if $\Delta I \leq 0$ (Decision 4). It was hypothesized that this change in the algorithm may lead to improved tracking ability as preliminary testing revealed oscillatory behaviour when choosing Decisions 4 and 5 repeatedly.

Experiment 1 Results

Shown in Figures 4.9 and 4.10 are the irradiance and power for the first experiment, respectively. The number of active stacks was maintained constant at 12 stacks for the entire duration of the experiment. The ambient temperature was measured to be constant and equal to 25 °C. Collected results for voltage and current can be found in Appendix B (see Figures B.18 and B.19).

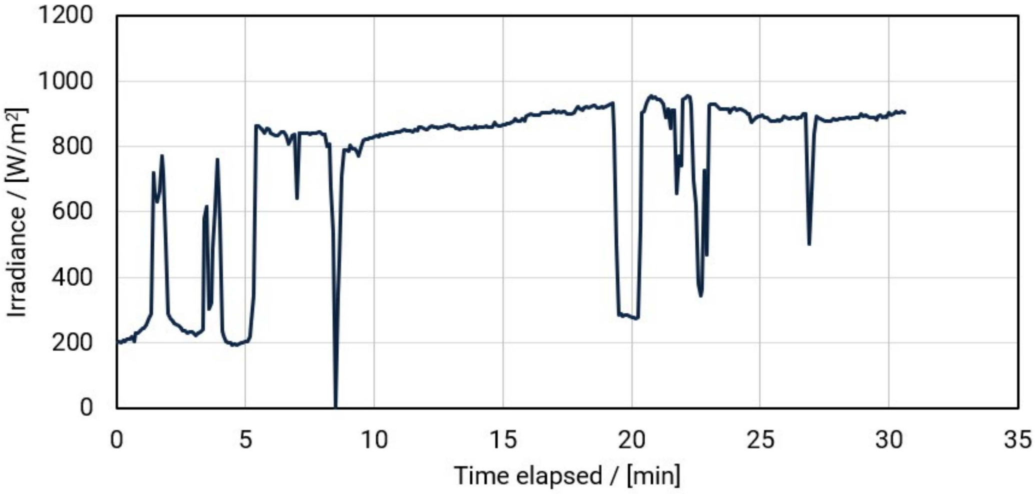

Figure 4.9: Irradiance data collected for Experiment 1. Average irradiance was 743.5 W m^{-2}, with a standard deviation of 245.9 W m^{-2}. The ambient air temperature was constant at 25 °C. The stacks used in this experimental setup were constructed solely for research purposes and their geometry and performance do not carry over to commercial XINTC systems.

The power for Experiment 1, shown in Figure 4.10, show an increasing gap between the real power delivered to the stacks and the maximum power available from the PV solar array. The size of the gap increases proportionally to the increase in irradiance. With all 12 stacks active, this gap in power confirms that the MPP for high irradiances lies outside the range of operating points for the experimental setup. This is due to a difference between the true performance of the system and the initial sizing estimation. Particularly at higher irradiances, the MPP will lie outside of the operating point, limiting the maximum power available with all stacks active. It should be noted that these experiments were conducted in warm and sunny climates in the summer. During periods of lower average irradiance, the change of the MPP being within the operating range of the HRES is significantly higher.

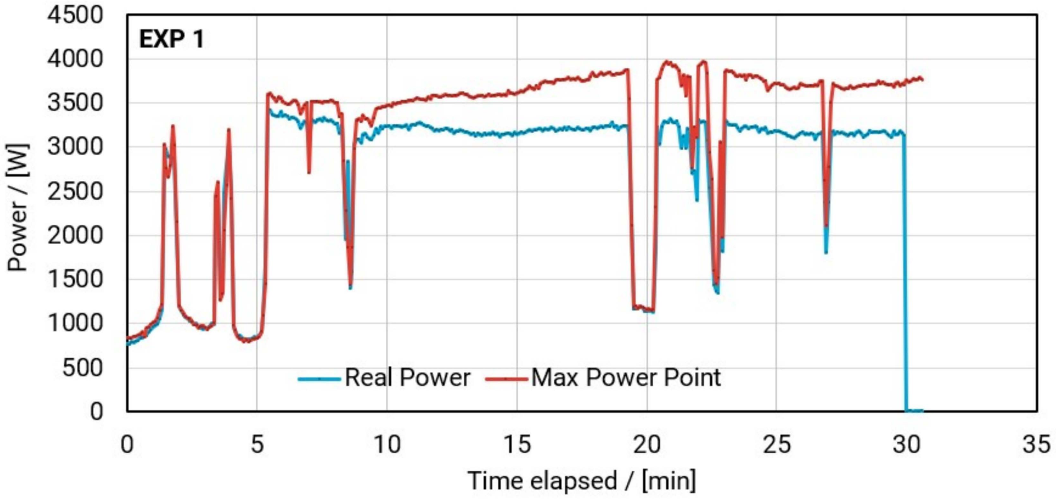

Figure 4.10: Power data collected for Experiment 1. The maximum power point curve is a calculated value, based on the collected irradiance and ambient temperature data. Using the Python PVlib library, the P-V curve is calculated and the corresponding maximum power point is recorded for each iteration. The stacks used in this experimental setup were constructed solely for research purposes and their geometry and performance do not carry over to commercial XINTC systems.

Experiment 2 Results

Shown in Figures 4.11, 4.12, and 4.13 are the irradiance, power and number of active stacks for Experiment 2, respectively. The number of active stacks varied based on the decisions made by the MHP algorithm as defined in Figure 3.27. The ambient temperature was measured to be constant and equal to 25 °C. Collected results for voltage and current can be found in Appendix B (see Figures B.20 and B.21).

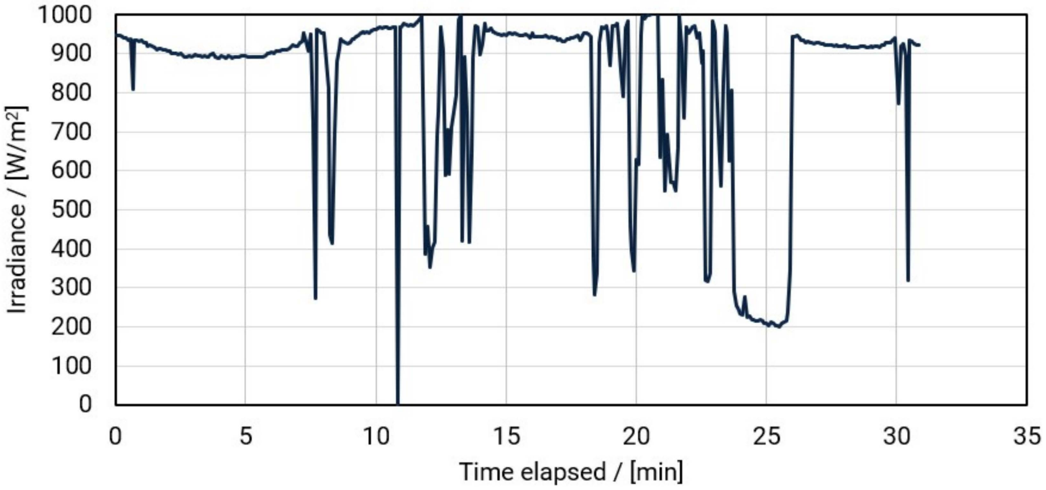

Figure 4.11: Irradiance data collected for Experiment 2. Average irradiance was 828.5 W m^{-2}, with a standard deviation of 222.4 W m^{-2}. The ambient air temperature was constant at 25 °C. The stacks used in this experimental setup were constructed solely for research purposes and their geometry and performance do not carry over to commercial XINTC systems.

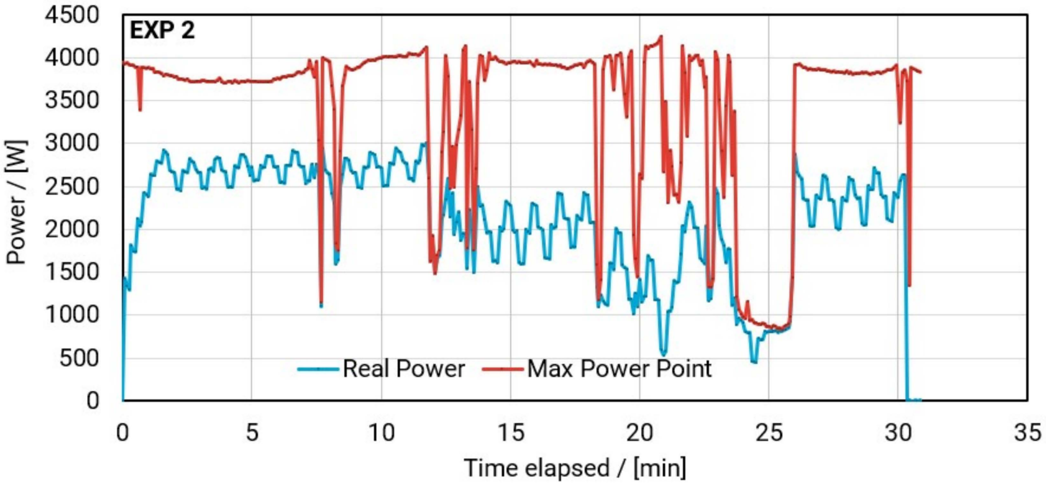

Figure 4.12: Power data collected for Experiment 2. The maximum power point curve is a calculated value, based on the collected irradiance and ambient temperature data. Using the Python PVlib library, the P-V curve is calculated and the corresponding maximum power point is recorded for each iteration. During periods of nearly constant irradiance, oscillations are observed in the real power delivered to the active stacks. The stacks used in this experimental setup were constructed solely for research purposes and their geometry and performance do not carry over to commercial XINTC systems.

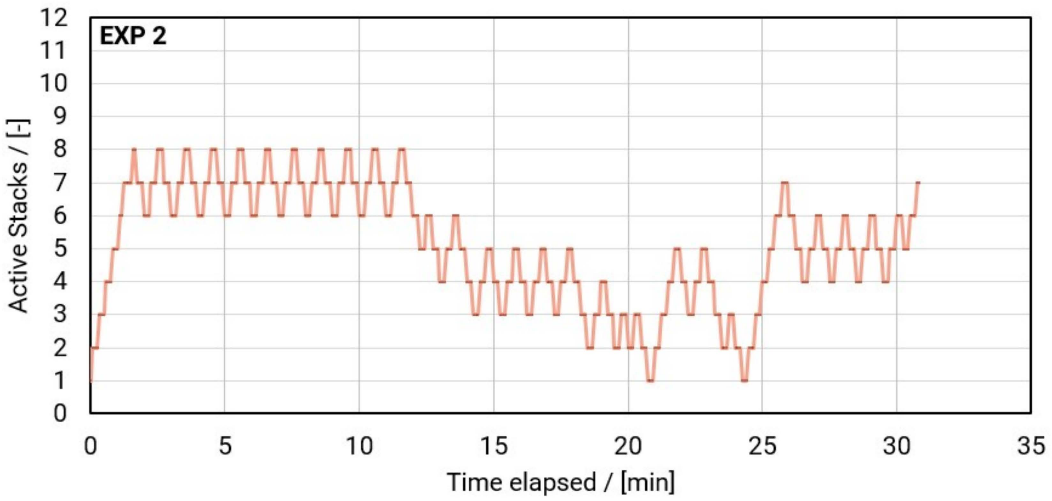

Figure 4.13: Active stack data collected for Experiment 2. The number of stacks does not reach higher than 8 (out of the 12 available), despite prolonged periods of high irradiance (>900 $\mathrm{W\,m^{-2}}$). The number of active stacks is also observed to periodically vary with an amplitude of 1 stack. The stacks used in this experimental setup were constructed solely for research purposes and their geometry and performance do not carry over to commercial XINTC systems.

Both the power and active stack results indicate oscillations during periods of nearly constant irradiance. During these oscillations, experimental results revealed that the MHP algorithm was only choosing between Decisions 4 and 5 in the flowchart (see Figure 3.27). Despite a high average irradiance (828.5 $\mathrm{W\,m^{-2}}$, with a standard deviation of 222.4 $\mathrm{W\,m^{-2}}$), the number of stacks did not exceed 8. The real power delivered during the experiment did not exceed 3 kW, which is less than the 3.3 kW achieved in Experiment 1. In minute 25, following a cloud passing over the PV solar array, the MHP algorithm correctly increases the number of stacks but it continues to oscillate before it reaches the optimal number of stacks for that irradiance.

Experiment 3 Results

Shown in Figures 4.14, 4.15, and 4.16 are the irradiance, power and number of active stacks for Experiment 3, respectively. The number of active stacks varied based on the decisions made by the MHP algorithm as defined in Figure 3.27, with the signs for Decisions 4 and 5 switched. This meant that

Decision 4 corresponded to a decrease in the number of active stacks and Decision 5 corresponded to an increase in the number of active stacks. The ambient temperature was measured to be constant and equal to 25 °C. Collected results for voltage and current can be found in Appendix B (see Figures B.22 and B.23).

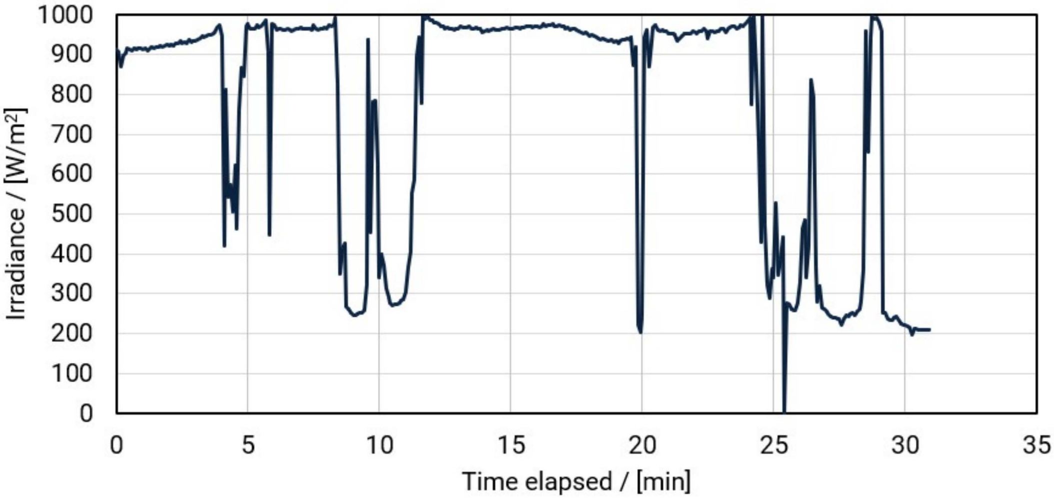

Figure 4.14: Irradiance data collected for Experiment 3. Average irradiance was 761.1 $\mathrm{W\,m^{-2}}$, with a standard deviation of 296.5 $\mathrm{W\,m^{-2}}$. The ambient air temperature was constant at 25 °C. The stacks used in this experimental setup were constructed solely for research purposes and their geometry and performance do not carry over to commercial XINTC systems.

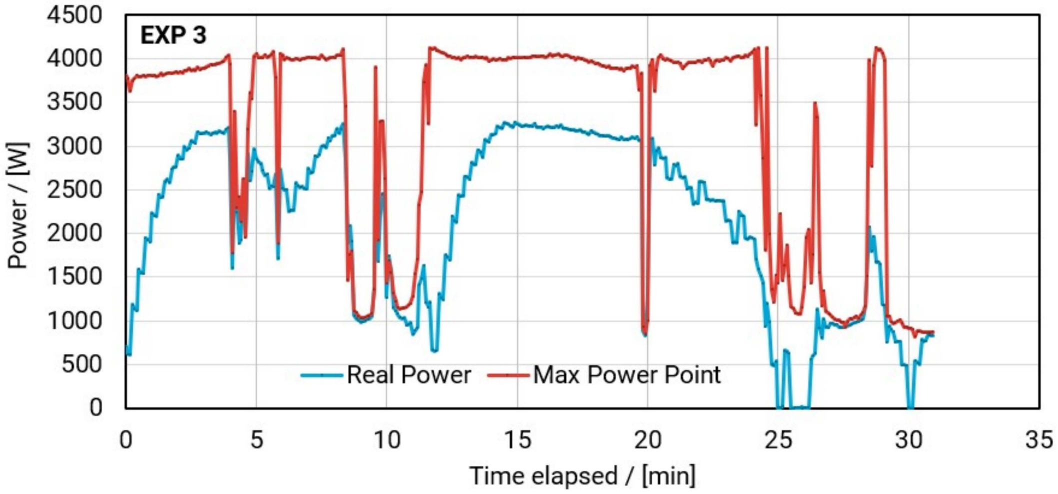

Figure 4.15: Power data collected for Experiment 3. The maximum power point curve is a calculated value, based on the collected irradiance and ambient temperature data. Using the Python PVlib library, the P-V curve is calculated and the corresponding maximum power point is recorded for each iteration. During periods of nearly constant irradiance, the real power delivered to the stacks is seen as increasing, until a power of approximately 3300 W is reached. At minutes 25 and 30, the power is zero for a brief moment. The stacks used in this experimental setup were constructed solely for research purposes and their geometry and performance do not carry over to commercial XINTC systems.

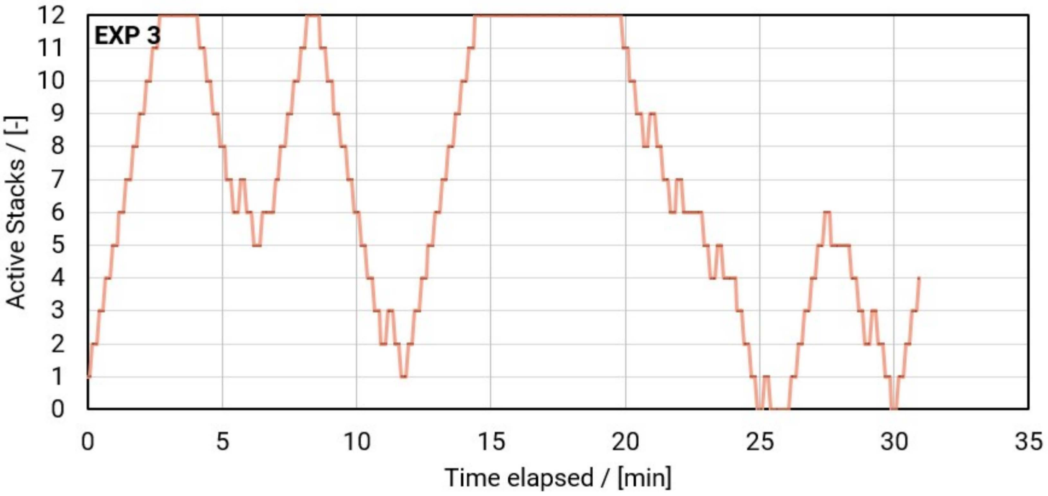

Figure 4.16: Active stack data collected for Experiment 3. During periods of nearly constant irradiance, the number of active stacks is consistently increased each iteration until all stacks are active. At minute 20, following a brief period of shade, the algorithm continues to decrease the number of active stacks despite high irradiance. The stacks used in this experimental setup were constructed solely for research purposes and their geometry and performance do not carry over to commercial XINTC systems.

Contrary to Experiment 2, the power and active stack results for Experiment 3 show behaviour which is more in line with the expectations for the MHP algorithm. Periods of constant irradiance reflect a steady increase in the number of active stacks. As a result, the real power delivered to the active stacks increases slowly until the same 3.3 kW limit is reached as seen in Experiment 1. Periods of scattered clouds between minutes 0 to 15 result in decreases in the number of active stacks. As a result, the real power delivered to the active stacks is relatively more steady than the decrease in irradiance. At minute 20, following a brief period of cloud interference, the number of active stacks is decreased despite high irradiance conditions. The number of active stacks is further decreased at minute 25, during a longer period of cloud coverage. This briefly causes the real power delivered to drop to zero.

4.3.4. Discussion

Shown in Figure 4.17 is the MPPT efficiency for each of the three performed experiments. The MPPT efficiency is the instantaneous ratio of the real power to the calculated MPP for that irradiance and cell temperature. Due to estimations of the cell temperature and the irradiance experienced by the PV solar array (which are modelled using the Python PVlib library), the MPP can have an approximation error. This results in the MPPT efficiency exceeding 100% in some instances. The overall MPPT efficiencies for Experiments 1, 2, and 3 were 86.5%, 60.2%, and 66.8%, respectively. This indicates that the uncontrolled benchmark experiment outperformed the two controlled experiments for this high-irradiance climate, using the first practical implementation of the MHP algorithm discussed in this research.

The oscillatory behaviour seen in Experiment 2 is further reflected in the MPPT efficiency. While Experiment 3 does not share these oscillations, the MPPT efficiency in Experiment 1 is greater than that of the other experiments for the majority of the time. With the industrial standard for MPPT efficiencies at >95%, even the benchmark scenario does not match these standards. This can be attributed to the difference in polarization curves for the model (used for sizing) and the true performance of the electrolyzer stacks. In the scenarios where the experiments were running with all 12 stacks active and under high irradiance, the maximum attainable MPPT efficiency approaches 85%. Therefore, relatively speaking, an MPPT efficiency of 80% in minutes 15-19 of Experiment 3 during high irradiance comes close to the maximum attainable efficiency for this HRES configuration.

There are brief periods where the controlled experiments (Experiments 2 and 3) outperform the MPPT efficiency of Experiment 1. Although this does reflect an overall MPPT efficiency close to Experiment 1, it does demonstrate that a controlled algorithm is able to locally improve the MPPT efficiency of a directly coupled HRES featuring a PV solar array and a modular alkaline electrolyzer.

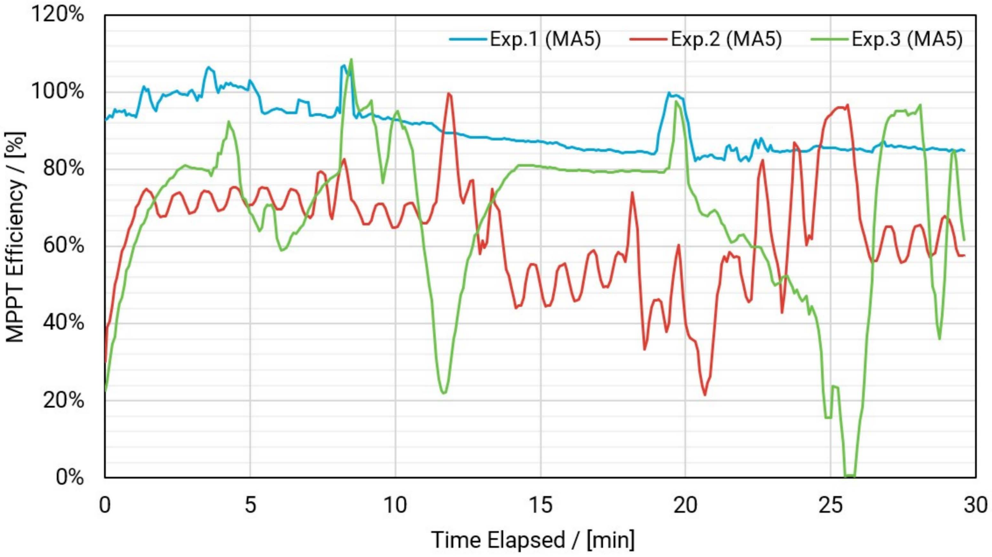

Figure 4.17: MPPT Efficiency for each of the three experiments conducted on the experimental setup. Efficiency figures may exceed 100% as the reference maximum power point used for the calculation is based on measured irradiance and calculated cell temperature data (based on ambient weather data). This may contain approximation errors. The stacks used in this experimental setup were constructed solely for research purposes and their geometry and performance do not carry over to commercial XINTC systems.

However, it is evident that the algorithm (and subsequent modification) used for Experiments 2 and 3 is not outperforming the benchmark. The analytically correct MHP algorithm used in Experiment 2 performed worse than the modified version with analytically incorrect flipped decision signs used in Experiment 3. The algorithm for Experiment 3 is distinctly different to the INC and P&O algorithms on which the MHP algorithm is based [57]. While there is no exact explanation for why this is the case, there are several factors which negatively influence the ability of the MHP algorithm to control the HRES made in the experimental setup. The MHP algorithm relies on the differences between two measurements to ascertain the correct direction in which to increase or decrease the number of active stacks. Commercial conventional DC-DC converters which use the INC algorithm on which the MHP algorithm is based have an iteration frequency in the order of magnitude of kilo Hertz. The experiments maintained a measurement frequency of iteration frequency of 0.2 Hz and an iteration frequency of 0.067 Hz. The significant increase in time between consecutive voltage and current measurements drastically increases the difference in conditions experienced by the two points of measurement. Cloud coverage can change in a matter of seconds, resulting in large differences in irradiance between two points of measurement. Regarding the electrolyzer, gas build-up and the temperature of the electrolyte can also change in the order of seconds. This results in both the P-V curve of the PV solar array and the polarization curve of the electrolyzer experiencing shifts significant enough to lead to errors in the decision made by the algorithm.

Kilohertz iteration frequencies for HRES with modular alkaline electrolysis may not be realistically achievable using this configuration of control electronics. When switching on/off of an active stack, there is a brief spike in the experienced current flowing through the DC bus bar. The faster the switching frequency, the larger the magnitude of this initial peak in current. Furthermore, it takes multiple seconds for the electrolyzer stacks to develop a flow of gasses, and several minutes before steady state gas supply is achieved. Additionally, the rapid switching of stacks can also have negative effects on the lifetime of the stacks themselves as degradation is highest when switching. All of these factors prevent higher switching frequencies.

4.4. Economic Results

This section focuses on the economic analysis conducted as part of the results presented in this chapter. By studying the economic dimensions of the thesis research, the aim is to highlight the implications and broader significance of the HRES and corresponding control systems proposed in this paper.

4.4.1. Input Parameters

As mentioned in Chapter 2 (see Section 2.3.4), renewable energies can be compared to one another by evaluating the Levelized Cost of Electricity (LCOE). In addition to the LCOE, the Levelized Cost of Hydrogen (LCOH) calculates the end-to-end cost of production per kilogram of hydrogen over the lifespan of a hydrogen-producing system. These terms can be expressed as follows:

$$\text{LCOE} = \frac{\text{CAPEX} + \sum_{t=1}^{t_{\text{life}}} \frac{\text{OPEX}_t}{(1 + r_{\text{discount}})^t}}{\sum \text{Electricity Produced over Lifetime}} \tag{4.3}$$

$$\text{LCOH} = \frac{\text{CAPEX} + \sum_{t=0}^{t_{\text{life}}} \frac{\text{OPEX}_t}{(1 + r_{\text{discount}})^t}}{\sum \text{Hydrogen Produced over Lifetime}} \tag{4.4}$$

In the above relations, OPEX_t denotes the operational expenses made in year t, which is summed from the start of the system lifetime ($t = 0$) until the end ($t = t_{\text{life}}$. As these operational expenses occur in the future, they are discounted using a discount rate, r_{discount}. Capital expenditure (CAPEX) is the initial investment cost incurred to purchase and install the HRES. It is assumed that the replacement of faulty stacks, as well as any other unexpected additional CAPEX payments, are included and discounted in the initial CAPEX payment.

The European Union Fuel Cell and Hydrogen Observatory have developed economic models that calculate the LCOH for different European regions, using different renewable energies and inputs. Shown in Figure 2.17 is a geographical display of the LCOH when produced through PV solar power.

The HRES used for this analysis is the directly coupled system discussed in this paper. The system features a 120-stack modular alkaline electrolyzer coupled directly to a 2860-panel PV park (13 panels in series, 220 in parallel). The rated power of the PV park is taken to be the product of the number of panels and the reference maximum power of each panel as mentioned in the datasheet. In order to compare the results, a benchmark system is designed. The benchmark system features two subsystems, which are connected to one another via the national electricity grid. The nominal power and size of the individual sub-systems are the same as the proposed directly-coupled HRES. The CAPEX breakdowns for a PV solar park and an alkaline electrolyzer were discussed in Chapter 2, in figures 2.15 and 2.16.

Due to the decentralized and direct nature of the proposed HRES, there is no need for costs associated with inverters, grid connection, and power electronics. As a result, these costs are excluded from the CAPEX for the directly-coupled HRES. It is assumed that the operational expenses remain equal between both systems. Regular operation and maintenance are still necessary, and the materials are the same resulting in a similar rate of degradation and maintenance. Shown in table 4.6 are the other inputs and variables necessary to provide an economic outlook.

Table 4.6: Overview of the constants used as the basis for the economic analysis. All shown currencies have been converted into 2022 euros. The electrolyzer is oversized with respect to the PV solar park, as a result of the system design as detailed in Section 3.2. It is assumed that the alkaline electrolyzer is only operational when there is sunlight and the PV solar park is producing electricity. Shown OPEX values do not consider electricity prices as it is assumed that all of the electricity requirements are met through the PV solar park. It is also assumed that the HRES is not connected to the grid.

Variable	Value	Units	Comments	Source
PV Park size	1158.3	kW	81.3% of the Electrolyzer capacity	
Electrolyzer size	1425.6	kW	123.1% of the PV Park capacity	
Conventional Electrolyzer CAPEX	919.8	€/kW	in 2022	Fraunhofer Institute for Solar Energy [97]
Direct Electrolyzer CAPEX	742.8	€/kW	in 2022	Fraunhofer Institute for Solar Energy [97]
Conventional PV Park CAPEX	976.6	€/kW	in 2022	International Renewable Energy Agency [10]
Direct PV Park CAPEX	863.5	€/kW	in 2022	International Renewable Energy Agency [10]
Electrolyzer OPEX	22.2	€/kW/year	in 2022	Fraunhofer Institute for Solar Energy [97]
PV Park OPEX	10	€/kW/year	in 2022	International Renewable Energy Agency [10]
Industry standard inverter sizing ratio	79.4	%	Percentage of nominal PV park power	Deschamps et al. [107]
Research standard inverter sizing ratio	90.4	%	Percentage of nominal PV park power	Zidane et al. [108]
Interter power losses	8	%	of pre-inverter power yield	Zidane et al. [108]
Electrolyzer annual decay rate	0.186	%	Percentage of yield per year	EU Fuel Cell and Hydrogen Obersvatory [109]
PV panel annual decay rate	0.450	%	Percentage of yield per year	National Renewable Energy Agency [110]
Discount rate	4	%	in The Netherlands	Planbureau voor de Leefomgeving [111]
Project lifetime	25	years		International Renewable Energy Agency [10]
Industry standard benchmark	51.2	kWh/kg	in 2020	U.S. Government [112]
Research standard benchmark	48.0	kWh/kg	in 2050	U.S. Government [112]

The discount rate is set at 4%, in accordance with the Dutch government rate for risk-free investments that positively impact an irreversible negative externality (i.e., through reduction of global carbon footprint) [111]. The project lifetime is assumed to be 25 years, with the electrolyzer exclusively utilizing PV solar power. The active operating hours of the electrolyzer over the course of its lifetime are constrained by the total number of solar hours available, estimated to be 37.5 thousand hours over 25 years, assuming 1500 hours of sun in The Netherlands annually. As a result of the lower required stack lifetime, the analysis assumes a higher tolerable rate of degradation for the stacks. This is because it is not necessary to use the stacks beyond the 25-year period. It should be noted that the frequent switching on and off of the system would be expected to increase the rate of degradation. Decay rates of 0.45% and 0.186% per year are assumed for the PV solar park and the electrolyzer, respectively, representing the annual decrease in delivered power or hydrogen [109, 110]. The benchmark estimate of LCOH for green hydrogen produced in The Netherlands from solar power ranges between € 5.14/kg and € 6.69/kg, based on European Union sources [109].

4.4.2. Electricity and Hydrogen Yield Results

Table 4.7: Electricity and hydrogen yield for the industrial and research benchmarks, compared to the yield obtained through the use of the MHP algorithm. Shown values for the MHP algorithm are summations of the maximum production figures from each month. In months with low irradiance, MHP algorithm yields without m-tracking was used. The absence of clipping losses and inverter power losses results in the MHP algorithm outperforming both electricity generated and hydrogen produced when compared to both benchmarks.

	Electricity Generated		**Hydrogen Produced**	
	MWh	*% w.r.t. Industry*	*tons*	*% w.r.t. Industry*
Industry Benchmark	1474.4	0.0 %	28.8	0.0 %
Research Benchmark	1522.8	+3.3 %	31.5	+9.3 %
MHP Algorithm	1584.4	+7.5 %	31.8	+10.4 %

The first results to be compared are shown in table 4.7 (monthly results tables can be found in appendix B, tables B.3 and B.4). Here, an overview is given of the electricity and hydrogen yield for the MHP algorithm (i.e., the directly-coupled HRES), the industry benchmark and the research benchmark. The absence of clipping losses and inverter power losses results in the MHP algorithm outperforming both electricity generated and hydrogen produced when compared to both benchmarks. Results indicate that the MHP algorithm slightly outperforms the research benchmark on hydrogen production. For the total electricity generated, the MHP algorithm outperforms the research benchmark by 4%. This can be attributed to the low specific cost of hydrogen production assumed for the research benchmark of 48 $\mathrm{kW\,h\,kg^{-1}}$. In comparison, the average specific cost of hydrogen production for the MHP algorithm for the full TMY was 49.9 $\mathrm{kW\,h\,kg^{-1}}$.

These results can be further confirmed when evaluating figures 4.18 and 4.19. These figures illustrate the yield of the new HRES as a fraction of the benchmark yields. Figure 4.18 shows that the directly-coupled HRES produces 2% more electricity in all months of the TMY, with the highest difference in yield amounting to 12% and 7% for the industrial and research benchmarks, respectively. On average, these yields are higher than the hydrogen yields, displayed in Figure 4.19. It can be seen that the research benchmark outperforms the hydrogen yield of the MHP algorithm in the months of January, August, October, November and December. This corresponds to the same months in which tracking performance was worse due to an artefact in the algorithm. The non-physical results which cause extended periods of zero values lower the overall produced hydrogen for months with low average irradiance.

In order to compare the yield of the system, the Capacity Factor (CF) of the system can be calculated. This non-dimensional metric is a measure of how much the nominal power of the PV solar park is actually utilized throughout the year. In mathematical form:

$$\mathrm{CF} = \frac{\sum \text{Annual Electricity Generated}}{P_{\mathrm{PV}} \cdot 8760} \tag{4.5}$$

Here, P_{PV} denotes the nominal power of the PV park, and it is multiplied by the number of hours in a year, 8760. With 1714.6 sun hours in The Netherlands (averaged from 1990 to 2020), the maximum

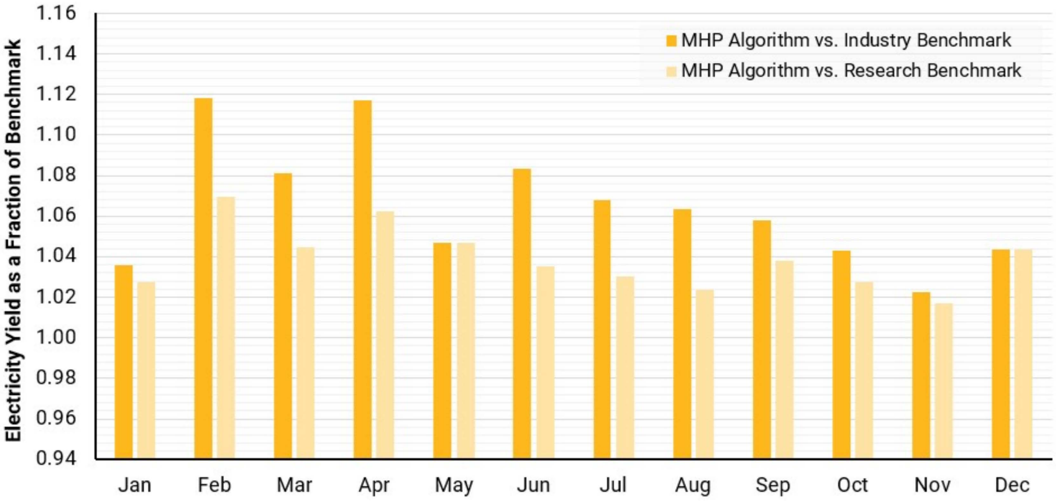

Figure 4.18: Electricity yield as a fraction of the two benchmark simulations. Without clipping losses due to inverter sizing, and without power losses as a result of the inverter, the algorithm beats both simulations for electricity yield, throughout the whole year.

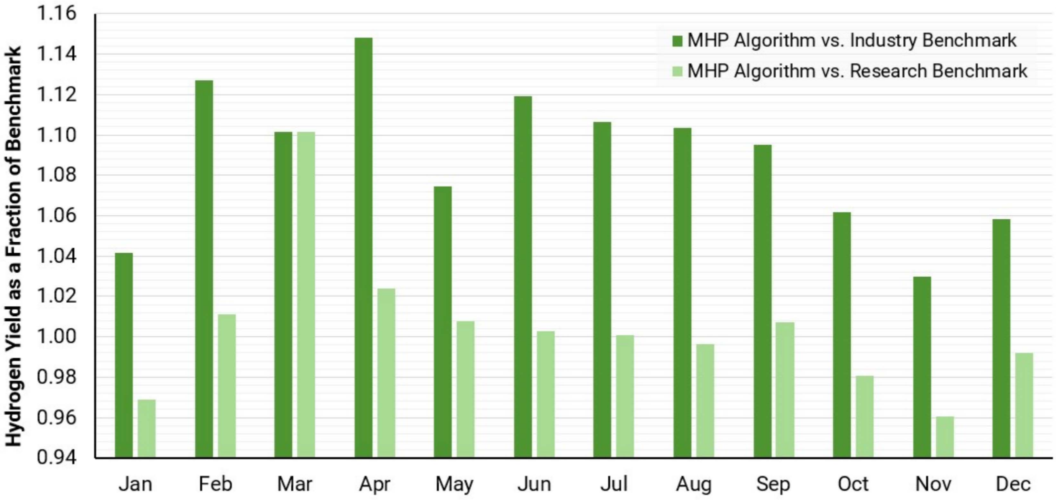

Figure 4.19: Hydrogen yield as a fraction of the two benchmark simulations. Results show that the industry benchmark is surpassed every month. The research benchmark is beaten in the spring and summer months but yields less hydrogen than the benchmark in the autumn and winter months. Low yield in the winter months and May can be attributed to poor algorithm performance during times of low irradiance.

attainable CF would equate to the PV park delivering full power during all of the sun hours. This would result in a maximum CF of 19.6%. For the HRES discussed in this paper, the CF is calculated to 0.156 for the MHP algorithm. For the industrial and research benchmarks, the capacity factors are 0.150 and 0.145, respectively. Shown in Figure 4.20 are the average PV solar CFs for the simulations of the HRES discussed in this paper, compared to regional European averages.

Results indicate that analogous to the yield results, the absence of inverter clipping and inverter power losses, the relatively higher yield in electricity results in a higher CF. Compared to regional averages, only Southern Europe exceeds the calculated CFs. It should be noted that other power losses to control electronics and operational maintenance are not taken into account here.

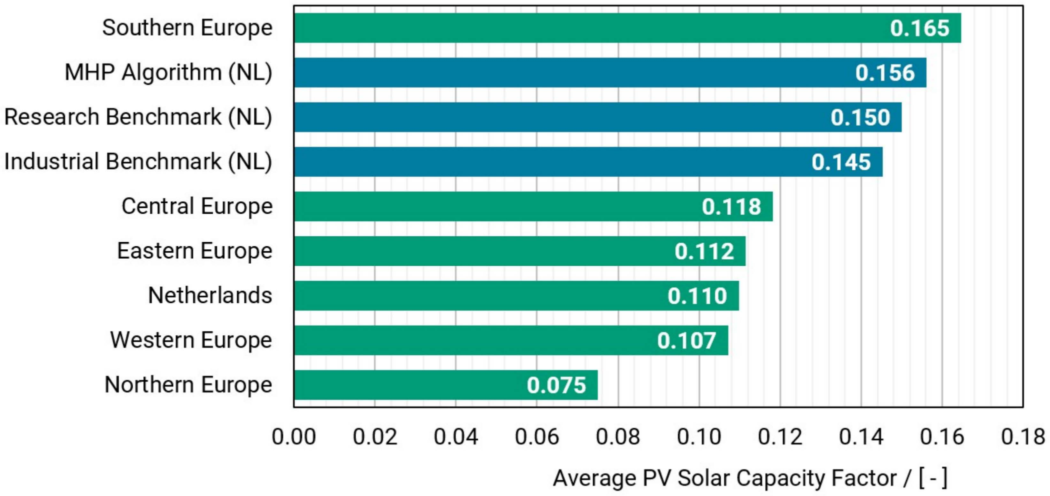

Figure 4.20: Average Capacity Factor (CF) for solar energy production for the HRES discussed in this paper, compared to various regions across Europe. Computed CF results (blue color) do not account for power lost to auxiliary systems (i.e., control electronics, and operational maintenance). Results show that the absence of power losses to clipping and inverters increase the average CF. Only Southern Europe has a higher CF, as that region has a much sunnier climate. Data source: EU FCHO [98].

4.4.3. LCOE and LCOH Results

In addition to the yield results, table 4.8 presents the resulting LCOE and LCOH figures as calculated using Equations 4.3 and 4.4. These metrics are calculated using the same TMY dataset as the rest of the research presented in this paper.

Table 4.8: Levelized Cost of Electricity (LCOE) and Hydrogen (LCOH) of the reference system (according to both industry and research standards) and of the newly proposed directly coupled system. The new system is shown with results corresponding to a static programming of m ($m = 0$), a dynamic programming of m (to increase hydrogen production) and the best combination of both. A higher electricity yield is coupled with a lower cost of hydrogen production to create the difference in LCOH between the industry benchmark and the MHP algorithm. All currency values shown are 2022 euros. The assumed discount rate was 4%, as per Dutch governmental guidelines.

	LCOE		**LCOH**	
	€/MWh	*% w.r.t. Industry*	*€/kg H_2*	*% w.r.t. Industry*
Industrial Benchmark	36.51	0.00 %	4.32	0.00 %
Research Benchmark	35.35	-3.18 %	3.95	-8.52 %
MHP Algorithm ($m = 0$)	30.69	-15.95 %	3.46	-19.85 %
MHP Algorithm ($m \neq 0$)	31.01	-15.08 %	3.48	-19.52 %
MHP Algorithm (max)	30.62	-16.15 %	3.44	-20.37 %

The removal of inverters and DC-DC converters have resulted in both a lower investment cost and a higher electricity yield. Both of these factors serve to decrease the LCOE, as it requires a lower investment cost to achieve a higher yield. For the LCOH, the industrial benchmark-specific cost of hydrogen production is 51.2 $\mathrm{kW\,h\,kg^{-1}}$, which is significantly higher than for this HRES (49.9 $\mathrm{kW\,h\,kg^{-1}}$) or for the research benchmark (48.0 $\mathrm{kW\,h\,kg^{-1}}$). As a result, a higher yield is coupled with a lower cost of hydrogen production to create the 20.4% difference in LCOH between the industry benchmark and the MHP algorithm.

5

Conclusion and Recommendations

5.1. Conclusion

The introduction stated that the rapid growth of renewable energy resources poses a monumental challenge to our energy infrastructure. Governments, industries, and consumers alike are being urged to electrify their energy supply, placing increased pressure on grid infrastructure.

Within renewable energy, PV solar technology is quickly emerging as the largest source of renewable electricity. To handle the intermittent and electrical nature of PV solar, hydrogen technology can play a significant role in buffering and alleviating pressure on congested electrical grids. While the green hydrogen market is in its early stages, the decreasing price of electrolyzers makes it increasingly more lucrative for renewable energy resources to be coupled with hydrogen assets for direct production.

To realize a green hydrogen solution that enables a competitive Levelized Cost of Hydrogen (LCOH), there is an ongoing pursuit to lower costs and integrate parts of the system to achieve synergies. Removing inverters and other power electronic components could lower the investment costs associated with a PV solar park. The use of a modular electrolyzer consisting of multiple stacks could allow for the stacks themselves to balance the intermittent loads common to PV solar parks. This would eliminate the need for DC-DC converters to regulate voltage and track the maximum power point of the PV system.

Based on these identified problems and areas of research, the main research question of this work, as stated in the introduction (see Chapter 1), was formulated as:

How can a PV solar park be integrated with a modular alkaline electrolyzer without grid-based buffering and through minimal use of power electronics?

To answer the main research question, three secondary questions were posed:

1. How should a directly coupled system of PV solar panels and a modular alkaline electrolyzer be sized with respect to one another to optimize hydrogen production?
2. To what extent is it possible to control a directly coupled system of PV solar panels and a modular alkaline electrolyzer?
3. How economically-viable is a hybrid renewable energy system consisting of PV solar panels and a modular alkaline electrolyzer?

In Chapter 2, the literature pertaining to PV solar systems, alkaline electrolyzers, and HRES combining these technologies was investigated. To obtain a refined understanding of the fundamental principles governing each constituent technology, a literature study provided an overview of all the research currently ongoing in the field of HRES. On-grid HRES are more investigated than off-grid HRES. On-grid systems often aim to utilize the grid connection for buffering and reduce peak net loads on the grid. The current hydrogen infrastructure has not yet been integrated with grid-connected HRES on a large scale. Off-grid systems are usually investigated with applications in rural and remote areas, resulting in rudimentary systems void of expensive new technologies like electrolyzers. Research regarding the direct coupling of a modular alkaline electrolyzer to PV solar assets has not been properly documented. Only a single paper has documented the beneficial effects of electrolyzer modularity on overall system efficiency, albeit with the use of DC-DC converters [96].

In Chapter 3, the methodology used to design, construct and control an HRES featuring a directly-coupled, megawatt-scale PV solar park and a modular alkaline electrolyzer was detailed. All constituent elements of the HRES are modelled, accounting for physical limits and constraints. The system elements were sized and configured to complement one another, ensuring that the resulting operating points allow for maximum hydrogen production. The control algorithm for the HRES was derived. A new algorithm was developed to maximize hydrogen production for directly-coupled HRES. The algorithm discretized the step sizing and implemented a variable step size which is applicable to any target slope. Using a dynamically-programmable target slope enabled the possibility for the algorithm to move its goal towards the point of maximum hydrogen production per unit of time instead of the point of maximum power. These points are not equivalent as the voltage of the maximum power point does not coincide with the voltage for maximum hydrogen production. Tracking biases were also added to adjust for possible overshoot errors as a result of the unique interaction between the electrolyzer stacks and the PV solar park.

Results were discussed in Chapter 4. An overview was made of the Typical Mean Year dataset on which the simulations are based, as well as the location of the simulation (Cabauw, The Netherlands). Three simulations were carried out. First, the number of stacks was increased, demonstrating that a higher discrete resolution (i.e., more individually controllable stacks) leads to a higher tracking efficiency. Second, the configuration of the PV panels (in series/parallel) was changed, showing that the sizing and configuration of the PV solar park are crucial to the system hydrogen yield. Third, a comparison was made between the algorithm with and without m-tracking. The addition of dynamic goal-seeking led to 0.8% higher hydrogen yield in the months without a low average irradiance (<250 $\mathrm{W\,m^{-2}}$). Months with a lower average irradiance experienced an artefact in the algorithm, resulting in prolonged periods of zero power output. M-tracking leads to a higher yield for higher irradiances as the ideal value of m (the target slope) for hydrogen production deviates further from zero. Experimental results showed that the low iteration frequency of this system with respect to conventional solar MPPT systems results in lower MPPT efficiencies. There were significant and unpredicted fluctuations in the current and voltage signals in the experimental setup due to the behaviour of the electrolyzer stacks and the relatively large time in between measurements. Lastly, an economic analysis yielded an LCOH of € 3.44 per kilogram of H_2, which is 20% and 13% lower than industrial and research benchmarks, respectively.

Each of the three secondary research questions is answered below, followed by an answer to the main research question.

How should a directly coupled system of PV solar panels and a modular alkaline electrolyzer be sized to optimize hydrogen production?

- An HRES featuring the direct coupling of PV solar to modular alkaline electrolysis should be sized through precise modelling and simulation of the system components, analyzing the hydrogen production for each point of operation. Where possible, polarization curves should be confirmed with experimental results before critical decisions regarding HRES size are made.
- The key parameters in the sizing process are the number of PV solar panels in series, the number of cells per electrolyzer stack, and the total number of stacks in the system.
- The electrolyzer stacks exhibit a more limited range of operating voltages compared to the PV solar panels. This demands close consideration and modelling of the relevant voltage and current limitations during the sizing process.

To what extent is it possible to control a directly coupled system of PV solar panels and a modular alkaline electrolyzer?

- Simulations show that it is possible to control a directly coupled system of PV solar panels and a modular alkaline electrolyzer. With an MPPT efficiency of 95.0%, the discrete and directly coupled system approaches the standard for conventional MPPTs (which use DC-DC converters).

- For a typical meteorological year in Cabauw (The Netherlands), both the electricity and hydrogen yield of the proposed system and corresponding algorithm are higher than industrial and research benchmarks (14.9% and 4.2% for hydrogen yield, respectively).
- Optimizing the algorithm for hydrogen production reduces the MPPT efficiency and the power generated, whilst increasing hydrogen production by 0.8% in months with a higher average irradiance.
- The operating ranges of the electrolyzer stacks allow for the stacks to absorb small changes in irradiance, while larger changes in irradiance are accommodated by changing the number of stacks turned on.
- The ability to control the system diminishes with a lower number of stacks to turn on/off as this reduces the number of operating points from which the algorithm can choose.
- Experimental results demonstrated that an HRES featuring a direct coupling between PV solar panels and a modular alkaline electrolyzer is possible. However, the iteration and measuring frequencies need to be significantly higher to reduce tracking errors by the algorithm.

How economically viable is an HRES consisting of PV solar panels and a modular alkaline electrolyzer?

- An HRES consisting of a 1.1 MW PV solar park and a 1.4 MW, 120-stack modular alkaline electrolyzer can realize an LCOH of € 3.44 per kilogram of H_2 when placed in The Netherlands (assuming a 25-year lifespan and a discount rate of 4%). Comparable analyses using both industrial and research figures are a benchmark and resulted in LCOH values of € 4.32 per kilogram of H_2(+25.6%) and € 3.95 per kilogram of H_2(+14.8%), respectively.
- The LCOH is expected to decrease even more relative to the benchmarks when evaluating the performance of the system in locations with higher irradiance. Locations like Southern Europe and Northern Africa are suitable locations for such a directly coupled system. Not only will m-tracking increase hydrogen production, but the increased sun hours will also lead to a higher yield and a lower LCOH as a result.
- The true economical viability will depend on the ability to effectively use all of the produced hydrogen. The range of applications for this system is also dependent on hydrogen post-processing and storage systems which aim to purify, compress and/or store the hydrogen product for use. If considered as its own full system, the HRES proposed in this paper is suitable for applications which do not mandate a consistent flow of hydrogen. Examples include the co-firing of hydrogen in ovens, or as a separate small-scale system to assist in the production of hydrogen feedstock.

To what extent can a PV solar park be integrated with a modular alkaline electrolyzer without grid-based buffering and through minimal use of power electronics?

- An HRES featuring PV solar and modular alkaline electrolysis is technologically viable without the use of grid-based buffering and with minimal use of power electronics.
- The proposed HRES requires careful modelling and design of the PV solar park configuration and the number of electrolyzer stacks in the modular system. Without power electronics to adjust for load imbalances, more than 60 electrolyzer stacks are required to provide sufficient resolution for the control algorithm.
- The removal of power electronics results in a 20.4% and 12.9% decrease in LCOH compared to industrial and research benchmarks, respectively. Therefore, it is economically competitive to directly couple PV solar assets to modular alkaline electrolyzers.
- In order to deliver a consistent flow of hydrogen, the proposed HRES will still be dependent on storage facilities for buffering mechanisms. These storage facilities can be in either electrical form, hydrogen form, or a combination of both. However, the storage facilities can be implemented without the use of local energy grids.

5.2. Recommendations

There are several recommendations that can be made for future work. These are listed below:

- Concerning the HRES discussed in this research, further research can be carried out into improving the MHP algorithm performance in periods of extended low irradiance. The effectiveness of the algorithm in a full-scale system is yet to be tested and improved upon.
- Looking beyond the HRES in this paper, the HRES configuration can be augmented to include wind energy, either on its own or in combination with PV solar. Investigating the implementation of wind energy into the HRES discussed in this paper would be an interesting and relevant area of research.
- Investigations can be made into improving the consistency of hydrogen production for directly-coupled HRES. Energy storage technologies, both in batteries and in hydrogen, can aid in providing a consistent hydrogen supply by collecting surplus electricity/hydrogen for release during periods of lower irradiance. This would increase commercial viability as many industrial applications demand a reliable and controllable flow of hydrogen. The directly-coupled nature of these HRES allows for multiple types and sizes of storage technologies.
- For the modular electrolyzer itself, further research could be conducted into the effect of switching frequency on the durability of the electrolyzer stacks. Other forms of electrolysis like PEM and Solid-oxide electrolysis may perform differently in such a directly-coupled system.
- The scalability of the proposed HRES can be investigated as well. Increasing or decreasing the size of individual electrolyzer stacks may influence the agility, efficiency, and yield of the system as a whole. Similarly, it can be investigated whether the proposed HRES also works effectively at larger system sizes (10-100 MW scale).
- Regarding the algorithm, an interesting future area of research would see Artificial Intelligence (AI) methods of maximum power point tracking being integrated into the algorithm detailed in this work. For larger PV solar parks, where partial shading may be more relevant to economic viability, AI algorithms may be a solution.

A
Draft Journal Article

A.1. Abstract

Renewable energy resources like wind and solar have the potential to revolutionize our energy infrastructure and enable a decarbonized society. The intermittent nature of renewables poses a challenge for ensuring a consistent and reliable electricity supply. Hydrogen technology is emerging as a promising solution for stabilizing renewable energy systems. There is still significant technological development required to cost-effectively integrate hydrogen with renewable energy assets. Conventional PV solar installations require power electronics for their operation, like charge controllers and inverters. Not only are these power electronic components costly and in high demand, but they also degrade faster than PV solar panels. Removing power electronic components could significantly lower the investment costs associated with a PV solar park.

This work focuses on how PV solar panels can be directly coupled to a modular alkaline electrolyzer, without grid-based buffering or the use of an inverter. Literature research revealed that hydrogen technology has seen little exploration in on-grid Hybrid Renewable Energy Systems (HRES) and no exploration in off-grid HRES. To appropriately investigate whether a directly-coupled HRES would be technically feasible, a megawatt-scale system was modelled and simulated. All elements of the HRES were modelled, duly accounting for physical limits and constraints. Components were sized and configured to complement one another, optimizing for maximum hydrogen production. To experimentally verify the validity of the proposed HRES, a 5 kW pilot system was constructed. To control the HRES, a new algorithm was developed using the Incremental Conductance maximum power point tracking algorithm as a basis. Within the new Maximum Hydrogen Production (MHP) algorithm, the step sizing was discretized and a variable step size was implemented which can be applied to any target slope. This allows for the system to target operational points which optimize hydrogen yield instead of electricity yield. Furthermore, the addition of tracking bias helped adjust for the asymmetric nature of the interaction between electrolyzer stacks and the PV solar park.

Simulation results in The Netherlands demonstrated that the feasibility of the HRES is dependent on the configuration of the PV solar park and on the number of electrolyzer stacks in the system. Compared to industrial and research benchmarks, the proposed HRES increased hydrogen production by 14.9% and 4.2%, respectively. Dynamic 'm-tracking' of the MHP algorithm goal increased hydrogen production by 0.8% in months of high irradiance. Months with a lower average irradiance experienced an artefact in the MHP algorithm, resulting in prolonged periods of zero power output. An experimental setup confirmed the simulation results, showing that it is possible to control a system of PV solar panels directly coupled to a modular alkaline electrolyzer. Experimental results revealed the need for moving average filtering to prevent fluctuations due to changing conditions of the electrolyzer and the weather from causing poor algorithm tracking ability. The low performance of the experimental setup can be attributed to a low iteration and measuring frequency, which increase the likelihood of a tracking error due to rapidly changing operating conditions. Economic analysis of the proposed HRES yielded an LCOH of €3.44, 20% and 13% lower than industrial and research benchmarks, respectively. Therefore, an HRES featuring PV solar and modular alkaline electrolysis is technologically and economically viable without the use of charge controllers and inverters.

A.2. Introduction

Renewable energy sources such as wind and solar hold the key to revolutionizing our energy infrastructure and achieving a decarbonized society [15]. However, the intermittent nature of renewables poses a challenge to ensuring a consistent and reliable electricity supply. Enter hydrogen technology, a versatile energy carrier with minimal greenhouse gas emissions, with applications across multiple sectors within the industry. With substantial EU investments in hydrogen infrastructure, it is emerging as a promising solution for stabilizing renewable energy systems. However, there is still significant technological development required to cost-effectively integrate hydrogen with renewable energy assets.

The integration of renewable energy sources into local energy infrastructure has led to a paradigm shift, decentralizing the generation process. Wind turbines and solar panels are now strategically placed in locations with optimal weather conditions, moving away from large, centralized facilities [17]. Consequently, there is an increasing need for residential and commercial clients to balance their own renewable energy systems. This is driven by both the desire for energy independence and by the strain on grid infrastructure. However, limited technologies exist to empower these clients to effectively decentralize their energy supply.

Conventional PV solar installations require power electronics for their operation (i.e., DC-DC charge controllers and DC-AC inverters). Not only do these power electronics demand 10% of the initial capital investment, but they also tend to degrade faster than other PV solar panels [3]. Bypassing most of the power electronic systems can increase overall energy yield and reduce costs throughout the system's lifespan.

This research was conducted in close collaboration with XINTC, a Dutch Original Equipment Manufacturer (OEM) that designs, produces, assembles and markets smart Alkaline Water Electrolyzers (AWEs). With product capacities ranging from 150 kW to 50 MW, XINTC is able to develop standardized modular products whilst delivering client-specific solutions.

A.3. Methodology

A.3.1. System Modelling

The modelling of the system can be divided into the two constituents that make up the system: The PV solar array and the modular alkaline electrolyzer. In order to accurately model system behaviour, a bottom-up approach is used to model the components.

XINTC Modular Alkaline Electrolyzer

The XINTC containerized modular alkaline electrolyzer is made up of 120 stacks, which can be independently turned on and off. These stacks are subdivided into 8 sections, with each section having its own flash tanks and electrolyte pump. In addition to the number of stacks, the physical stack dimensions, the degradation rate and the operating pressure/temperature of the stacks are all constrained and assumed as constant.

The voltage is constrained on the lower end by the laws of thermodynamics. As mentioned in Chapter 2 (Section 2.2.1, figure 2.9), the lower limit of voltage can be taken in the neighbourhood of the thermoneutral voltage of 1.48 V. The upper voltage limit is set to 572 V, as an absolute boundary to prevent cell damage.

For the cell current, there is no lower limit as an idle cell will have a current of zero. The upper limit is defined by the rate of bubble formation on the electrode surface and mass diffusion limitations. The soft limit for current is set to 27 A. with 'soft' indicating that the limit can be exceeded, but only for a short duration so as to not wear out the cell and drive down system efficiency.

One critical assumption about the electrolyzer is that there is zero bypass current. Bypass current is a current leak, which can take place at both system- and stack-level. At both levels, current can be conducted through the electrolyte or the frame from one pole to another. In a single stack, bypass current can result in less current passing through the electrodes, leading to a lower hydrogen production rate for the same power input. Due to a lack of empirically-defined loss parameters, losses due to bypass currents are not taken into account.

Another limitation to the modelling of the electrolyzer is that the modelled characteristics are not temperature-dependent. The temperature of the electrolyte is assumed to be constant during both start-up and regular operation. In practice, electrolyte temperature will vary between the ambient temperature and the operational temperature of the electrolyzer. However, the XINTC electrolyzer operates at relatively low temperatures, meaning that errors as a result of assuming a constant temperature are negligible on a large timescale.

An overview of the system is shown in figure A.3. Each stack in the system is connected in parallel. As a result, the system voltage is equivalent to the single-stack voltage.

$$V_{\text{EL, model}} = V_{\text{section}} = V_{\text{stack}} \tag{A.1}$$

The current flowing through the system does not stay constant with the number of stacks. Due to the series configuration of the cells in the stack, the single-cell current is equivalent to the stack current. However, the parallel configuration of stacks in the system sees the total electrolyzer current as a product of the number of active stacks in the system and the single-stack current. There is no need to differentiate between active and inactive stacks as inactive stacks experience no current flow.

$$I_{\text{EL, model}} = I_{\text{stack}} \cdot n_{\text{stacks, active}} = I_{\text{cell}} \cdot n_{\text{stacks, active}} \tag{A.2}$$

With existing relationships for current and voltage, the power delivered by the electrolyzer at any moment can be expressed as the product of the voltage and current experienced by the electrolyzer:

$$P_{\text{EL}} = V_{\text{EL}} \cdot I_{\text{EL}} \tag{A.3}$$

The rate of production of hydrogen ($\dot{n}_{\text{H2, molar}}$) can be expressed as a function of the number of active stacks ($n_{\text{active stacks}}$), the Faradaic efficiency (ϵ_{F}), the single-stack current (I_{stack}), and the Faraday constant. The molar production rate of hydrogen is directly proportional to the current flowing through any given cell. The mass flow rate of hydrogen, is expressed in $\text{kg}\,\text{h}^{-1}$. For this conversion, the molar mass of hydrogen is required. It is assumed that the purity of hydrogen is sufficiently high that the molar mass of other byproducts is negligible.

$$\dot{n}_{\text{H2, molar}} = n_{\text{active stacks}} \cdot n_{\text{cells}} \cdot \epsilon_{\text{F}} \cdot \frac{I_{\text{stack}}}{2F} \tag{A.4}$$

$$\dot{m}_{\text{H2}} = \dot{n}_{\text{H2, molar}} \cdot M_{\text{H2}} \tag{A.5}$$

The Faradaic efficiency is a function of the current flowing through the cell. A model for the Faradaic efficiency was developed by A. Rahbari at XINTC based on various sources from literature [47, 99, 100, 101].

The specific production cost of hydrogen (ψ_{H2}) is defined as the electrical power required per kilogram of produced hydrogen (units $\text{kW}\,\text{h}\,\text{kg}^{-1}$). This is expressed as the ratio of the electrolyzer power to the mass flow rate of hydrogen as a result of that same electrolyzer power.

$$\psi_{\text{H2}} = \frac{P_{\text{EL}}}{\dot{m}_{\text{H2}}} \tag{A.6}$$

There is a single optimal point of hydrogen generation regardless of the number of active stacks. At a voltage of 348.5 V, there is a minimum specific cost of hydrogen production of 47.5 $\text{kW}\,\text{h}\,\text{kg}^{-1}$. Whilst the hydrogen production at this voltage may not be maximum, it will lead to the lowest average cost. Alternatively, for higher electrolyzer voltages, the increasing resistances in the electrodes and the electrolyte will result in higher specific costs of production.

PV Solar Array

For the modelling of an array of PV solar panels, several assumptions are made to construct an efficient yet accurate model. Firstly, concerning the modelling of the cell temperature, solar panel heat loss through forced convection as a result of wind is not included. This is due to a lack of wind speed data that matches the measurements for incident irradiance and ambient cell temperature. Solar parks are often located in areas with high solar exposure, which is often negatively correlated with average wind speed.

Another assumption essential to the modelling of the PV solar array is that there is no partial shading. The P-V curve for a PV system under partial shading conditions varies significantly from that same system under non-partial shading conditions. Given that partial shading only occurs when two different areas of the same solar array experience different incident irradiances, the total time in which partial shading is applicable is assumed as negligible.

Concerning the PV solar panel itself, each panel is assumed equal in rated performance, internal circuitry and in orientation. In an array, the panels are mounted next to each other, horizontally on the ground and oriented facing True North. Furthermore, for an array of panels connected in series, the voltage is equal to the single panel voltage multiplied by the number of panels in series and the current is the same through each panel. Consequently, for an array of panels connected in parallel, the voltage is the same and equal across each panel and the current is equal to the current of a single panel multiplied by the number of panels placed in parallel.

The irradiance data used for the modelling is assumed to be the sum of the direct and diffuse radiation. PV Solar panels are solid-state semiconductor machines. As such, the performance of the cells that constitute a panel is dependent on its surroundings. Semiconducting materials like silicon have temperature-dependent properties, requiring an accurate model of cell temperature for useful simulations. Shown in figure A.4 is a diagram of the heat balance which can be made over the surface of a PV panel. Incident irradiation (G)

hits the panel surface and is both reflected and absorbed. The absorbed fraction of the irradiation is calculated using the solar radiation absorption coefficient (α). The absorbed irradiance is further split up into radiation which can be usefully transferred to electrical energy and the remaining energy which must be dissipated as heat. The useful electrical energy is obtained through the PV module efficiency (η_{mod}), which is provided by the PV panel manufacturer and ranges between 15-25% [102]. This absorbed energy results in the gradual heating of the PV panel, raising its temperature (T_{cell}) above that of the environment (T_{amb}). As a result of this temperature difference, heat is lost to the environment through convection (with heat transfer coefficient h_c). The true thermal energy that is absorbed can be written as:

$$\dot{Q}_{\text{absorbed}} = \alpha(1 - \eta_{\text{mod}}) \cdot G \tag{A.7}$$

When divided by the area to express the thermal energy per unit area, this can be set equivalent to the heat lost to the environment. The heat loss can be written as:

$$\dot{q}_{\text{absorbed}} = h_c(T_{\text{cell}} - T_{\text{amb}}) \tag{A.8}$$

Setting both equations equivalent to one another, and solving for the cell temperature, the following result is obtained:

$$T_{\text{cell}} = T_{\text{amb}} + \frac{\alpha(1 - \eta_{\text{mod}}) \cdot G}{h_c} \tag{A.9}$$

Radiation heat losses are negligible due to the low emissive properties of PV solar panel materials. This relationship was experimentally proved to be accurate to ± 2 °C by D. Faiman in 2008 [103]. The Python PVlib library has incorporated this model into one of its functions, allowing for an accurate and computationally efficient method of modelling the cell temperature for a PV solar cell.

The irradiance incident on PV solar panels is highly dependent on the location of the panel, as well as its mounting angle and orientation. Modelling the characteristic curve of a PV cell from its irradiance is achieved through the use of the Single-Diode Model (SDM). The Single Diode model aims to solve the following equation:

$$I = I_L - I_0 \left(\exp \frac{V + IR_s}{n \cdot N_{\text{series}} \cdot V_{\text{thermal}}} - 1 \right) - \frac{V + IR_s}{R_{\text{shunt}}} \tag{A.10}$$

$$V_{\text{thermal}} = \frac{k \cdot T_{\text{cell}}}{q} \tag{A.11}$$

Here, I_L and I_0 are the light-generated current and the diode saturation current under desired IV curve conditions, respectively. R_s and R_{shunt} are the series resistance and shunt resistance, respectively. The usual diode ideal factor (n), the number of cells in series (N_{series}), and the cell thermal voltage (V_{thermal}) under the desired I-V curve conditions make up the remaining variables. The thermal voltage can be further expressed in terms of the Boltzmann constant (k), cell temperature (T_{cell}) and elementary charge of an electron (q).

The SDM equation must be solved iteratively. In 2004, A. Jain et al. proved that it was possible to solve for an exact closed-form solution of the SDM equation using the Lambert W-function [104]. Other methods of iterative solving like the Newton-Raphson root-finding method or the Brent bisection search method can also be used to solve the SDM equation, albeit not as an exact solution.

The aforementioned variables that are required for the SDM cannot be found in the datasheet of a PV panel. Manufacturer datasheets only contain information about the performance at the MPP. For the SDM equation, more information is required to calculate the input parameters. As a result, W. De Soto et al. created the Five Parameter model in 2006. This model estimates the required variables for the SDM using datasheet-provided parameters and semi-empirical equations [54]. For this paper, the PV panel used for modelling and simulation is a DMEGC Solar panel, with product number DM410M10-54HSW/-V, originally manufactured on 04-10-2021. PV panel datasheet data can be combined with a dataset containing the incident irradiance and corresponding cell temperature to generate the I-V and P-V curves of the PV panel at every time step.

A.3.2. System Design

Contrary to HRES found in literature, which featured a DC-DC converter between the PV array and the load resistance, a directly coupled system requires more design considerations to ensure proper working. Shown in figure A.5 is a diagram of the proposed HRES, featuring a direct coupling between the PV array and the modular alkaline electrolyzer. Diodes are required in between to ensure there is no backward flow of current and to ensure current is not discharged from the electrolyzers.

The timescale of the transient interaction between a PV panel and an electrolyzer is on the order of microseconds. The system is expected to reach a steady state within seconds after establishing an electrical connection. The point of operation reached in a steady state can be defined as any of the finite points of operation between the PV array and the electrolyzer. For any number of stacks ranging from 1 to the maximum number of stacks in the system (120 for this application), there will be an equivalent load resistance which is experienced by the PV array. In practice, as the electrochemical reaction within the electrolyzer matures, the true electrical resistance may vary depending on gas bubble formation on the electrodes and the changing temperature of the electrolyte.

It can be stated that there is a single point of operation for a given PV array and number of active stacks in the system, for a given irradiance and ambient air temperature. If this point of operation is found for every possible irradiance curve and cross-referenced with every single configuration of active stacks, a graph can be made which displays all of the possible points of operation in the HRES. Figure A.6 shows the hydrogen production vs. voltage graph of an HRES consisting of a PV array and a modular alkaline electrolyzer.

On the lower side of the voltage range, the stacks in the electrolyzer are voltage limited. Similarly, operating points at higher voltages than 405 V are also not preferred as these would lead to exceeding the 27 A soft-limit for current. Theoretically, there are 120 unique operating points for a given irradiance. However, due to voltage and current limitations, the true number of operating points is lower, decreasing with increasing irradiance.

The unique shape of the electrolyzer curves also provides a varying spacing between any two operating points. For lower irradiances, spacing between operating points (especially for a low number of active stacks) is larger than at higher irradiances or for a larger number of stacks. When evaluating the MPP of the system for a given irradiance, the nearest operating point to the true MPP serves as the operational point of maximum power delivery.

Whilst the MPP is the main control objective for ordinary PV solar parks, HRES with electrolyzers aim to maximize hydrogen production, not electrical power. This distinct difference with respect to previous work requires a new design methodology.

A.3.3. System Control

This section presents the control algorithm used to connect a PV solar array to a modular alkaline electrolyzer without the use of a DC-DC converter. The primary objective of this control algorithm is to maximize the hydrogen produced for the given weather conditions. The control algorithm must also ensure that renewable energy resources are efficiently utilized to generate hydrogen at both extremely high production values and extremely low production values.

The Incremental Conductance Algorithm

The control algorithm for a system of PV solar panels and a modular alkaline electrolyzer starts from an existing control algorithm for PV solar panel maximum power point tracking. Conventional PV solar parks vary the duty cycle of DC-DC converters to change the voltage of the PV solar system and stay at the MPP. Perturb & Observe MPPTs are a subset of algorithms which are widely researched, low in mathematical complexity, and widely used in PV solar tracking. Shown in figure A.10 is the algorithm flowchart for a standard Incremental Conductance MPPT.

In order for any P&O algorithm to work for a renewable energy system featuring a modular alkaline electrolyzer, several changes need to be made. First, the duty cycle must be replaced by the number of active stacks in the electrolyzer. Second, the INC algorithm method needs to be modified to allow the algorithm to approach other points aside from the MPP. Third, variable step sizing is introduced. Last, a dynamically programmable tracking bias is introduced in addition to a method of optimizing stack selection to minimize degradation.

Changing Duty Cycle for Stack Number

The duty cycle in a DC-DC converter results in a Pulse-Width Modulation (PWM) signal, where the key parameter (D) indicates the percentage of time that the signal is in the ”on” state. Depending on whether the DC-DC converter aims to step-up or step-down the voltage, increasing the duty cycle can increase or decrease the voltage, respectively. As per figure A.10, it is indicated that increasing the duty cycle by ΔD will lead to an increase in voltage, and vice versa.

For the HRES discussed in this research, there is no duty cycle or PWM signal that can be altered between 0-100%. Instead, the number of stacks connected to the PV solar park (S) can be changed between 1 stack and the maximum stack number (assumed to be 120). In order to translate the duty cycle changes (ΔD) into changes of the number of stacks (ΔS), the behaviour of a system of electrolyzer stacks must be considered. Under the same load, an increase in the number of stacks connected to the system (in parallel) will lead to a decrease in the voltage per stack. This is directly opposite to the aforementioned behaviour of voltage for a change in duty cycle. As a result, to increase the operating voltage of the PV solar array, the number of stacks should be altered to $S_n = S_{n-1} - \Delta S$. Similarly, a desired decrease in PV solar array operating voltage can be achieved by altering the number of stacks to $S_n = S_{n-1} + \Delta S$.

Adding Variable Tracking Point

Instead of setting the gradient of power with respect to voltage to zero, it is set equivalent to a constant m.

$$\frac{\mathrm{d}P}{\mathrm{d}V} = m \tag{A.12}$$

Substituting power with the product of current and voltage, and using the chain rule:

$$\begin{aligned}\frac{\mathrm{d}P}{\mathrm{d}V} &= \frac{\mathrm{d}(V \cdot I)}{\mathrm{d}V} && \text{(A.13a)}\\ &= I \cdot \frac{\mathrm{d}V}{\mathrm{d}V} + V \cdot \frac{\mathrm{d}I}{\mathrm{d}V} && \text{(A.13b)}\\ &= I + V \cdot \frac{\mathrm{d}I}{\mathrm{d}V} && \text{(A.13c)}\\ &= m && \text{(A.13d)}\end{aligned}$$

For the INC method (and any variations thereof) to be applicable in a real-life setting, it must be discretised. This is done using n as the current time step and $n-1$ as the previous time step:

$$\begin{aligned}\Delta I &= I_n - I_{n-1} && \text{(A.14a)}\\ \Delta V &= V_n - V_{n-1} && \text{(A.14b)}\end{aligned}$$

Substituting in the discretizations:

$$\begin{aligned}I + V \cdot \frac{\mathrm{d}I}{\mathrm{d}V} &= m && \text{(A.15a)}\\ I + V \cdot \frac{\Delta I}{\Delta V} &= m && \text{(A.15b)}\end{aligned}$$

If $m = 0$, the algorithm defaults back to the original version of the Incremental Conductance algorithm, as it aims to find the point where the slope is zero (i.e., the MPP). However, if $m > 0$, then the algorithm attempts to find a slope greater than zero. Assuming no partial shading conditions, the P-V curve of the PV solar array only has a positive slope to the left of the MPP. Similarly, when $m < 0$, the algorithm goal is to find a slope less than zero, occurring only to the right of the MPP.

Variable Step Sizing

Varying the step size depending on the deviation from the MPP results in a superior tracking ability, especially for rapidly changing irradiance. Shown below are two variable step size relationships which have been proven effective in conventional solar MPPTs:

$$\text{step}_1 = \left|\frac{\mathrm{d}P}{\mathrm{d}V}\right| \tag{A.16}$$

$$\text{step}_2 = \left|\frac{\mathrm{d}P}{\mathrm{d}V - \mathrm{d}I}\right| \tag{A.17}$$

In order to apply the variable step size relationships discussed in this paper to the HRES, a non-dimensionalization process must be performed first. In order to do so, a reference state (V_{ref}, I_{ref}) is defined which is applicable for all of the PV solar array operating conditions. To ensure that the reference state is known for all PV solar panels and all HRES configurations, the reference state was chosen to be the MPP as defined on the PV panel datasheet. This MPP is established under standard testing conditions (1000 $\mathrm{W\,m^{-2}}$ and 25 °C), and operational MPPs will be of the same order of magnitude. Non-dimensionalizing the variable step-size relationships using the reference state:

$$P_{\text{ref}} = V_{\text{ref}} \cdot I_{\text{ref}} \tag{A.18}$$

$$\text{step}_1 = \left|\frac{\mathrm{d}P/P_{\text{ref}}}{\mathrm{d}V/V_{\text{ref}}}\right| \tag{A.19}$$

$$\text{step}_2 = \left|\frac{\mathrm{d}P/P_{\text{ref}}}{\mathrm{d}V/V_{\text{ref}} - \mathrm{d}I/I_{\text{ref}}}\right| \tag{A.20}$$

The point of maximum hydrogen production does not coincide with the point of maximum power. Similarly, the point where the production of hydrogen costs the least amount of energy also does not coincide with the MPP. Therefore, as derived in the previous section, it may be advantageous to vary the target slope of the P-V curve for the HRES. In order to do so, the variable step size needs to be adjusted to include a varying value of the target slope (m). Intuitively, the new variable step size relationship must be such that at a value of $m = 0$, the step size reverts back to equations A.19 and A.20. To realize this, the variable step size can be amended with an extra term which would be equal to zero at $m = 0$. Let $\text{step}_{1,\text{m}}$ and $\text{step}_{2,\text{m}}$ be the additional terms which are added to the existing non-dimensional variable step size relationships such that:

$$\text{step}'_1 = \text{step}_1 + \text{step}_{1,\text{m}} \tag{A.21}$$

$$\text{step}_2' = \text{step}_2 + \text{step}_{2,\text{m}} \tag{A.22}$$

Following a derivation, the step size gives the final form of the adjusted step size using method 1:

$$\text{step}_1' = F_1 \cdot \left(\left| \frac{\mathrm{d}P/P_{\text{ref}}}{\mathrm{d}V/V_{\text{ref}}} \right| - \frac{m}{I_{\text{ref}}} \right) \tag{A.23}$$

To plot the above-derived variable step size, it is helpful first to consider the different values that m can realistically assume. Shown in figure A.7 is the P-V curve for a single PV solar panel for an irradiance of 750 $\mathrm{W\,m^{-2}}$ and a cell temperature of 25 °C. Shown in figure A.8 is the result of the variable step size for varying values of m.

The step size function performs well for values of $m < 0$, as there is a large step far away from the target point which decreases exponentially as the target draws closer. For $m \geq 0$, however, there is little increase in step size for deviations to the left of the target point.

For method 2, another derivation is made, starting with the less strict (non-absolute) dimensional form of the conventional step size. The resulting equation for the extra term step_2' is given below. Analogous to method 1, a correction factor (F_2) is introduced to proportionally scale the variable step size.

$$\text{step}_2' = \tag{A.24}$$
$$F_2 \cdot \left(\left| \frac{\mathrm{d}P/P_{\text{ref}}}{\mathrm{d}V/V_{\text{ref}} - \mathrm{d}I/I_{\text{ref}}} \right| + \frac{m}{I_{\text{ref}} + V_{\text{ref}} \cdot \left(\frac{I-m}{V}\right)} \right)$$

The resulting graph of step sizes for varying values of m is shown in figure A.9.

In contrast to method 1, the step sizes for method 2 are worse in shape and performance for $m < 0$, and better for $m \geq 0$. For values of $m > 11$, the relative change in slope is too minute to produce any variable step size relationship which can evenly ramp up the step size on both sides of the target point. However, in practice, it is not expected that the target point will be set so far away from the MPP. The design of the HRES can be made such that optimal operation is far away from values of $m > 10$.

Given the two methods of variable step sizing, a final adjusted step size relationship can be made by combining the two methods. Method 1 can be used for values of $m < 0$ and method 2 for values of $m \geq 0$. This gives the following final equation:

$$\text{step}' = \begin{cases} 35 \cdot \left(\left| \frac{\mathrm{d}P/P_{\text{ref}}}{\mathrm{d}V/V_{\text{ref}} - \mathrm{d}I/I_{\text{ref}}} \right| + \frac{m}{I_{\text{ref}} + V_{\text{ref}} \cdot \left(\frac{I-m}{V}\right)} \right) \\ \qquad \forall\, m \geq 0 \\ 5 \cdot \left(\left| \frac{\mathrm{d}P/P_{\text{ref}}}{\mathrm{d}V/V_{\text{ref}}} \right| - \frac{m}{I_{\text{ref}}} \right) \forall\, m < 0 \end{cases} \tag{A.25}$$

Stack Selection Algorithm

Besides determining the required number of active stacks in each iteration for the PV solar array, the specific selection of stacks to turn on/off holds significant importance. Thoughtful stack selection can lead to reduced maintenance costs, enhanced system responsiveness to power input fluctuations, and improved overall energy efficiency.

As defined earlier, the S^n is defined as the number of stacks turned on in each iteration. For each stack, let s_{i}^n be the status of stack i. When the stack is turned on, the status registers $s_{\text{i}}^n = 1$. If turned off, the stack status registers a zero.

$$s_{\text{i}}^n = \begin{cases} 1 & \text{if stack } i \text{ is turned on} \\ 0 & \text{if stack } i \text{ is turned off} \end{cases} \tag{A.26}$$

Relating the individual stack status to the total number of active stacks:

$$S^n = \sum_{i=1}^{n_{\text{active stacks}}} s_{\text{i}}^n \tag{A.27}$$

In order to keep track of electrolyzer stack lifetime and degradation, another parameter is necessary to track single stack lifetime ($t_{\text{life},i}^n$). This can be defined as the single stack lifetime in the previous iteration plus the stack status in the current iteration:

$$t_{\text{life},i}^n = t_{\text{life},i}^{n-1} + s_i^{n-1} \tag{A.28}$$

In order to select an S^n number of stacks to turn on/off in each iteration, a criteria-based ranking system can be constructed. Each stack is evaluated based on a predefined list of criteria. The S^n stacks with the highest rank are chosen to be turned on/off in each iteration. Stack selection is achieved using a weighted criteria mechanism. Three main criteria are evaluated for every single stack. These criteria evaluate the lifetime of the stack, the temperature of the stack, and whether the stack is turned on in the previous iteration. The higher the value of a criterion, the more preferable that stack is for an active role in the next iteration. Each criterion is non-dimensionalized. It can reach a minimum value of zero and a maximum value of one.

$$\text{criteria}_{1,i}^{n} = 1 - \frac{t_{\text{life},i}^{n}}{\max\left(t_{\text{life}}^{n}\right)} \tag{A.29}$$

$$\text{criteria}_{2,i}^{n} = s_{i}^{n} \tag{A.30}$$

$$\text{criteria}_{3,i}^{n} = \begin{cases} \max\left(0, 2\left(\frac{T_i^n - (T_{\text{opt}} - 15)}{T_{\text{opt}} - 15}\right)\right) \\ \qquad \forall\, T \leq T_{\text{opt}} \\ \\ \max\left(0, 5 - 5\left(\frac{T_i^n - (T_{\text{opt}} - 20)}{T_{\text{opt}} - 20}\right)\right) \\ \qquad \forall\, T > T_{\text{opt}} \end{cases} \tag{A.31}$$

$$\sum_{i=1}^{3} \alpha_i = \alpha_1 + \alpha_2 + \alpha_3 \tag{A.32a}$$

$$= 1 \tag{A.32b}$$

$$\text{score}_{i}^{n} = \alpha_1 \cdot \text{criteria}_{1,i}^{n} + \tag{A.33a}$$

$$\alpha_2 \cdot \text{criteria}_{2,i}^{n} + \alpha_3 \cdot \text{criteria}_{3,i}^{n} \tag{A.33b}$$

Final Modified INC Algorithm

Incorporating all of the aforementioned modifications to the INC algorithm, a new flowchart can be made to represent the newly generated Maximum Hydrogen Production (MHP) algorithm. Shown in figure A.11 is a flowchart representing the MHP algorithm.

There are several key differences with respect to the original INC algorithm. Firstly, the acceptable values for ΔV and ΔI have been set to ranges ΔV_{min} and ΔI_{min}, respectively. Due to the high standard of computational resolution achieved by control electronics, there exists a near-zero change of the changes in voltage or current ever being exactly zero. Such events are only seen in simulations, which are void of static noise and current leaks.

The second main difference is the addition of the variable m, the slope of the P-V curve. This variable represents the target slope that the algorithm uses as its goal. If set to zero, the algorithm (and corresponding step sizes) revert back to the original INC algorithm goal.

The next modification covers the removal of the equality:

$$\frac{\Delta I}{\Delta V} = \frac{m - I}{V} \tag{A.34}$$

The reasoning for this is that, in order to practically implement such a logic rule, a range of acceptable values is required. However, it is not possible to define a range of values for a relationship that compares the fraction of two differences with a fraction of absolute variables. The above-stated equation only has an effect when it is exactly equal, which is not practically feasible. As a result, it was removed from the algorithm, and replaced by more lenient definitions of ΔV_{min} and ΔI_{min} to ensure that the algorithm does not change its operating point when sufficiently close to its goal.

The last two additions to the algorithm were the modification of step sizes and the addition of bias through multiplication with constants. Both of these additions require the introduction of four new constants: F_1, F_2, F_3, and F_4. All in all, these modifications aid in designing an algorithm which maximizes the hydrogen production of a given HRES.

A.4. Results

The evaluation of the MHP algorithm performance utilizes a dataset obtained from the Baseline Surface Radiation Network (BSRN) [105]. This network acquires radiation data from various stations worldwide through the World Radiation Monitoring Center (WRMC). The data collection frequency of the BSRN is set at 1-minute intervals, rendering it suitable for testing the MHP algorithm. Within the WRMC, The Netherlands has a weather station in Cabauw, operated by the KNMI. To determine the appropriate date selection of the dataset for evaluation, the Typical Meteorological Year (TMY) methodology is employed. A TMY dataset consists of meteorological data values throughout the years, specifically tailored to a specific geographical location. Data from 2005 to 2023 was used in the selection of the TMY. From this data, for each month of the year, data was chosen that accurately represents the meteorological conditions of that particular time of year.

A.4.1. Simulation Results

The simulation aimed to investigate the effect on electricity and hydrogen yields if the algorithm can dynamically adapt its objective based on input conditions. To enable this dynamic adjustment of the algorithm goal, a function can be established to determine the optimal value of m ($m_{\text{max H2}}$) that maximizes hydrogen production. This function is derived from the relationship between hydrogen production, voltage, and a range of irradiances. By identifying the operating point that corresponds to the maximum hydrogen production on this plot, the same operating point can be projected onto a P-V curve. The slope of this operating point, associated with the highest hydrogen production ($m_{\text{max H2, true}}$), can then be documented and fitted using a linear relationship.

In the absence of a sensor for the true irradiance incident on the PV solar arrays, an irradiance estimator function can be made based on empirical measurements. There exists a high correlation between the output power of the PV solar park and the irradiance. Utilizing this correlation, the power of the PV solar park can be divided by the reference power (i.e., the maximum power point under standard test conditions). Subsequently, a linear function can be fit to provide an estimator function for the irradiance.

$$G_{\text{est.}} = 10.586 + 0.368 \cdot \frac{n_{\text{panels}} \cdot P}{P_{\text{ref}}} \tag{A.35}$$

$$m_{\text{max H2, calc.}} = 0.0019 \cdot G_{\text{est.}} - 0.0177 \tag{A.36}$$

Back-testing the estimator function against real irradiance data reveals a median absolute error of 5.3%, which was within the acceptable range for use in the simulation. The irradiance is used to calculate the target for the algorithm.

These functions, referred to as 'm-tracking,' empower the algorithm to dynamically select the target slope, m. The simulation modelled the entire dataset, representing a complete TMY. Two distinct cases were compared: the first case involved the algorithm consistently tracking the point where $m = 0$. The second case employed m-tracking, allowing the algorithm to dynamically target a different point that maximizes hydrogen production.

In order to validate the accuracy of the irradiance estimator function, a third case was executed where the true irradiance served as input for the m-tracking function. Results indicated that the discrepancy between the estimated irradiance (G) and the true value of G was minimal, confirming the accuracy of the estimator function. A summary of the simulation results for the aforementioned cases is presented in Table A.1.

The analysis of the full-year simulation results reveals that the m-tracking function implemented in the algorithm yields lower power and a reduced hydrogen output. Moreover, the m-tracking functions exhibit a 52% increase in the number of switches per stack per hour, which can impact the lifespan of the electrolyzer stacks.

Comparing the performance of the m-tracking function using the irradiance estimator function to that using the true irradiance, no significant difference is observed, except for the number of instances where voltage and current limits were exceeded.

To determine whether the m-tracking functions universally result in lower yields compared to the scenario without any m-tracking, a closer investigation of the monthly yields is warranted. When looking at the monthly yields, the months of January, May, October, November, and December exhibit lower yields compared to the simulation without m-tracking. In these specific months, the average irradiance amounts to 188 $\mathrm{W\,m^{-2}}$.

To provide a comprehensive overview of the simulation results, Table A.2 presents the outcomes for all months, excluding the aforementioned months characterized by their low average irradiance. This table offers a more representative evaluation of the performance of the m-tracking function in months when solar power is more abundant.

In the months characterized by a higher average irradiance, the total power delivered by the system with m-tracking functions is comparable to that of the scenario without m-tracking. However, there is an increase in hydrogen yield, which is 0.81% higher than the case without m-tracking. Additionally, the percentage of instances where the soft current limit is exceeded exhibits a decrease.

Similar to the findings for the entire TMY, the switching frequency per stack per hour remains significantly higher when employing the m-tracking functions compared to the scenario without m-tracking.

This algorithm artefact only occurs during periods of extremely low irradiance, and there is no physically correct explanation for the initial jump to zero voltage/current. In a practical system, whilst there are still periods of extremely low irradiance, sensor noise and varying resistances will always result in minute changes in voltage and/or current. As a result, it is not expected that such an error occurs in a practical setting. Even if it were to occur, it would be of shorter duration as minor changes in voltage and current can prompt the algorithm to change its number of active stacks and pull itself out of the loop.

A.4.2. Economic Results

This section focuses on the economic analysis conducted as part of the results presented in this chapter. By studying the economic dimensions of the thesis research, the aim is to highlight the implications and broader significance of the HRES and corresponding control systems proposed in this paper.

Renewable energies can be compared to one another by evaluating the Levelized Cost of Electricity (LCOE). In addition to the LCOE, the Levelized Cost of Hydrogen (LCOH) calculates the end-to-end cost of production per kilogram of hydrogen over the lifespan of a hydrogen-producing system. These terms can be expressed as follows:

$$\text{LCOE} = \frac{\text{CAPEX} + t_{\text{life}} \cdot \text{OPEX}}{\sum \text{Electricity Produced over Lifetime}} \tag{A.37}$$

$$\text{LCOH} = \frac{\text{CAPEX} + t_{\text{life}} \cdot \text{OPEX}}{\sum \text{Hydrogen Produced over Lifetime}} \tag{A.38}$$

The European Union Fuel Cell and Hydrogen Observatory have developed economic models which calculate the LCOH for different regions in Europe, using different renewable energies and inputs.

The HRES used for this analysis is the directly coupled system discussed in this paper. The system features a 120-stack modular alkaline electrolyzer coupled directly to a 2860-panel PV park (13 panels in series, 220 in parallel). The rated power of the PV park is taken to be the product of the number of panels and the reference maximum power of each panel as mentioned in the datasheet. In order to compare the results, a benchmark system is designed. The benchmark system features two sub-systems, which are connected to one another via the national electricity grid. The nominal power and size of the individual sub-systems are the same as the proposed directly-coupled HRES.

Due to the decentralized and direct nature of the proposed HRES, there is no need for costs associated with inverters, grid connection, and power electronics. As a result, these costs are excluded from the CAPEX for the directly-coupled HRES. It is assumed that the operational expenses remain equal between both systems. Regular operation and maintenance are still necessary, and the materials are the same resulting in a similar rate of degradation and maintenance.

The discount rate is set at 4%, in accordance with the Dutch government rate for risk-free investments that positively impact an irreversible negative externality (i.e., through reduction of global carbon footprint) [111]. The project lifetime is assumed to be 25 years, with the electrolyzer exclusively utilizing PV solar power. The active operating hours of the electrolyzer over the course of its lifetime are constrained by the total number of solar hours available, estimated to be 37.5 thousand hours over 25 years, assuming 1500 hours of sun in The Netherlands annually. As a result of the lower required stack lifetime, the analysis assumes a higher tolerable rate of degradation for the stacks. This is because it is not necessary to use the stacks beyond the 25-year period. It should be noted that the frequent switching on and off of the system would be expected to increase the rate of degradation. Decay rates of 0.45% and 0.186% per year are assumed for the PV solar park and the electrolyzer, respectively, representing the annual decrease in delivered power or hydrogen [109, 110]. The benchmark estimate of LCOH for green hydrogen produced in The Netherlands from solar power ranges between € 5.14/kg and € 6.69/kg, based on European Union sources [109].

The first results to be compared are shown in table A.3. Here, an overview is given of the electricity and hydrogen yield for the MHP algorithm (i.e., the directly-coupled HRES), the industry benchmark and the research benchmark. The absence of clipping losses and inverter power losses results in the MHP algorithm outperforming both electricity generated and hydrogen produced when compared to both benchmarks. Results indicate that the MHP algorithm slightly outperforms the research benchmark on hydrogen production. For the total electricity generated, the MHP algorithm outperforms the research benchmark by 4%. This can be attributed to the low specific cost of hydrogen production assumed for the research benchmark of 48 kW h kg^{-1}. In comparison, the average specific cost of hydrogen production for the MHP algorithm for the entire TMY was 49.9 kW h kg^{-1}.

In addition to the yield results, table A.4 presents the resulting LCOE and LCOH figures as calculated using the method detailed earlier in this section. The presented results indicate a substantial reduction in both LCOE and LCOH. Compared to the industrial standard, the LCOE and LCOH are 16% and 20% lower, respectively. This can be attributed to several factors. First, inverter clipping results in less power delivery in times of high irradiance. While the inverter sizing ratio is 10% higher for the research benchmark, it still causes a noticeable discrepancy. Second, the 8% assumed power losses incurred by the inverter also claim a portion of the energy that could otherwise be used to generate hydrogen.

A.5. Conclusion

To what extent can a PV solar park be integrated with a modular alkaline electrolyzer without grid-based buffering and through minimal use of power electronics?

- An HRES featuring PV solar and modular alkaline electrolysis is technologically viable without the use of grid-based buffering and with minimal use of power electronics.
- The proposed HRES required careful modelling and design of the PV solar park configuration and the number of electrolyzer stacks in the modular system. Without power electronics to adjust for load imbalances, more than 60 electrolyzer stacks are required to provide sufficient resolution for the control algorithm.
- The removal of power electronics results in a 20.4% and 12.9% decrease in LCOH compared to industrial and research benchmarks, respectively. Therefore, it is economically competitive to directly couple PV solar assets to modular alkaline electrolyzers.
- The proposed HRES will still be dependent on storage facilities for buffering mechanisms. These storage facilities can be in either electrical form, hydrogen form, or a combination of both. However, the storage facilities can be implemented without the use of local energy grids.

A.6. Images

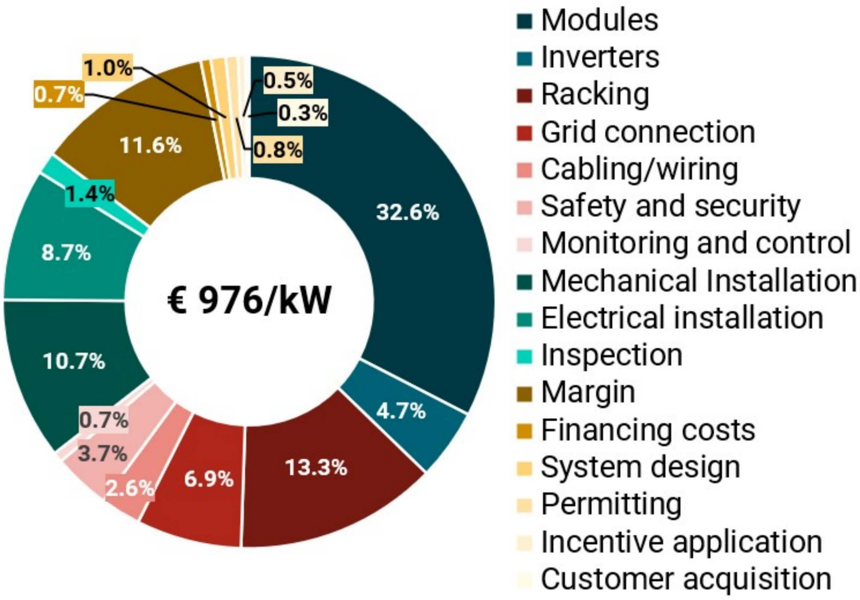

Figure A.1: Capital expenditure breakdown of a PV solar park. Shown expenditure covers all of the capital expenditure needed to build and install a utility-scale PV solar park. Currency values exchanged to be expressed in 2022 Euro. Data source: Fraunhofer Institute for Solar Energy Systems [97]

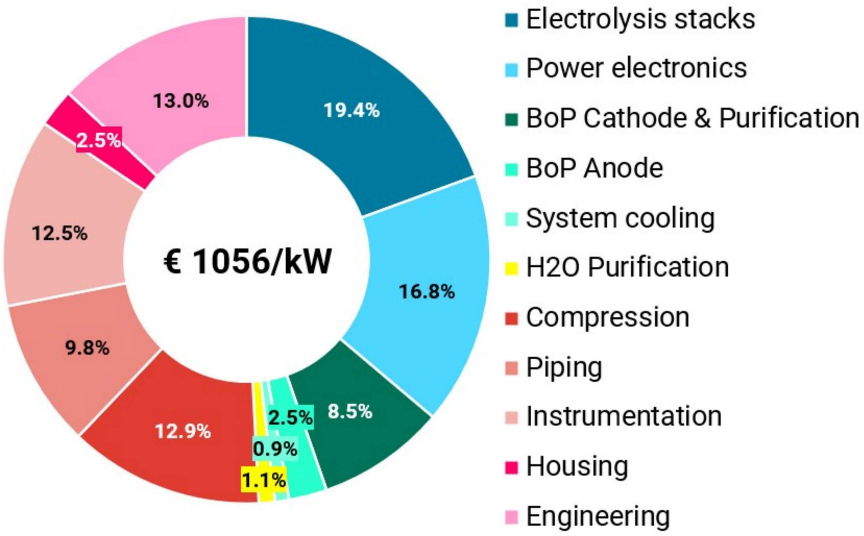

Figure A.2: Capital expenditure breakdown of an alkaline electrolyzer. Shown expenditure covers all of the capital expenditure needed to build and install a utility-scale liquid alkaline electrolyzer. Currency values exchanged to be expressed in 2022 Euro. Data source: International Renewable Energy Agency [10]

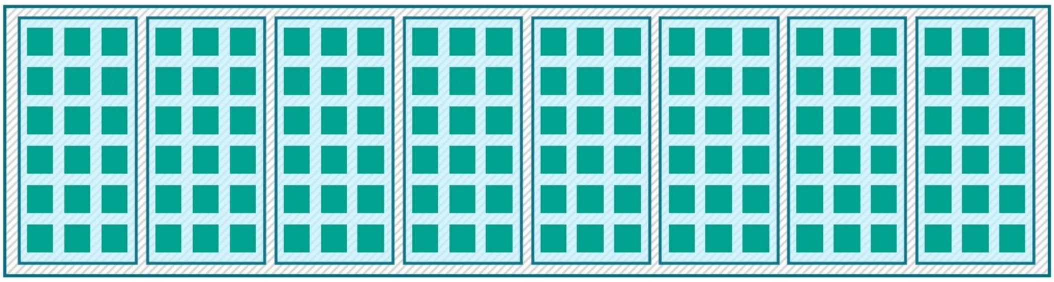

Figure A.3: Diagram of the full modular alkaline electrolysis system. The full system consists of 120 stacks divided over 8 sections. Each section contains 15 stacks and its own pump and gas separator system. The final contained measures 40 feet long (12.03 m in length, 2.4 m in width and 2.39 m in height).

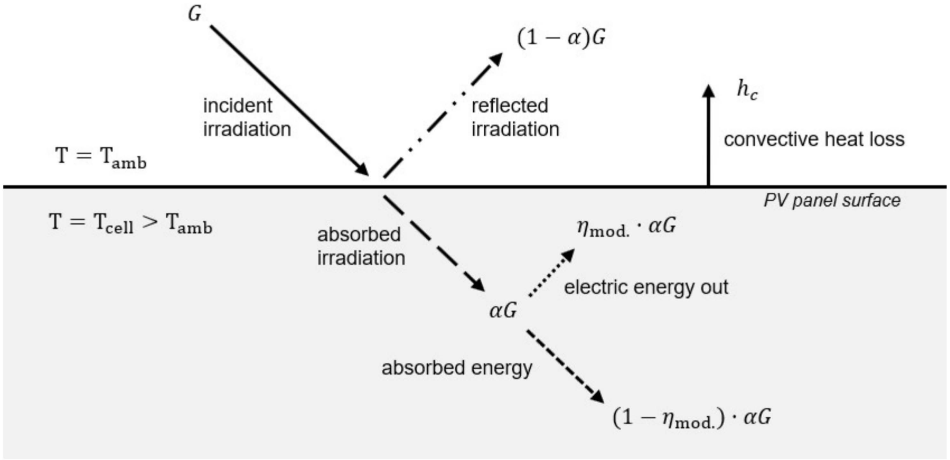

Figure A.4: Energy balance diagram of a PV solar panel. The cell temperature is defined as the ambient temperature plus the ratio of the absorbed radiation to the heat loss transfer coefficient. Shown variables are incident irradiation (G), solar radiation absorption coefficient (α), PV module efficiency (η_{mod}), cell temperature (T_{cell}), ambient temperature (T_{amb}), and heat transfer coefficient (h_c). Radiative and conductive heat losses are assumed to be negligible. Forced convective heat losses due to wind are ignored due to a lack of data.

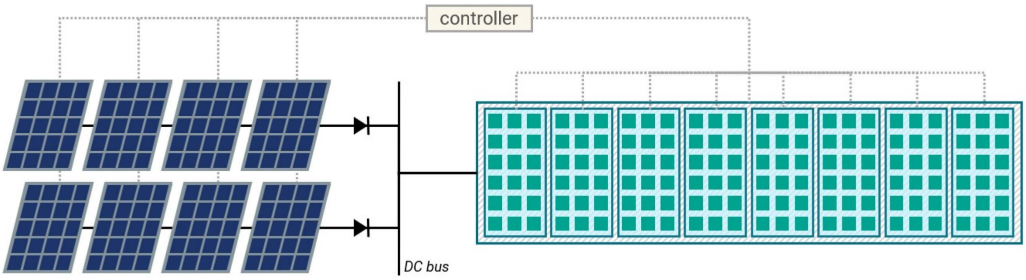

Figure A.5: Schematic diagram of an HRES consisting of a PV solar array and a modular alkaline electrolyzer. The PV solar array is directly coupled to the electrolyzer, separated only by a selection of diodes to prevent a backward flow of current. A controller is implemented to gauge the ideal voltage for the PV panels, and subsequently turns on/off enough stacks to generate a resistance which results in the desired bus bar voltage.

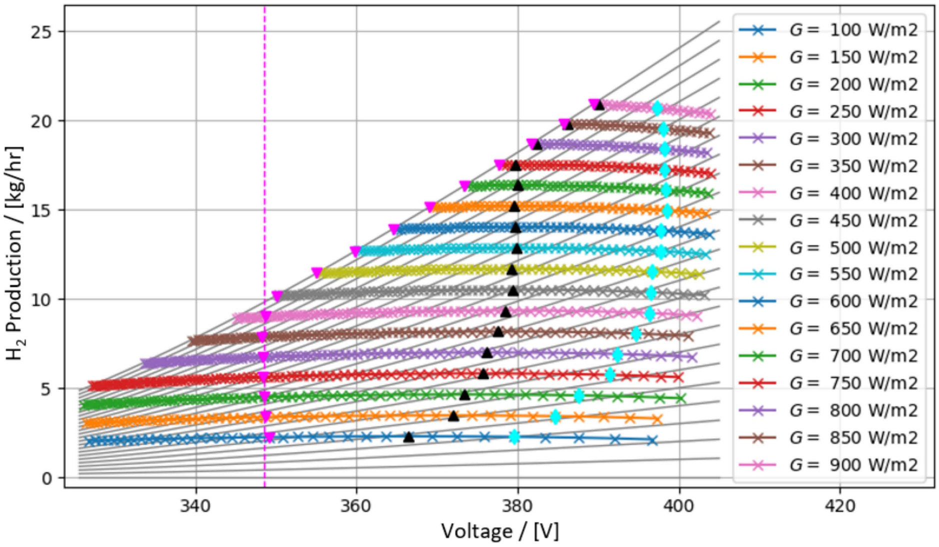

Figure A.6: Hydrogen production - Voltage graph of a directly coupled HRES containing a PV solar park and an alkaline electrolyzer. The grey lines indicate electrolyzer power curves, increasing in steps of 5 stacks (up to 120). Cyan points indicate MPPs, and magenta points indicate the points of lowest cost of hydrogen production. Black points indicate the points of highest hydrogen production. (Data source: BSRN [105])

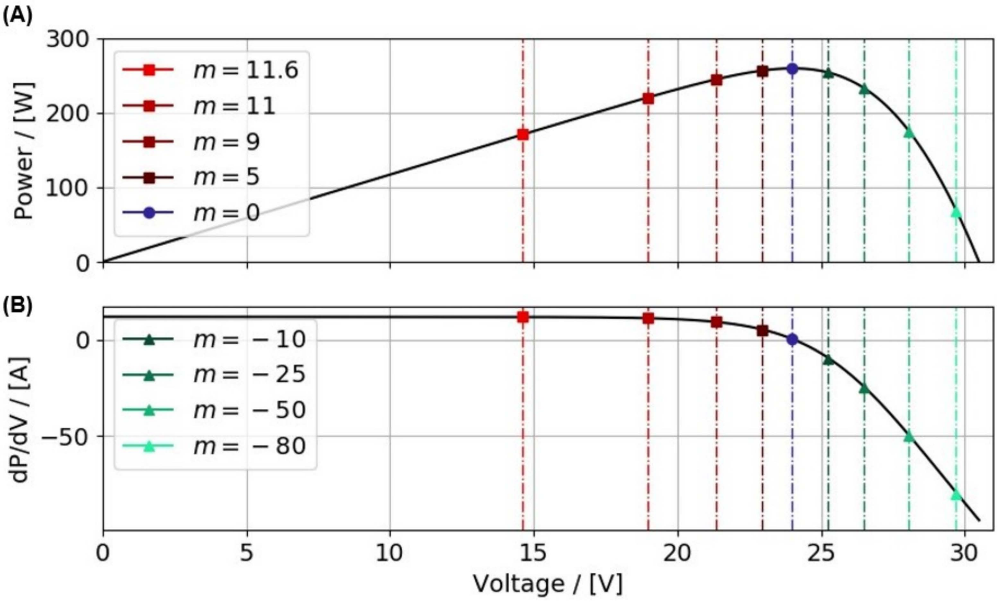

Figure A.7: Various values of the slope (m) for a P-V curve of a single PV solar panel at an irradiance of 750 $\mathrm{W\,m^{-2}}$ **and a cell temperature of 25** $^{\circ}$C. Positive values of m only reach until $m \approx 11.72$, whereas negative values of m reach as far as $m \approx -93.40$. Curve generated using the Python PVlib library.

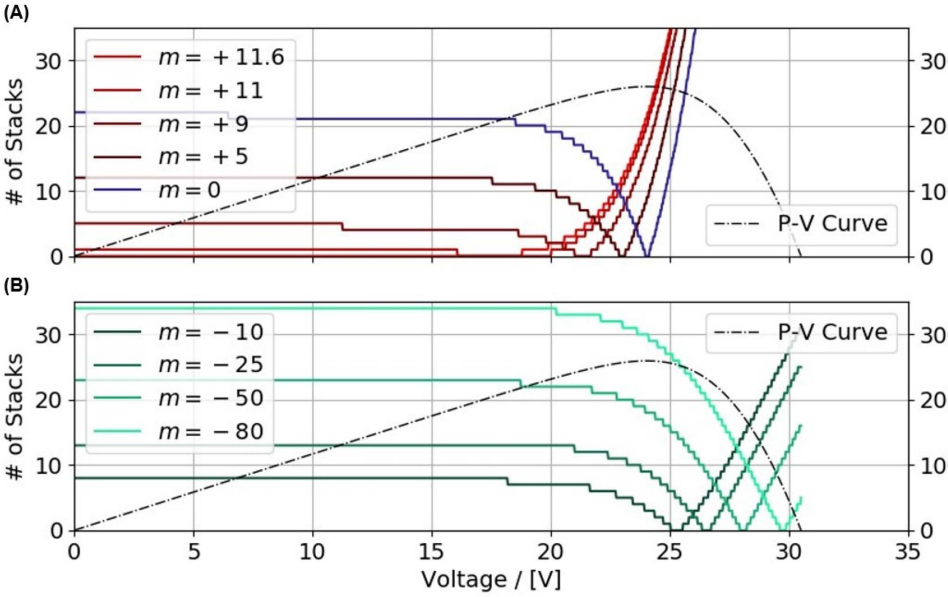

Figure A.8: Variable step size for varying values of m, using the adjusted step size method 1. Variable step size curves discretized to signify individual stacks based on a maximum stack number of 120. The variable step size curve for varying values of m intersects the voltage axis precisely at the voltage at which the slope of the P-V curve is equal to m. P-V curve generated using the Python PVlib library.

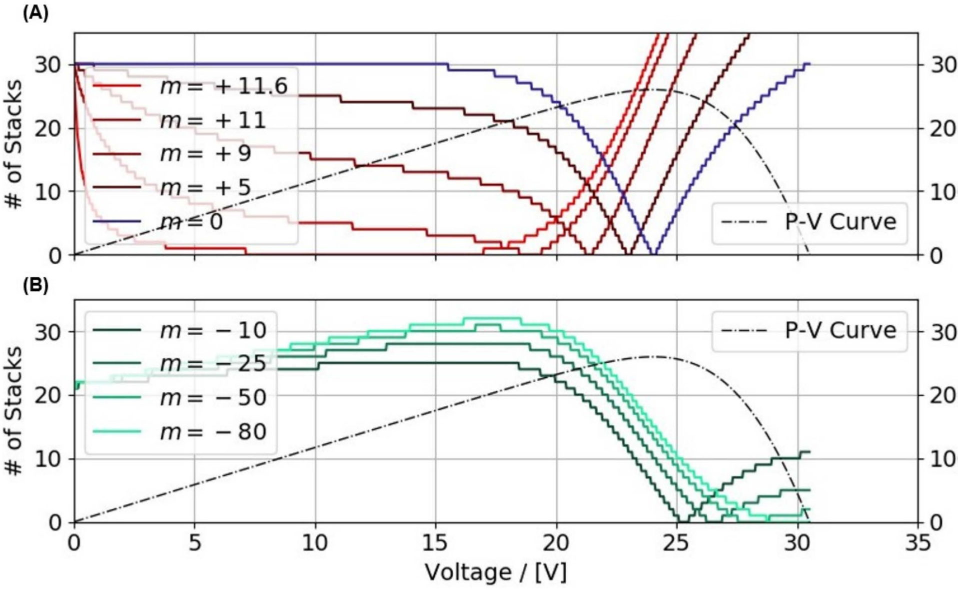

Figure A.9: Variable step size for varying values of m, using the adjusted step size method 2. Variable step size curves discretized to signify individual stacks based on a maximum stack number of 120. The variable step size curve for varying values of m intersects the voltage axis precisely at the voltage at which the slope of the P-V curve is equal to m. P-V curve generated using the Python PVlib library.

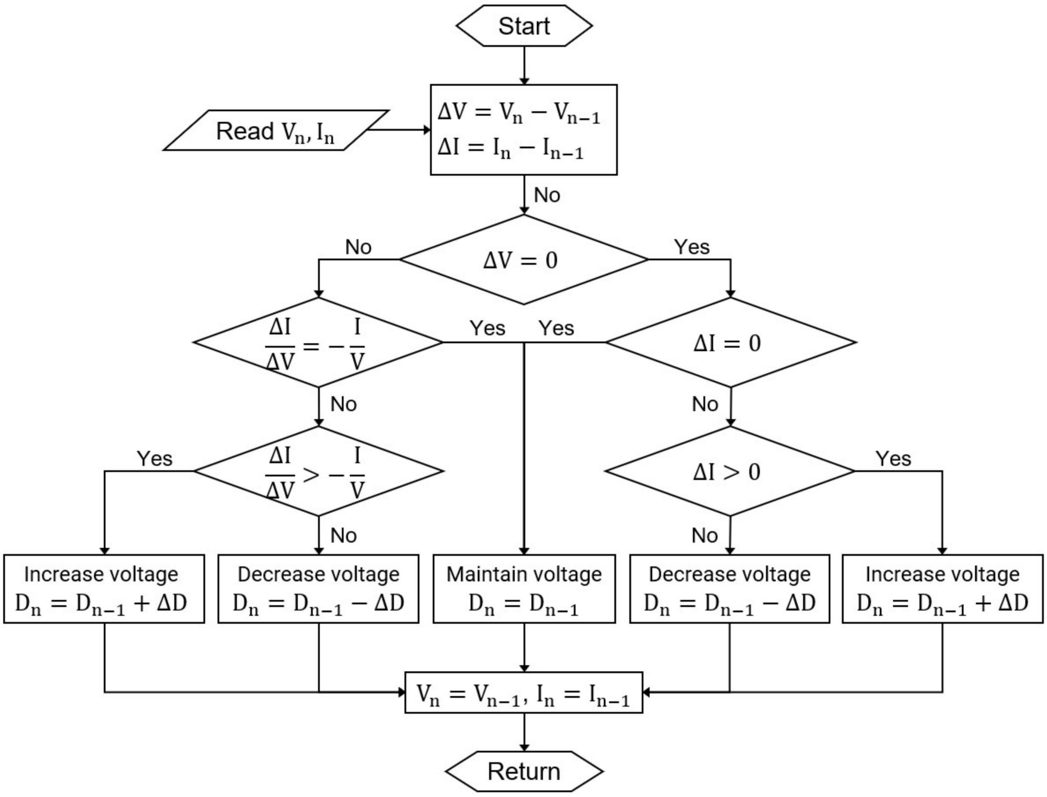

Figure A.10: Standard Incremental Conductance MPPT Flowchart. This algorithm uses the voltage and current of the system as inputs, and the duty cycle ($0 < D \leq 100\%$) of the DC-DC converter as an output. Increasing the duty cycle results in a proportional increase in operating voltage, and vice versa. If the differences in voltage and current are sufficiently small, the algorithm decides not to make any choice, as the current operating point is sufficient.

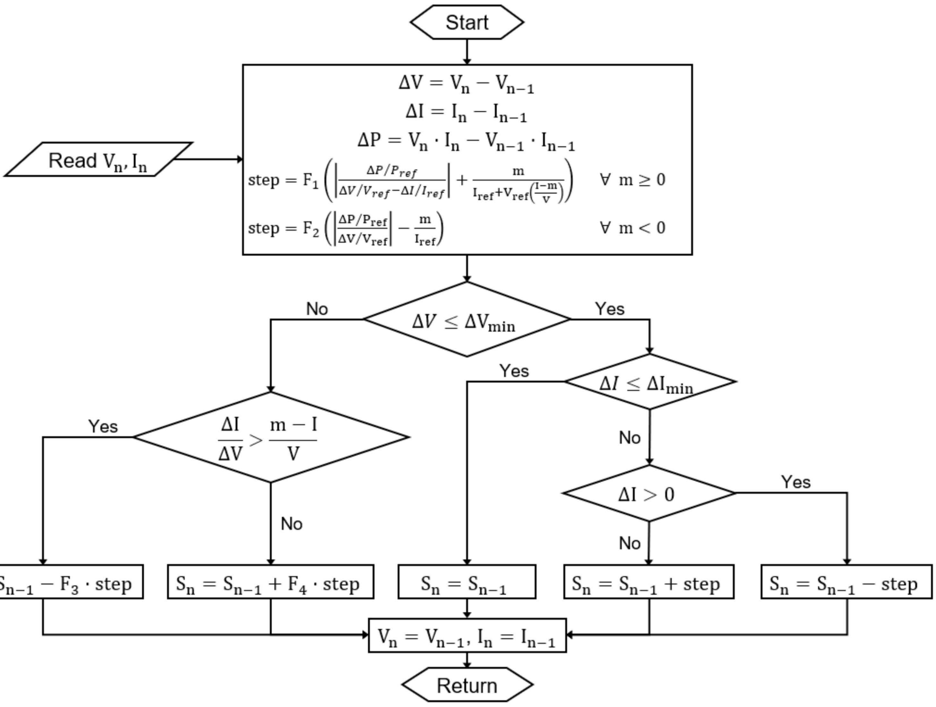

Figure A.11: Final MHP Algorithm Flowchart. This algorithm uses the voltage, current, and power of the system as inputs. The step size of the algorithm is not constant. The output of the algorithm is the number of electrolyzer stacks which need to be turned on ($0 < S \leq n_{\text{stacks}}$). Variables F_1, F_2, F_3, and F_4 are constants and may be calibrated unique to each system.

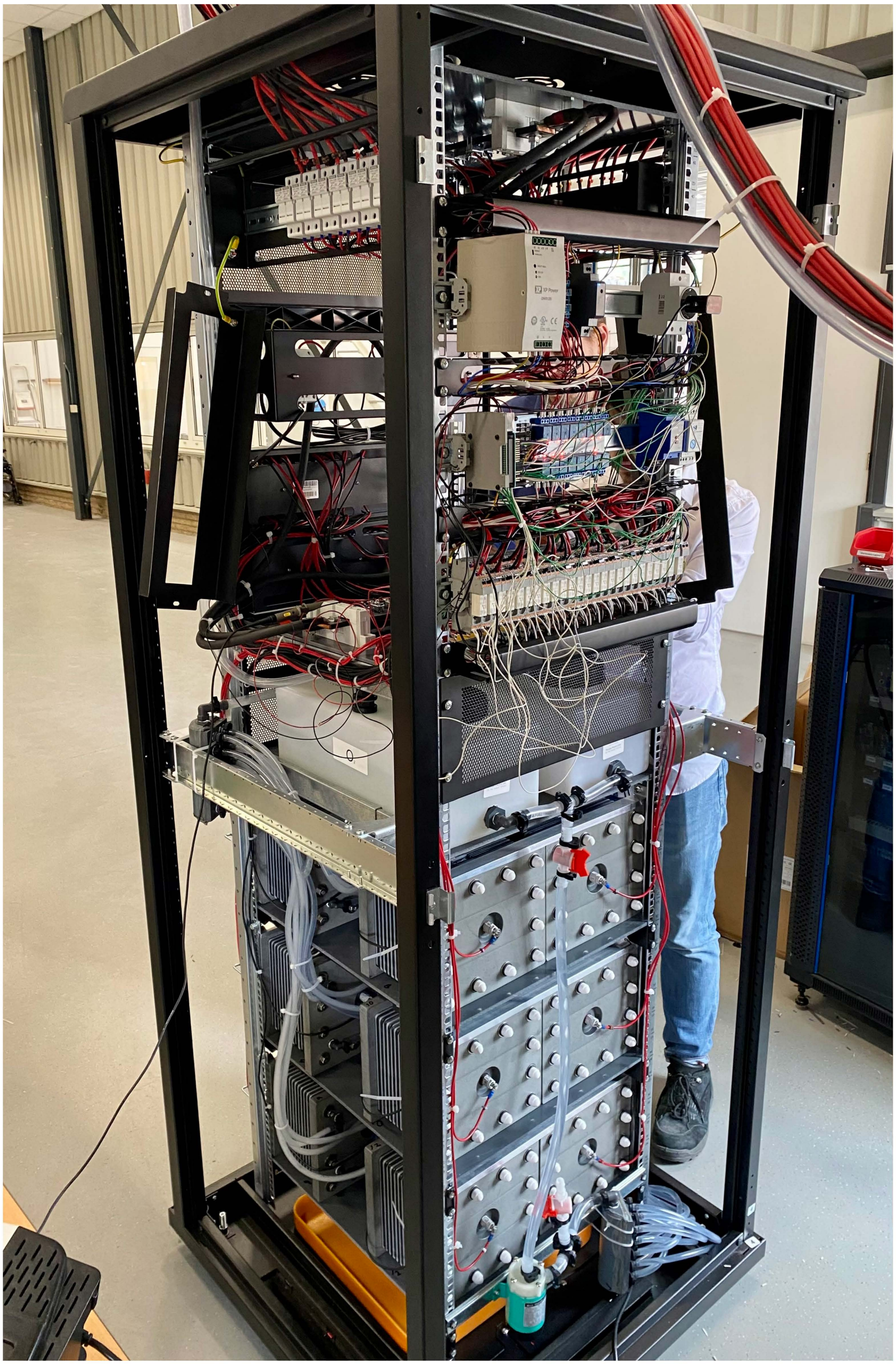

Figure A.12: Control electronics and electrolyzer stacks for the experimental setup. There are 12 stacks. The stacks are configured in parallel and are all fed by one pump.

Table A.1: Summarized results from a simulation investigating the difference between m-tracking and conventional MPPT algorithm goals. M-tracking performance was modelled using both an estimator function for the irradiance and using the true value for the irradiance itself. Temperature effects were not taken into account in the irradiance estimator. (Data source: BSRN [105])

m-tracking	Total Power Delivered MW h	Total Hydrogen Produced *tons*	Overall MPPT Efficiency *%*	Switches per Stack per Hour *#/hr*	% of Times Soft Current Limit Exceeded *%*	% of Times Voltage Limit Exceeded *%*
no	1580.7	31.6	94.5%	15.6	23.0%	6.8%
yes ($G_{\text{est.}}$)	1564.5	31.4	92.3%	23.8	7.1%	18.3%
yes (G_{true})	1564.7	31.5	92.3%	23.8	7.3%	20.4%

Table A.2: Summarized results from a simulation investigating the difference between m-tracking and conventional MPPT algorithm goals, excluding the months of January, May, October, November and December. M-tracking performance was modelled using both an estimator function for the irradiance and using the true value for the irradiance itself. Temperature effects were not taken into account in the irradiance estimator. Five months are excluded as their average irradiance is below 250 W m^{-2}, which hinders the ability of the m-tracking function to work properly. (Data source: BSRN [105])

m-tracking	Total Power Delivered MW h	Total Hydrogen Produced *tons*	Overall MPPT Efficiency *%*	Switches per stack per hour *#/hr*	% of Times Soft Current Limit Exceeded *%*	% of Times Voltage Limit Exceeded *%*
no	1262.3	25.3	95.0%	20.0	20.7%	5.1%
yes ($G_{\text{est.}}$)	1263.7	25.5	95.0%	32.7	7.7%	13.9%
yes (G_{true})	1263.7	25.5	95.0%	32.7	5.5%	9.3%

Table A.3: Electricity and hydrogen yield for the industrial and research benchmarks, compared to the yield obtained through the use of the MHP algorithm. Shown values for the MHP algorithm are summations of the maximum production figures from each month. In months with low irradiance, MHP algorithm yields without m-tracking was used.

	Electricity Generated		**Hydrogen Produced**	
	MWh	*% w.r.t. Industry*	*tons*	*% w.r.t. Industry*
Industry Benchmark	1474.4	0.0 %	28.8	0.0 %
Research Benchmark	1522.8	+3.3 %	31.5	+9.3 %
MHP Algorithm	1584.4	+7.5 %	31.8	+10.4 %

Table A.4: Levelized Cost of Electricity (LCOE) and Hydrogen (LCOH) of the reference system (according to both industry and research standards) and of the newly proposed directly coupled system. The new system is shown with results corresponding to a static programming of m ($m = 0$), a dynamic programming of m (to increase hydrogen production) and the best combination of both. All currency values shown are 2022 euros. The assumed discount rate was 4%, as per Dutch governmental guidelines.

	LCOE		**LCOH**	
	€/MWh	*% w.r.t. Industry*	*€/kg H2*	*% w.r.t. Industry*
Industrial Benchmark	36.51	0.00 %	4.32	0.00 %
Research Benchmark	35.35	-3.18 %	3.95	-8.52 %
MHP Algorithm ($m = 0$)	30.69	-15.95 %	3.46	-19.85 %
MHP Algorithm ($m \neq 0$)	31.01	-15.08 %	3.48	-19.52 %
MHP Algorithm (max)	30.62	-16.15 %	3.44	-20.37 %

B
Additional Results

B.1. Modelling Results

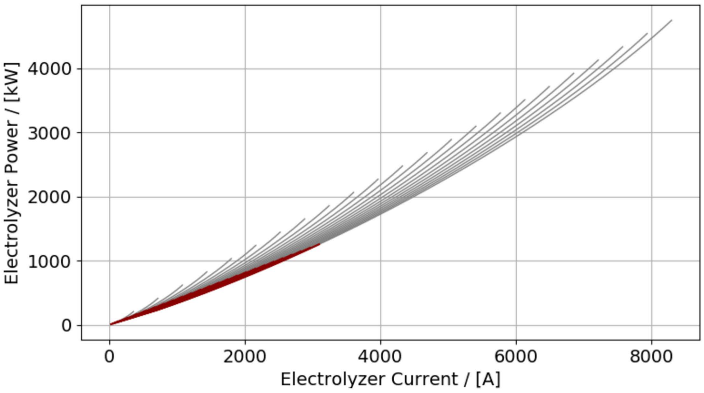

Figure B.1: Current-power curves for a modular alkaline electrolyzer system of 120 stacks. Each line represents an increment of 5 stacks, going from 0 to 120 stacks. The grey area of the line indicates the part of the curve which exceeds the soft current limit.

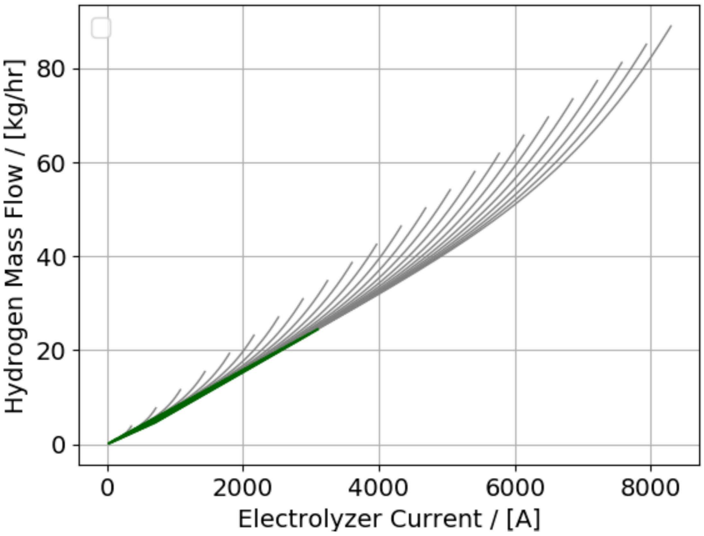

Figure B.2: Current-Hydrogen mass flow curves for a modular alkaline electrolyzer with 120 stacks. Each line represents an increment of 5 stacks, going from 0 to 120 stacks. The grey area of the line indicates the part of the curve which exceeds the soft current limit.

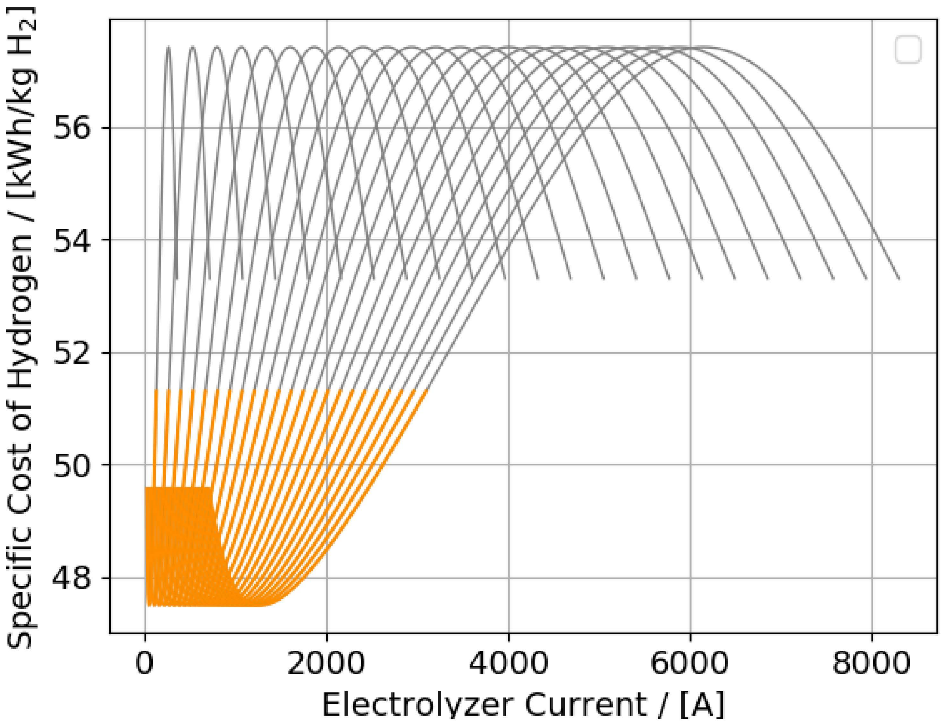

Figure B.3: Specific cost of hydrogen production expressed in terms of current for a modular alkaline electrolyzer with 120 stacks. Each line represents an increment of 5 stacks, going from 0 to 120 stacks. The grey area of the line indicates the part of the curve which exceeds the soft current limit.

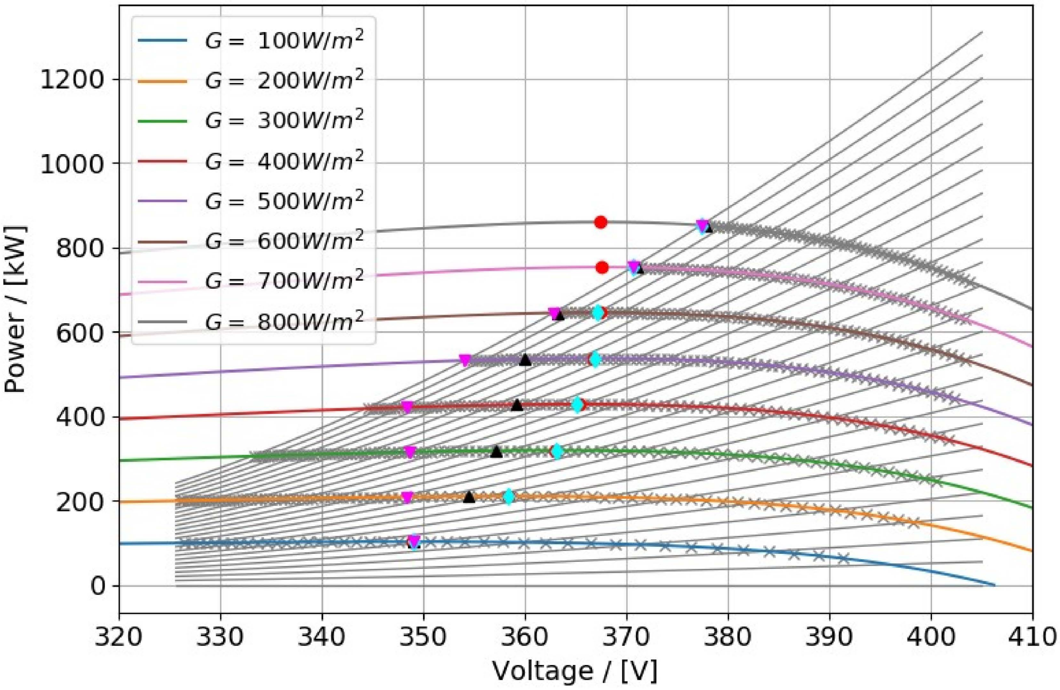

Figure B.4: P-V curve of an HRES consisting of a 1.07 MW **PV solar array and a 1.25** MW **modular alkaline electrolyzer.** PV array configuration is 12 panels in series and 220 panels in parallel. The electrolyzer curves are only shown for every 5 stacks, with the grey curve at the top of the figure indicating 120 stacks. Grey crosses mark the operating points of the system. Red dots indicate PV array MPPs, cyan diamonds indicate the MPP operating points of the HRES, and magenta triangles indicate the operating points which have the lower specific cost of hydrogen production. The magenta dotted line indicated the voltage at which the lower specific cost of hydrogen production is achieved ($\psi_{\text{min}} = 47.5$ kW h kg^{-1}). The black triangles denote the operation points which produce the highest hydrogen mass flow rate. Curves were created using the Python PVlib library.

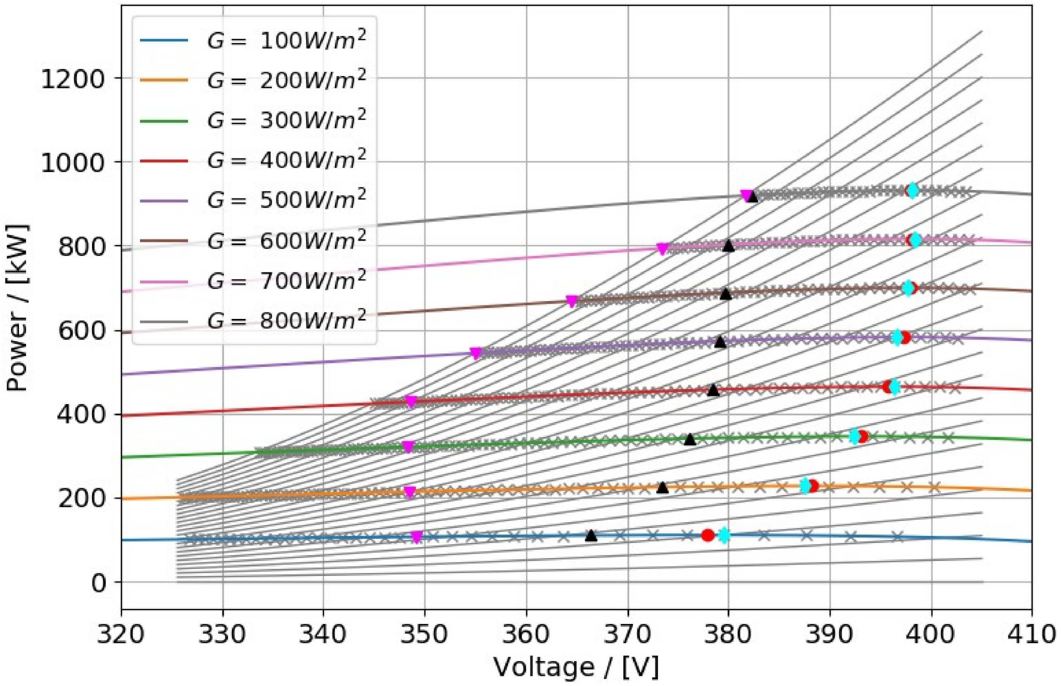

Figure B.5: P-V curve of an HRES consisting of a 1.16 MW PV solar array and a 1.25 MW modular alkaline electrolyzer. PV array configuration is 13 panels in series and 220 panels in parallel. The electrolyzer curves are only shown for every 5 stacks, with the grey curve at the top of the figure indicating 120 stacks. Grey crosses mark the operating points of the system. Red dots indicate PV array MPPs, cyan diamonds indicate the MPP operating points of the HRES, and magenta triangles indicate the operating points which have the lower specific cost of hydrogen production. The magenta dotted line indicated the voltage at which the lower specific cost of hydrogen production is achieved ($\psi_{\text{min}} = $47.5 kW h kg^{-1}). The black triangles denote the operation points which produce the highest hydrogen mass flow rate. Curves were created using the Python PVlib library.

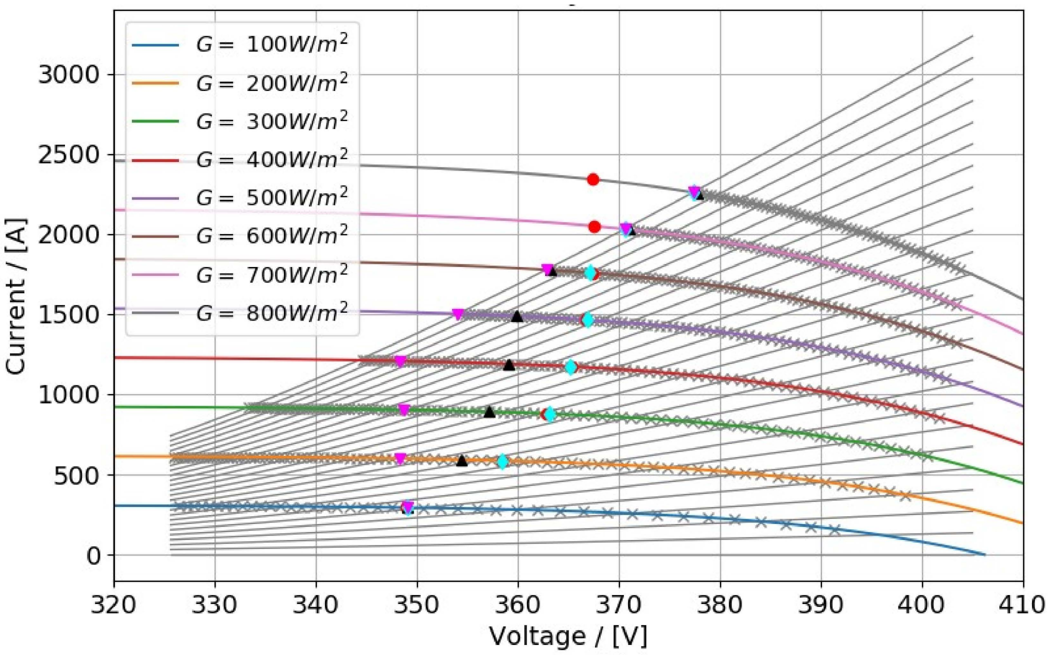

Figure B.6: I-V curve of an HRES consisting of a 1.16 MW PV solar array and a 1.25 MW modular alkaline electrolyzer. PV array configuration is 12 panels in series and 220 panels in parallel. The electrolyzer curves are only shown for every 5 stacks, with the grey curve at the top of the figure indicating 120 stacks. Grey crosses mark the operating points of the system. Red dots indicate PV array MPPs, cyan diamonds indicate the MPP operating points of the HRES, and magenta triangles indicate the operating points which have the lower specific cost of hydrogen production. The black triangles denote the operation points which produce the highest hydrogen mass flow rate. Curves were created using the Python PVlib library.

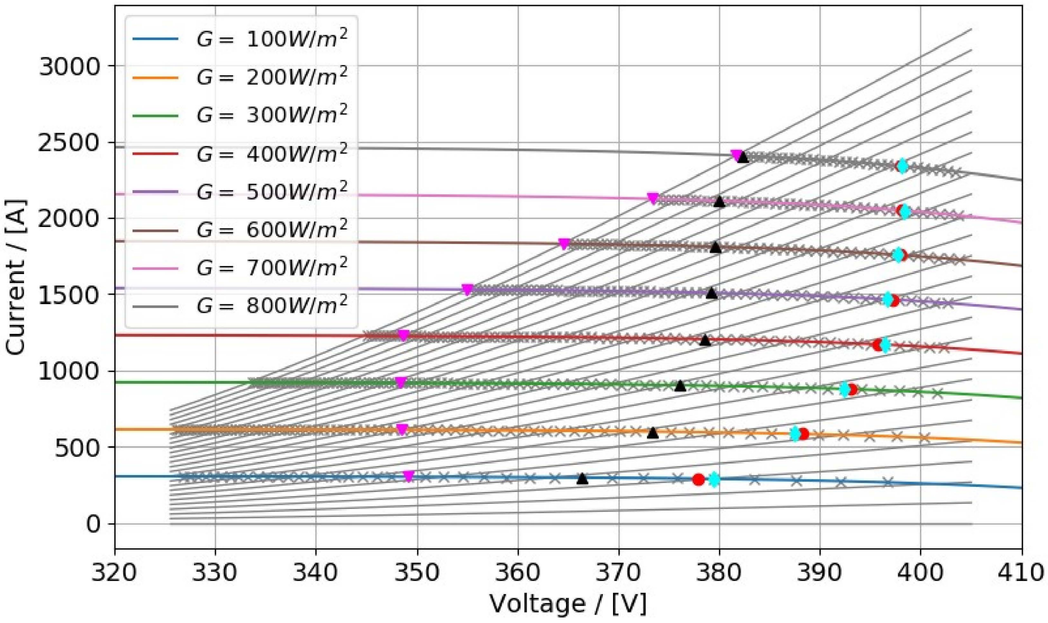

Figure B.7: I-V curve of an HRES consisting of a 1.16 MW PV solar array and a 1.25 MW modular alkaline electrolyzer. PV array configuration is 13 panels in series and 220 panels in parallel. The electrolyzer curves are only shown for every 5 stacks, with the grey curve at the top of the figure indicating 120 stacks. Grey crosses mark the operating points of the system. Red dots indicate PV array MPPs, cyan diamonds indicate the MPP operating points of the HRES, and magenta triangles indicate the operating points which have the lower specific cost of hydrogen production. The black triangles denote the operation points which produce the highest hydrogen mass flow rate. Curves were created using the Python PVlib library.

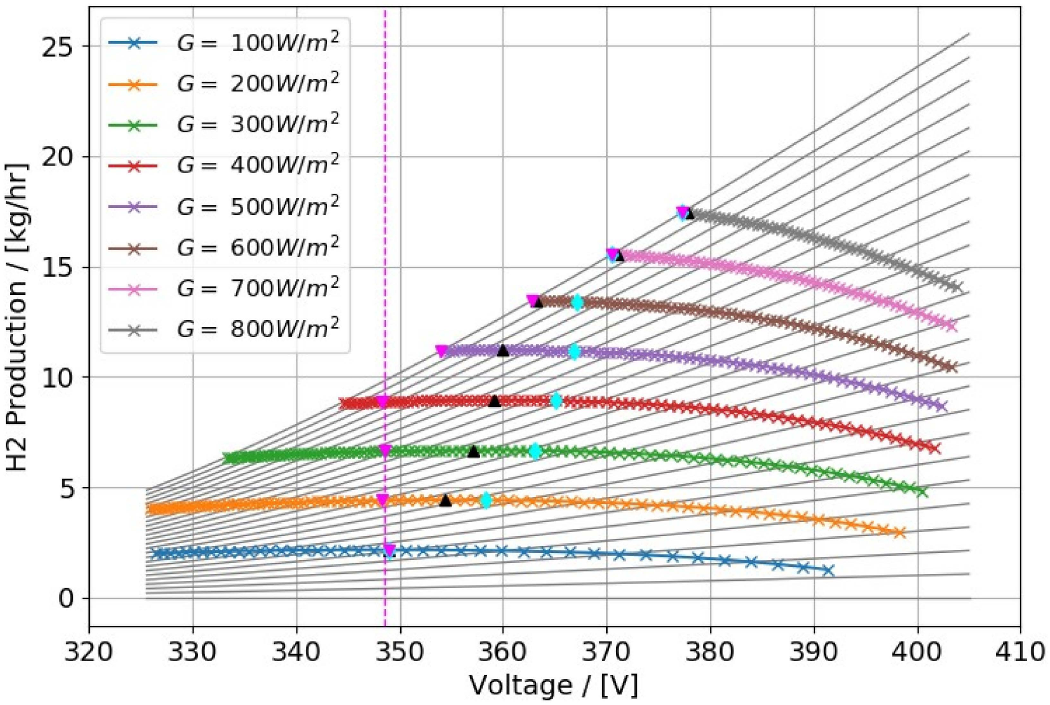

Figure B.8: Hydrogen production rate vs. voltage curve of an HRES consisting of a 1.16 MW PV solar array and a 1.25 MW modular alkaline electrolyzer. PV array configuration is 12 panels in series and 220 panels in parallel. The electrolyzer curves are only shown for every 5 stacks, with the grey curve at the top of the figure indicating 120 stacks. Colored crosses mark the operating points of the system. The cyan diamonds indicate the MPP operating points of the HRES, and magenta triangles indicate the operating points which have the lower specific cost of hydrogen production. The magenta dotted line indicates the voltage at which the lower specific cost of hydrogen production is achieved (ψ_{min} =47.5 kW h kg^{-1}). The black triangles denote the operation points which produce the highest hydrogen mass flow rate. Curves were created using the Python PVlib library.

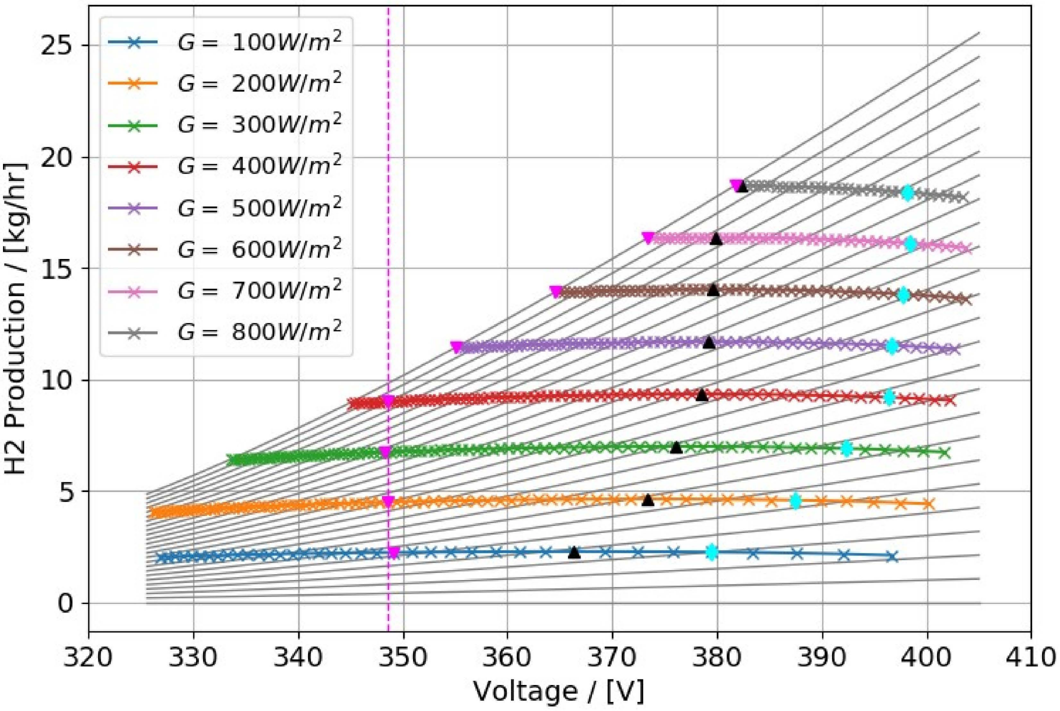

Figure B.9: Hydrogen production rate vs. voltage curve of an HRES consisting of a 1.16 MW PV solar array and a 1.25 MW modular alkaline electrolyzer. PV array configuration is 13 panels in series and 220 panels in parallel. The electrolyzer curves are only shown for every 5 stacks, with the grey curve at the top of the figure indicating 120 stacks. Colored crosses mark the operating points of the system. The cyan diamonds indicate the MPP operating points of the HRES, and magenta triangles indicate the operating points which have the lower specific cost of hydrogen production. The magenta dotted line indicates the voltage at which the lower specific cost of hydrogen production is achieved (ψ_{min} =47.5 kW h kg^{-1}). The black triangles denote the operation points which produce the highest hydrogen mass flow rate. Curves were created using the Python PVlib library.

B.2. Irradiance Estimator Results

Table B.1: Results of a function to estimate the optimum value of slope m to maximize hydrogen production. Function fit using simulated data, and excludes any data points which are skewed due to the operating region of the electrolyzer.

G W m^{-2}	$m_{\text{max H2, true}}$ A	$m_{\text{max H2, calc.}}$ A
100	0.171	0.172
150	0.255	0.267
200	0.365	0.362
250	0.457	0.457
300	0.572	0.552
350	0.665	0.647
400	0.756	0.742
450	0.845	0.837
500	0.955	0.932
550	1.038	1.027
600	1.142	1.122
650	1.243	1.217
700	1.314	1.312
750	1.408	1.407

B.3. M-Tracking Results

Table B.2: Simulation results for the proposed directly coupled HRES. Comparison is made between the scenario where the goal of the control algorithm is constant (i.e., no m-tracking) and the scenario where the goal is adjusted based on an estimator function of the irradiance ($G_{\text{est}} = f(P, P_{\text{ref}})$).

	m-tracking	**Total Power Delivered**	**Total Hydrogen Produced**	**Overall MPPT Efficiency**	**Switches per stack per hour**
	-	MW h	*tons*	*%*	*#/hr*
January	no	44.3	0.87	93.5%	5.7
	yes ($G_{\text{est.}}$)	40.9	0.81	86.4%	6.7
February	no	135.0	2.66	96.3%	11.1
	yes ($G_{\text{est.}}$)	133.9	2.66	95.5%	15.9
March	no	131.4	2.59	94.3%	14.6
	yes ($G_{\text{est.}}$)	130.1	2.61	93.3%	20.9
April	no	218.1	4.34	95.9%	22.3
	yes ($G_{\text{est.}}$)	218.1	4.38	95.9%	37.0
May	no	100.2	2.01	94.9%	18.2
	yes ($G_{\text{est.}}$)	93.0	1.86	88.1%	21.6
June	no	229.5	4.61	94.7%	26.2
	yes ($G_{\text{est.}}$)	230.4	4.65	95.1%	44.9
July	no	206.2	4.15	94.7%	24.4
	yes ($G_{\text{est.}}$)	207.2	4.19	95.1%	40.6
August	no	198.7	4.01	94.8%	24.4
	yes ($G_{\text{est.}}$)	199.7	4.05	95.3%	42.6
September	no	143.5	2.89	94.5%	17.3
	yes ($G_{\text{est.}}$)	144.2	2.92	95.0%	27.1
October	no	81.8	1.63	93.3%	11.3
	yes ($G_{\text{est.}}$)	80.2	1.60	91.4%	14.6
November	no	47.7	0.94	92.3%	6.3
	yes ($G_{\text{est.}}$)	45.4	0.90	88.0%	7.3
December	no	44.4	0.88	94.7%	6.0
	yes ($G_{\text{est.}}$)	41.3	0.82	88.1%	6.9

B.4. Sunny Day Simulation Results

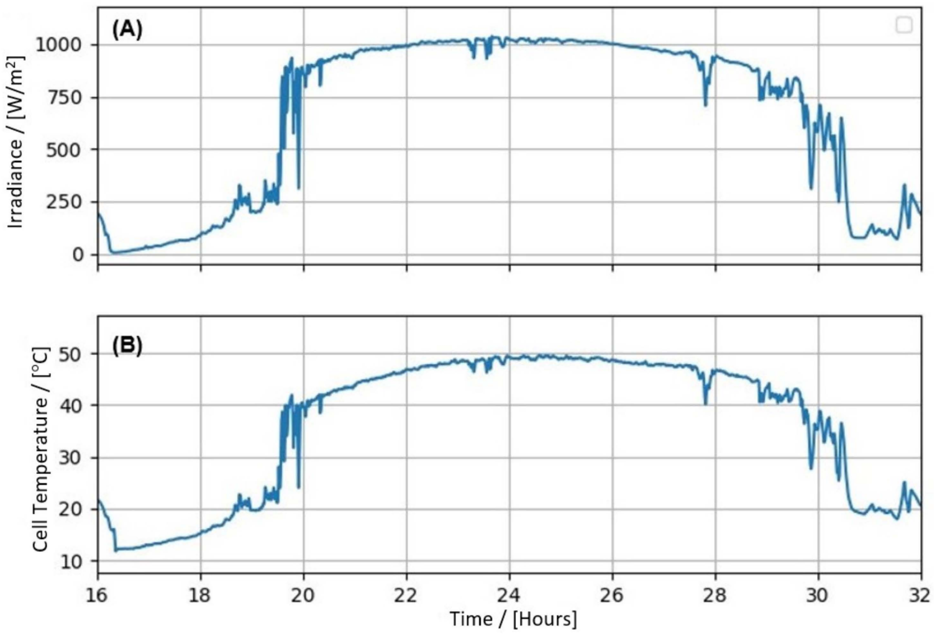

Figure B.10: Irradiance and cell temperature for a simulation of weather data from June 2009 in Cabauw, The Netherlands. Plot (A) shows the irradiance data (diffuse + direct) at the Cabauw weather station. Plot (B) shows the calculated cell temperature, a function of the incident irradiance and the ambient temperature at the Cabauw weather station.

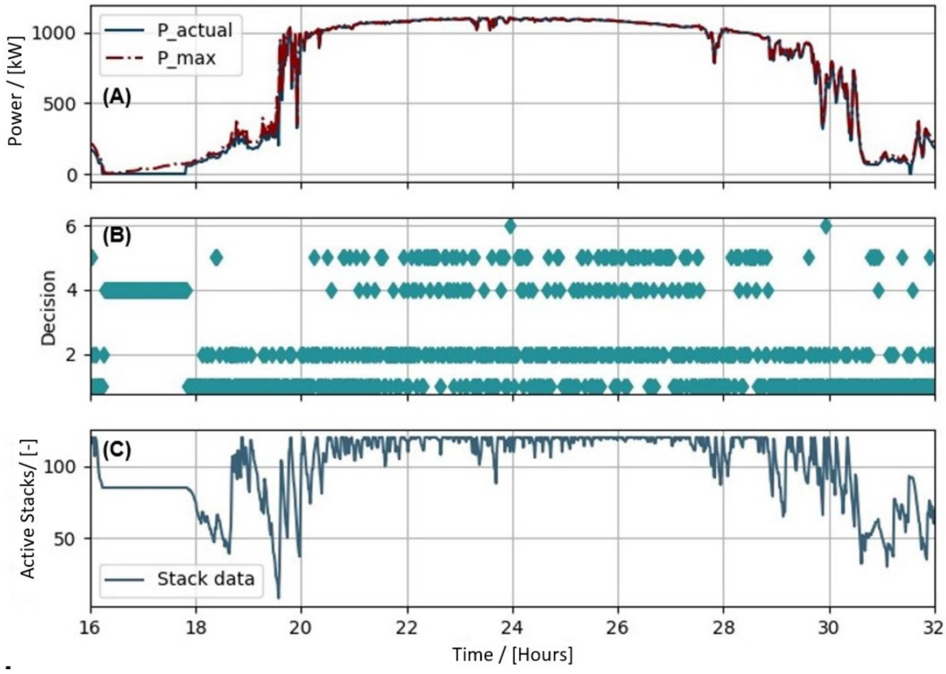

Figure B.11: System power, decision log, and active stack log for a simulation of weather data from June 2009 in Cabauw, The Netherlands. Plot (A) shows the power delivered to the modular alkaline electrolyzer as well as the reference maximum possible power if the system operated at the MPP in every iteration. Plot (B) shows the decision made in each iteration. Decision choices 1 and 6 indicate a decrease in stacks, choices 2 and 5 indicate an increase in stacks, and choices 3 and 4 indicate the stack number stays the same. Plot (C) shows the number of stacks active in each iteration.

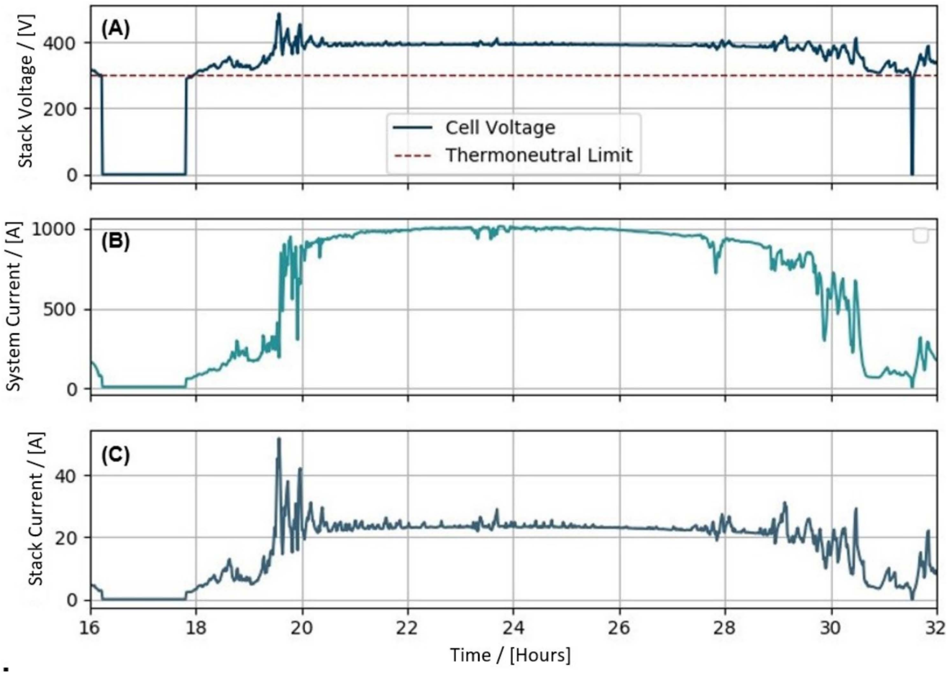

Figure B.12: Stack voltage, system current and stack current for a simulation of weather data from June 2009 in Cabauw, The Netherlands. Plot (A) shows the stack voltage, including the thermo-neutral voltage limit. Plot (B) shows the system current, which is the sum of all current flowing through each of the stacks. Plot (C) shows the current divided by the number of active stacks, representing the stack current.

B.5. Cloudy Day Simulation Results

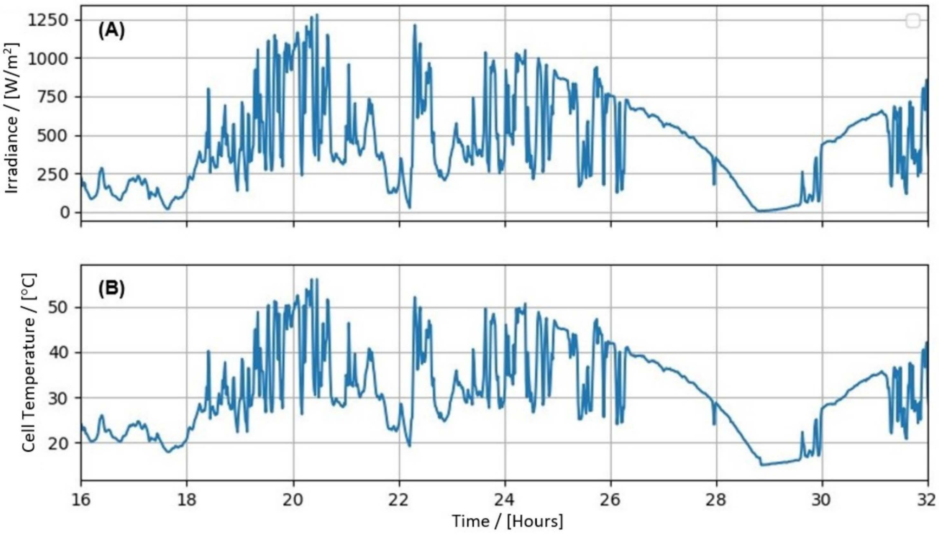

Figure B.13: Irradiance and cell temperature for a simulation of weather data from August 2013 in Cabauw, The Netherlands. Plot (A) shows the irradiance data (diffuse + direct) at the Cabauw weather station. Plot (B) shows the calculated cell temperature, a function of the incident irradiance and the ambient temperature at the Cabauw weather station.

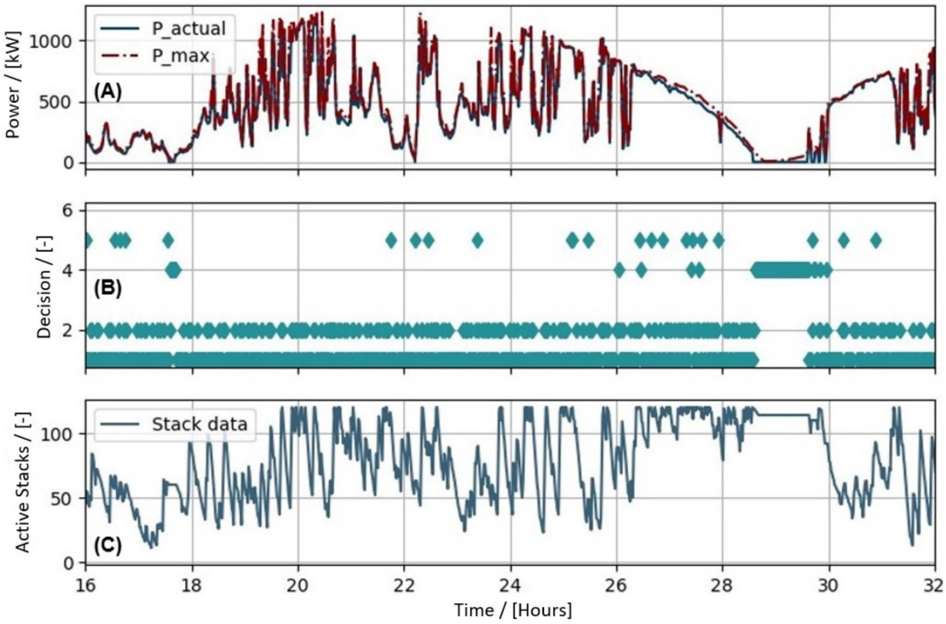

Figure B.14: System power, decision log, and active stack log for a simulation of weather data from August 2013 in Cabauw, The Netherlands. Plot (A) shows the power delivered to the modular alkaline electrolyzer as well as the reference maximum possible power if the system operated at the MPP in every iteration. Plot (B) shows the decision made in each iteration. Decision choices 1 and 6 indicate a decrease in stacks, choices 2 and 5 indicate an increase in stacks, and choices 3 and 4 indicate the stack number stays the same. Plot (C) shows the number of stacks active in each iteration.

Table B.3: Electricity yield per month of a typical meteorological year in Cabauw, The Netherlands. The results shown are for the MHP algorithm, compared to an industrial and a research benchmark. Shown values for the MHP algorithm are summations of the maximum production figures from each month. In months with low irradiance, MHP algorithm yields without m-tracking was used.

Month *[-]*	**Sun Hours** *hrs*	**MHP Algorithm** *MWh*	**Industry Benchmark** *MWh*	**Industry Benchmark** *MWh*
Jan	249.1	44.3	42.8	43.2
Feb	274.4	135.0	120.8	126.2
Mar	358.7	131.4	121.5	125.8
Apr	411.1	218.1	195.3	205.3
May	497.7	100.2	95.7	95.7
Jun	486.8	230.4	212.6	222.6
Jul	482.1	207.2	194.1	201.1
Aug	428.4	199.7	187.8	195.1
Sep	366.5	144.2	136.4	139.0
Oct	320.8	81.8	78.4	79.6
Nov	249.5	47.7	46.6	46.9
Dec	230.4	44.4	42.6	42.6
TOTAL	**4355.6**	**1584.4**	**1474.4**	**1522.8**

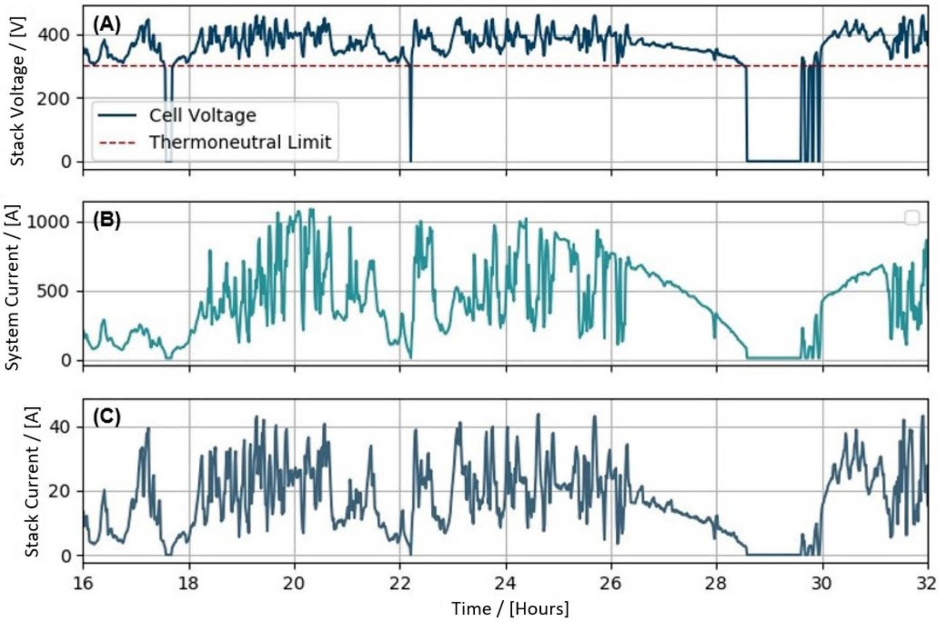

Figure B.15: Stack voltage, system current and stack current for a simulation of weather data from August 2013 in Cabauw, The Netherlands. Plot (A) shows the stack voltage, including the thermo-neutral voltage limit. Plot (B) shows the system current, which is the sum of all current flowing through each of the stacks. Plot (C) shows the current divided by the number of active stacks, representing the stack current.

Table B.4: Hydrogen yield per month of a typical meteorological year in Cabauw, The Netherlands. The results shown are for the MHP algorithm, compared to an industrial and a research benchmark. Shown values for the MHP algorithm are summations of the maximum production figures from each month. In months with low irradiance, MHP algorithm yields without m-tracking was used.

Month *[-]*	**Sun Hours** *hrs*	**MHP Algorithm** *kg*	**Industry Benchmark** *kg*	**Industry Benchmark** *kg*
Jan	249.1	870.9	836.0	899.0
Feb	274.4	2658.6	2358.6	2629.7
Mar	358.7	2613.7	2372.6	2372.6
Apr	411.1	4379.7	3814.3	4276.9
May	497.7	2008.0	1868.5	1993.1
Jun	486.8	4648.8	4153.1	4636.8
Jul	482.1	4192.9	3790.0	4189.9
Aug	428.4	4048.3	3667.9	4063.8
Sep	366.5	2916.8	2663.3	2895.3
Oct	320.8	1626.5	1531.7	1658.5
Nov	249.5	937.4	910.4	976.1
Dec	230.4	879.5	831.2	886.6
TOTAL	**4355.6**	**31781.1**	**28797.6**	**31478.2**

B.6. Power & Hydrogen Yield Compared to Benchmark Results

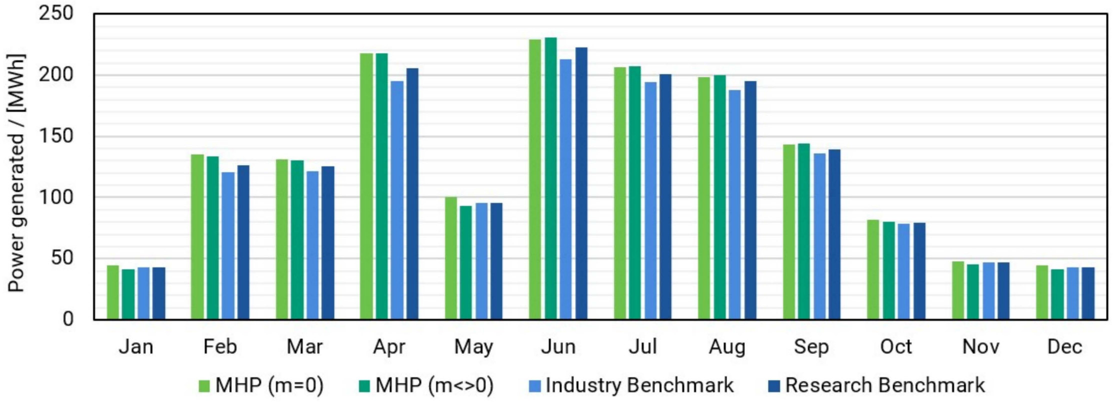

Figure B.16: Power generated per month for both the proposed HRES (directly coupled, both with and without m-tracking) and for the benchmarks (both industrial and research). Results for the month of May indicate an outlier with a lower average irradiance than usual.

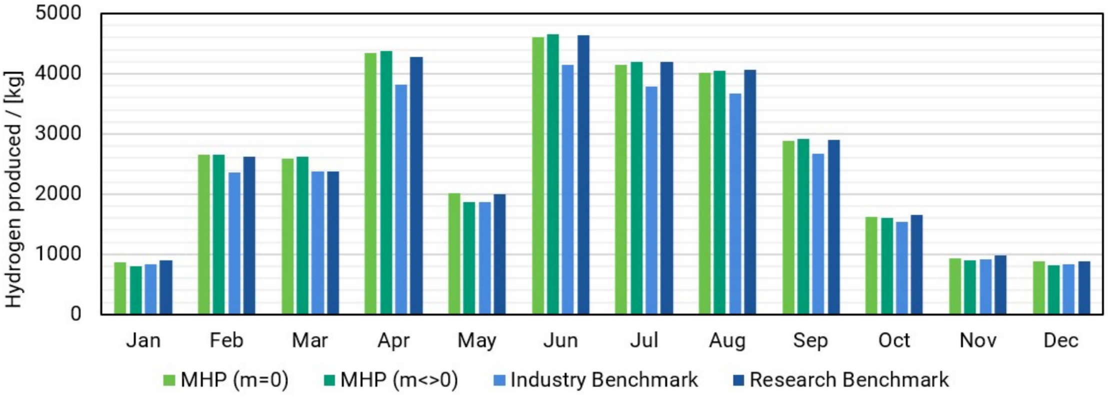

Figure B.17: Hydrogen produced per month for both the proposed HRES (directly coupled, both with and without m-tracking) and for the benchmarks (both industrial and research). Results for the month of May indicate an outlier with a lower average irradiance than usual.

B.7. Experimental Results

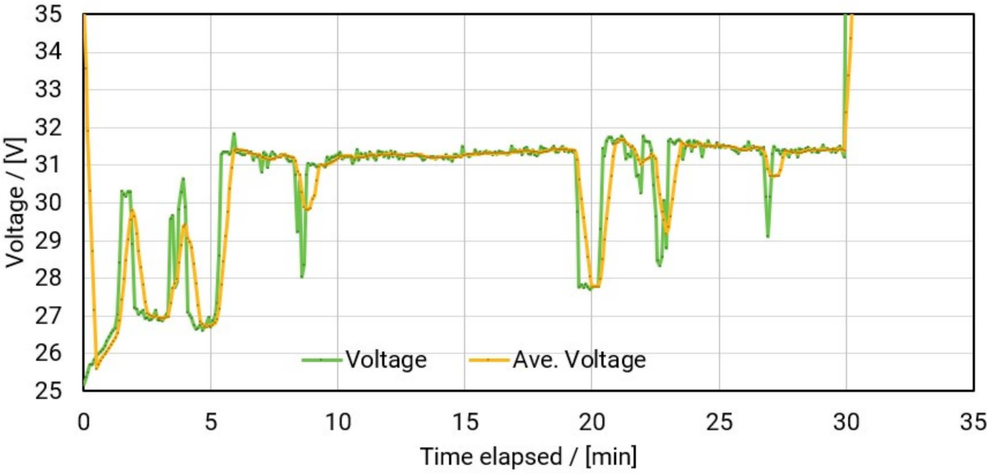

Figure B.18: Voltage and average voltage for Experiment 1. Experiment 1 was a benchmark, with all 12 stacks in the system active for the entire duration. The stacks used in this experimental setup were constructed solely for research purposes and its geometry and performance do not carry over to commercial XINTC systems.

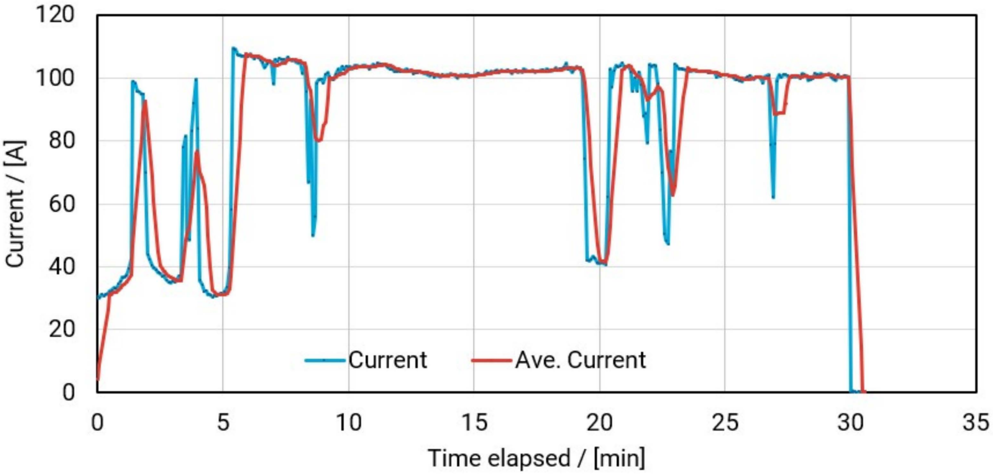

Figure B.19: Current and average current for Experiment 1. Experiment 1 was a benchmark, with all 12 stacks in the system active for the entire duration. The stacks used in this experimental setup were constructed solely for research purposes and its geometry and performance do not carry over to commercial XINTC systems.

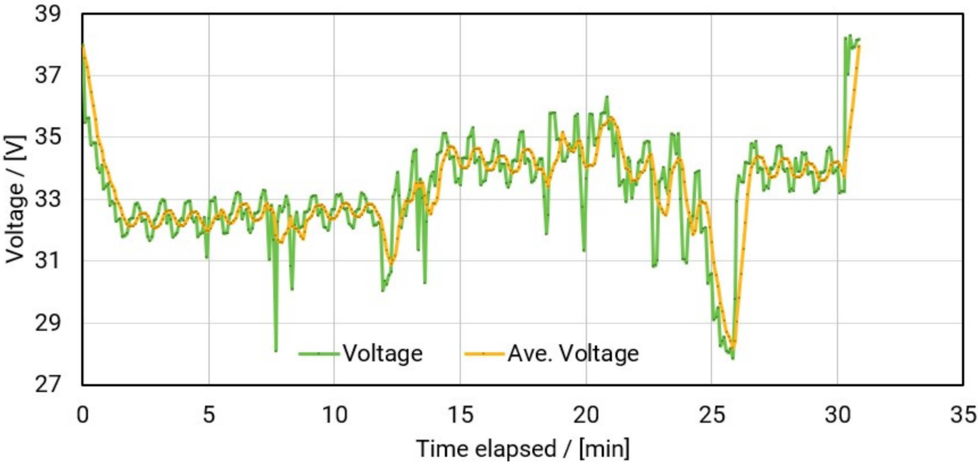

Figure B.20: Voltage and average voltage for Experiment 2. Experiment 2 was a test using the MHP algorithm as defined in Figure 3.27. The stacks used in this experimental setup were constructed solely for research purposes and its geometry and performance do not carry over to commercial XINTC systems.

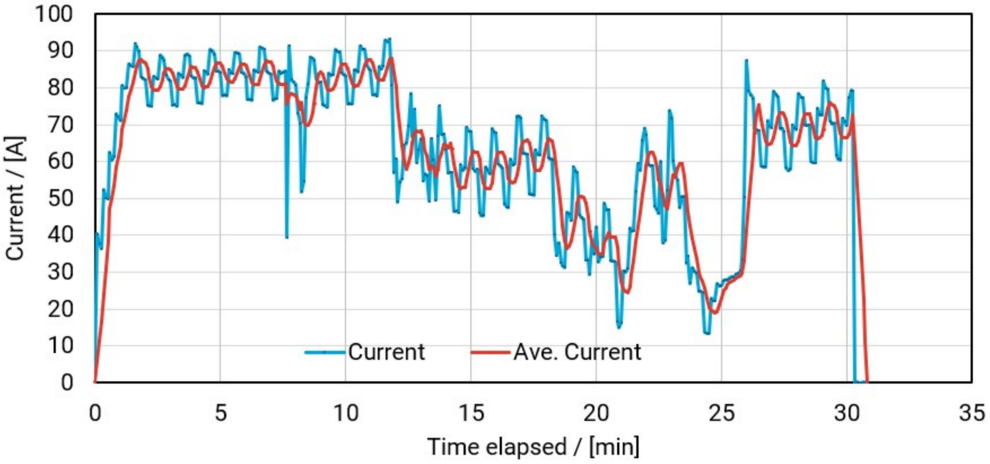

Figure B.21: Current and average current for Experiment 2. Experiment 2 was a test using the MHP algorithm as defined in Figure 3.27. The stacks used in this experimental setup were constructed solely for research purposes and its geometry and performance do not carry over to commercial XINTC systems.

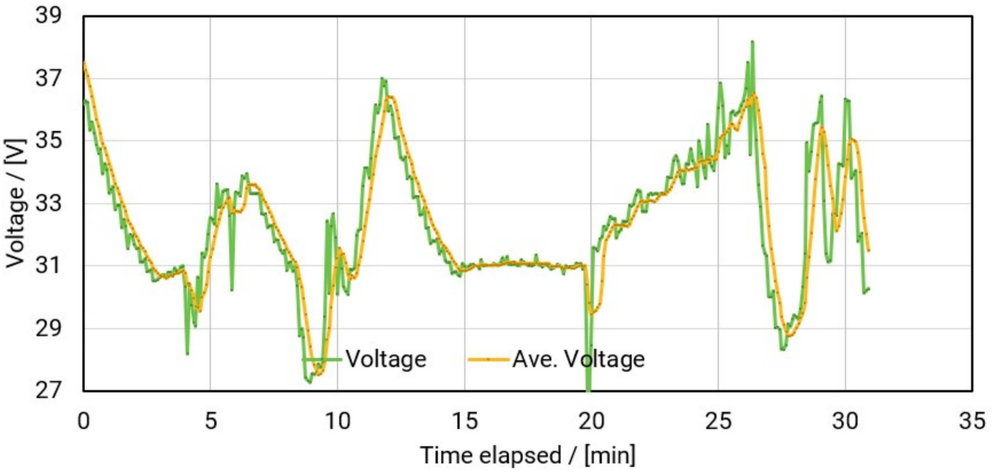

Figure B.22: Voltage and average voltage for Experiment 3. Experiment 3 was a test using the MHP algorithm as defined in Figure 3.27, but the signs for increasing and decreasing the number of stacks in the furthest right two choices (where $|\Delta V|$ is small and $\Delta I > 0$) are flipped. The stacks used in this experimental setup were constructed solely for research purposes and its geometry and performance do not carry over to commercial XINTC systems.

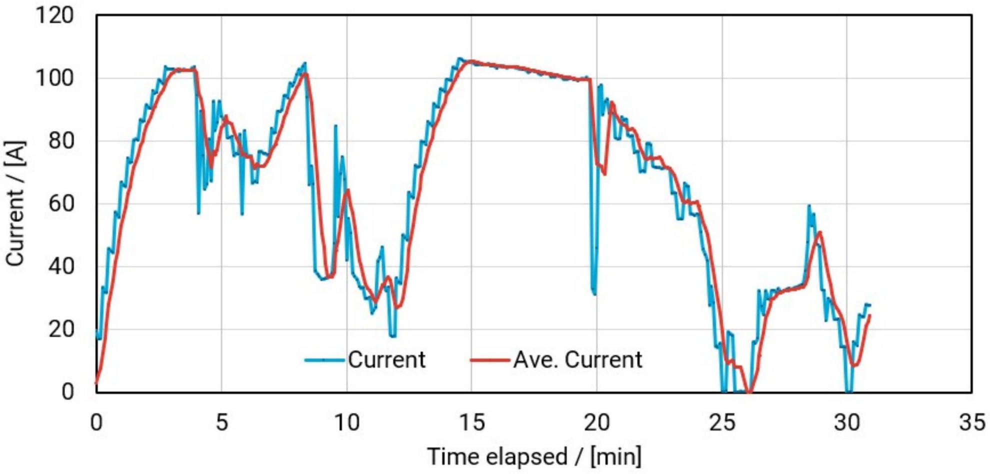

Figure B.23: Current and average current for Experiment 3. Experiment 3 was a test using the MHP algorithm as defined in Figure 3.27, but the signs for increasing and decreasing the number of stacks in the furthest right two choices (where $|\Delta V|$ is small and $\Delta I > 0$) are flipped. The stacks used in this experimental setup were constructed solely for research purposes and its geometry and performance do not carry over to commercial XINTC systems.

References

[1] National Geographic Society. “Age of Earth Collection”. In: *National Geographic website* (2023).

[2] United Nations. “World population to Reach 8 billion on 15 November 2022”. In: *Department of Economic and Social Affairs* (2022).

[3] International Energy Agency IEA. “Renewables Data and Information”. In: *OECD* (2021).

[4] World Wildlife Fund WWF. “Effects of Climate Change”. In: *WWF Online Website* (2023).

[5] G. S. Callendar. “The artificial production of carbon dioxide and its influence on temperature”. In: *Quarterly Journal of the Royal Meteorological Society* 64.275 (Apr. 1938), pp. 223–240.

[6] World Meteorological Organization. “Greenhouse Gases”. In: *Public Website* (2022).

[7] NASA’s Goddard Institute for Space Studies GISS. “How Do We Know Climate Change Is Real?” In: *NASA Jet Propulsion Laboratory | California Institute of Technology* (2023).

[8] United Nations Climate Change UNCC. “The Paris Agreement”. In: *UNFCCC Process* (2015).

[9] Statistical Review of World Energy BP. *Our World In Data - Solar PV Cumulative Capacity*. Online Publication. 2022.

[10] IRENA International Renewable Energy Agency. “Global Renewables Outlook: Energy Transformation 2050”. In: *IRENA* (2020).

[11] S. Bouckaert et. al. *A Roadmap for the Global Energy Sector*. Tech. rep. International Energy Agency, 2022.

[12] European Commission. “A Hydrogen Strategy for a Climate-neutral Europe”. In: *European Parliament* (July 2020).

[13] Fuel Cells and Hydrogen 2 Joint Undertaking. *Hydrogen roadmap Europe: a sustainable pathway for the European energy transition.* Publications Office, 2019.

[14] BNEF BloombergNEF. “Hydrogen Economy Outlook”. In: *Bloomberg Finance L.P.* (Mar. 2020).

[15] International Energy Agency (IEA). “Utility-scale PV Investment Cost Structure by Component and by Commodity Breakdown”. Oct. 2022.

[16] Centraal Bureau voor Statistiek. “Nederlandse Elektriciteitscentrales”. Jan. 2021.

[17] ROM3D. “Zon Op Kaart”. Jan. 2022.

[18] Eva Rooijers. *Investeringen nodig om stroomtekort in 2030 af te wenden*. Dutch. Financieel Dagblad. Jan. 2023. URL: `https://fd.nl/bedrijfsleven/1464514/investeringen-nodig-om-stroomtekort-in-2030-af-te-wenden-mpa3caRnkyaP`.

[19] Bas Knoop. *Klimaatdoel voor wind en zon blijft haalbaar, maar stagnatie dreigt*. Dutch. Financieel Dagblad. Dec. 2022. URL: `https://fd.nl/samenleving/1460498/klimaatdoel-voor-wind-en-zon-blijft-haalbaar-maar-stagnatie-dreigt-mpa3caRnkyaP`.

[20] Puck Voorhoeve. *Overbelast stroomnet raakt bedrijven en woningbouw*. Dutch. NOS. May 2022. URL: `https://nos.nl/nieuwsuur/artikel/2427174-overbelast-stroomnet-raakt-bedrijven-en-woningbouw`.

[21] Reinder Smit. *Overbelast elektriciteitsnet zorgt voor problemen: ’Vergunningen moeten sneller’*. Dutch. RTL Nieuws. Nov. 2021. URL: `https://www.rtlnieuws.nl/economie/artikel/5265776/overbelast-elektriciteitsnet-zorgt-voor-problemen`.

[22] Tjerk Gualthérie van Weezel. *Toezichthouder ACM adviseert om salderingsregeling voor zonnepanelen snel af te schaffen*. Dutch. Volkskrant. Jan. 2023. URL: `https://www.volkskrant.nl/nieuws-achtergrond/toezichthouder-acm-adviseert-om-salderingsregeling-voor-zonnepanelen-snel-af-te-schaffen~bbe08eb3/?referrer=https://www.google.com/`.

[23] Ryan Kennedy. "How long do residential solar inverters last?" Sept. 2021.

[24] Global Wind Energy Council (GWEC). *Global Wind Report 2022*. Online Publication. Apr. 2022.

[25] Axelle Viré Michiel Zaaijer. "Introduction to Wind Turbines: Physics and Technology". Internal Reader for Students of the Delft University of Technology. Sept. 2022.

[26] Omar Ellabban, Haitham Abu-Rub, and Frede Blaabjerg. "Renewable energy resources: Current status, future prospects and their enabling technology". In: *Renewable and Sustainable Energy Reviews* 39 (Nov. 2014), pp. 748–764.

[27] Emily Grubert. "Conventional hydroelectricity and the future of energy: Linking national inventory of dams and energy information administration data to facilitate analysis of hydroelectricity". In: *The Electricity Journal* 33.1 (Jan. 2020), p. 106692.

[28] Rahmi Deniz Özbay et al. "Towards Environmental Sustainability in China: Role of Globalization and Hydroelectricity Consumption". In: *Sustainability* 14.7 (Mar. 2022), p. 4182.

[29] Seungwoo Kang, Sandrine Selosse, and Nadia Maïzi. "Strategy of bioenergy development in the largest energy consumers of Asia (China, India, Japan and South Korea)". In: *Energy Strategy Reviews* 8 (July 2015), pp. 56–65.

[30] Junnian Song et al. "Modeling the development and utilization of bioenergy and exploring the environmental economic benefits". In: *Energy Conversion and Management* 103 (Oct. 2015), pp. 836–846.

[31] John W. Lund and Tonya L. Boyd. "Direct utilization of geothermal energy 2015 worldwide review". In: *Geothermics* 60 (Mar. 2016), pp. 66–93.

[32] Hasal Kulasekara and Vaithehi Seynulabdeen. "A Review of Geothermal Energy for Future Power Generation". In: *2019 5th International Conference on Advances in Electrical Engineering (ICAEE)*. IEEE, Sept. 2019.

[33] Marcelo Carmo et al. "A comprehensive review on PEM water electrolysis". In: *International Journal of Hydrogen Energy* 38.12 (Apr. 2013), pp. 4901–4934.

[34] S. Shiva Kumar and V. Himabindu. "Hydrogen production by PEM water electrolysis – A review". In: *Materials Science for Energy Technologies* 2.3 (Dec. 2019), pp. 442–454.

[35] Boreum Lee et al. "Economic feasibility studies of high pressure PEM water electrolysis for distributed H2 refueling stations". In: *Energy Conversion and Management* 162 (Apr. 2018), pp. 139–144.

[36] Everett B. Anderson et al. "Large Scale Energy Storage Using MW-Size PEM Electrolysis". In: *ASME 2014 12th International Conference on Fuel Cell Science, Engineering and Technology*. American Society of Mechanical Engineers, June 2014.

[37] Mohamed Keddar et al. "Power quality improvement for 20 MW PEM water electrolysis system". In: *International Journal of Hydrogen Energy* 47.95 (Dec. 2022), pp. 40184–40195.

[38] Bernd Emonts et al. "A Holistic Consideration of Megawatt Electrolysis as a Key Component of Sector Coupling". In: *Energies* 15.10 (May 2022), p. 3656.

[39] Iain Staffell et al. "The role of hydrogen and fuel cells in the global energy system". In: *Energy and Environmental Science* 12.2 (2019), pp. 463–491.

[40] J.O. Abe et al. "Hydrogen energy, economy and storage: Review and recommendation". In: *International Journal of Hydrogen Energy* 44.29 (June 2019), pp. 15072–15086.

[41] Yisong Zhang et al. "Life Cycle Optimization of Renewable Energy Systems Configuration with Hybrid Battery/Hydrogen Storage: A Comparative Study". In: *Journal of Energy Storage* 30 (Aug. 2020), p. 101470.

[42] Rodolfo Dufo-López, José L. Bernal-Agustín, and Javier Contreras. "Optimization of control strategies for stand-alone renewable energy systems with hydrogen storage". In: *Renewable Energy* 32.7 (June 2007), pp. 1102–1126.

[43] Pablo García et al. "Optimal energy management system for stand-alone wind turbine/photovoltaic/hydrogen/battery hybrid system with supervisory control based on fuzzy logic". In: *International Journal of Hydrogen Energy* 38.33 (Nov. 2013), pp. 14146–14158.

[44] Ali Izadi et al. “Transient simulation and techno-economic assessment of a near-zero energy building using a hydrogen storage system and different backup fuels”. In: *International Journal of Hydrogen Energy* 47.74 (Aug. 2022), pp. 31927–31940.

[45] Zachariah Iverson et al. “Optimal Sizing of Hybrid Renewable Energy Sytems Using a Hydrogen Storage System for Various Power Demand Applications”. In: *Volume 6: Energy, Parts A and B*. American Society of Mechanical Engineers, Nov. 2012.

[46] Paolo Marocco et al. “The role of hydrogen in the optimal design of off-grid hybrid renewable energy systems”. In: *Journal of Energy Storage* 46 (Feb. 2022), p. 103893.

[47] XINTC B.V. *XINTC Electrolyzers - Contributing to a viable future*. Digital. Jan. 2023.

[48] Elizabeth Chu and D. Lawrence Tarazano. “A Brief History of Solar Panels”. In: *Smithsonian Magazine* (2018).

[49] U.S. Energy Information Administration. “Solar Explained: Photovoltaics and Electricity”. Mar. 2022.

[50] AERL. “History of AERL and the MPPT Solar Charge Controller”. In: (1985).

[51] Michael Woodhouse et. al. *The Role of Advancements in Solar Photovoltaic Efficiency, Reliability, and Costs*. Research rep. National Renewable Energy Laboratory (NREL) and the U.S. Department of Energy (DOE), May 2016.

[52] Soteris A. Kalogirou. “Photovoltaic Systems”. In: *Solar Energy Engineering*. Elsevier, 2014, pp. 481–540.

[53] Eneko Ortega, Gerardo Aranguren, and Juan Carlos Jimeno. “Photovoltaic modules transient response analysis and correction under a fast characterization system”. In: *Solar Energy* 221 (June 2021), pp. 232–242.

[54] W. De Soto, S.A. Klein, and W.A. Beckman. “Improvement and validation of a model for photovoltaic array performance”. In: *Solar Energy* 80.1 (Jan. 2006), pp. 78–88.

[55] Greg Kopp and Judith L. Lean. “A new, lower value of total solar irradiance: Evidence and climate significance”. In: *Geophysical Research Letters* 38.1 (Jan. 2011), n/a–n/a.

[56] Ali Omar Baba, Guangyu Liu, and Xiaohui Chen. “Classification and Evaluation Review of Maximum Power Point Tracking Methods”. In: *Sustainable Futures* 2 (2020), p. 100020.

[57] Dezso Sera et al. “On the Perturb-and-Observe and Incremental Conductance MPPT Methods for PV Systems”. In: *IEEE Journal of Photovoltaics* 3.3 (July 2013), pp. 1070–1078.

[58] Abdelhamid Loukriz, Mourad Haddadi, and Sabir Messalti. “Simulation and experimental design of a new advanced variable step size Incremental Conductance MPPT algorithm for PV systems”. In: *ISA Transactions* 62 (May 2016), pp. 30–38.

[59] P. Guerriero et al. “A simple test-bench to evaluate partial shading effects on the MPPT efficiency of a PV inverter”. In: *2013 International Conference on Clean Electrical Power (ICCEP)*. IEEE, June 2013.

[60] R. de Levie. “The Electrolysis of Water”. In: *Journal of Electroanalytical Chemistry* 476.1 (Oct. 1999), pp. 92–93.

[61] Marcelo Carmo. “Introduction to Liquid Alkaline Electrolysis”. In: *DOE Hydrogen Energy Earthshot Experts Meeting on Advanced Liquid Alkaline Water Electrolysis*. NEL. Jan. 2022.

[62] Kevin H. R. Rouwenhorst, Anthony S. Travis, and Leon Lefferts. “1921–2021: A Century of Renewable Ammonia Synthesis”. In: *Sustainable Chemistry* 3.2 (Apr. 2022), pp. 149–171.

[63] Mostefa Ouki Ali Habib. *Egypt’s Low Carbon Hydrogen Development Prospects*. Research rep. Oxford Institute for Energy Studies, Nov. 2021.

[64] Port of Rotterdam. “Shell to Start Building Europe’s Biggest Green Hydrogen Plant”. In: *Port of Rotterdam Website* (July 2022).

[65] Balkan Green Energy News BGEN. “Sinopec Building World’s Largest Green Hydrogen Plant in China”. In: *Institute for Energy Economics and Financial Analysis* (Aug. 2022).

[66] Oikonomidis Silvestros. “Modeling Gas Crossover in Alkaline Waterel Ectrolysers”. MA thesis. Delft University of Technology, Oct. 2022.

[67] Rodney L. LeRoy, Christopher T. Bowen, and Donald J. LeRoy. “The Thermodynamics of Aqueous Water Electrolysis”. In: *Journal of The Electrochemical Society* 127.9 (Sept. 1980), pp. 1954–1962.

[68] Ernesto Amores et al. “Development of an operation strategy for hydrogen production using solar PV energy based on fluid dynamic aspects”. In: *Open Engineering* 7.1 (June 2017), pp. 141–152.

[69] Isao Abe. *Energy Carriers And Conversion Systems With Emphasis On Hydrogen*. Ed. by Tokio Ohta. Vol. 1. UN Educational, Scientific and Cultural Organization - Encyclopedia of Life Support Systems (EOLSS), 2009. ISBN: 978-1-905839-29-2.

[70] San Ping Jiang and Qingfeng Li. “Alkaline Fuel Cells”. In: *Introduction to Fuel Cells*. Springer Singapore, Aug. 2021, pp. 623–648.

[71] R GILLIAM et al. “A review of specific conductivities of potassium hydroxide solutions for various concentrations and temperatures”. In: *International Journal of Hydrogen Energy* 32.3 (Mar. 2007), pp. 359–364.

[72] Dohyung Jang, Hyun-Seok Cho, and Sanggyu Kang. “Numerical modeling and analysis of the effect of pressure on the performance of an alkaline water electrolysis system”. In: *Applied Energy* 287 (Apr. 2021), p. 116554.

[73] Damien Le Bideau et al. “Review of necessary thermophysical properties and their sensivities with temperature and electrolyte mass fractions for alkaline water electrolysis multiphysics modelling”. In: *International Journal of Hydrogen Energy* 44.10 (Feb. 2019), pp. 4553–4569.

[74] M. Hammoudi et al. “New multi-physics approach for modelling and design of alkaline electrolyzers”. In: *International Journal of Hydrogen Energy* 37.19 (Oct. 2012), pp. 13895–13913.

[75] Tohid Adibi, Atta Sojoudi, and Suvash C. Saha. “Modeling of thermal performance of a commercial alkaline electrolyzer supplied with various electrical currents”. In: *International Journal of Thermofluids* 13 (Feb. 2022), p. 100126.

[76] Hamid Shaker, Hamidreza Zareipour, and David Wood. “Impacts of large-scale wind and solar power integration on California׳s net electrical load”. In: *Renewable and Sustainable Energy Reviews* 58 (May 2016), pp. 761–774.

[77] Christina E. Hoicka and Ian H. Rowlands. “Solar and wind resource complementarity: Advancing options for renewable electricity integration in Ontario, Canada”. In: *Renewable Energy* 36.1 (Jan. 2011), pp. 97–107.

[78] Xiayue Fan et al. “Battery Technologies for Grid-Level Large-Scale Electrical Energy Storage”. In: *Transactions of Tianjin University* 26.2 (Jan. 2020), pp. 92–103.

[79] Matthias Resch et al. “Impact of operation strategies of large scale battery systems on distribution grid planning in Germany”. In: *Renewable and Sustainable Energy Reviews* 74 (July 2017), pp. 1042–1063.

[80] Paul Zummo. “America’s Electricity Generaton Capacity: 2022 Update”. In: *American Public Power Association* (Mar. 2022).

[81] D. Das et al. “An optimal design of a grid connected hybrid wind/photovoltaic/fuel cell system for distributed energy production”. In: *31st Annual Conference of IEEE Industrial Electronics Society, 2005. IECON 2005.* IEEE, 2005.

[82] International Renewable Energy Agency. “Renewable Capacity Highlights”. In: *IRENA* (Apr. 2022).

[83] Rohit Sen and Subhes C. Bhattacharyya. “Off-grid electricity generation with renewable energy technologies in India: An application of HOMER”. In: *Renewable Energy* 62 (Feb. 2014), pp. 388–398.

[84] Getachew Bekele and Getnet Tadesse. “Feasibility study of small Hydro/PV/Wind hybrid system for off-grid rural electrification in Ethiopia”. In: *Applied Energy* 97 (Sept. 2012), pp. 5–15.

[85] Abdullah Al-Sharafi et al. “Techno-economic analysis and optimization of solar and wind energy systems for power generation and hydrogen production in Saudi Arabia”. In: *Renewable and Sustainable Energy Reviews* 69 (Mar. 2017), pp. 33–49.

[86] Augusto Montisci and Marco Caredda. “A Static Hybrid Renewable Energy System for Off-Grid Supply”. In: *Sustainability* 13.17 (Aug. 2021), p. 9744.

[87] Roshani Kaluthanthrige and Athula D. Rajapakse. “Operational Optimization of a Remote Off-Grid Hybrid Renewable Energy System in Northern Canada”. In: *2019 IEEE 7th International Conference on Smart Energy Grid Engineering (SEGE)*. IEEE, Aug. 2019.

[88] M. Kalantar and S.M. Mousavi G. “Dynamic behavior of a stand-alone hybrid power generation system of wind turbine, microturbine, solar array and battery storage”. In: *Applied Energy* 87.10 (Oct. 2010), pp. 3051–3064.

[89] Nabil A. Ahmed, Masafumi Miyatake, and A.K. Al-Othman. “Power fluctuations suppression of stand-alone hybrid generation combining solar photovoltaic/wind turbine and fuel cell systems”. In: *Energy Conversion and Management* 49.10 (Oct. 2008), pp. 2711–2719.

[90] Fred Guterl. “The Rise Of The Hybrids: This Plant Combines Wind And Solar Power To Keep Renewable Electricity Flowing”. June 2018.

[91] Luis M. Gandía et al. “Renewable Hydrogen Production: Performance of an Alkaline Water Electrolyzer Working under Emulated Wind Conditions”. In: *Energy Fuels* 21.3 (Mar. 2007), pp. 1699–1706.

[92] Irem Firtina-Ertis, Canan Acar, and Ercan Erturk. “Optimal sizing design of an isolated stand-alone hybrid wind-hydrogen system for a zero-energy house”. In: *Applied Energy* 274 (Sept. 2020), p. 115244.

[93] A. Ganguly, D. Misra, and S. Ghosh. “Modeling and analysis of solar photovoltaic-electrolyzer-fuel cell hybrid power system integrated with a floriculture greenhouse”. In: *Energy and Buildings* 42.11 (Nov. 2010), pp. 2036–2043.

[94] Alejandro Ibáñez-Rioja et al. “Simulation methodology for an off-grid solar–battery–water electrolyzer plant: Simultaneous optimization of component capacities and system control”. In: *Applied Energy* 307 (Feb. 2022), p. 118157.

[95] S.M. Muyeen, R. Takahashi, and J. Tamura. “Electrolyzer switching strategy for hydrogen generation from variable speed wind generator”. In: *Electric Power Systems Research* 81.5 (May 2011), pp. 1171–1179.

[96] Dayi Yamashita et al. “A new solar to hydrogen conversion system with high efficiency and flexibility”. In: *2017 IEEE 6th International Conference on Renewable Energy Research and Applications (ICRERA)*. IEEE, Nov. 2017.

[97] Marius Holst et al. *Cost Forecast for Low-Temperature Electrolysis – Technology Driven Bottom-Up Prognosis for PEM and Alkaline Water Electrolysis Systems*. Research rep. Fraunhofer Institute for Solar Energy Systems ISE, Oct. 2021.

[98] Fuel Cells and Hydrogen Observatory (FCHO). *Levelised Cost of Hydrogen of EU Countries + UK and Norway*. Digital Publication. 2022.

[99] Kristian Mera. “Thermal Modelling of an Alkaline Electrolyer Under Variable Load”. MA thesis. Delft University of Technology, Sept. 2022.

[100] Burin Yodwong et al. “Faraday’s Efficiency Modeling of a Proton Exchange Membrane Electrolyzer Based on Experimental Data”. In: *Energies* 13.18 (Sept. 2020), p. 4792.

[101] Øystein Ulleberg. “Stand-alone power systems for the future: optimal design, operation and control of solar-hydrogen energy systems”. In: (1998).

[102] National Renewable Energy Laboratory. *Champion Photovoltaic Module Efficiency Chart*. Website Publication. Apr. 2022.

[103] David Faiman. “Assessing the outdoor operating temperature of photovoltaic modules”. In: *Progress in Photovoltaics: Research and Applications* 16.4 (June 2008), pp. 307–315.

[104] A Jain. “Exact analytical solutions of the parameters of real solar cells using Lambert W-function”. In: *Solar Energy Materials and Solar Cells* 81.2 (Feb. 2004), pp. 269–277.

[105] Amelie Driemel et al. *Baseline surface radiation data (1992-2017)*. en. 2018.

[106] Koninklijk Nederlands Meteorologisch Instituut. *Weer Waarnemingen*. Digital Publication on Own Platform. June 2023.

[107] Eduardo Martins Deschamps and Ricardo Rüther. “Optimization of inverter loading ratio for grid connected photovoltaic systems”. In: *Solar Energy* 179 (Feb. 2019), pp. 106–118.

[108] T. Zidane et al. “PV array and inverter optimum sizing for grid-connected photovoltaic power plants using optimization design”. In: *Journal of Physics: Conference Series* 1878.1 (May 2021), p. 012015.

[109] European Union Fuel Cells and Hydrogen Joint Undertaking. *Levelised Cost of Hydrogen*. Research rep. Fuel Cells and Hydrogen Observatory, Mar. 2022.

[110] D. C. Jordan and S. R. Kurtz. “Photovoltaic Degradation Rates-an Analytical Review”. In: *Progress in Photovoltaics: Research and Applications* 21.1 (Oct. 2011), pp. 12–29.

[111] Gusta Renes Gerbert Romijn. *General Guidance for Cost-Benefit Analysis*. Research rep. PBL Netherlands Environmental Assessment Agency, June 2015.

[112] United States Office of Energy Efficiency & Renewable Energy. *Technical Targets for Liquid Alkaline Electrolysis*. Digital Publication. 2022.